Electrochemistry in anisotropic etching of silicon in alkaline solutions

A kinematic wave analysis

Q.D. Nguyen

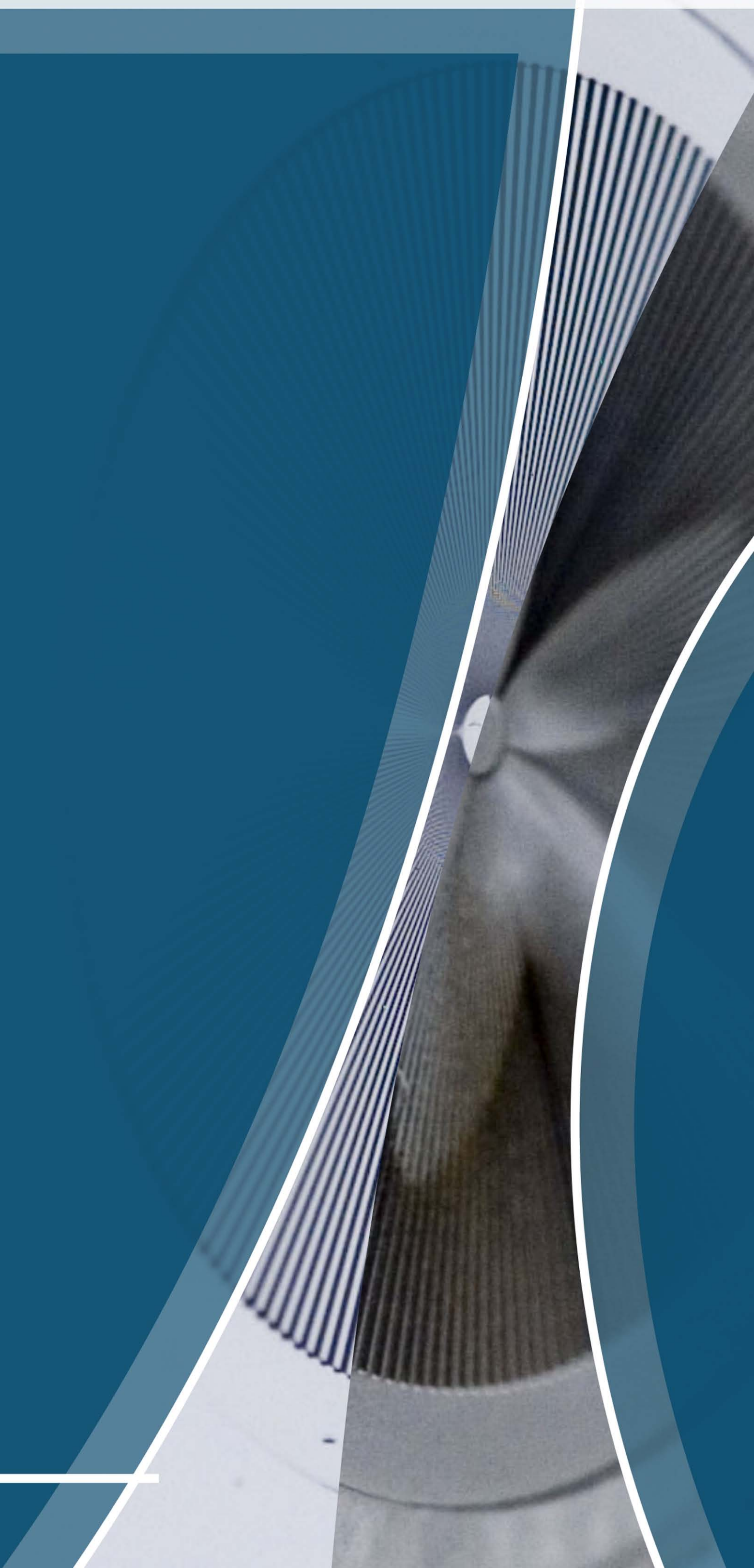

Electrochemistry in anisotropic etching of silicon in alkaline solutions

A kinematic wave analysis

Quoc Duy Nguyen

The research described in this thesis was carried out at the Transducers Science and Technology Group of the MESA+ Research Institute at the University of Twente, Enschede, The Netherlands. The project was financially supported by the Dutch Technology Foundation (STW).

Promotiecommisie:

Voorzitter	
Prof. dr. P.J. Gellings	Universiteit Twente
Secretaris	
Prof. dr. ir. A.J. Mouthaan	Universiteit Twente
Promotor	
Prof. dr. M.C. Elwenspoek	Universiteit Twente
Leden	
Prof. Dr. Eng. K. Sato	Nagoya University
Prof. dr. P. French	Technische Universiteit Delft
Prof. dr. J.J. Kelly	Universiteit Utrecht
Prof. dr. E. Vlieg	Radboud Universiteit Nijmegen
Prof. dr. J.G.E. Gardeniers	Universiteit Twente
Dr. ir. H.V. Jansen	Universiteit Twente
Dr. E. van Veenendaal	Polymer Vision ltd.

Cover:
The cover shows a collage of etched and unetched wagon-wheel patterns used for the measurement of the anisotropic etch rate of silicon in alkaline solutions.

Electrochemistry in anisotropic etching of silicon in alkaline solutions:
A kinematic wave analysis
Q.D. Nguyen
Ph.D. Thesis, University of Twente, Enschede, The Netherlands
ISBN: 978-90-365-2551-0

Printed by Wohrmann Printservice, Zutphen, The Netherlands

ELECTROCHEMISTRY IN ANISOTROPIC ETCHING OF SILICON IN ALKALINE SOLUTIONS

A KINEMATIC WAVE ANALYSIS

PROEFSCHRIFT

ter verkrijging van
de graad van doctor aan de Universiteit Twente,
op gezag van de rector magnificus,
prof. dr. W.H.M. Zijm,
volgens het besluit van het College voor Promoties
in het openbaar te verdedigen op
donderdag 27 september 2007 om 13.15 uur

door

Quoc Duy Nguyen
geboren op 30 september 1978
te Saigon, Vietnam

Dit proefschrift is goedgekeurd door de promotor:

Prof. dr. M.C. Elwenspoek

"Discover the force of the heavens O Men;
once recognised it can be put to use."
Johannes Kepler (1602)

Contents

Chapter 1

Introduction

This chapter provides a brief outline of anisotropic wet chemical etching of silicon in alkaline solutions. It is examined at increasingly smaller scale, starting from its role in MEMS technology. A closer look is given to the silicon surface morphology, where features such as pyramidal hillocks and hexagonal etch pits are commonly observed. On an even smaller scale, the crystal structure of silicon is discussed. Important features, such as periodic bond chains and step terminations, are highlighted. On a chemical level the etch mechanism of a single surface atom is outlined. At the end of this chapter, an outline of this thesis is given.

1.1 Anisotropic etching of silicon

Etching is the process of using an acidic or caustic chemical to cut into unprotected areas of a particular material. Initially used in the 15th century for decorating plate armor and sword blades, the metal surface (typically steel or copper) was first covered with a wax-like material. Part of the wax was removed to create decorative patterns. These were subsequently transfered into the metal by submerging the surface in an acid solution (the etchant). The German artist Daniel Hopfer is believed to be the first to use the etching process in printmaking, competing with the, at the time more common, engraving techniques. For artists, its great advantage lies in the simplicity of the technique which does not require special skills in metal working. Scratching the drawings directly into the waxlayer allowed for highly detailed etchings and prints. This technique has been used by many great artist throughout the centuries.

This etch process is naturally not restricted to metal alone. The etching of silicon-based materials is also quite common, as decorative glass is often etched in fluoride-based etchants. With the emergence of semiconductor technology, pure silicon (Si) has gained importance, as it has become by far the most used semiconductor material[35]. This has, for a large part, been made possible by the introduction of the Czochralski method[81] for making doped ultra pure single-crystal silicon. The combination of low raw material cost, relatively simple processing and good material characteristics makes it currently the best compromise among the various competing semiconducter materials. Si ingots are grown from a silicon melt using a seed crystal. The crystal is dipped into the melt and slowly pulled upwards while rotating. The rate of pulling and rotation determines the size of the cylindrical ingot. For the required semiconductor properties, Si can be doped. This can be done relatively easy by dissolving the appropriate elements into the Si melt, such as phosphorous for n-type and boron for p-type Si. From the ingots, Si wafers are cut and subsequently polished. The crystal orientation of the Si ingot and the wafers are determined by the original seed crystal. The most common wafers are (100) and (111) oriented, (110) oriented wafers are also often produced but are less commonly used.

The need to ‘shape’ the silicon wafer surface in semiconductor technology has resulted in the development of silicon etching. Instead of concentrated acids, as in the case of metals, alkaline solutions or fluoride based etchants are commonly used. Instead of wax-based materials, silicon oxide (SiO_2), silicon nitride (SiN_x) or even metal are used as masklayers. While materials such as metals commonly etch isotropically, a crystalline material such as Si, can be etched anisotropically.

Isotropic etching is where the removal rate of the material is not orientation dependent. A common isotropic etchant for Si is the HNO_3/HF mixture. *Anisotropic* etching, on the other hand, is when the etch rate is not equal in all directions. Alkaline solutions such as NaOH, KOH or TMAH etch Si anisotropically. The reason for this difference can be traced back to the difference between the surface reaction rate and the etchant diffusion rate. If the surface (etch) reaction is significantly larger then the diffusion of the etchant to the surface, the overall etch rate will be effectively controlled by the diffusion. Being dependent on concentration gradients, diffusion controlled etching is isotropic and will result in rounded etch shapes. If, however, the surface reaction is significantly slower then the diffusion rate, the overal etch rate is controlled by the surface reaction. In the case of Si, the surface reaction depends on the crystallographic orientation of the exposed Si surface (anisotropic). Etch profiles are then not necessary round but can be rectangular or triangular in shape shapes.

The shape of the etch profiles are clearly linked to the Si crystal structure. With this in mind, several guidelines can be used to predict the etch shape of Si in anisotropic etchants. Etching a convex shape will ultimately result in a structure that is determined by the fastest etching crystal orientations. Etching a concave structure, on the other hand, will ultimately result in a structure bound by the slowest etching planes. For Si the slowest etching crystal orientations are the (111) family. Identifying the fastest etching crystal orientations is however not as straight forward. It is well known and also reflected in the measurement within this thesis that, the etch rate maxima do not correspond to any of the major crystal orientations ((100), (111) or (110)). This gives rise to complex faceting of convex structures. One of the challenges in 'shaping' silicon in micromachining is predicting, controlling or avoiding this faceting. However, by using these simple guidelines alone it is often possible to fabricate complex structures.

1.2 A closer look: MEMS level

The need to fabricate 3-dimensional structures in Si has gained importance with the development of MEMS technology. MEMS, which is an acronym for micromechnical electrical systems, is an evolution of the silicon technology developed in the field of integrated circuits (IC). It encompasses the design and fabrication of devices with micro-sized features. These include a large variety of electro-mechanical devices such as sensors, actuators and micro-fluidics systems. Although currently not as prevalent as IC technology, MEMS has quietly integrated into certain every day applications such as inkjet printer heads[9, 10] or airbag sensors in modern cars[113]. The ability to combine a large number of functions within a single smaller package can cut costs and maintenance. Additionally, the smaller size introduces these devices to a wider field of use. This makes it highly interesting for applications such the integrated impact sensor systems in the automotive industry, integrated optical devices[16] or biomedical and chemical analytical systems (the lab-on-a-chip concept[1]).

Micromachining is a general term used to describe the fabrication process of MEMS devices[28]. It contains a wide range of fabrication processes which can be split into bulk and surface micromachining. Starting with single-crystal silicon wafers as a substrate, bulk micromachining is used to fabricate structures into the Si wafer itself. In surface micromachining the structures are fabricated on a layer deposited on top of the Si wafer surface. A typical fabrication process of a complex MEMS design require the use of both micromachining technologies.

Anisotropic etching of Si in alkaline solutions is one of the earliest bulk-micromachining techniques available. By exploiting the difference in etch rate of the crystal surfaces (such as (111) vs. (100)), complex Si structures can be fabricated. Even though more advanced bulk micromachining technologies, such as directional reactive ion etching (DRIE), offer more design and fabrication flexibility, wet chemical etching has remained an important tool in the MEMS designer's arsenal. The simplicity and relative low cost are difficult

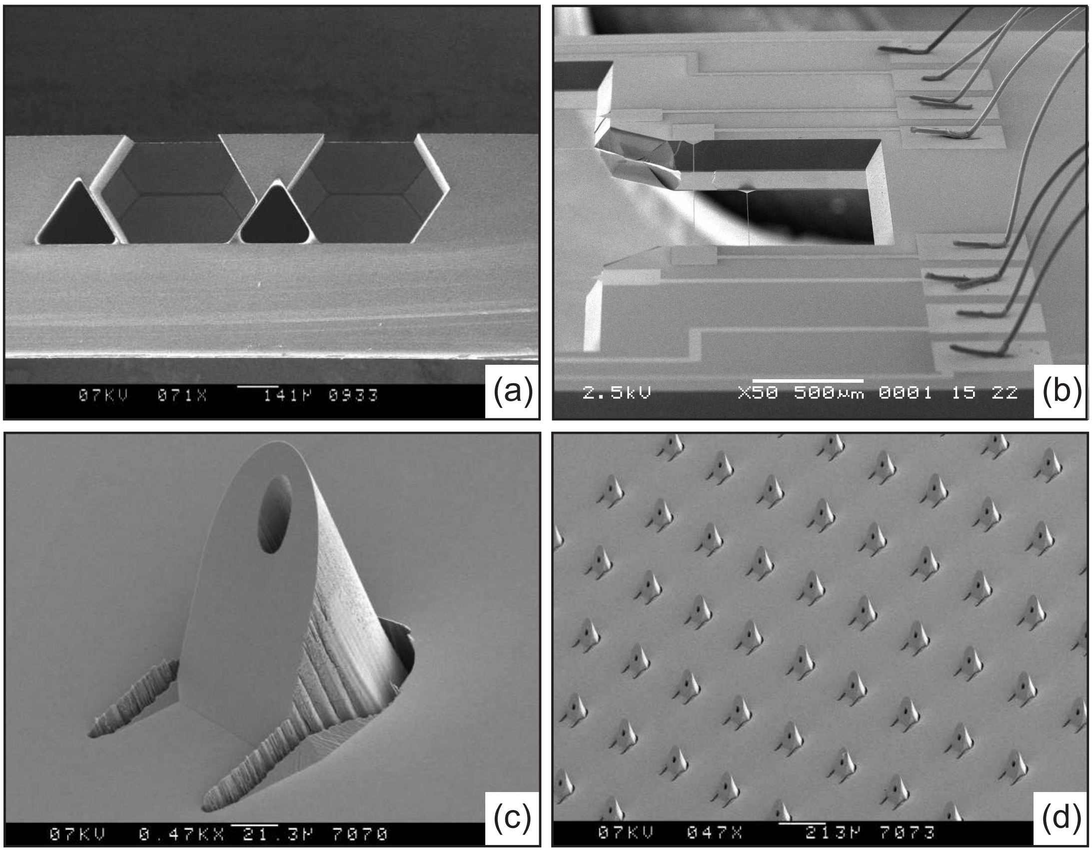

Figure 1.1: *Some examples of some MEMS devices which rely heavily on anisotropic etching in the fabrication process. (a) shows a cross section of the duckbill check valve for fluidics designed by Oosterbroek et al.[73]. The smooth side walls are (111) crystal planes, which are exposed using anisotropic etching. (b) shows a microflown[24] which consists of two suspended wires, which are etched free using KOH. (c) shows a micromachined microneedle developed by Gardeniers et al.[34], which is fabricated using combination of dry and wet chemical etching. (d) shows an array of these microneedles.*

to match. As anisotropic etching is controlled by the crystal structure of the Si, structures with very specific crystallographic surface orientations can be fabricated. This is very usefull for MEMS devices such as Si AFM tips[108], nanochannels[44] or in-plane microvalves[73] where flat, well-defined surfaces are required (see figure 1.1a) . The process is also very suitable for the removal large amounts of silicon, creating access holes and free standing[55] or suspended structures[63] (see figure 1.1b).

However, this link with the Si crystal structure is also its Achilles' heel, as the device designs are restricted to a limited number of (well-defined) surface orientations. This has an additional disadvantage that only flat surfaces can be fabricated. With smart mask designs and fabrication procedures, especially in combination other micromachining techniques, complex structures can be still fabricated (see figure 1.1c and d).

The demands for increasingly smaller structures and better Si surface qualities requires a high degree of predictability and control over anisotropic etching. Looking closer at the process, issues such as surface roughness, macroscopic surface features, morphology, etch inhomogeneity and faceting become a problem. Understanding the physical and chemical background behind the etch process, allows for more control over the fabrication process.

1.3 A closer look: microscopic level

Many MEMS applications require smooth, flat Si surfaces for optimal device performance. Creating a smooth Si surface using wet chemical etching is, however, not trivial. Etched silicon surfaces generally show a large variety of microscopic features depending on the surface orientation. It is important to understanding how and under what conditions these features are formed. For practical applications, it is especially important to investigate ways to suppress the formation of these features.

A large amount of research is available concerning the characterisation and formation mechanism of these etch features and typical surface morphologies under different etching conditions[25, 30, 87, 100, 118]. Others have used the microscopic features to investigate the etch mechanism and surface kinetics[39, 49].

Several of these distinct surface features can be highlighted. One of the most common is the pyramidal hillock[17, 60, 72, 83]. These micrometer sized, four- or eight-sided hillocks (see figure 1.2a) are generally observed on (100) surfaces etched in concentrated KOH solutions. The stability if these features remains unclear. As the hillocks are convex, they are expected to be etched away rapidly. Kinetic Monte Carlo (kMC) simulations have, however, shown that these features can be stable if several requirements are met[41]. One of the main requirements is the local stabilisation of the apex of the pyramidal hillock. The nature of such a stabilisation under 'normal' etching conditions remains the major question. It is clear that the presence of an artificially created micro mask (consisting of an etchant-resistant materials such as silicon nitride (SiN_x) or silicon oxide (SiO_2)) can create similar features[115]. It is, however, unlikely that a micro mask of the size and stability of an artificial SiN_x/SiO_2 mask can be created spontaneously. Several micro-masking mechanisms have been suggested, including the adsorption of silicate particles[72, 99], or certain metal ions[41, 91] and the adhesion of hydrogen bubbles [11, 83]. Lacking direct evidence for these mechanisms, it remains difficult to explain the (required) stability of such a micro mask on top of an evolving (etching) surface. As (100) Si wafers are most commonly used in MEMS technology, investigating ways to suppress these hillocks is also important. It has been shown that process conditions such as very high temperature[92] or the application of a anodic electrical potential[17] can suppress hillock formation. The use of organic additives[20] or chemical oxidisers[17] can have similar results.

For the creation of flat surfaces, (111) surfaces are often more suitable. Although the (111) surface is typically much smoother then (100), it is still not entirely flat. Figure 1.2b shows a typical etched (111) surface which is covered with shallow concave etch pits with a triangular/hexagonal shape. Etch experiments have shown that the presence of these pits are almost unavoidable when etching in alkaline solutions for a long period of time. How these pits are formed remains unclear as they requires a local increase of the etch rate at the bottom of the pits. Bulk material defects, which can be caused by interstitial oxygen atom[47], can be responsible for this local etch rate increase. To account for a surface totally covered with the pits, however, the dislocation density of the bulk material

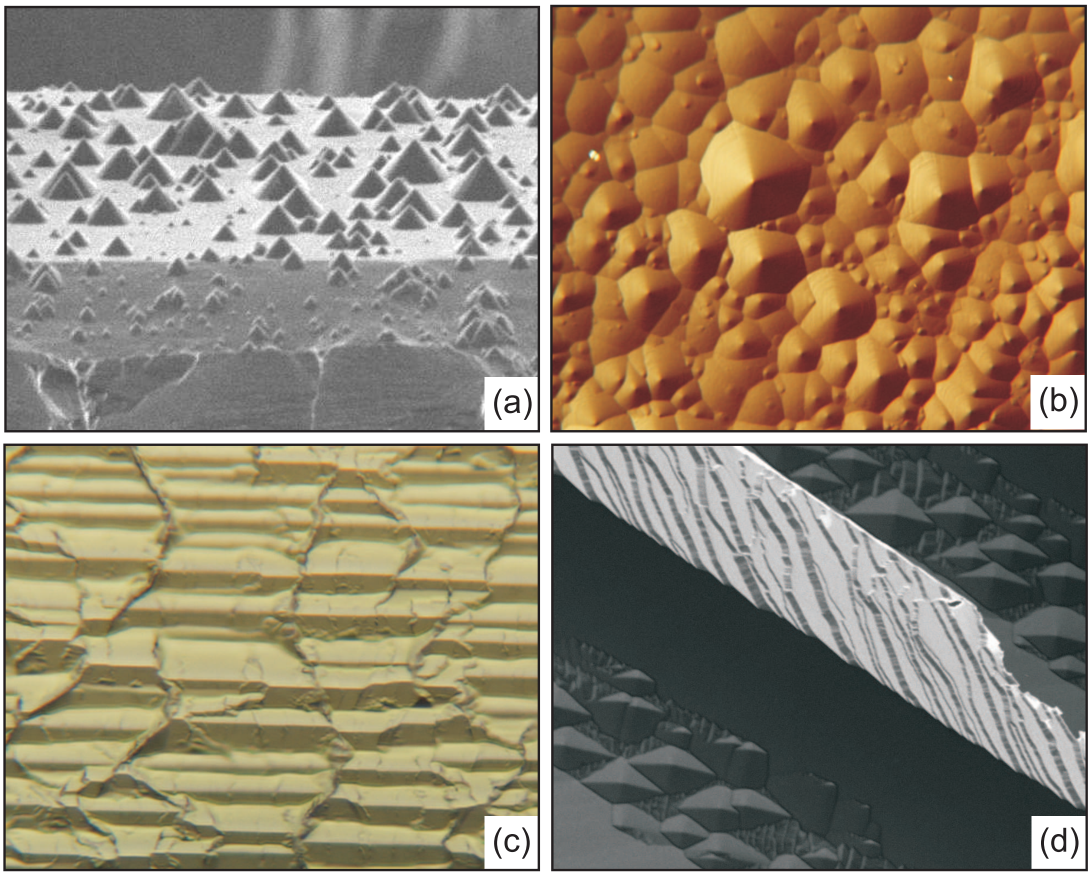

Figure 1.2: *Outline of typical etch features and morphology observed on etched Si surfaces. SEM image (a) shows a detail of the top a convex structure. The (100) surface on top is covered with pyramidal hillocks. The (111) surface in image (b) is covered with triangular/hexagonal etch pits. The image is obtained using differential interference contrast (DIC) microscopy. A microscope image of the typical (110) roof-tile morphology is shown in (c). The SEM image in (d) shows 'bunched' steps on the side wall of a Si convex structure.*

would have to be very high.

Unlike both (100) and (111) surfaces, which can produce near-smooth surfaces under certain conditions, the typical morphology of an etched (110) surface consists of large roof-tile structures (see figure 1.2c). In other conditions such as very high KOH concentrations or positive applied potential, trapezoidal hillocks can be observed. The (110) morphology will be discussed in detail in chapter 7. Both the formation and apparent stability of these features also remain unclear

A final microscopic feature that is often observed are bunched macro steps. As outlined in chapter 2, anisotropic etching follows a stepflow mechanism. It is often observed that these steps have a tendency to 'bunch' together forming higher macro steps which can be visible with optical microscopy. A bunched step tends to etch differently from a 'normal' step. The cause of this step bunching is not clear. Simulations performed by both Gosalvez et al.[41] and Garcia et al.[32] have shown that local fluctuations in temperature and/or etchant concentration can cause step bunching. If this is the actual mechanism behind the step bunching phenomenon remains unclear.

The previous paragraphs have outlined several microscopic features commonly observed on various silicon surfaces. It is important to emphasize that direct evidence for a formation mechanism of these features is still lacking. Isolating and testing the proposed mechanisms, without either influencing other chemical/physical parameters or creating an environment where these features will form regardless of their 'natural' occurrence, remain one of the main challenges.

1.4 A closer look: crystal level

As stated in the previous sections, the basis for the observed etch anisotropy lies within the crystal structure of silicon. The unit cell of Si consists of a diamond structure as shown in figure 1.3. The surfaces of the three major orientations are also shown. Examining the surface structure of the major Si orientations, it is evident that (111) surfaces contain Si surface atoms with a single 'dangling' hydrogen atom and three back bonds to the bulk Si-atoms, while (100) surface atoms have two dangling hydrogen atoms and two Si-Si back bonds. It is tempting to primarily ascribe the observed etch rate difference between these two surface to the difference in the number of Si-Si backbonds of (111) and (100) surface sites. Examining the (110) surface, however, shows that it also contains three Si-backbonds while it generally is the fastest etching surface. This is most likely due to the basic structure of (110) surface which resembles chains of tilted (111). This can result in a far different interaction between a surface site with the etching components and even the neighbouring Si atoms, resulting in a higher etch rate than expected. These facts illustrate the complexity of the Si etching mechanism.

Within this work we deal with two molecular features important to anisotropic etching. Step termination and periodic bond chain orientations. Step termination is regarded as the molecular structure of a monolayer step edge on a stable surface. It is generally described in terms of the number of dangling hydrogen atoms bonded to the Si step site. The two main types are dihydrides and monohydrides, which contain two and one attached hydrogen atom, respectively. Although trihydrides are possible, they are considered very

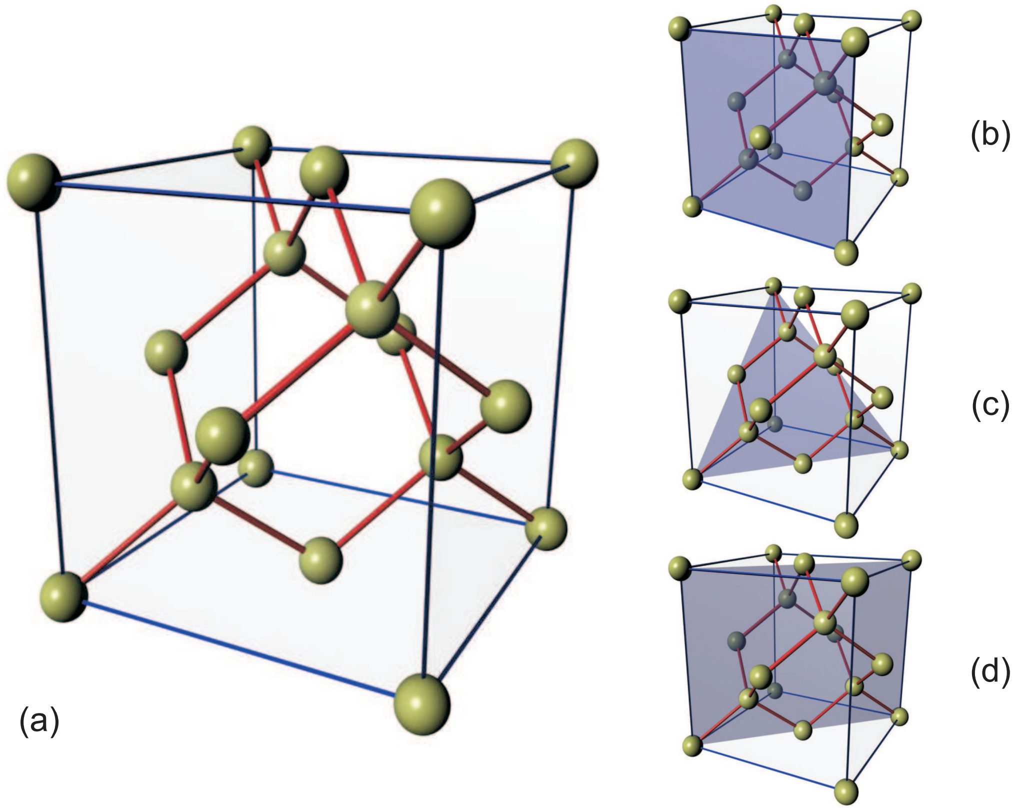

Figure 1.3: *Silicon unit cell (a). The three main crystal orientations (100) (b), (111) (c) and (110) (d) are indicated.*

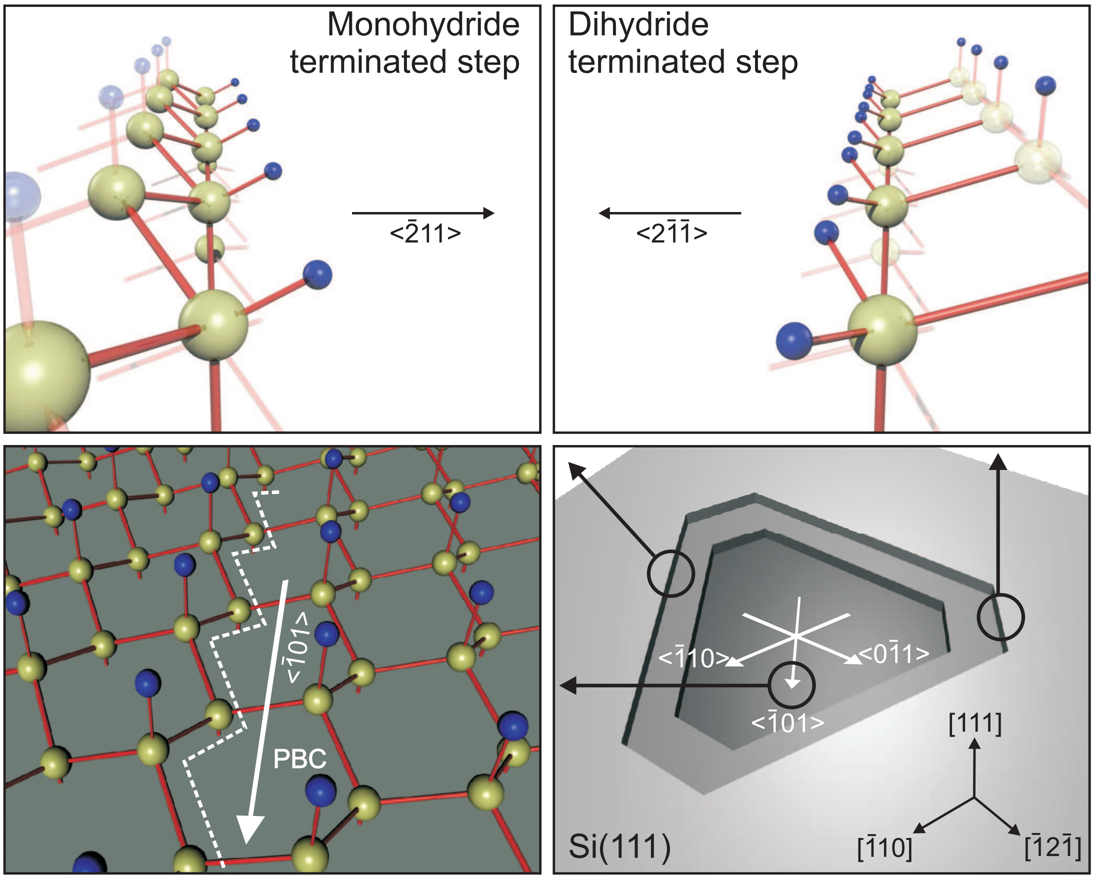

Figure 1.4: *Diagram showing the structure of a dihydride terminated step (top right) and a monohydride terminated step (top left). Bottom left figure shows a PBC on (111). The asymmetry in the molecular structure is clearly visible which leads to the difference in step termination of steps aligned to the same PBC direction. Bottom right figure shows the PBC directions on (111) together with the mono-and dihydride terminated step orientations. Note the 3-fold symmetry which is connected to the three PBC directions.*

unstable with a very short lifetime on the surface.

Gosalvez et al. and Flidr et al. have made even more detailed distinction between surface and step sites, beyond the number of hydrogen atoms alone. Their work included both the orientation of the surface site and even the structure of the surrounding crystal surface. Within this work, a (111) surface step consisting of only dihydrides at the step edge is called a *dihydride terminated step*, while a step consisting only of monohydrides is called a *monohydride terminated step* (see figure 1.4). This difference in molecular structure has large repercussions on the anisotropic etch rates and surface kinetics. Many of the observed phenomena are the result of a difference in reactivity between the step types. These phenomena include triangular/hexagonal shapes of (111) etch pits (see figure 1.2b), the shape and orientation of hexagonal convex etch shape of hemispherical samples (chapter 4) and changes in (110) morphology (chapter 7).

Periodic bond chains (PBC) on the other hand deal with distinct crystal directions. The definition of a periodic bond is that of a straight chain of uninterrupted Si-Si bonds

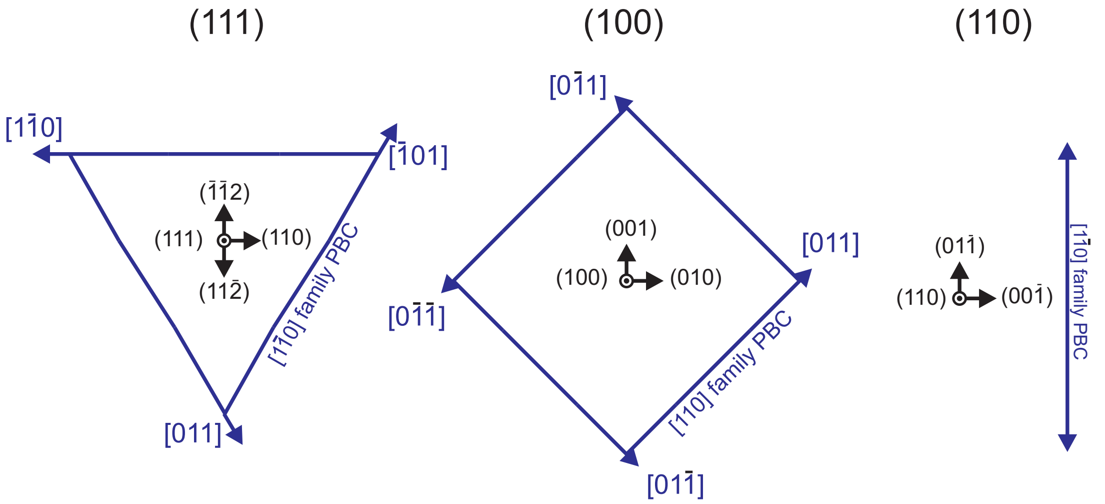

Figure 1.5: *The PBC directions of (111) (left), (100) (middle) and (110) (right) surfaces. Note that the actual PBCs on (111) are asymmetrical in molecular structure, which means that both the slowest and fastest etching (111) step orientations are aligned with respect to the PBC. The (100) PBCs are symmetrical and the most stable steps are aligned with respect to those directions. (110) surfaces only contain a single (symmetrical) PBC which coincides with the PBC directions of (111).*

on the surface, the direction of which does not change at each monolayer[45, 46]. Crystal surfaces where multiple PBC intersect and form a connected net, are stable surfaces[14]. Surface steps where the edge corresponds to a PBC, are considered stable steps. Monohydride terminated steps on (111) surfaces are generally the most stable steps and it is not surprising that these steps are aligned with the PBC. However, the faster etching step, the dihydride terminated step, is also aligned with the PBC (180° rotated from the monohydride terminated step orientation). This is due to the fact that the PBCs on (111) surfaces are asymmetrical. The structure of the step edge depends on which side of the PBC is exposed (figure 1.4). Si(111) surfaces contain a total of three (asymmetrical) PBC directions (figure 1.5) which form a triangular connected net. On the (110) surfaces, a single symmetrical PBC can be defined along the roof-tile morphology (figure 1.5). On (100) surfaces a single symmetrical PBC can be identified, the direction of which changes 90° with each monolayer. The PBCs therefore do not form a connected net which means that the (100) surface is not stable. However, due to surface reconstruction[6], (100) behaves as a stable surface. Both PBC directions then coincide with the most stable steps present on (100) surfaces. Within this work, for all intents and purposes, (100) can be considered a stable surface containing two PBC directions (figure 1.5).

1.5 A closer look: chemical level

Despite the fact that chemical etching of silicon in concentrated alkaline solution has been investigated for several decades, many questions still exist concerning the actual etch mechanism and how this mechanism results in the observed etch anisotropy. Currently,

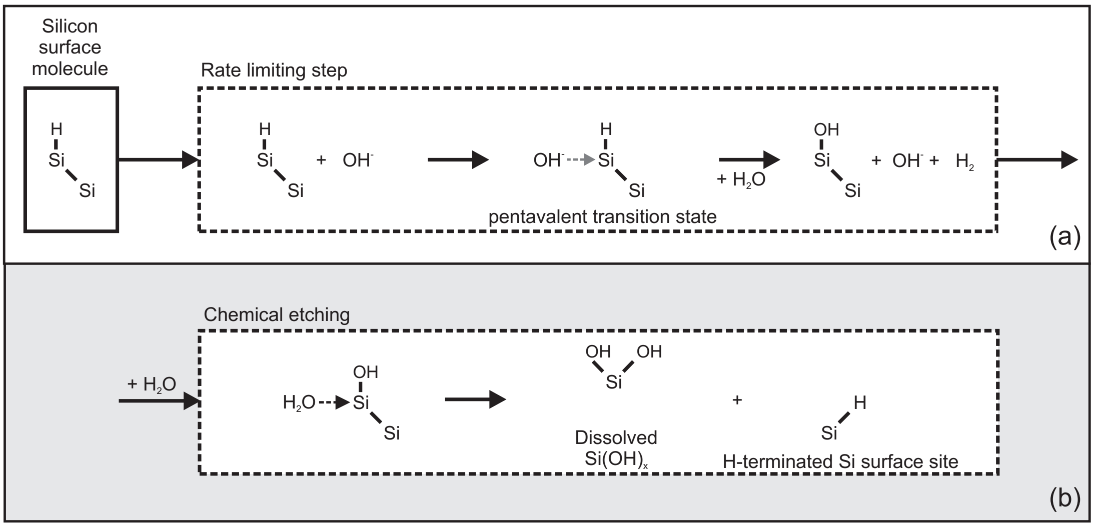

Figure 1.6: *Diagram of Si etch reaction mechanisms in alkaline solution showing (a) the first oxidation step via the pentavalent reaction intermediate. This step is considered to be the rate limiting step. The subsequent chemical etching step is shown in (b), where a reaction with water results in a dissolved Si(OH)$_x$ and a new exposed hydrogen-terminated Si*

the etch reaction of silicon is most commonly described as a two step mechanism [4, 110]. Figure 1.6 shows a diagram of the chemical reaction path. For simplicity, only a single Si-Si back bond is considered in this figure. The reaction is essentially repeated for every additional Si-Si back bond. A hydrogen terminated Si surface atom is first oxidised to a hydroxide terminated Si atom[13, 11, 18, 107, 110] via a pentavalent intermediate[13, 11, 51]. Hydrogen in the form of H_2 is formed in this step. The OH^- present in the etching solution acts as a catalyst within the reaction. This means that there is no net consumption of OH^-. The subsequent reaction step is the actual etching reaction as the hydroxide terminated Si surface atom reacts with H_2O, resulting in a dissolved silicate molecule ($Si(OH)_x$) and the exposure of a new Si-H surface site. The overall etch rate is dependent on the (OH^-) concentration[84] which indicates that the first oxidation reaction is the rate limiting step. More specifically, the formation of the pentavalent transition state is the major factor controlling the absolute etch rate.

The formation itself is determined by a large number of factors including the surface topology (such as terrace or step sites), molecular configuration (i.e. specific type of surface or step sites), additional steric and electrostatic interaction between the molecular configuration, reaction components, nearest and next-nearest neighbouring Si atoms[49, 50, 40, 41]. These factors not only determine the absolute etch rate but also the etch anisotropy as mentioned in the previous section. However, the reaction, as outlined in figure 1.6, does not consider these factors. It can therefore not account for the observed anisotropy in etch rate. It is necessary to include this additional information to obtain a better description of the anisotropic etch mechanisms. These also include topological information in the form of microscopic processes such as step flow, surface roughening and step bunching. Additionally, molecular information such as specific surface sites and surface and step termination is also necessary. Within this work the kinematic wave theory was used to obtain information concerning several of these microscopic processes.

1.6 Aim of this thesis

As the previous section has shown, anisotropic etching of silicon in alkaline solutions is a highly complex system. While the current understanding and control of the etching process is sufficient for most MEMS designs and applications, a better understanding of the etch process can increase its controllability and predictability. This can result in improved device performance and yield, or the design and fabrication of more intricate structures and devices. A full understanding of anisotropic etching, including the etch mechanism, the formation of different etch features and the influence of different physical and chemical parameters, requires an in-depth understanding of the process at different scales. To make matters worse, electrochemical aspects have become increasingly important in recent years. This adds an additional level of complexity to the process. As the electrochemistry has often not been included in the literature, it is of importance to gain a better understanding of its influence on the etch mechanism. The electrochemistry of bulk Si in alkaline solution is well established on a chemical scale. How this translates to larger (microscopic) scale is largely unknown. On this scale, properties such as step velocity and terrace roughening are important, but are very difficult to measure directly.

This thesis aims to investigate the influence of the electrochemistry on this microscopic scale. The kinematic wave theory provides a method of investigating the anisotropic etch rate in terms several microscopic properties. In combination with etch experiments using specific sample designs (which include wagon-wheel patterns and hemispherical samples), the impact of the electrochemistry can then be investigated. While an etch model, based on the kinematic wave theory, is used to interpret the experimental data, the experimental data, in turn, is used to improve the etch model itself to incorporate observed etch patterns and phenomena. In addition, control of the electrochemistry allows for the investigation of several other parameters and features. In this work we have investigated the TMA^+ interaction with silicon, in an attempt to gain more insight into the role of (ionic) additives. Additionally, electrochemical controlled in-situ measurements were performed to investigate morphology evolution and formation of morphology features on (110) surfaces.

1.7 Thesis outline

As the title suggests, this thesis relies on the kinematic wave theory to analyse the obtained experimental results. In chapter 2, an outline is given of the theory and its application to anisotropic etching of silicon, as proposed by van Veenendaal et al.[104]. The controlling etch mechanisms on which the model is based, are discussed from an atomistic point of view. The construction of the basic etch model is subsequently outlined in a step-by-step manner.

In chapter 3 the influence of the electrochemistry on the etch process is investigated. The design and fabrication of micromachined sample geometries, capable of measuring the etch rate of a large number of surface orientations, are discussed. These sample designs include a pre-etched wagon-wheel pattern and a masked pre-etched trench pattern. The influence of an applied potential is expressed in terms of microscopic processes (such as terrace roughening and step/kink velocity) using the kinematic wave theory. Additionally, the occurrence of step anisotropy reversal due to increased electrochemical oxidation is discussed.

Experiments using hemispherical Si samples were performed at the Micromachining and MEMS lab in Nagoya, Japan. These detailed measurements show the presence of several etch phenomena which cannot be observed using wagon-wheel patterns or predicted by the basic etch model used in chapter 3.

The observed hexagonal etch pattern in the vicinity of the (111) orientations is consistent with the fact that a step/kink based view of the (111) step anisotropy is incomplete. A more detailed distinction between (111) step sites is required and is discussed in chapter 4. To integrate these observations together with the step anisotropy reversal observed in chapter 3, the basic model is extended to a 10-parameter model. The accuracy of the the extended model is compared to the basic etch model. Examining the change in (111) step velocity obtained from the experimental data provides additional information concerning the effect of TMA^+ interaction and electrochemical oxidation on specific (111) step sites.

A second feature of interest is located in the vicinity of the (110) orientation. Here the measurements show a peculiar saddle point in the etch rate. To describe this feature, a pseudo stepflow/birth-and-spread mechanism is proposed in chapter 5, replacing the (110) phenomenological corrections outlined in chapter 2. This mechanism is integrated into the extended model in chapter 4. The resulting 14-parameter model is compared to the extended 10-parameter model and its usability in combination with the experimental data is discussed.

The observations obtained from the wagon-wheel patterns have shown that the electrochemistry can be used to investigate the interaction mechanism between Si and TMAH. In chapter 6, a proposed electrostatic interaction mechanism between the TMA^+ cation and Si (111) step sites is examined using electrochemical controlled etch experiments on hemispherical Si samples. The interaction mechanism is discussed together with the expected change to the (111) step velocity as a result of an additional applied potential. The step velocity is obtained using the 10-parameter extended model outlined in chapter 4. The changes to the step velocity and step anisotropy as a function of both the applied potential and TMA^+ concentration are examined. The results provides information on, not only the proposed electrostatic interaction mechanism, but also on step-site specific interaction of both TMAH and applied potentials.

General observations of the (110) morphology in chapter 3 show large variations at different etching conditions. In chapter 7 the (110) morphology changes induced by electrochemical oxidation are investigated in-situ. An outline of the (110) morphology from an atomistic point of view is given based on kMC simulations in the literature. The morphology is subsequently investigated using different etchant concentration and the addition of a chemical oxidiser. In-situ measurements allows for the formation and evolution of the morphology to be monitored. To quantify the observations and detect subtle changes, an image analysis procedure is used to express the observations in terms of three morphology parameters. The formation and evolution of the (110) morphology are investigated both under OCP and an applied potential.

Finally, chapter 8 provides a general conclusion of this thesis together with recommendations for future research.

Chapter 2

Kinematic wave theory: General outline and implementation

Van Veenendaal et al. have used the kinematic wave theory specifically to describe the anisotropic etching of silicon. Based on both the stepflow and birth-and-spread mechanisms, the model consists of a continuous function which is dependent on the crystal surface orientations and several physical parameters. It is therefore suitable as a characterisation method by expressing Si etch systems in terms of physical parameters and microscopic properties. In this chapter the kinematic wave theory together with the stepflow and birth-and-spread mechanisms are outlined. The actual construction of the etch model for silicon in alkaline solutions using the elementary network assembly method is outlined in detail.

2.1 Introduction

Experimentally investigating the impact of process parameters, such as etchant compositions or electrochemical conditions, poses several problems. Using only experimental data, the influence of these parameters is generally evaluated in terms of the change in overall anisotropic surface etch rate. For a better understanding of the influence of these factors, information on a more basic level is desirable. Information in terms of chemical or physical processes allow for a better understanding of, not only the effect of these external factors, but also of the etch mechanism as a whole. The etch systems have to be characterised in a smaller set of physical/chemical processes. This can be achieved by analysing the etch data using anisotropic etching models. Arguably one of the most valuable physical based models has been kinetic Monte Carlo (kMC). Models based on kMC have a strong physical basis and have been used for a wide variety of systems dealing with surface reactions including etching[40], crystal growth[19] and surface catalysis[58]. Typical kMC simulation evaluates the process by dividing the surface into discreet cells each with a specific reaction rate and reaction probability. More complex systems can incorporate secondary effects such as the topography of the surface or nearest and next-nearest neighbour interaction. For etching, kMC is very suitable for the evaluation of small scale surface morphology features and formation[39, 49, 102]. However, it also means that scaling kMC to simulate larger systems and surfaces is difficult as it is limited by available computer power and memory requirements. Features and properties that require a large model system, such as the evaluation of high-index planes or the determination of overall surface etch rates, are difficult to model using kMC. Direct comparison between kMC predictions and experimental measurements is therefore impractical as the test structures are generally far too large to be directly modeled in kMC. Models such as cellular automata (CA)[37] are based on kMC but aim at circumventing these difficulties at the expense of physical accuracy. A different approach is the use of the kinematic wave theory as an etch system characterisation method. The model first proposed by van Veenendaal et al.[96, 98, 104] is a continuous (analytical) description of the etch systems, unlike the discrete approach of kMC or CA. It describes anisotropic etching in terms of the interaction between two distinct physical processes: stepflow and birth-and-spread mechanism. The model implementation used by van Veenendaal et al. directly calculates anisotropic etch rates as a function of the crystal surface orientation. It is therefore directly usable as an analysis and characterisation method for anisotropic etch experiments. The etch system can then be characterised in terms of a smaller number of parameters controlling macroscopic properties. These properties, including surface/terrace roughening and step velocity, are easier to observe and verify experimentally than single site reaction parameters as used in kMC.

2.2 Theory

2.2.1 Kinematic wave theory

The anisotropic etch model introduced by van Veenendaal et al. is based on the kinematic wave theory by Frank and Chernov[31]. In its classical form the theory consists of a continuum description of propagating interfaces, of which the propagation velocity is dependent on the orientation of the interface. As the theory is a general description of this propagation, it does not specify any underlying physical mechanism or process responsible for both the propagation and the orientation dependence. It has therefore been used for widely different systems that show orientation dependence, ranging from the irrigation patterns in dry soil[7] to sedimentation within chemical reactors[82]. Frank and Chernov et al. applied the kinematic wave theory specifically for crystal growth which resulted in a continuous description of the shape evolution of a perfect single crystal within a homogeneous parent phase. The crystal growth rate is then only dependent on the crystal orientation of the exposed surfaces. The step from a crystal growth system to a crystal etch system is a relatively small one as etching is essentially equivalent to negative growth. However, implementing the kinematic wave theory for a realistic non-perfect etching system (such as is used in bulk micromachining) does present several challenges. Within these systems, phenomena such as the interaction with mask edges, effects of surface morphology or crystal imperfections are important and are not considered in the classical kinematic wave theory.

Van Suchtelen et al.[95, 96] have extended the kinematic wave theory of growth to consider both orientation-dependent etching (anisotropic etching) of a single crystal and the above-stated phenomena in a generalised form. This was achieved by introducing the velocity source concept. A velocity source is defined as a localised deviation from the (classical) kinematic wave theory. It can be seen as a local point on the crystal surface where the etch rate (or growth) is determined by factors other then the surface orientation alone. Phenomena such as dislocations or mask-crystal junctions, which can lead to a local increase in etch rate[68, 69] compared to the surrounding surface, can be defined as velocity sources. As the velocity source is a generalised concept, it does not specify the nature of the etch rate deviation. Similar consideration can therefore be made for phenomena that can locally reduce the anisotropic etch rate (such as micro masking[72] or step bunching[52, 56, 107]). Using van Suchtelen's extended kinematic wave theory as a basis, van Veenendaal et al. have introduced a model specifically designed to describe the anisotropic etching of silicon in alkaline solutions. The model consists of a continuous function describing the etch rate as a function of the crystal surface orientations. The model uses several physical parameters which can be coupled to the relevant process conditions (such as temperature or etchant compositions).

In the following sections the kinematic wave theory for etching is outlined from primarily an atomistic point of view together with the underlying physical and chemical etch mechanisms. The mathematical equations describing each of these mechanisms are outlined together with the specific conditions for which these equations can be applied. Subsequently, the elementary network assembly is described which is used to combine these mechanisms into a single continuous function. Finally, the practical implementation of the kinematic wave theory and elementary network assembly is shown for silicon anisotropic etching in alkaline solutions resulting in a functional model.

2.2.2 Kinematic wave theory: an atomistic approach

Stepflow: surface anisotropy

The kinematic wave theory for etching systems can be considered from a continuum or an atomistic point of view. Within this thesis the atomistic approach is predominantly used. It provides a more convenient way of visualising the actual etch mechanisms. The crystal itself and the etch process are ultimately not continuous processes due the crystal structure and the finite size of the smallest etchable element (one crystal atom). Note that the following sections deal solely with the etching of silicon, the same mechanisms and considerations also apply for different systems including crystal growth (on which all these mechanisms are originally based).

From an atomistic point of view, the orientation dependence of anisotropic etching of Si is based on the stepflow mechanism[19]. This mechanism assumes that any crystal surface with an arbitrary inclination from a stable crystal plane is composed of average height steps on that particular stable plane (see figure 2.1). In chapter 1.4 it is outlined that stable planes have strict crystallographic definitions related to the periodic bond chains. As such only a limited number of crystal planes are stable on which these steps can be present. The mechanism states that etching only occurs on the edges of these steps. As the steps have an average height and constant terrace lengths (which depends on the inclination angle), the steps will 'flow' across the stable crystal plane during etching with the same constant velocity, hence the stepflow mechanism. The actual perpendicular etch rate of the inclined surface is then directly related to the step density of that particular surface. From this, it is straightforward to derive a relationship between the inclination angle (α), the constant step velocity (v_{step}) and the perpendicular etch rate ($R_{\perp}$) (equation 2.1). This function contains a cusp minimum where no steps are present on the stable crystal plane ($R_{\perp} = 0$ at $\alpha = 0$).

$$R_{\perp} = v_{step} \left|\sin \alpha\right| \tag{2.1}$$

When only considering the stepflow mechanism, a perfect stable crystal plane ($\alpha = 0$) would not etch at all. In reality a finite etch rate can be observed on these orientations indicating that terraces do etch although far slower than steps.

Birth-and-spread: terrace roughening

Any crystal surface is subject to thermal and kinetic roughening which, within an etching system, will result in a perpendicular surface etch rate. Although both roughening processes have different physical basis, the resulting surfaces will look similar. The main difference is the physical process responsible for the roughening of the surface and the relationship behind the roughening and the driving force.

Within the kinematic wave theory, both these roughening processes are described by the birth-and-spread mechanism[48]. This mechanism describes the etching of smooth surfaces and terraces due to roughening. It can be visualised as a continuous random single terrace atom removal, creating step sites (birth). These step sites will subsequently etch outward (spread) resulting in an overall perpendicular etch rate of the surface (figure

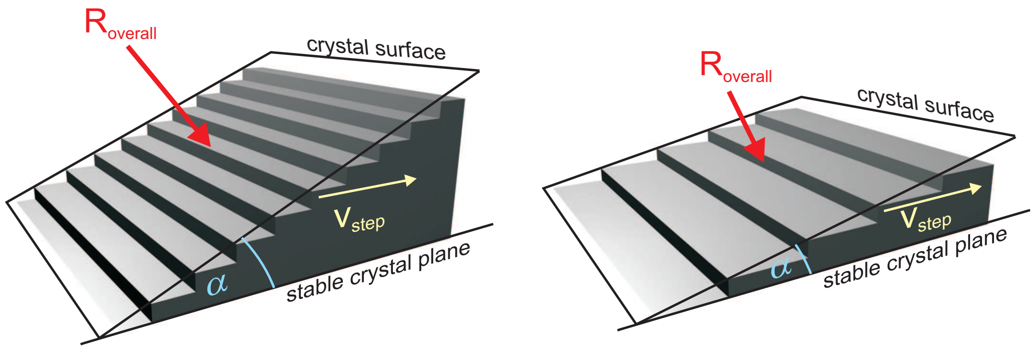

Figure 2.1: *Outline of the stepflow mechanism. The figure shows the relationship between the overall surface etch rate ($R_{overall}$), the step density and the surface inclination angle (α)*

2.2). The perpendicular etch rate is then a function of the step velocity (v_{step}) and a 2-dimensional or terrace roughening parameter (ε^{2D}) (equation 2.2).

$$R_{\perp,\alpha=0} = v_{step} \frac{\varepsilon^{2D}}{\sqrt{1-\left(\varepsilon^{2D}\right)^2}} \tag{2.2}$$

Stepflow: step anisotropy

For silicon, the step velocity is also dependent on the planar orientation (θ) (figure 2.2) of the steps (step anisotropy) and coupled to that the kink density present on those steps. This is clearly observable in macroscopic phenomena such as triangular etch pits present on an etched (111) surface. Within the Si crystal structure certain step orientations can be defined which are aligned along periodic bond chains (outlined in chapter 1.4). On a molecular scale these PBCs are uninterrupted Si-Si chains which, if aligned with the step orientation, form the most stable step edges. The planar orientation (θ) of the steps is defined with regards to the PBC. Analogous to the stepflow mechanism on crystal planes, where the step density determines the surface etch rate, the kink density determines the step etch velocity. Steps perfectly aligned with respect to the PBC ($\theta = 0$) do not contain kinks and are considered stable. Similar to equation 2.1, the equation of the step anisotropy contains a cusp minimum at $\theta = 0$ from the PBC orientation (equation 2.3).

$$v_{step} = v_{kink} \left|\sin\theta\right| \tag{2.3}$$

Although the mechanism suggests that at these orientations a smooth step is present (no kinks, analogous to a smooth terrace/crystal plane at $\theta = 0$), this is actually not the case. From a thermodynamic standpoint, steps are inherently rough with a non-zero step density. However, as actual crystals contain steps with a finite step length, the kink density can be such that the average distance between two kinks on a step is larger than the actual step length. This will effectively result in a smooth step.

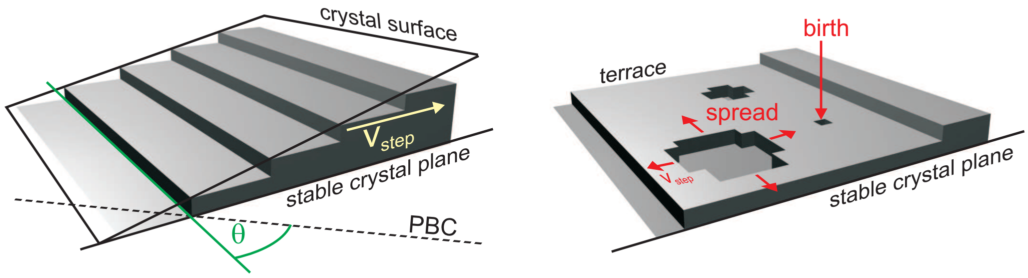

Figure 2.2: *The right figure shows the birth-and-spread mechanism. The figure shows the single terrace site removal (birth), which is etched outwards on terraces (spread). The left figure shows the planar orientation (θ) of the surface steps with regards to a periodic bond chain orientation.*

Similar to terrace etching, steps aligned to PBCs do etch. The etch rate here is controlled by the 1-dimensional step roughening (ε^{1D}) which can be visualised as single kink formation on smooth steps (equation 2.4).

$$v_{step,\theta=0} = v_{kink} \frac{\varepsilon^{1D}}{\sqrt{1-(\varepsilon^{1D})^2}} \tag{2.4}$$

The processes outlined above describe the orientation dependence of the etch rate within a limited range of orientations. Both stepflow on surfaces and steps are valid at small inclination angles (α or θ). The 2-dimensional and 1-dimensional roughening are only valid at α=0 and θ=0, respectively. Also in a 3-dimensional crystal, more then one plane is present at which all these processes occur. To combine these mechanisms on all stable planes into a single continuous function, which is valid for any 3-dimensional crystal orientation, the elementary network assembly method was applied[96, 104].

2.2.3 Elementary network assembly method

The elementary network assembly is a universal method to combine elements with different topologies within a single continuous function. This method has its basis in classical linear networks and can be used for a wide range of systems including electrical networks. The topology of an individual element defines the nature of the element as a function of one particular variable. In the case of anisotropic etching, the topology is the orientation dependent etch rate. A second important aspect is the strength and nature of the interaction between the individual elements. Two types of interactions can be defined:

- Parallel interaction, which defines an interaction between two processes which are mutually reinforcing.

- Serial interaction, which defines an interaction between two processes which are mutually competitive.

Equation 2.5 shows the general function for the assembly of k elements:

$$F_{ass} = \sqrt[a]{\sum_{i=1}^{k} F_i^a} \tag{2.5}$$

'Inverted' elements can also be assembled which will result in the following general equation with k elements and p inverted elements (equation 2.6).

$$F_{ass} = \sqrt[a]{\sum_{i=1}^{k} F_i^a - \sum_{j=1}^{p} F_j^a} \tag{2.6}$$

The type and strength of the interaction is defined by the interaction parameter a. To visualise the effects of the different interactions, it is convenient to examine the assembled function graphically. This can be done by expressing the different types of mechanism and interactions in terms of the change in the graphical plot of the assembled function. In the following section, the specific types of interactions are outlined using the stepflow and birth-and-spread mechanisms as single elements within the assembly.

Cusp-smoothing interaction

The stepflow element is valid for small inclination angles α but not for $\alpha = 0°$. Here the birth-and-spread element determines the etch rate. This indicates a parallel interaction between both elements where the assembled function is determined by the largest valued element at a particular inclination angle α. A parallel interaction with $a > 0$ is also called the cusp-smoothing interaction. From a graphical point of view, the zero cusp minima of the stepflow function are smoothed so as to form a continuous function where the height of the minima are determined by the terrace roughening. The value of parameter a determines the strength of the interaction, with a higher value resulting in a more constrained interaction. The combined graph will then follow the original graphs more closely. Equation 2.7 shows an example assembly of a birth-and-spread element and a stepflow element with an interaction parameter $a = 2$. Figure 2.3 shows the resulting graph of the assembly.

$$R_{\perp}(\alpha) = v \sqrt[2]{(|\sin\alpha|)^2 + \left(\frac{\varepsilon}{\sqrt{1-(\varepsilon)^2}}\right)^2} \tag{2.7}$$

Upward-limiting interaction

In the above example it is clear that if the roughening parameter ε approaches 1, the combined graph goes to infinity. From an atomistic point of view, this can be seen as the surface roughening dominating the perpendicular etch rate regardless of the stepflow

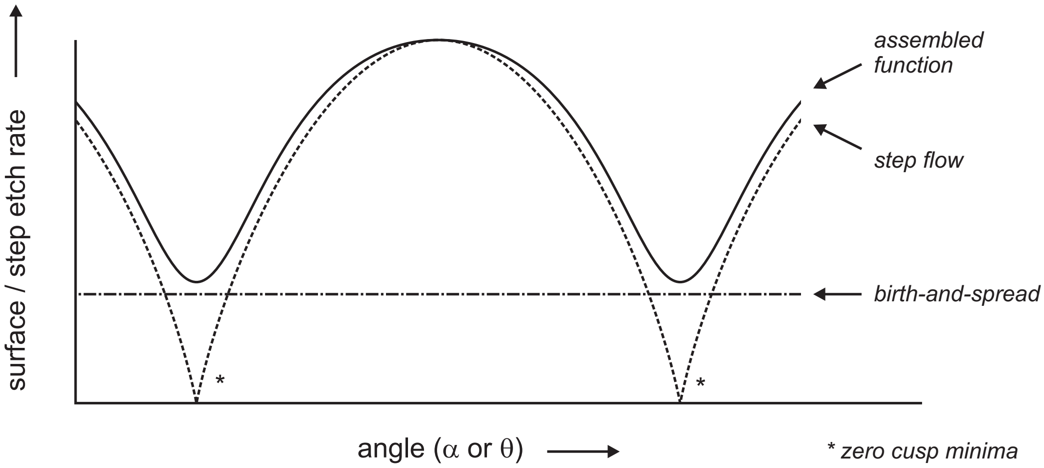

Figure 2.3: *Graphical result of a cusp-smoothing assembly between an arbitrary stepflow and birth-and-spread element*

process. In reality, terrace pits which are formed due to terrace roughening will have to etch with the fixed step velocity of the resulting step types. This means that there is a practical limit by which etching can occur, corresponding to the actual step velocity. In this case we can define a serial interaction between the stepflow/birth-and-spread etch rate and a constant step velocity limit. For this interaction $a < 0$, which is called the upwards-limiting interaction. This method limits the assembled function while retaining a continuous smooth graph (figure 2.4). The resulting assembled function with an interaction parameter $a = -4$ takes the form of equation 2.8.

$$R_{\perp}(\alpha)_{lim} = \sqrt[-4]{(R_{\perp}(\alpha))^{-4} + (v)^{-4}} \tag{2.8}$$

Cusp-combining interaction

A different situation involves several elements with similar topology but shifted in the spatial axes (in this case α). An example of this situation is the stepflow process on three different (neighbouring) stable crystal planes. The only difference between these elements is the position of the cusp minima on the 3-dimensional unit sphere. Inclination angles (α_1, α_2 and α_3) are then determined for each stepflow element depending on the relative orientation of the corresponding stable crystal plane. An assembly of all three elements will describe the anisotropic etch rate of all orientations between these three stable crystal planes. For this situation, a serial interaction is defined where the three elements are competitive. Using an interaction parameter $a < 0$, the minima are preserved in the assembled function. This method is therefore called the cusp-combining interaction. Equation 2.9 shows an assembled function of the above described situation with $a = -4$. Figure 2.5 shows the graphical results of this type of assembly.

$$R_{\perp} = v \sqrt[-4]{(|\sin\alpha_1|)^{-4} + (|\sin\alpha_2|)^{-4} + (|\sin\alpha_3|)^{-4}} \tag{2.9}$$

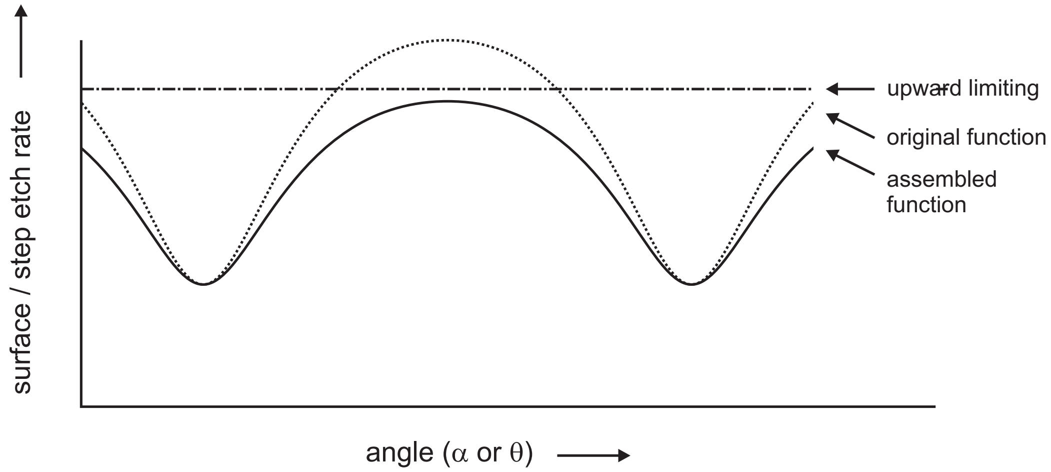

Figure 2.4: *Graphical result of an upward-limiting assembly assembly of an arbitrary α-dependent function*

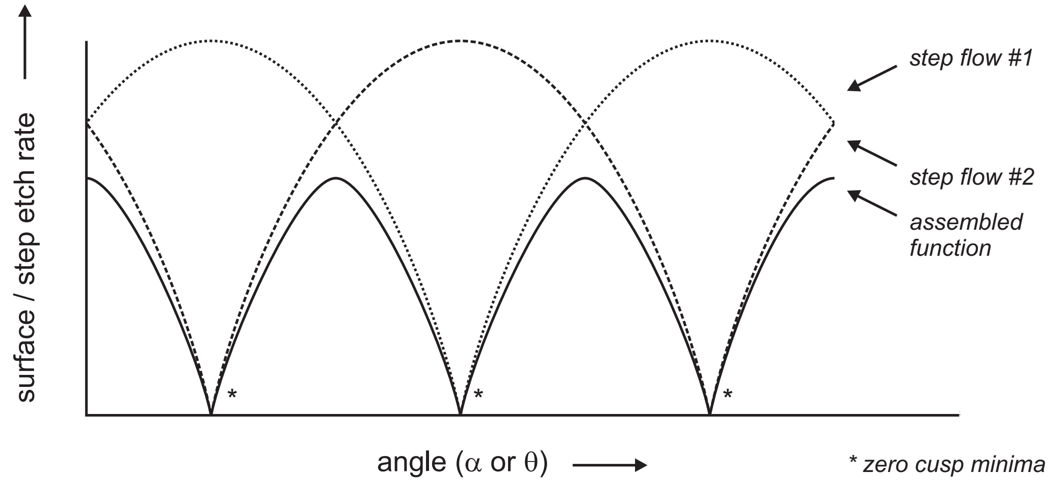

Figure 2.5: *Graphical result of a cusp-combining assembly between two α-dependent functions*

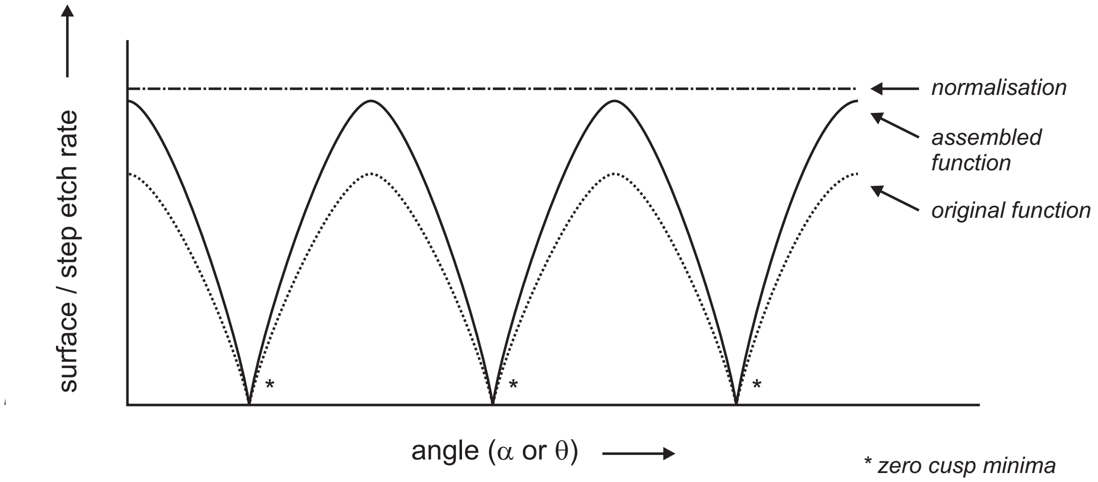

Figure 2.6: *Graphical result of the normalising assembly of an arbitrary α-dependent function*

Normalising interaction

The graphical plot of the assembled function (equation 2.9) shows that, in the vicinity of the minima, the assembled function deviates significantly from the original unassembled graphs. This effect is amplified when more elements are assembled. The correct orientation dependence close to the minima should resemble equation 2.1. The deviation from this equation is compensated by assembling the function with an 'inverted' element. The interaction type used is an upwards limited interaction with an 'inverted' element. In the case of n elements the inverted element will be $-n^{\frac{1}{a}}v$ and the interaction parameter $a > 0$. Using this assembly, the graph is effectively scaled to a range of 0 to v (figure 2.6, which corresponds to the original range of the individual elements. This means that this type of assembly can be seen as a normalisation interaction (equation 2.10).

$$R_\perp = v \sqrt[-4]{(|\sin\alpha_1|)^{-4} + (|\sin\alpha_2|)^{-4} + (|\sin\alpha_3|)^{-4} - \left(3^{-\frac{1}{4}}\right)^{-4}} \qquad (2.10)$$

This covers all the relevant basic interaction types between stepflow and birth-and-spread mechanisms i.e. the parallel cusp combining interaction, the serial cusp smoothing, upward limiting and normalisation interactions.

2.2.4 Implementation

The following section will outline the practical implementation of the kinematic wave theory and elementary network assembly in constructing a complete 3-dimensional model specifically for anisotropic etching of silicon in alkaline solutions. The silicon crystal has a diamond structure (chapter 1.4) in which two families of stable crystal planes can be identified. The (100) family consists of six planes and the (111) family of eight planes. Stepflow and birth-and-spread mechanisms apply to all these planes individually. The construction of the model for the (111) family, which is the more complicated family, is outlined in the following sections in a step-by-step manner.

Constructing (111) stepflow elements for steps

On each individual crystal plane belonging to the (111) family, three PBC directions are present, oriented in a triangular fashion along to the $[1\bar{1}0]$, $[\bar{1}01]$, and [011] directions (figure 2.7). For the entire θ-dependent step-anisotropy function, three step flow elements (equation 2.3) will therefore be assembled, each with the cusp minimum position corresponding to the appropriate PBC. It is important to note that, for steps present on (111), a difference exists between steps that are aligned with the same orientation, but moving in opposite directions. Steps along the [110] but moving in $[11\bar{2}]$ direction are different from those moving in the $[\bar{1}\bar{1}2]$ direction. This difference is linked to the molecular structure of the step edges and is observable as a difference in absolute step velocity (chapter 1.4). When regarding a single step flow element such as the one corresponding to [110] PBC, steps aligned with [110] and moving in $[\bar{1}\bar{1}2]$ direction correspond to the most stable step orientation which is identified as a zero cusp minimum in the function. Steps moving in the $[11\bar{2}]$ direction correspond to the fastest etching step orientation. The function should show a maximum at this orientation. Using equation 2.3 directly, will correctly result in a minimum at $\theta = 0°$ corresponding to the most stable step orientations. However, the function also contains a minimum at $\theta = 180°$, which is the orientation corresponding to the fastest etching step. It is clear that a single (111) stepflow element should only contain a single minimum at $\theta = 0°$. For the step flow element for (111) steps equation 2.11 is therefore used.

$$v_s = 2v_k \left|\sin \frac{1}{2}\theta\right| \tag{2.11}$$

Within equation 2.11 the step velocity is v_s and the kink velocity is v_k and θ the planar orientation with regards to the PBC orientation (most stable step orientation). The single minimum in the function is achieved by replacing θ by $\frac{1}{2}\theta$. Although this results in the correct number and position of the minima, it also results in deviation of the absolute step velocity close to the minima compared to the correct stepflow equation 2.3. To retain the original θ-dependency, the equation is multiplied by a factor 2. This correction is valid as equation 2.12 is only applicable at small values of θ. This can be clearly seen in figure 2.8a.

$$v_k \left|\sin \theta\right| \approx 2v_k \left|\sin \frac{1}{2}\theta\right| \tag{2.12}$$

Constructing (111) step anisotropy function on a single crystal plane

As chapter 1.4 has outlined, (111) contains three PBC directions, each with its own stepflow element. Each element evaluates the step velocity as a function of the step orientation (θ) with regards to its corresponding PBC orientation (θ_1, θ_2 and θ_3). Examining the actual PBC directions, the following can be derived: $\theta_1 = \theta$, $\theta_2 = \left(\theta + \frac{2}{3}\pi\right)$ and $\theta_3 = \left(\theta + \frac{4}{3}\pi\right)$. To combine all three (111) step flow elements (figure 2.8b), a cusp combining assembly is used with an interaction parameter $a = -4$. Van Veenendaal et al. have estimated the parameter setting from experimental values and determined that -4 is appropriate in these cases[98] (see equation 2.13 and figure 2.8c).

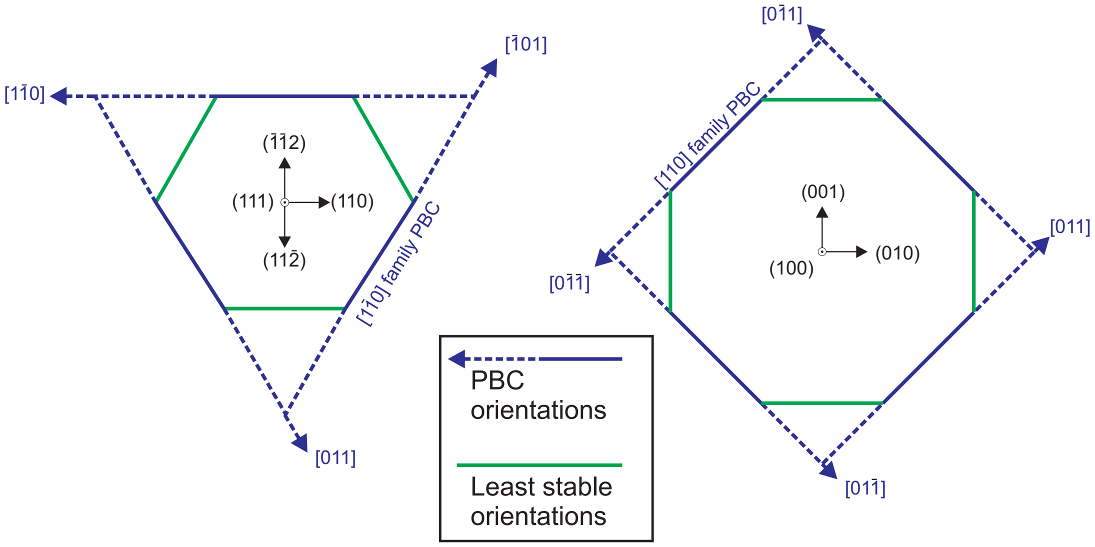

Figure 2.7: *Diagram showing the PBC orientations of both the (111) crystal plane (left) and the (100) crystal crystal planes (right). Due to the asymmetry of the (111) PBC, the least stable orientations on (111) also coincide with the PBC direction (outlined in chapter 1.4. On (100), the PBC's are symmetrical. The fastest etching step orientations then coincides with step orientations in between the PBC's.*

$$v_s = v_k \sqrt[-4]{\left(2\left|\sin\frac{1}{2}\theta_1\right|\right)^{-4} + \left(2\left|\sin\frac{1}{2}\theta_2\right|\right)^{-4} + \left(2\left|\sin\frac{1}{2}\theta_3\right|\right)^{-4}} \tag{2.13}$$

It is necessary to normalise the assembled function to retain the correct orientation dependence near the graph minima corresponding to equation 2.3. This is done by adding a normalisation factor to the assembly which results in a function for the normalised step velocity $v_{s,n}$ (equation 2.14). Note that the function is normalised using the $2v_k\left(3^{-\frac{1}{4}}\right)$ element instead of the $v_k\left(3^{-\frac{1}{4}}\right)$ element due to the modifications outlined in equation 2.12.

$$v_{s,n} = v_k \sqrt[-4]{\left(2\left|\sin\frac{1}{2}\theta_1\right|\right)^{-4} + \left(2\left|\sin\frac{1}{2}\theta_2\right|\right)^{-4} + \left(2\left|\sin\frac{1}{2}\theta_3\right|\right)^{-4} - \left(2\left(3^{\frac{1}{4}}\right)\right)^{-4}} \tag{2.14}$$

To describe the step etch velocity at the zero cusp minima, the birth-and-spread element for steps is integrated by using a cusp smoothing assembly with the 1-dimensional roughening element (equation 2.4 and figure 2.9b). This will result in a continuous function describing the step velocity ($v_s(\theta)$) as a function of the entire planar orientation range of steps on one particular stable crystal plane of the (111) family (equation 2.15).

$$v_s(\theta) = \sqrt[2]{\left(v_{s,n}\right)^2 + \left(v_k\frac{\varepsilon^{1D}}{\sqrt{1-\left(\varepsilon^{1D}\right)^2}}\right)^2} \tag{2.15}$$

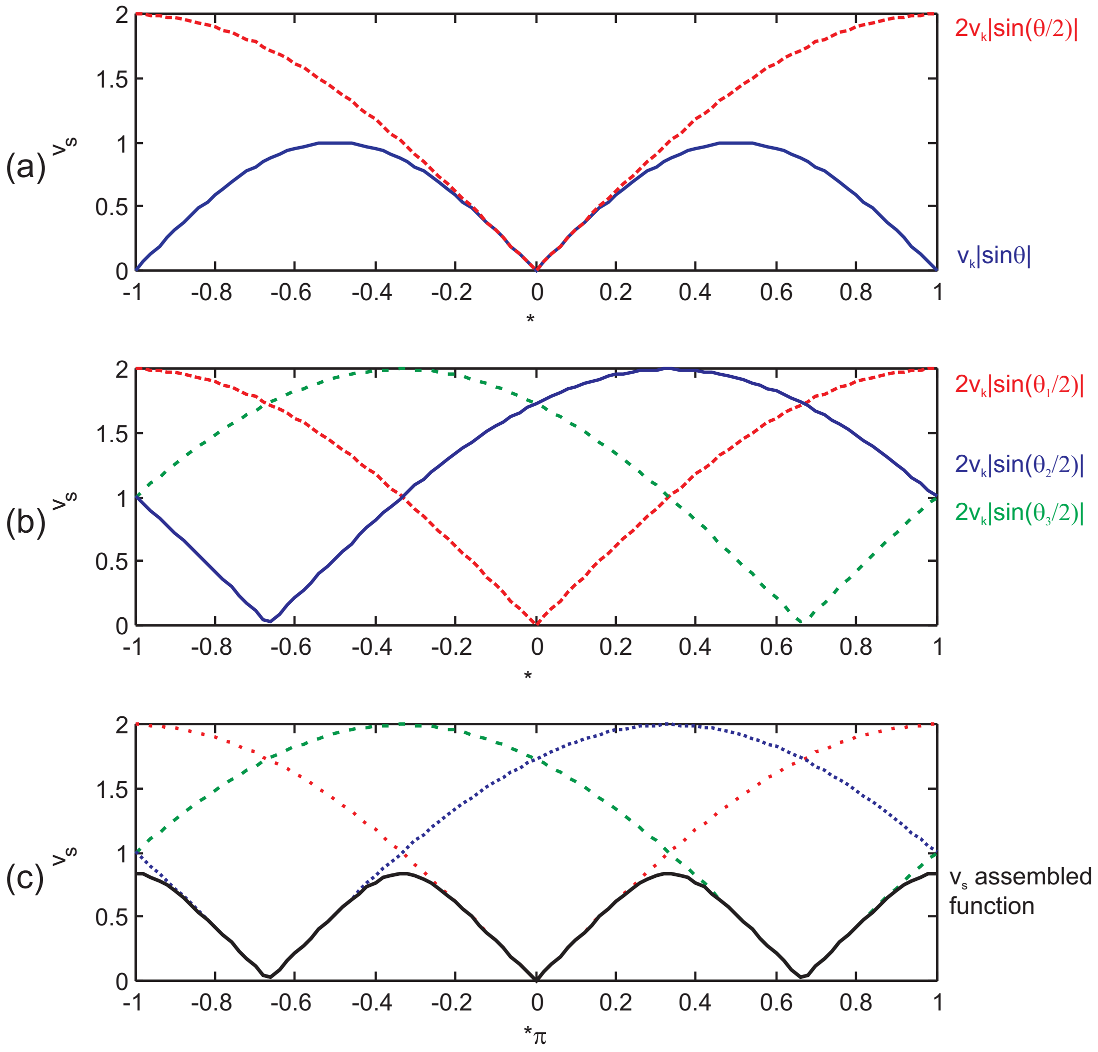

Figure 2.8: *Graphical plots corresponding to the construction of (111) step anisotropy function. (a) shows the modified stepflow equation compared to the basic function. (b) shows the three stepflow elements present on a single (111) surface plotted simultaneously. (c) shows the cusp combining assembly of the three stepflow elements.*

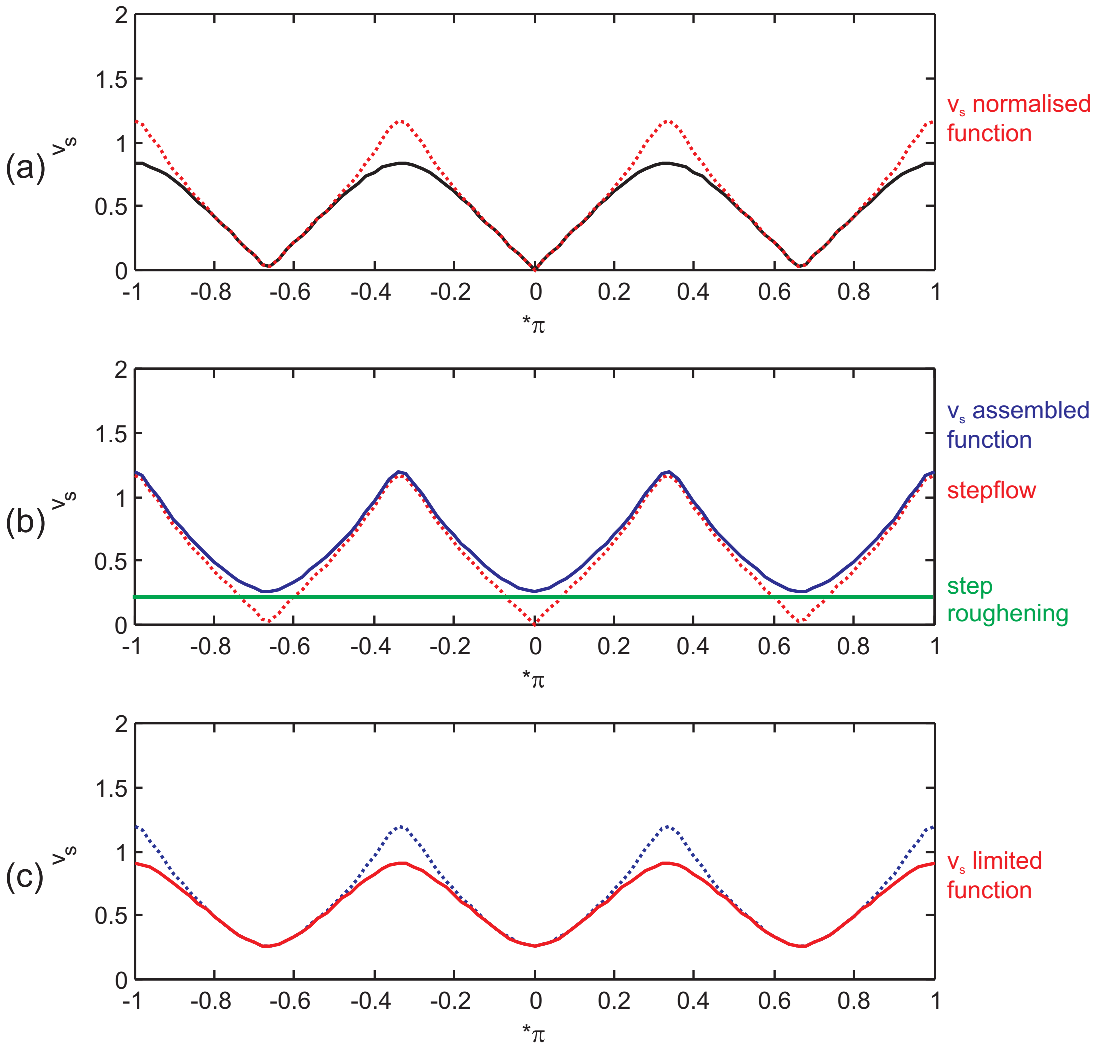

Figure 2.9: *Graphical plots corresponding to the construction of (111) step anisotropy function. (a) shows the normalisation of the assembled function containing three (111) stepflow elements. (b) shows the assembly of the stepflow element with the birth-and-spread (step roughening element) using the cusp smoothing assembly. (c) shows the final upward limiting assembly resulting in a step anisotropy function for a single (111) crystal plane.*

As described in the previous section, it is necessary to limit this function with the kink velocity v_k using the upward limiting interaction and an interaction parameter $a = -4$ (equation 2.16 and figure 2.9c). The resulting function describes the θ-dependent step velocity (step anisotropy function) for a single (111) plane.

$$v_{s,l}(\theta) = \sqrt[-4]{\left(v_s(\theta)\right)^{-4} + \left(v_k\right)^{-4}} \tag{2.16}$$

This procedure can be repeated for each stable crystal plane within that particular family. For the (111) family this would result in a total of eight step anisotropy functions. For the (100) family the procedure is similar but less complicated. One (100) surface only contains two directions which can be regarded as PBC's (see chapter 1.4). Due to the symmetry, the modifications to both the step anisotropy functions and the normalisation interaction are not necessary. Although the (100) family contain six crystal planes, some are identical due to crystal symmetry. It is therefore only necessary to define three step anisotropy functions.

Figure A.1 in appendix A shows graphical illustrations of the kinematic wave etch model construction. A similar notation as van Veenendaal et al. is used which is a convenient way of illustrating the model elements and the interaction between the elements. Figure A.1a shows the assembly of the (111) step anisotropy.

Constructing (111) surface anisotropy function

The anisotropic etch rate as a function of the inclination angle can be constructed by first defining a step anisotropy function (equation 2.16) for each (111) plane. The stepflow element is again used to evaluate the orientation dependence. Analogous to the step orientation θ, the angle from the surface orientation α with respect to each of the eight (111) plane is evaluated (α_1 to α_8) individually. For a single family, all the stepflow elements are combined using a cusp combining interaction. As with the step velocity assembly, a normalisation element using v_k is integrated in the assembly to retain the original features near the minima (equation 2.17).

$$R_{\perp,(111)} = \sqrt[-4]{\sum_{m=1}^{8}\left(2v_{s,l}(\theta)\cdot\left|\sin\frac{1}{2}\alpha_m\right|\right)^{-4} - \left(\left(2v_k 8^{-\frac{1}{4}}\right)\right)^{-4}} \tag{2.17}$$

Due to the crystal symmetry of Si, the same consideration and corrections are made for the (111) surface anisotropy as with (111) step anisotropy (see equation 2.12). Also a factor 8 is used for the normalisation element as a total of 8 (111) step anisotropy elements are assembled. The final step is integrating the birth-and-spread mechanism for terraces. Analogous to the equation 2.15, an assembly of equation 2.17 with the birth-and-spread element will result in a continuous surface anisotropy function of the etch rate of the (111) family (equation 2.18).

$$R_{\perp,(111)}(\alpha) = \sqrt[2]{\left(R_{\perp,(111)}\right)^2 + \left(v_k\frac{\varepsilon^{2D}}{\sqrt{1-\left(\varepsilon^{2D}\right)^2}}\right)^2} \tag{2.18}$$

Figure A.2 in appendix A outlines the construction of the entire (111) element of the surface anisotropy.

Constructing 3-dimensional anisotropic etch rate function

The previous procedure can be performed for the (100) family as well. The modifications applied to both the stepflow for step elements (equation 2.11, 2.14 and 2.16) and stepflow for surface elements (equation 2.17) are not necessary when dealing with (100) orientations. Due to the crystal structure, steps and surfaces of (100) show minima at both $\theta = 0°$ and $\theta = 180°$. Equations 2.1 and 2.3 can therefore be used directly. This also means that, for the construction of the (100) surface anisotropy function, it is sufficient to considered only three planes as the same functions will also describe the remaining three planes (an outline of the (100) assembly is given in figures A.1b and A.2 in appendix A). With both (100) and (111) surface anisotropy functions constructed, the last step is to combine both crystal plane families into a single continuous function. This is achieved by using the cusp combining interaction (see equation 2.19 and figure A.3a).

$$R_{\perp} = \sqrt[-4]{\left(R_{\perp,(111)}\left(\alpha\right)\right)^{-4} + \left(R_{\perp,(100)}\left(\alpha\right)\right)^{-4}} \tag{2.19}$$

This is the basic model, which contains a total of 6 parameters (figure 2.10). All these parameters have a physical basis within the stepflow/birth-and-spread mechanism. To use the basic model as a 3-dimensional model where the etch rate can be calculated from any surface orientation, the angle between that surface and all the (111) and (100) planes (α_i) will have to be determined. Additionally the step orientation and the angle with respect to all the PBCs on each individual surface planes are also determined (see figure 2.11). In practice, the sheer number of these angle calculations determines for a large part the actual calculation speed of the model.

Phenomenological corrections: step bunching

Examining etch results using hemispherical samples[104], van Veenendaal et al. have added three additional parameters to the model in order to described the observed differences between the predicted etch rates and the experimental data. Examining the step velocity experimental data in the vicinity (111) indicates an increase in step velocity ($v_s(\alpha)$) as a function of the inclination angle α. Van Veenendaal et al. attributed this deviation to step bunching. Experimental measurements [53, 104, 107] have shown that steps on silicon surfaces tend to bunch together creating higher macro steps. These macro steps exhibit a different step etch velocity compared to the monolayer steps. The mechanism behind the formation of steps is not entirely known. Both Garcia et al.[32] and Gosalvez et al.[42] suggested that diffusion effects creating local etchant or temperature fluctuations near the surfaces are responsible for step bunching. Nijdam et al.[68, 72] attribute the formation of macro steps to absorbed foreign particles (polysilicates) on the surface and/or steps. What is clear is that step bunching is a function of the step density, with a higher step density (smaller terrace width) resulting an increased macro-step formation. This has led to the addition of a step bunching mechanism to the model in the form of α-dependent (111) kink velocity (equation 2.20).

6 – parameter basic model			
parameter	Range	Description	Physical description
$v_{k,100}$	> 0	(100) kink velocity	Kink site etch velocity
$V_{k,111}$		(100) kink velocity	
ε^{2D}_{100}	0 – 1	(100) 2D Terrace roughening	Single atom pit nucleation on terraces
ε^{2D}_{111}		(111) 2D Terrace roughening	
ε^{1D}_{100}	0 – 1	(100) 1D Step roughening	Kink nucleation on steps
ε^{1D}_{111}		(111) 1D Step roughening	
Phenomenological corrections			
C_{111}		(111) Step bunching	
v_{ms}	> 0	(110) macrostep element	
v_{is}	> 0	(110) isotropic element	

Figure 2.10: *Table showing the parameters used for the basic 6-parameter model. Additionally the three parameters corresponding to the phenomenological corrections are outlined.*

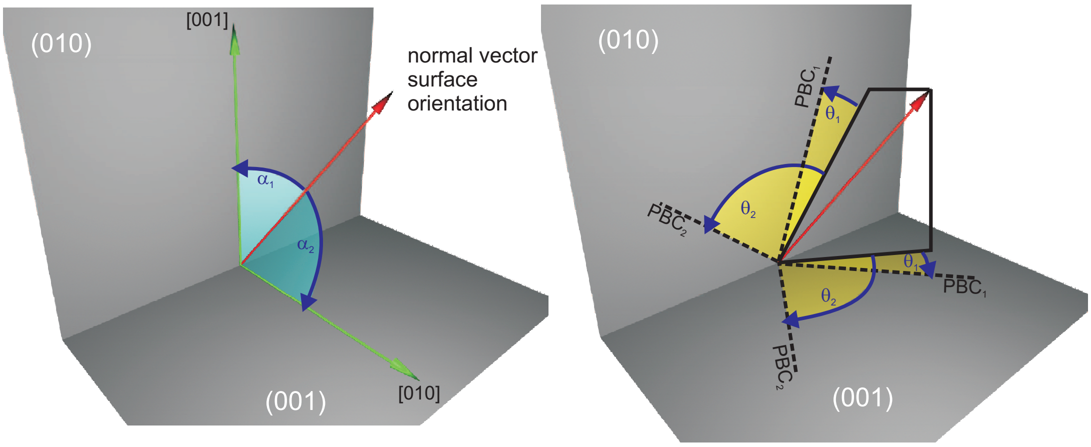

Figure 2.11: *Figure illustrating the angle calculation when using the kinematic wave etch model as a 3-dimensional model. As an example, only two (100) surfaces are shown. In reality these angle calculation apply to all the (100) and (111) surfaces. The surface normal of a arbitrary surface is denoted with the red arrow. To calculate the etch rate of that surface, the angle between that surface and both (100) surfaces are determined (α_1 and α_2) for the surface anisotropy function (left). For the step anisotropy functions, the angle with respect to the PBC orientations (θ_1 and θ_2 are calculated for each (100) surface (right).*

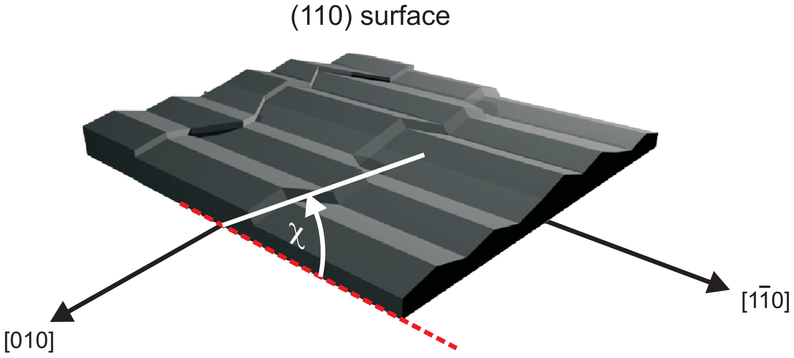

Figure 2.12: *Diagram showing the inclination angle χ relative to the (110) surface. The figure also shows the typical (110) roof-tile morphology (see chapter 1.3*

$$v_k^b = v_{k,111}^0 \cdot (1 + C_{111} \left|\sin \alpha\right|) \tag{2.20}$$

The 'bunched' kink velocity is then a function of the surface inclination angle, the original (111) kink velocity $v_{k,111}^0$ and the step bunching parameter C_{111}. It is important to note that the C_{111} parameter, which controls the magnitude of the step bunching, can by either positive or negative. This means that within the model, step bunching can either result in an increase or decrease of local kink velocity. Step bunching is integrated into the model by replacing the kink velocity v_k with v_k^b within equations 2.11 to 2.14 for the (111) family of planes. The α used in equation 2.20 is determined for each corresponding (111) plane (each θ-dependent stepflow element in the left tree of figure A.2b). The kink velocity v_k in equations 2.15 and 2.16 however remain the original $v_{k,111}^0$. Within the birth-and-spread elements (equation 2.2) the original kink velocity is used. The surface roughening is an isotropic process, independent on the surface orientation and inclination angle. The effect of the birth-and-spread element is also restricted to orientations close to the minima (α is close to 0) where the effect of step bunching can be neglected. The roughening is then a function of the $v_{k,111}^0$. For the normalisation interaction in equation 2.17 $v_k = v_{k,111}^0$. This element is also independent of the inclination angle.

Phenomenological corrections: (110) morphology

Comparison between the experimental etch data obtained using hemispherical samples by Sato et al. and van Veenendaal et al. and the model predictions, a serious deviation is observed in the vicinity of (110) orientations. The data shows trends which cannot be predicted by the stepflow/birth-and-spread mechanisms alone. Van Veenendaal et al. have attributed the etch mechanisms to intrinsic instabilities coupled to the specific morphology observable at the (110) surface (the so called zigzag or roof-tile structure)[39, 87]. The corrections suggested by van Veenendaal take the form of two additional elements. The macrostep element describes the (110) etch rate when inclining the (110) around the [010] axis (figure 2.12).

Etch experiments suggest that the etch rate here follows a sine function which leads to the following equation 2.21 for this element.

$$R^{ms}_{\perp(110)} = v_{ms} \cdot |\sin \chi| \tag{2.21}$$

The perpendicular surface etch rate when inclining the (110) surface around the [010] axis is a function of the inclination angle χ with regards to the (110) surface and the macro-step velocity v_{ms}. The second element is an isotropic etch rate trend observed when inclining the (110) surface towards the (111). Here the perpendicular etch rate is isotropic and only depending on the v_{is} resulting in equation 2.22.

$$R^{is}_{\perp(110)} = v_{is} \tag{2.22}$$

These two elements are mainly considered phenomenological elements as they do not have a strong physical basis. Primary goal of integrating these elements is obtaining a more accurate description of the etch rate in the vicinity of (110) when compared to the experimental data, regardless of physical/chemical mechanisms. Implementing these two elements in the etch rate function can be done in a similar way to the (100) and (111) surfaces. The (110) family of crystal planes consists of six planes each containing both the macro-step and isotropy element. The six macro-step elements are combined using the cusp combining interaction with an interaction parameter of -4 (equation 2.23).

$$R^{ms}_{\perp(110)} = \sqrt[-4]{\sum_{m=1}^{6} \left(v_{ms} \cdot |\sin \chi|\right)^{-4}} \tag{2.23}$$

The macro-step assembly and the isotropy element are combined by using a cusp smoothing assembly using $a = 1$ (equation 2.24).

$$R_{\perp(110)}(\chi) = R^{ms}_{\perp(110)} + R^{is}_{\perp(110)} \tag{2.24}$$

Integrating this assembly in equation 2.19 requires a cusp combining interaction with parameter $a = -10$. The choice of such a high negative parameter value is to ensure that the interaction of the (110) assembly is restricted to the (110) orientations (equation 2.25 and figure A.3b) and that the resulting function closely resembles the correction. It is important to note that, in this case, the absolute value of a is of less importance as long as it is significantly large.

$$R_{\perp,total} = \sqrt[-10]{\left(R_{\perp,(100),(111)}(\alpha)\right)^{-10} + \left(R_{\perp,(110)}(\chi)\right)^{-10}} \tag{2.25}$$

It should be noted that to further ensure that the (110) elements do not interfere with the (100) and (111), elements should be further restricted depending on the crystal orientation (limiting of the possible χ angles depending on the experimental dataset). In a practical sense, this makes the implementation of these element more complicated, as it is necessary to 'fine tune' the restrictions depending on the data set used. The final model function as was defined by van Veenendaal uses a total of 9 parameters (table 2.10) which proved to be very accurate[104] in describing the anisotropic etch rate. Within this work however we opted to use either the 6-parameter basic model or a 7-parameter model (basic + step bunching) due to the lack of physical basis of the (110) elements. Experimental data in the vicinity of (110) (see chapter 3 are then ignored.

2.3 Conclusions

Using the kinematic wave theory van Veenendaal et al. have constructed a continuous function describing the anisotropic etch rate of Si in alkaline solutions of any surface orientation. The model is based on two distinct (atomistic) processes: stepflow mechanism and the birth-and-spread mechanism. Each of these processes, present on the stable crystal planes of both the (100) and (111) family together with the steps present on these planes, can be defined as individual elements within the model. Using the elementary network assembly method all these individual elements are combined into a single continuous function which constitutes the basic 6-parameter model. Examining the observed discrepancies in the anisotropic etch rates, van Veenendaal et al. have introduced three phenomenological corrections. One correction deals with the observed step bunching phenomenon on (111) steps. The other two corrections describes the etch rates in the vicinity of (110). The final 9-parameter model has proven accurate compared to the experimental data. However in this work we have opted not to use the (110) corrections. The practical issues in implementing these corrections together with the lack of a strong physical basis have led us to either use the 6-parameter model or the 7-parameter model (which includes (111) step bunching) as the basic model.

Chapter 3

Anisotropy in electrochemical oxidation of surface steps

Anisotropic etch rates of silicon in KOH solutions were studied as a function of an externally applied potential. A combination of three micromachined samples consisting of dry-etched wagon-wheel patterns and masked trench offset patterns was used to measure the etch rates at a large number of crystallographic orientations simultaneously. The measured data was described in terms of microscopic properties including step velocity, terrace roughening and step anisotropy using an etch model based on the kinematic wave theory. All parameters show distinct changes due to the applied potential and the additional electrochemical reaction path. Electrochemical oxidation and subsequent passivation of the Si surface is reflected in the decrease in step velocity. Terrace roughening shows a minimum and there is a corresponding change in anisotropic etch rate ratio at -1250 mV vs SCE. The observed decrease in step anisotropy and subsequent step anisotropy reversal at more positive potentials indicates an anisotropy in, not only chemical etching, but also in electrochemical oxidation of (111) surface steps.

3.1 Introduction

Anisotropic wet chemical etching of silicon in concentrated alkaline solution has proven to be a simple, reliable and widely used bulk micromachining process for MEMS[28]. The difference in etch rates of various crystallographic orientations in a silicon single crystal provides a relatively simple fabrication process of complex structures where etchants such as potassium hydroxide (KOH) and tetramethyl ammonium hydroxide (TMAH) solutions are most commonly used. The fundamental basis of the etching mechanism however still presents many questions. On a chemical level it seems relatively clear how the etching process can be described in terms of chemical reaction mechanisms. How these mechanisms translate to a microscopic scale, where properties such as surface roughening and step anisotropy are important, is still unclear. This is of particular interest when including additional electrochemical reaction paths. Previous studies[4, 84, 110] have shown that the overall anisotropic etch rate is a function of the electrochemical potential. Electrochemical oxidation caused by chemical oxidizers[18, 109] or applied potentials can reduce overall etch rates. Electrochemical studies have additionally shown that the electrochemical oxidation rate depends on the crystallographic orientation of the exposed surface[75]. These results, however, typically involve the major crystal surfaces such as (100) and (111). In this work we have measured the anisotropic etch rate of a large number of orientations as a function of a constant applied potential. This was done by performing etch experiments using micromachined wagon-wheel patterns on two different substrate types and a masked trench offset pattern. This combination resulted in etch rate measurements on a wide range of surface orientations. The kinematic wave theory was used to quantify the effect of an applied potential on microscopic properties such as step velocity, step roughening and terrace roughening. The measurements show distinct influences on both the step velocity and step anisotropy. Furthermore, the data indicate that electrochemical oxidation on surface steps is not isotropic and favours dihydride terminated steps present on (111) surfaces over monohydride terminated steps. In addition a minimum was observed in the terrace roughening which translates to a maximum in the anisotropic etch rate ratio at a potential different from the open circuit potential (OCP).

3.2 The chemical / electrochemical etch mechanism

3.2.1 Chemical reaction mechanism

As outlined in chapter 1.5, the chemical etch reaction mechanism of silicon is most commonly described as a two-step mechanism (figure 1.6). The OH^- acts as a catalyst for the initial oxidation of the hydrogen-terminated Si surface atom. The formation of the pentavalent transition state is considered the rate limiting step. The subsequent etching step consist of a reaction between the Si-Si back bond and a water molecule, resulting in a dissolved $Si(OH)_x$ and a newly exposed hydrogen-terminated Si surface atom. The ease with which the pentavalent transition state can be formed determines for a large part in the observed etch anisotropy. As stated earlier (chapter 1.3), the etch anisotropy is not limited to surfaces but is also observed on steps. This step anisotropy is observable in phenomena such as triangular shaped etch pits on (111) surfaces. In general, the chemical mechanism only considers single Si surface atoms. However, both surface and step anisotropy cannot be explained using the chemical reaction mechanism alone. Factors such as surface topology (such as terrace and step sites), molecular configuration and nearest and next-nearest interactions have to be taken into account. It is therefore necessary to include topological information in the form of microscopic processes such as stepflow, surface roughening and step bunching to obtain a better description of the anisotropic etch mechanism. In this chapter, the kinematic wave theory (outlined in chapter 2) has been used to gain insight into these processes.

3.2.2 Electrochemical properties of Si

In chapter 1.5, anisotropic etching of silicon in alkaline solutions is considered from a purely chemical point of view. In recent years however, the electrochemistry and electrochemical relevant factors have become increasingly important. Bressers et al.[18] and Neuwald et al. [64] have shown that the presence of strong oxidising agents can has a large influence on the overall etch rate. Applying an external anodic bias have been shown to have similar effects[59, 110, 112]. STM investigations by Allongue et al.[3, 4] have shown the influence of both cathodic and anodic bias on a surface step / terrace scale. It is therefore of importance to consider both the electrochemical component within the etch system and the basic electrical properties of the bulk silicon.

In MEMS technology, doped silicon is typically used as the basic material, which has distinct electrical/electrochemical properties. The electrochemical properties of a silicon surface in contact with an electrolyte (such as a alkaline solution) is well known[62]. In the absence of any chemical reaction, the silicon/electrolyte interface shows the properties of a Schottky diode when an external electrical potential is applied.

In the presence of an electrical circuit or electrochemical species, charge transfer between bulk and Si is determined by the surface kinetics. If we observe the general I-V curves of both n-type and p-type, the open circuit potential (OCP)[62] is a point where no electrical current flows through the system. This corresponds to the normal etching conditions in the absence any electrochemistry. When the Si surfaces is forced to a more positive potential than the original OCP (via either an externally applied potential or oxidisers), electrochemical oxidation of silicon occurs, resulting in an anodic current. This can be clearly observed using cyclic voltammetry (CV)[4, 110] (figure 3.1).

At very positive potentials, the electrochemical oxidation rate is such that the surface is covered with silicon oxide, preventing any further oxidation (the surface is passivated). Under these conditions, the anodic current measured is the sum of residual oxidation (as a result of continued chemical removal of oxide) and the leakage current.

A negative bias will result in a cathodic current due to significant hydrogen gas formation with n-type. Due to the lack of free electrons, this does not happen on p-type Si. However electrons can still be excited into the conduction band due to external factors (such as visible light illumination) resulting in a movement of the electrons towards the surface and hydrogen production[23]. This illustrates the importance of electrochemically controlling experimental condition. The presence of electrochemically active chemical components such as dissolved metals or oxygen can shift the system into conditions where secondary electrochemical reactions, such as oxidation or H_2 formation, can become

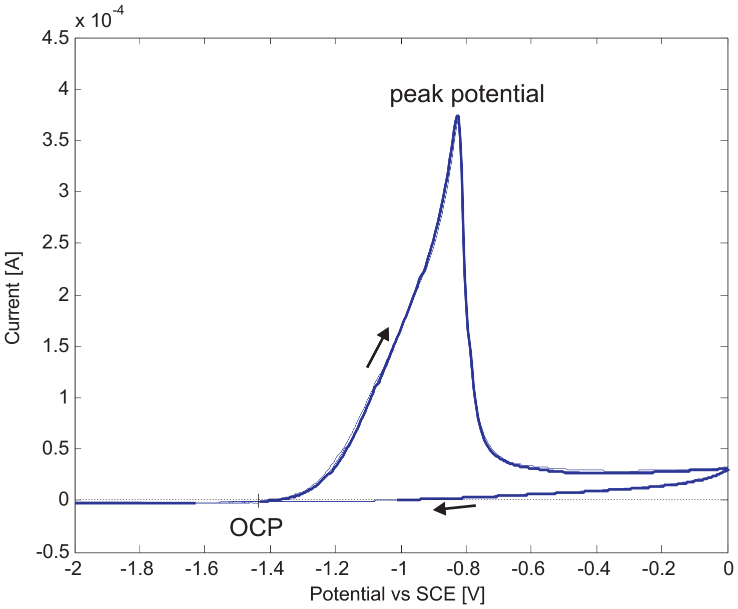

Figure 3.1: *Typical cyclic voltammogram of a p-type (110) silicon electrode in 5.0 mol/l KOH at 50° with a scan rate of 10 mv/s. The increase in anodic oxidation is clearly visible in the current. Above the peak potential, the surface passivates, preventing further oxidation. The current therefore decreases rapidly.*

significant.

3.2.3 Electrochemical reaction mechanism

If the silicon surface is anodically biased, electrochemical oxidation can occur, eventually resulting in the formation of SiO_2 on the surface. Experiments have shown that this electrochemically grown oxide only extends to few monolayers deep[64] but can still passivate the whole surface, preventing any further chemical etching of Si. The general formation mechanism of SiO_2 from Si is well known[4, 62, 112, 111]. The oxidation reaction (figure 3.2b) of an exposed silicon surface atom involves an oxidation reaction via two intermediates[75, 112] where electrons are injected into the conduction band. Depending on the driving force, the reaction can result in either a dissolved $Si(OH)_x$ together with a new exposed hydroxide terminated Si surface sites or a bridged Si-O-Si site. These reaction paths run parallel to the chemical reaction path of Si in alkaline solutions (figure 1.6 and 3.2a). It is also important to note that both the chemical and the electrochemical reaction paths share similar reaction intermediates[112, 75] and are therefore interconnected. The presence of SiO_2 means that a third reaction path will have to be taken into account. Silicon oxide can be chemically etched using alkaline solutions resulting in a dissolved $Si(OH)_x$ molecule and a hydrogen-terminated Si surface site (figure 3.2c).

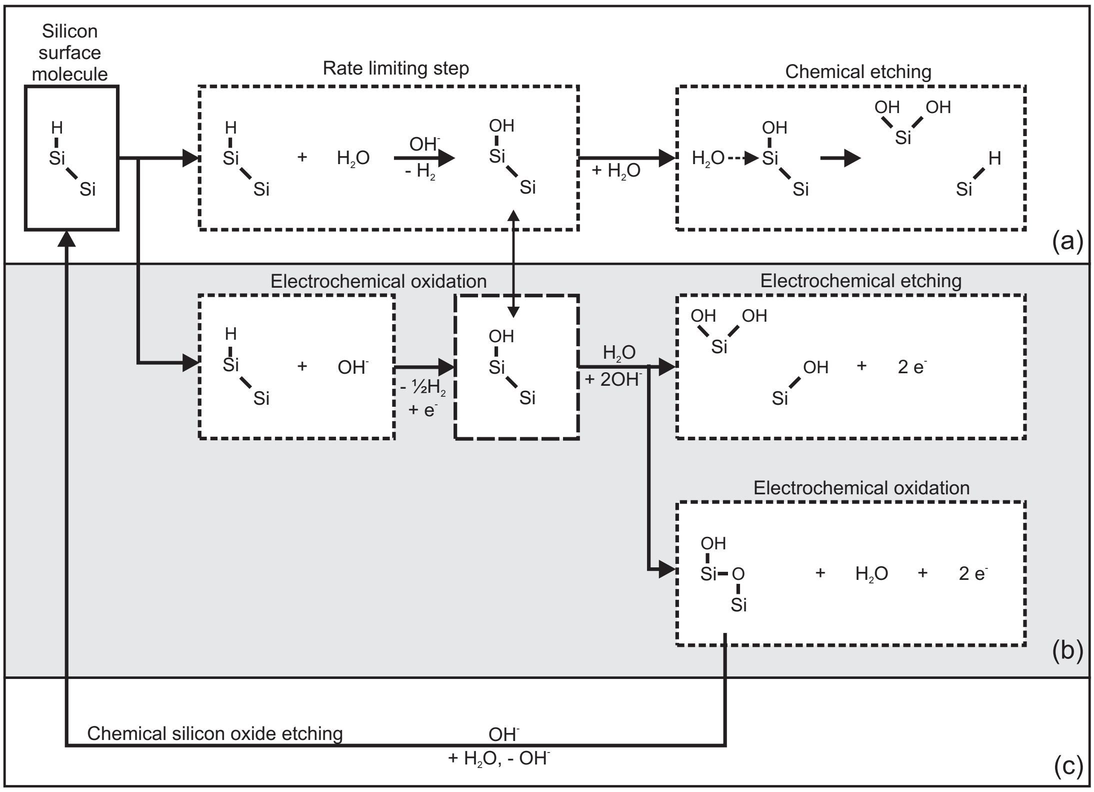

Figure 3.2: *Diagram of Si etch reaction mechanisms in alkaline solutions showing (a) the chemical reaction path, (b) the electrochemical reaction path and (c) the chemical* SiO_2 *etch path.*

3.2.4 Anisotropy in electrochemistry

When considering the (electro)chemical reactions such as those outlined in the previous sections, the focus generally lies on single-atom surface reactions. These single-atom surface reactions are not entirely representative of what actually occurs on the crystal surface as the specific surface species and the topology of the crystal plane are also of importance for the overall reaction mechanism (see chapter 1.4). For the chemical etch reaction, this is well established as these factors play an important role in the anisotropic etching of Si[41, 49]. For the electrochemical reaction, this is not known in such detail, although from STM measurements on small (111) steps and pits, Allongue et al. have shown a that electrochemical oxidation shows a preference towards specific (111) sites[3, 4]. On a bulk surface, it is known that different stable crystal planes have different electrochemical properties[75]. Both (100) and (110) surfaces show an OCP of approximately -1450 mV vs SCE. The most stable plane (111) however shows a more positive OCP of approximately -1300 mV vs SCE. This indicates that (111) is more stable towards electrochemical reaction as it is considered more ‘noble’. Previous work by Xia et al.[112] and more recently by Philipsen et al.[75, 76] has shown this anisotropy in electrochemical oxidation, between (100) and (111) crystal planes. This is observable both in the height and position of the passivation peak in CV measurement of both surfaces. The measurements have however been restricted to only the major crystal orientations. A more detailed picture of the anisotropy of the electrochemistry is desirable. This should not be limited to crystal planes and inclined surfaces but should include the electrochemical influence on particular surface species, surface steps and terrace sites. Understanding the influence of the electrochemistry on these properties will give insight into not only the electrochemical reaction mechanism but also the normal chemical etch mechanism on a microscopic scale.

3.3 Etch characterisation

3.3.1 The kinematic wave theory

The reaction mechanism, outlined in the previous sections, deals only with the surface reactions on a molecular scale. The mechanism does not provide any information on how the reactions and the influence of the electrochemistry translate to a microscopic scale where factors such as surface morphology also play a significant role. To investigate this we have used the kinematic wave theory[96, 101] to evaluate the anisotropic etch rate measurements. The theory describes anisotropic etching in terms of microscopic properties, the most important of which are terrace roughening, step velocity and step roughening. For a more detailed description of the model, physical background, and practical implementation see chapter 2. The basic model, as outlined by van Veenendaal et al, uses 9 parameters to characterise the anisotropic etch behaviour of silicon. Of these parameters, 6 have clear physical significance and they describe the microscopic properties outlined above. The remaining 3 are phenomenological parameters which were added primarily to account for discrepancies observed between the model and actual etch rate data. Two of these parameters deal with discrepancies at crystal orientations near the (110) family. The observed deviation in etch rates can be attributed to the atypical morphology of the surfaces. As such, these orientations contain little information concerning either the step flow or birth-and-spread mechanisms (which cannot directly account for the observed morphology). Both these corrections and the specific crystal orientations at which these corrections play a role are neglected within these measurements. A 7-parameter model is then used within this chapter which is the basic model including (111) step bunching (see chapter 2). Both chapters 5 and 7 deal with the (110) in more detail. Chapter 5 additionally outlines an extension to the model, specifically for the (110) orientation. However, as outlined in that chapter, the model extention requires more detailed etch-rate measurements which these wagon-wheel samples cannot provide.

3.3.2 Anisotropic Si etch rate measurement techniques

To obtain the microscopic properties from experimental data using the kinematic wave theory, a large range of anisotropic etch rates at various orientations are required. Measuring perpendicular etch rate of silicon at orientations other than the major crystal orientation (100), (111) and (110) presents many challenges. Methods which have been used in the literature are generally based on direct measurement of the etch depth[118] or the measurement of the underetch underneath a mask layer[75, 88]. These measurement techniques share a common element in the use of a mask (silicon nitride or silicon oxide) to act as reference point for the etch depth or underetch measurements. Nijdam et al. [69, 71] have shown that velocity sources can be present at the silicon/mask junction, acting as step nucleation sources. The presence of these velocity sources can have a significant impact on the overall surface etch rate, in particular at very slow-etching Si surfaces.

Another difficulty is the range of limited available Si surfaces with these measurement methods. As silicon wafers generally are used as substrates, the range of starting surfaces is restricted to the standard wafer surface orientations ((100), (111) and (110)). It is possible to obtain custom-made Si wafers with a specific miscut, thereby extending the experimental range[118]. As only one surface orientation can be measured with a single sample, using miscut wafers is both costly and time-consuming.

wagon-wheel pattern

An elegant measurement method is based on the use of a masked wagon-wheel pattern[84, 61, 88]. Etching samples containing these mask patterns will result in a concave etch shape underneath the mask. The resulting underetch pattern can be used to determine the anisotropic etch rate at a large number of surface orientations. Using this sample geometry however, the actual starting surfaces cannot be predefined as the resulting etch shape will determine which surfaces are exposed to the etching solution. Additionally, these measurements are subject to possible Si/mask junction effects. Wind et al. [106, 107] have introduced the use of a convex wagon-wheel pattern, in which the structure is etched into the Si using reactive ion etching (RIE). This creates a 3-dimensional convex Si structure of wedges in a radial pattern. Figure 3.3 shows photographic and SEM pictures of a unetched and etched wagon-wheel pattern. The side walls of these wedges form the starting surfaces of the etch experiments. The number and orientation of these starting

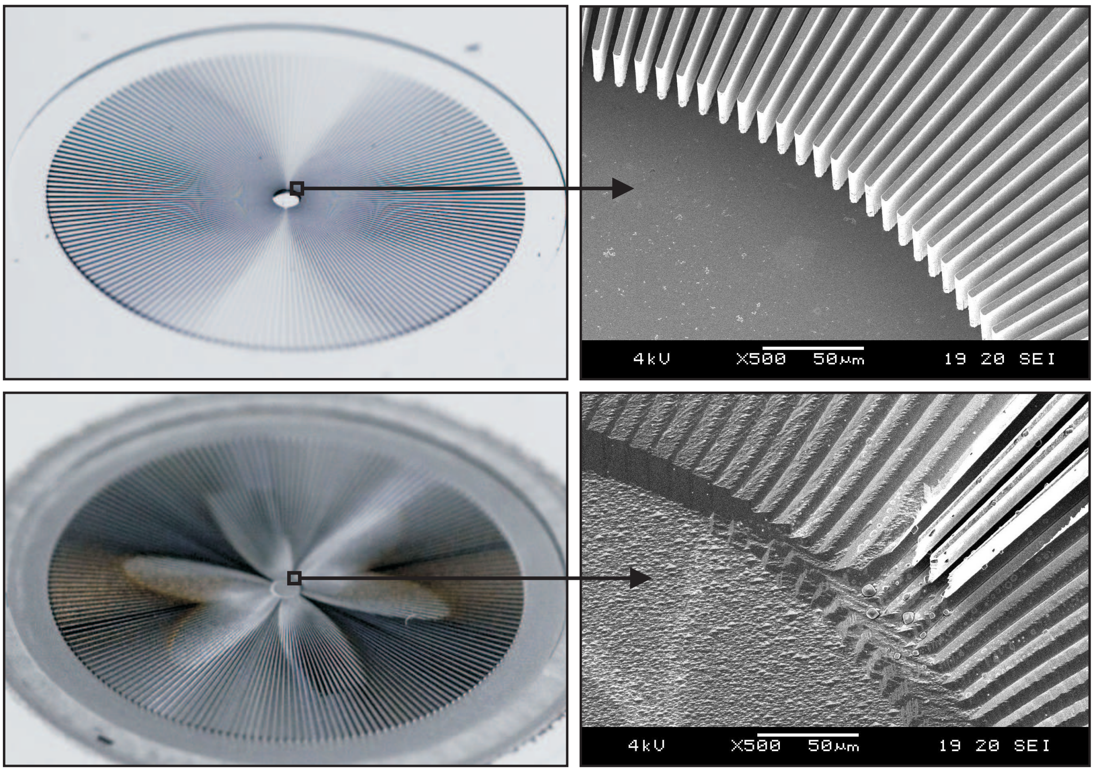

Figure 3.3: *This figure shows the dry-etched wagon-wheel pattern as used in this chapter. The top pictures show a photographic picture (left) and a detail of the wedge point using the SEM (right). The bottom pictures show similar images of an etched pattern. Note that the wedge retraction length is different due to anisotropic etching. This creates the characteristic 'flower' pattern in an etched wagon wheel.*

surfaces are then determined by the sample design. The etch rate of the side walls can be measured directly by determining the retraction length of the wedge tip. Due to a geometric amplification[106] (equation 3.1), the etch depth of the side walls (Δt) translates to a much larger wedge point retraction(Δl) (see figure 3.4a). This allows the etch rate to be determined by measuring the wedge point retraction using optical microscopy. The scale of the geometric amplification is determined by the wedge geometry, with a smaller wedge width (α) resulting in a larger amplification.

$$\Delta l = \Delta t \cot\left(\frac{\alpha}{2}\right) \tag{3.1}$$

One additional advantage of this wagon-wheel pattern design is the absence of a mask, which circumvents possible Si/mask junction effects. It does, however, result in faceting of the wedge top (figure 3.4c). This faceting is not a problem as long the wedge is high enough, preventing the facets from overlapping the wedge side walls. At very slow-etching surfaces, faceting (or rounding) of the actual wedge point is a problem. At these etch rates, the point retraction is a direct result of actual etching of the point itself and not the side walls (figure 3.4b). This means that this method is unsuitable for very low etching planes (such as near-(111) surfaces). Apart from these surfaces, the pre-etched wagon-wheel

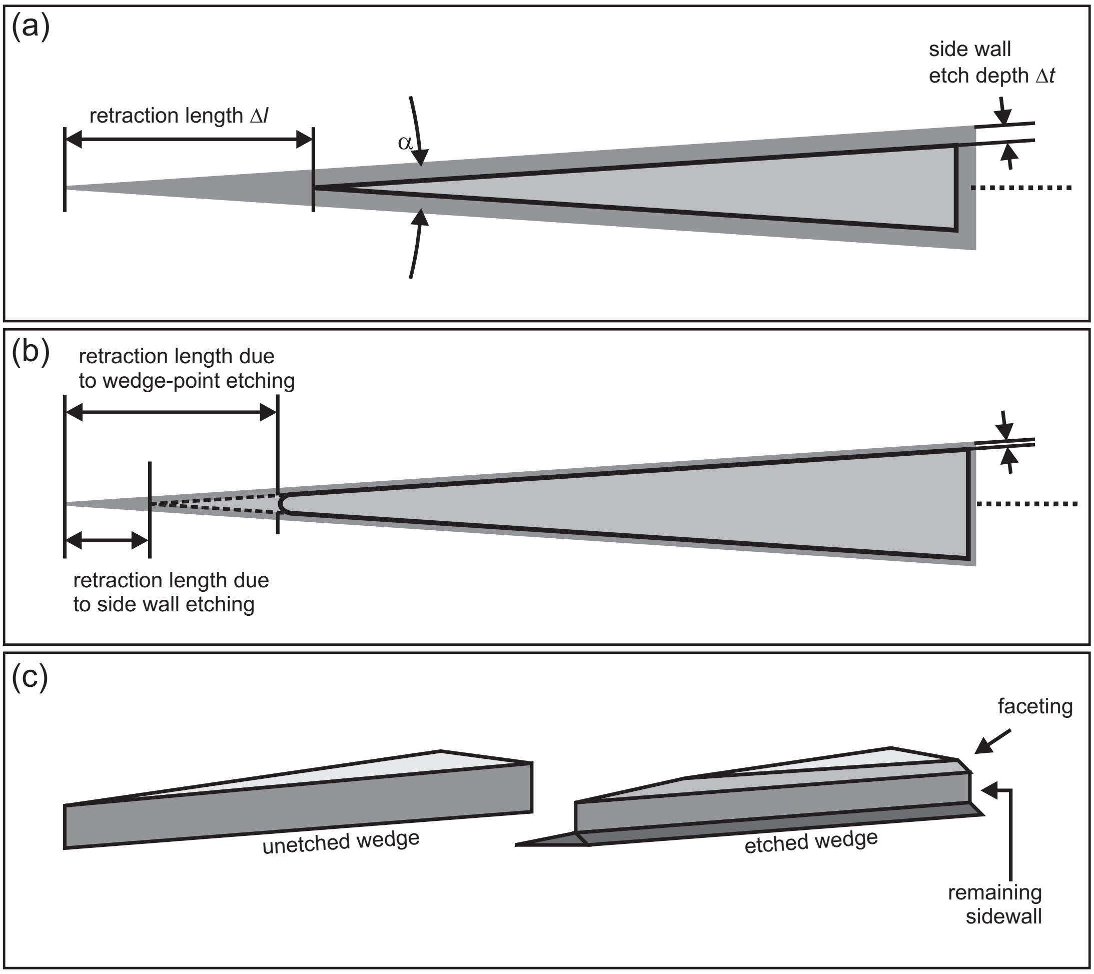

Figure 3.4: *Figure outlining the geometric amplification inherent to the etching of wedges (a). The faceting or rounding of the etch point is also shown (b). When etching of the side walls is too small, the etching of the wedge point determines the point retraction length. Faceting of the whole wedge is shown in (c). As long as the side walls are still present (the unetched wedge is high enough), the retraction length can be determined.*

geometry has proven to be suitable for the simultaneous measurement of the anisotropic etch rate of a large number of surface orientations.

3.4 Experimental

In this work we have measured anisotropic etch rates using three types of samples. These include dry-etched wagon-wheel patterns on (100) and (110) oriented Si wafers and masked offset trench patterns on (110) oriented wafers. The different types of samples were necessary to obtain the measurement range required for a reliable model fit using the kinematic wave theory.

3.4.1 Wagon-wheel pattern design

The wagon-wheel pattern designs used are similar to those first reported by Wind et al. [106, 107]. The design consists of 180 equally spaced convex wedges arranged in a 360° radial pattern. The wedges are 1° wide, 1400 μm long and approximately 50 μm high. All wagon-wheel samples were fabricated on Czochralski grown p-type (boron doped, 5-10 Ω.cm) silicon wafers supplied by Okmetic. Standard lithography was used to transfer the pattern onto the wafer, after which the convex wagon-wheel pattern was created using the Bosch process. Fluorocarbon deposits as a result of the Bosch process were removed via oxidation followed by oxide removal in 1% HF solution. The use of the Bosch process allows the creation of well-defined high aspect structures with a relatively low taper. Additionally, a layer of aluminium was deposited on the back of the wafer forming an electrical back contact necessary for electrochemical measurements. This was only done on the first batch of samples which were (110) oriented. It was replaced by a simpler GaIn procedure on all later samples. I-V measurements show that GaIn back contacts perform slightly better than the Al back contact, although this difference can be neglected in the actual experiments. Figure 3.5 shows a diagram of the fabrication process.

Both (110) and (100) oriented wafers were used as substrates for the wagon-wheel patterns. Using the former will result in etch rate measurements of orientations with a surface normal parallel to the (110) plane. These include all three major orientations: (100), (111) and (110) (figure 3.6a) together with the orientations in between. It, however, does not include the surface orientations between the (100) and (110). To obtain these, (100) oriented wafers were used which contain both (100) and (110) and those orientations in-between (figure 3.6b). The actual etch rate was determined by measuring the wedge point retraction length (figure 3.6b and c). This was done using a combination of optical microscopic observation and digital image processing and compositing. The etched pattern was viewed at an angle under oblique illumination. Using this setup, the side walls of the individual wedges are clearly visible, as opposed to viewing this structure from the top. The small width of the wedge point (sub micron range) makes microscope observations very difficult. By photographing the individual wedge points against fixed reference points and compositing the pictures digitally, the actual retraction length could be determined (figure 3.7).

3.4.2 Offset trench pattern

Wagon-wheel patterns have a disadvantage that, due to the way these convex wedge shapes etch, very low etch rates cannot be measured, in particular the near-(111) orientations. We have used the offset trench pattern design to specifically obtain the etch rates near the (111) orientations (figure 3.8a). This design consists of series of dry-etched rectangular trenches, of which the long sidewalls are at specific offset angles to the true (111) orientations. Etch rates are determined by measuring the under-etch distance beneath a nitride mask (figure 3.8b to d). The advantage of this method, as opposed to other underetch-based methods (such as v-grooves) is that (similar to wagon-wheel patterns) the starting surfaces are well-defined with specific inclination angles. A disadvantage compared to wagon-wheel patterns is that no geometric amplification is present. This means

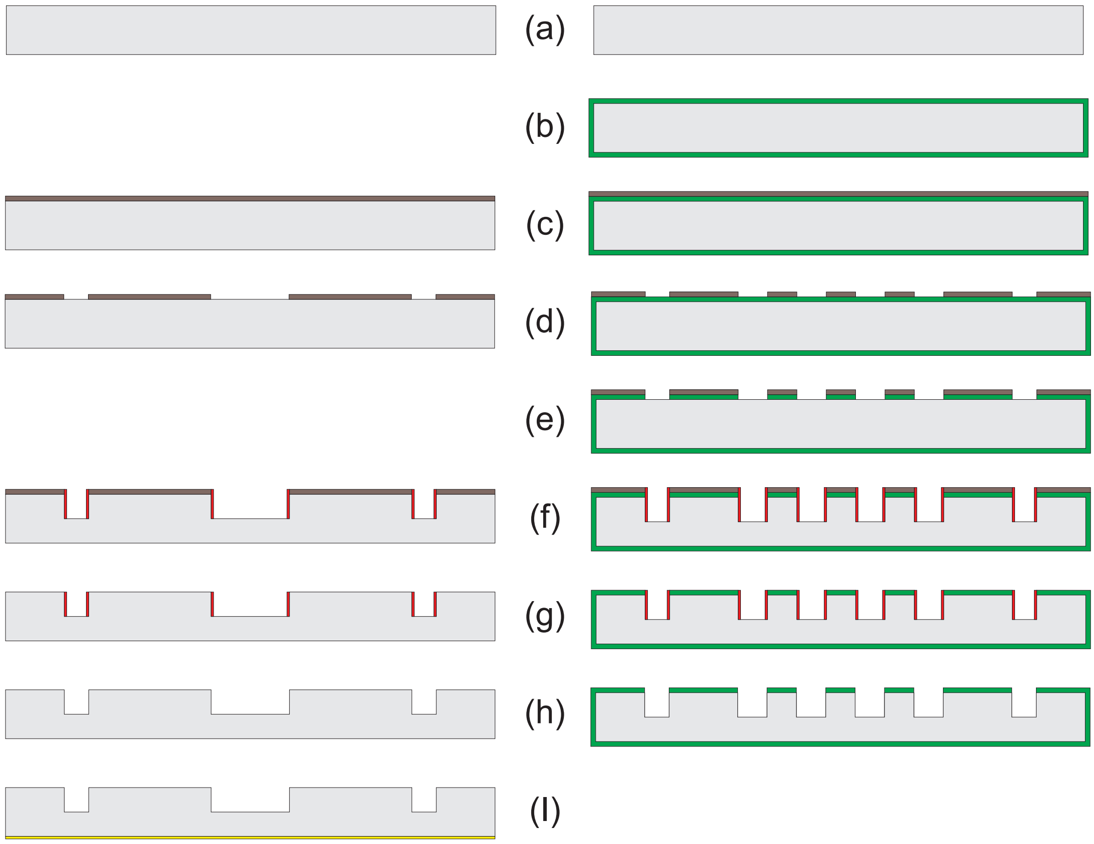

Figure 3.5: *Outline of the fabrication process of both the wagon-wheel patterns (left side) and the rectangle offset pattern (right side). The individual steps are indicated. Process starts with a (110) substrate for the rectangle offset pattern and a (110) or (100) substrate for the wagon-wheel pattern. (b) Depositing SiRN using LPCVD. (c) and (d) standard lithography using photoresist. (e) resist pattern to SiRN layer using reactive ion etching. (f) Deep etching using Bosch process using photoresist as mask material. (g) Removal of photoresist. (h) Removal of fluorocarbon deposits. (i) Creating aluminium back contact using sputtering.*

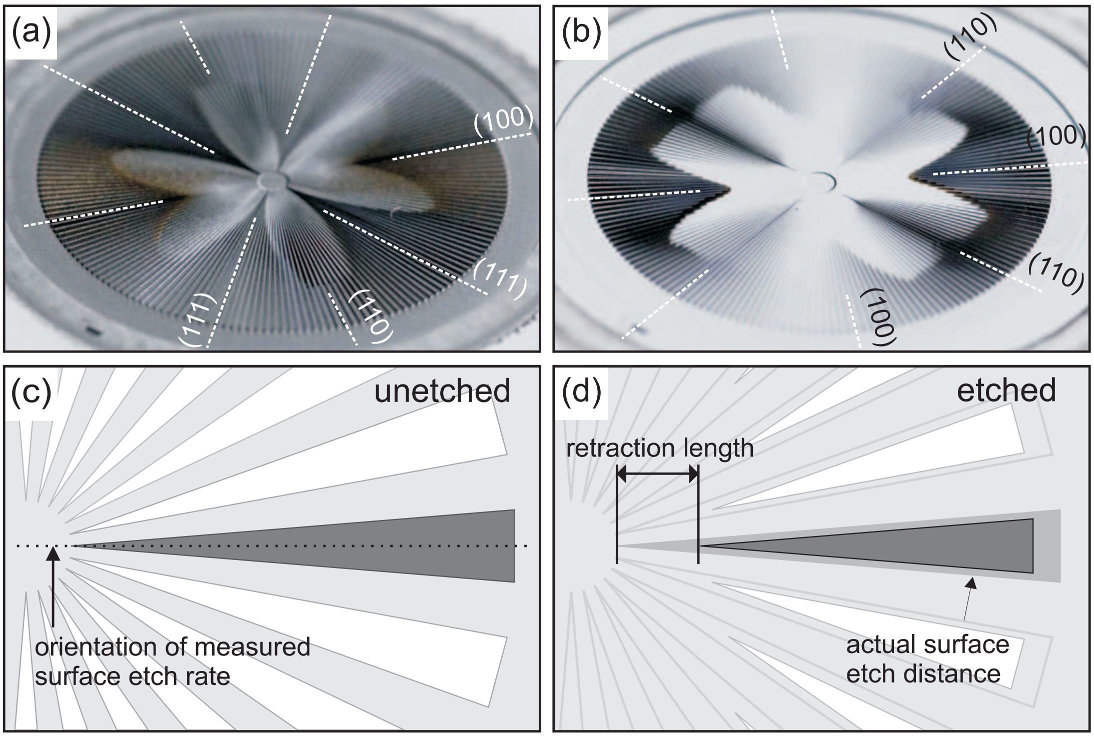

Figure 3.6: *Outline of micromachined wagon-wheel pattern. Top two pictures show an etched wagon wheel on a (110) (a) and (100) substrate(b), the major orientations are indicated. Diagrams (c) and (d) show the principle of the wagon-wheel pattern including the relative difference in size of the retraction length as compared to the actual perpendicular surface etch distance.*

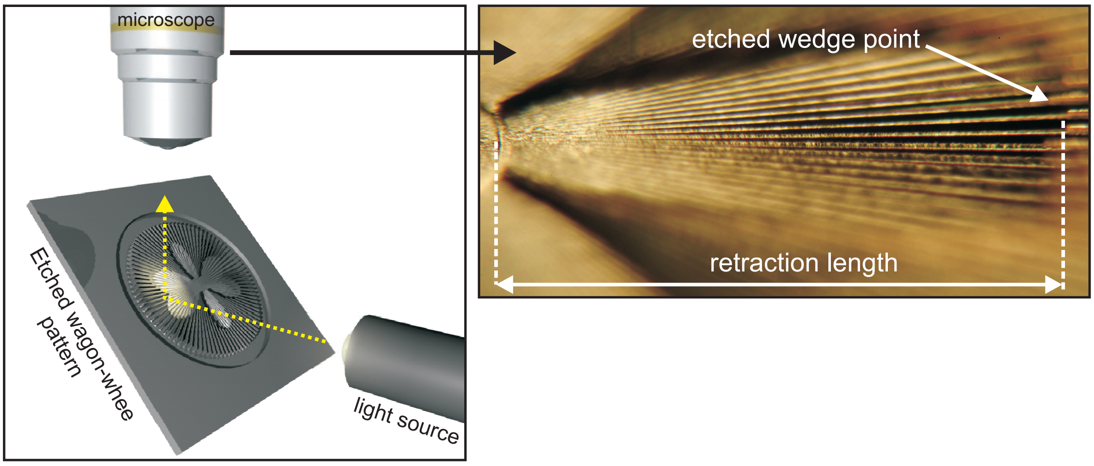

Figure 3.7: *Diagram of the measurement method. The sample is examined at an angle (left) under oblique lighting and a long working-distance microscope objective. The right picture shows a composite of two microscope pictures. The wedge point is clearly visible, and the retraction length can be measured.*

that for a reliable measurement, the etch time must be increased to obtain sufficiently large under-etch distances. Another issue is the possible interaction with the nitride mask. Nijdam et al.[68] have shown that, depending on the angle of the Si surface with the nitride mask , an etch rate increase can be observed as high as 4 times the minimum (111) etch rate. This minimum etch rate was shown to be at 90° (sidewalls are perpendicular to the mask) which is the case for the offset trench patterns. The total design consists of 61 separate trenches which have an inclination angle between -3.0° and +3.0° to the (111) orientation with a 0.1° step size. Each individual trench is 800 μm long, 100 μm wide and approximately 50 μm deep. These patterns were fabricated in the same p-type CZ (110) oriented wafers (as used for the wagon-wheel patterns). A layer of 300 nm low stress silicon rich nitride (SiRN) was deposited on the wafers using LPCVD. The offset trench pattern was transferred to the wafer using standard lithography. The pattern itself was aligned parallel to the (111) plane using the primary wafer flat with an automated mask aligner (EVG 620). The pattern was etched into the SiRN using reactive ion etching (RIE) and subsequently the trenches were etched using the Bosch process. Fluor carbon deposition was removed using the same procedure as with the wagon-wheel patterns. An outline of the manufacturing process is shown in figure 3.5. The underetch distances were determined using a combination of microscope observations and digital image analysis. Images of the specific underetch were subjected to a digital image profiling procedure, which could determine the under etch distances.

3.4.3 Experimental setup

Etch experiments were done in a Teflon cell. The electrochemical setup consisted of a platinum counter electrode (Radiometer M24Pt) and a saturated calomel electrode (SCE, Radiometer REF401) as a reference electrode. The sample, which acts as the working electrode, was mounted in a Kel-F holder (Kel-F is a mechanically stronger Teflon variant). The electrical back contact and the electrical connections were isolated from the solution using Viton O-rings. External potential differences were applied using a potentiostat (Princeton, 366A), current and voltage were monitored using a series of multimeters (HP 34401A) both connected to a computer for data acquisition.

3.4.4 Sample preparation

Prior to the etch experiments, all samples were cleaned in 65% HNO_3 (Merck GR for analysis) followed by deionised water (Millipore, 18 MΩ.cm) in order to remove contaminants. Samples with an aluminium back contact were protected to prevent damage to the metal layer due to cleaning by keeping the sample within the sample holder. For the other samples, an ohmic contact was made after cleaning by applying GaIn (Sigma Aldrich 99.99%+ GaIn eutectic) to the back after locally removing some of the native oxide or SiRN by scratching the back surface with a diamond tip pen. All etching experiments were done in a 5.0 mol/l KOH solution (prepared from Merck Selectipure pellets) at a temperature of 50°C in the dark. Prior to and during the experiments the solution was constantly bubbled with argon to remove dissolved oxygen. This, together with the hydrogen formation at the surface, caused convective mixing of the etching solution. Native oxide

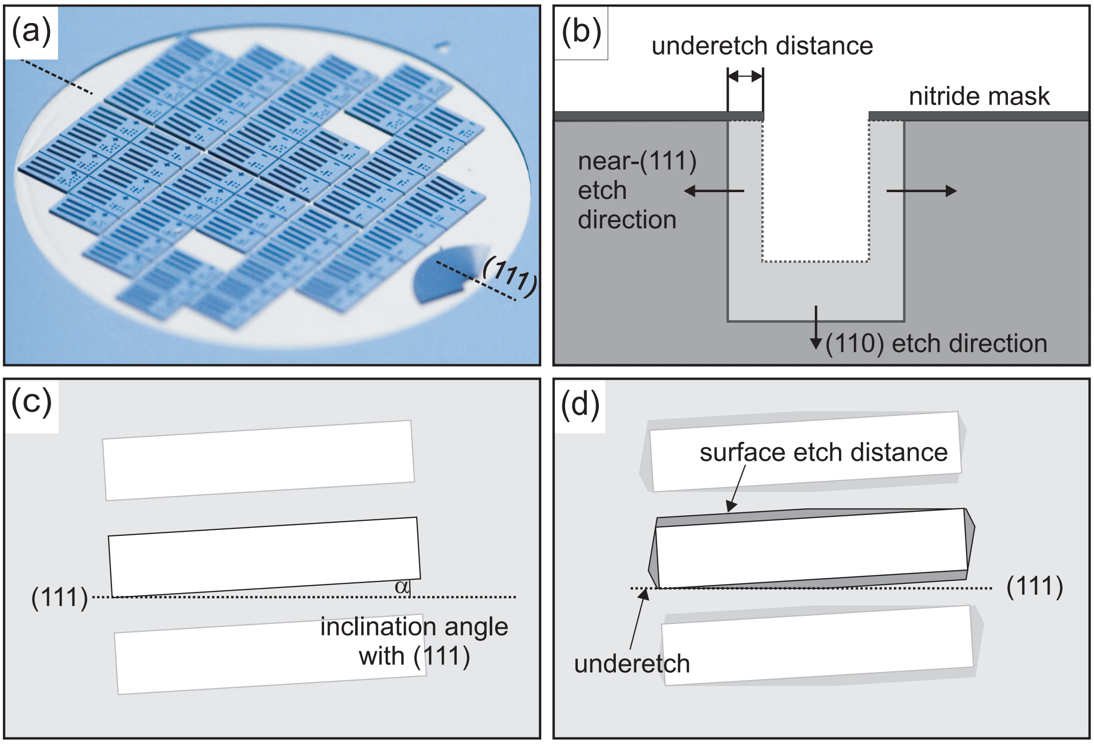

Figure 3.8: *Outline of trench offset pattern. (a) shows a picture of an unetched trench offset pattern with the (111) orientation indicated. (b) shows a schematic cross section of a trench and the etch directions. (c) and (d) show a schematic top view of a trench series, indicating the inclination angle and the underetch shape.*

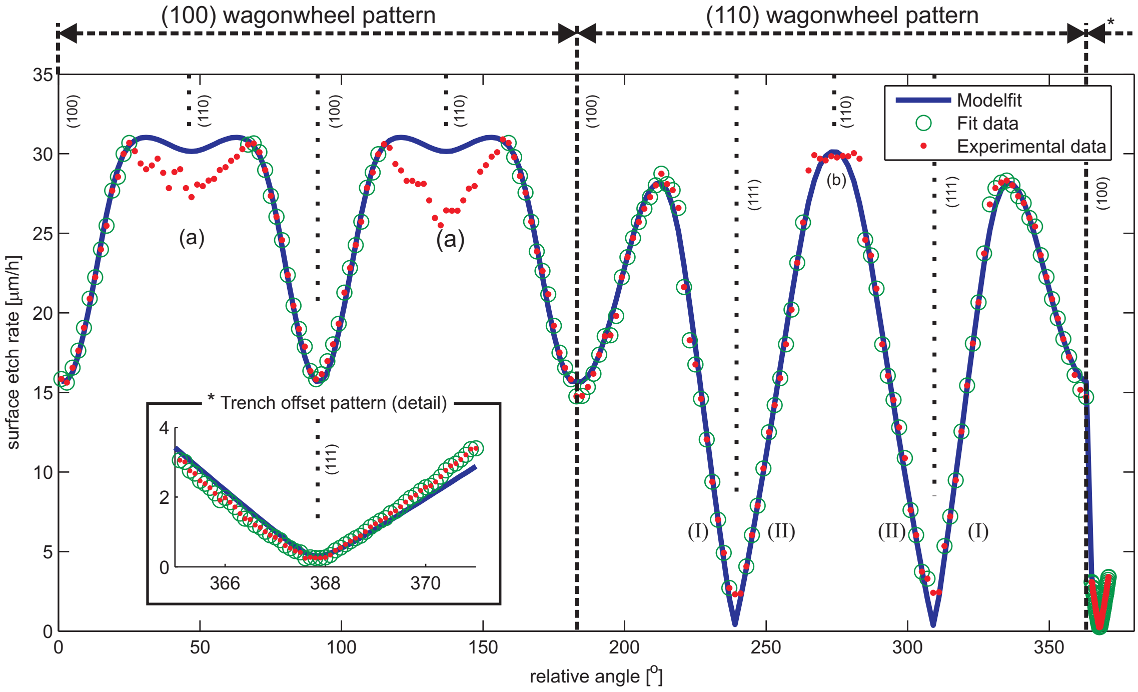

Figure 3.9: *Typical overview of anisotropic etch rate measurements at constant applied potential (-1000 mV vs. SCE) (dots). The solid line denotes the model fit and the open circles the actual data points used for the model fit. The major crystal orientations are indicated. The inset shows a detailed view of the data acquired from the trench offset pattern.*

was removed using the KOH etching solution itself and was monitored by measuring the OCP. A fixed potential was applied after the native oxide was removed. These potentials varied from -1500 mV to -875 mV vs. SCE. The etch time for the wagon-wheel pattern was 60 min and for the offset trench pattern 180 min. After etching the samples were briefly quenched in a diluted HNO_3 solution to stop the etching processes and remove KOH residues.

3.5 Results and discussion

Figure 3.9 shows a typical plot of the measured anisotropic etch rates at one particular applied potential. The measurements of the three different samples are plotted sequentially for clarity. Additionally, the 7-parameter model fit is shown together with the actual data points used for the fit. Note that the data near the (110) is not used for the data fit as outlined in a previous section. Examining both the etch results and the fitted parameters as a function of the applied potential will give a large amount of information concerning the influence of the electrochemistry on the etch mechanisms on a microscopic scale.

3.5.1 Vicinity of (111)

The measurements in the vicinity of the (111) crystal orientation (see inset of figure 3.9) show an expected minimum in anisotropic etch rate at the true (111) orientation. The shape of this minimum is characteristic of the dominant etch mechanisms at these orientations. The observed rounded shape of the minimum indicates a birth-and-spread mechanism, which is controlled by terrace roughening. A more flattened shape, for example, indicated a defect-driven terrace etch mechanism, while a sharp cusp indicates no pit nucleation[102, 103].

Terrace roughening

Figure 3.10 shows the (111) terrace roughening parameter (ε_{111}^{2D}) as a function of the applied potential. This is the controlling parameter for the birth-and-spread mechanism on terraces and largely determines the etch rate of surfaces with small inclination angles (see chapter 2, equation 2.2). The result shows a minimum of ε_{111}^{2D} at -1250 mV vs SCE and a general increase at more positive potentials. Terrace roughening can be regarded as step nucleation, which on a molecular scale translates to the random removal of single Si atoms from a terrace, ultimately producing a rougher surface. This would mean that at the ε_{111}^{2D} minimum, near-(111) surfaces become smoother. The mechanism behind this decrease in terrace roughening is unclear. The increase in roughening at positive potential, however, can be attributed to so-called OH-clustering [77, 105, 38, 37]. There is experimental evidence that the presence of an OH-terminated Si surface atom can increase the probability of the oxidation of a neighbouring Si atom. This OH-terminated surface Si can subsequently be chemically etched (see figure 3.2a) creating step sources. A higher electrochemical oxidation rate at more positive applied potential will result in a higher OH and SiO_2 coverage of the (111) silicon surface. These OH-surface atoms can either be etched directly (see figure 3.2) or contribute to OH-clustering. The nature of electrochemical oxidation on (111) terrace sites, means that OH formation and resulting step sources will be randomly distributed, overall increasing the terrace roughening and ε^{2D}.

It should be noted that of all the orientations, the (111) surface etch rate is the most difficult to measure reliably. Towards this end, the trench offset samples were design where the (111) etch rate is determined, not from a single measurement, but from the minimum in the etch rate of near-(111) surface orientations (see the inset of figure 3.9). It is clear that the etch rate of the (111) surface is determined by the birth-and-spread mechanism and is therefore primarily controlled by the ε^{2D} parameter (see chapter 2 for the effects of a change in roughening on the etch rate). Nonlinear regression has been used for the data fitting of all the parameters which gives a particular regression coefficient of the model fit. Visual evaluation of the model fit at the (111) orientation can indicate deviation of ε^{2D} for which the data fit is still acceptable. Note that due to the non-linear nature of the terrace roughening element (see equation 2.2 in chapter 2), a higher roughening will result in a larger possible deviation. This evaluation was only performed on the terrace roughening parameters as these parameters are effectively fitted with the least data points. The remaining parameters ((111) and (100) step velocity and step roughening) uses a larger number of data points which increases the accuracy considerably.

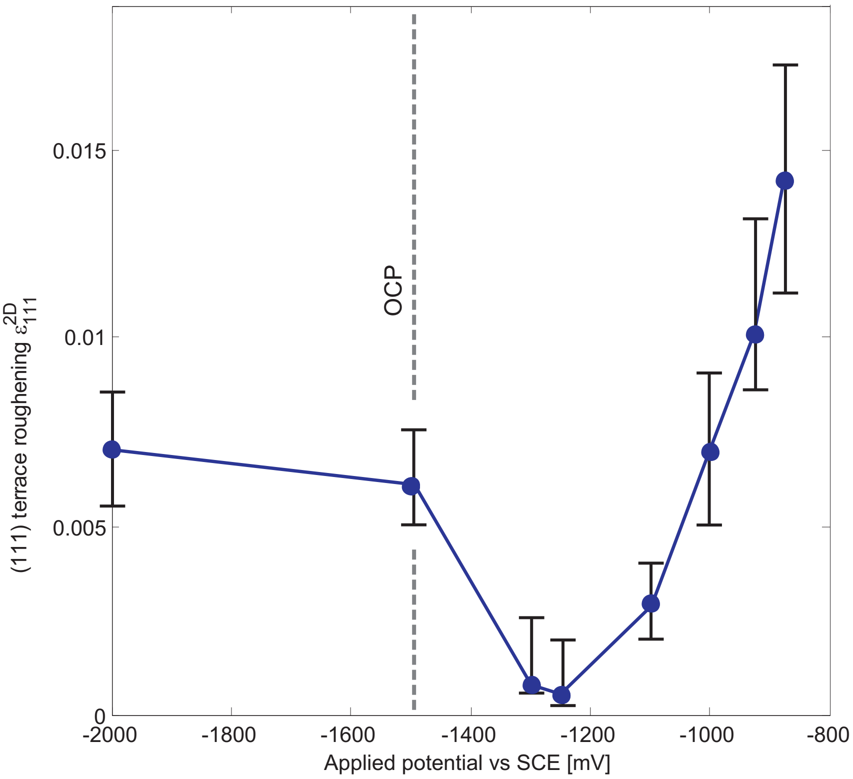

Figure 3.10: *Terrace roughening parameter of (111) surfaces (ε_{111}^{2D}) as a function of the applied potential*

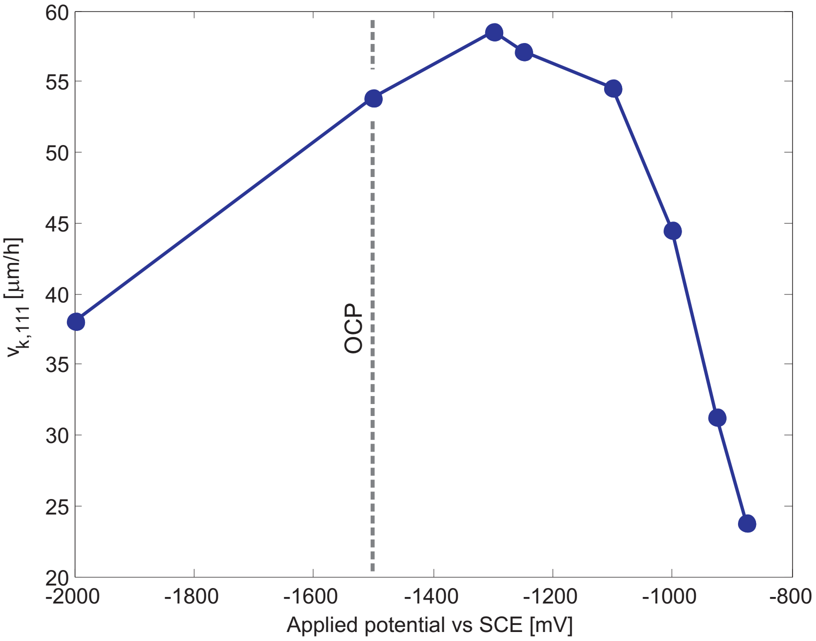

Figure 3.11: *The step velocity parameter of (111) steps (v_{k111}) as a function of the applied potential.*

Step velocity and passivation

Figure 3.11 shows the (111) step velocity parameter (v_{k111}) as a function of the applied potential. A decrease in step velocity is observed at more positive applied potential. Results above -875 mV vs. SCE shows the highest decrease as electrochemical oxidation of Si to SiO_2 becomes predominant, resulting in a passivated Si surface[59]. The results are consistent with CVs measured on large (111) surfaces[110]. The onset of electrochemical oxidation of the bulk (111) surface, reflected in the increase in anodic current in the voltammogram, coincides with the decrease in v_{k111}. Although called the step velocity parameter, it is important to emphasize that v_{k111} actually describes the kink velocity. This coincides with the step velocity of the fastest etching steps (as they consist of only kinks). The step velocity of the the slowest step is determined by the v_{k111} and the step roughening parameter ε_{111}^{1D}, as described in the following section.

Step anisotropy and anisotropy reversal

An anisotropic trend is present at both sides of the (111) orientation (see figure 3.9 range I and II). According to equation 2.1 the slope of this graph is equal to the (111) step velocity[104]. The graph shows a higher step velocity in range I (surface inclination towards (100)) than range II (inclination towards (110)). Surfaces with a surface normal inclined towards the $[1\ 1\ \bar{2}]$ (range I) contain monohydride terminated steps. These steps have Si atoms at the edges containing only one dangling hydrogen atom. In range II where the surface is inclined towards the $[\bar{1}\ \bar{1}\ 2]$ direction, the Si atoms on the edge have two dangling hydrogen atoms which are dihydride terminated steps. As outlined in chapter 1.4, the structural differences between these two types of steps indicate that dihydride

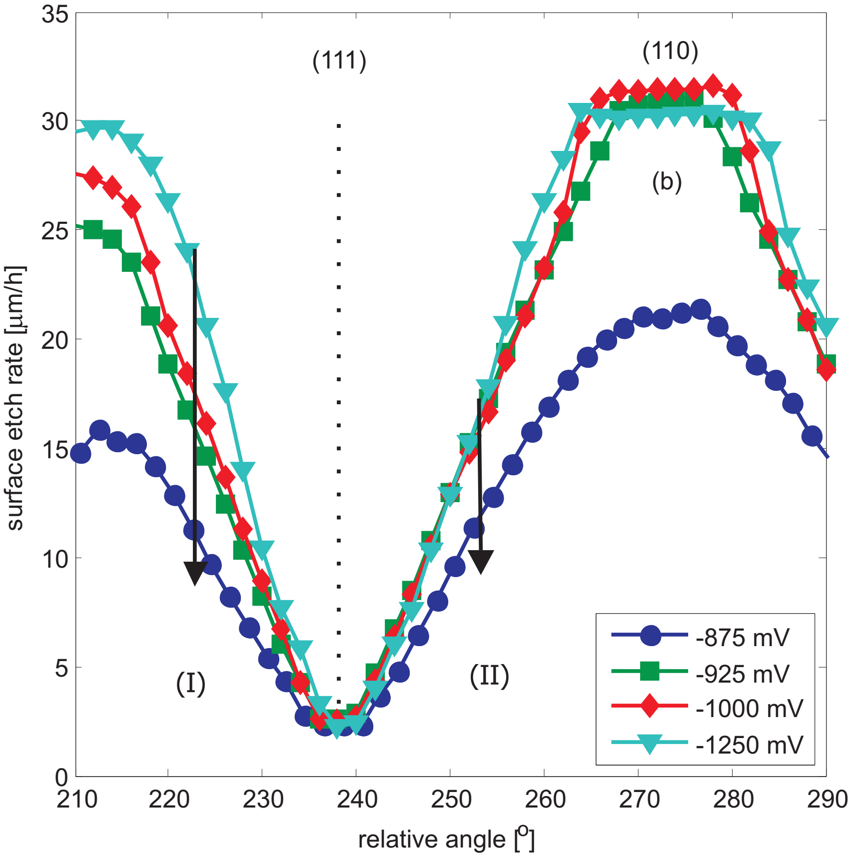

Figure 3.12: *Etch rates in the vicinity of (111) at various applied potentials, illustrating the step etch velocity change (slope in regions I and II) as a function of the applied potential.*

terminated steps are more reactive to chemical etching and would have a higher step velocity. From figure 3.12 it can be seen that at more positive applied potentials, the relative difference in step velocity becomes smaller. From these results it is clear that the general step etch velocity is both dependent on the electrochemistry and the actual planar orientation of the step on the surface (step anisotropy). Within the kinematic wave theory, this step anisotropy is described with the step roughening parameter (ε_{111}^{1D}). The parameter has a range from 0 to 1 with the following two limiting conditions (see equation 2.4).

- Maximum step anisotropy ($\varepsilon_{111}^{1D} = 0$): The most stable step orientations (coinciding with the (111) monohydride-terminated steps) have an effective step velocity of 0. The highest step velocity will be at the most unstable step orientations, exactly between the PBC directions. The absolute value will be determined by the step velocity parameter (v_{k111})
- Minimum step anisotropy or step isotropy ($\varepsilon_{111}^{1D} = 1$): Step velocity of all planar step orientations is the same and determined by the v_{k111} parameter.

Figure 3.13 shows ε_{111}^{1D} as a function of the applied potential. The results show an increase in step anisotropy (decrease in ε_{111}^{1D} value) at more positive potential up to -1250 mV vs SCE. At these potentials, electrochemical etching (see 3.2) is expected to occur which becomes more significant at increasing potentials. As electrochemical etching is different from pure chemical etching (in terms of reaction mechanism and driving force), it is possible that this reaction shows a different (step) anisotropy. The increase in step anisotropy indicate that additional electrochemical etching results in an increase in overall etch rate of the dihydride terminated steps compared to the monohydride terminated steps. This increase in step anisotropy, points to the fact that electrochemical etching favours the dihydride terminated steps. The parameter values also show a general decrease in step anisotropy (increase ε_{111}^{1D} value) at more positive applied potentials above -1250 mV vs SCE. At these potentials, electrochemical oxidation to SiO_2 become significant. As this reaction passivates the step sites, effectively reducing the overall step etch rate, an decrease in step anisotropy points to the fact that dihydride terminated steps are oxidised as as fast or faster than monohydride terminated steps. At approximately -900 mV vs. SCE the parameter value is 1 which indicates that the step velocities of the dihydride and monohydrides are the same. Although ε_{111}^{1D} remains 1 at more positive applied potentials, the step velocity determined from the slope in figure 3.12 indicates that above the -900 mV vs. SCE, monohydride-terminated steps etch faster than dihydride. This is called *step anisotropy reversal*. This situation cannot be directly described within the model as the most stable step orientations are predefined, coinciding with the monohydride terminated step orientations. In the case of step anisotropy reversal, dihydride-terminated step orientations are the most stable (see figure 3.14). Examining the slope of the graphs in figure 3.12 using equation 2.1 shows that anisotropy reversal indeed occurs above the -900 mV vs. SCE.

The decrease and subsequent increase in ε_{111}^{1D} at more positive applied potentials together with the occurrence of step anisotropy reversal demonstrates that electrochemical oxidation of surface step edges is not isotropic. As with chemical etching, the electrochemical oxidation reactions favour dihydride-terminated steps on (111) surfaces even to the extent that under very strong oxidizing conditions the dihydride-terminated steps etch slower than monohydride-terminated steps. This is consistent with observations by Allongue et al.[3, 4] where higher electrochemical oxidation rate is observed on (111) kink sites which are equivalent to dihydride sites.

Both the change in step anisotropy and anisotropy reversal are revealed in two phenomena. One is the shape of the triangular etch pits on (111) surfaces. As the sides of the pits are near-(111) surfaces consisting of steps, the triangular shape of the etch pits is a direct result of the step anisotropy. A decrease in step anisotropy results in the pits becoming more circular as there is less difference in the etch rate between the pit sides. Under step anisotropy reversal conditions, the orientation of the triangular shapes is reversed. A second phenomenon is the change in etch shape of a hemispherical silicon sample as used by Shikida et al.[87]. After anisotropic etching, spherical samples will show a triangular convex shape in the vicinity of the (111) orientation. The change in this convex shape is analogous to the (111) etch pits becoming more circular at lower etch anisotropy and changing orientation at anisotropy reversal (see chapter 4 and 6).

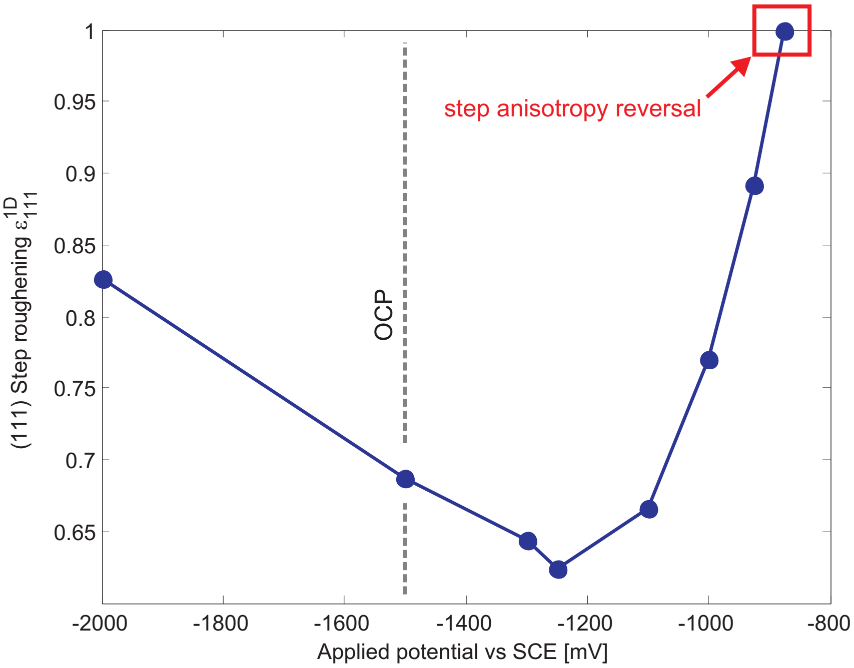

Figure 3.13: *Step anisotropy parameter for (111) type steps(and ε_{111}^{1D}) as a function of the applied potential. The applied potentials where step anisotropy reversal occurs are indicated.*

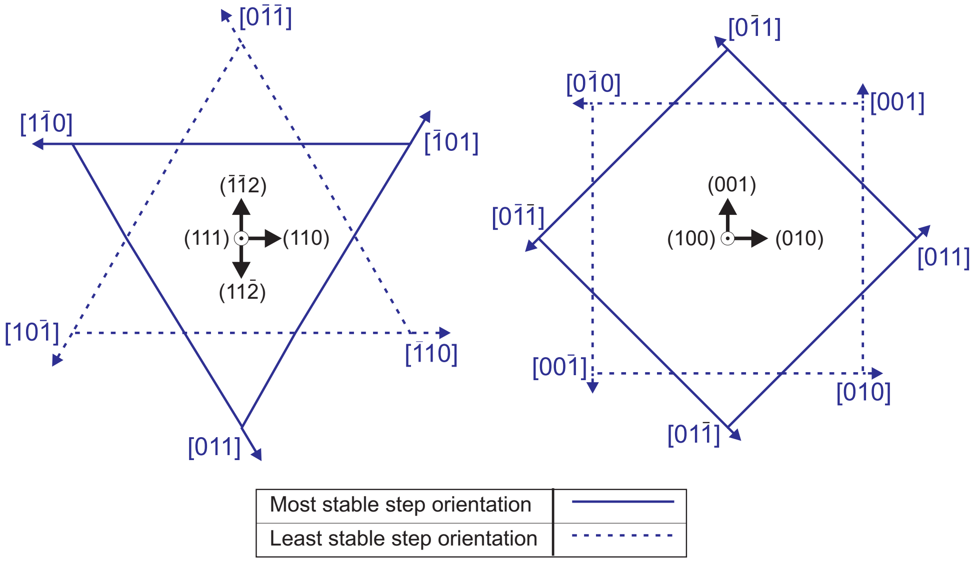

Figure 3.14: *The most and least stable step orientation on both (111) (left) and (100) surfaces (right). The most stable step orientations are denoted by the solid arrows. Under the etching conditions in this chapter, these orientations correspond to the monohydride-terminated steps on (111). The least stable or fastest etching step orientations are denoted by the dashed arrows and (on (111)) correspond to dihydride-terminated steps. Note that for (111) these orientations correspond to the PBC orientations, for (100) they do not. Under step anisotropy reversal conditions, these orientations are reversed, the most stable orientations become the fastest etching orientations.*

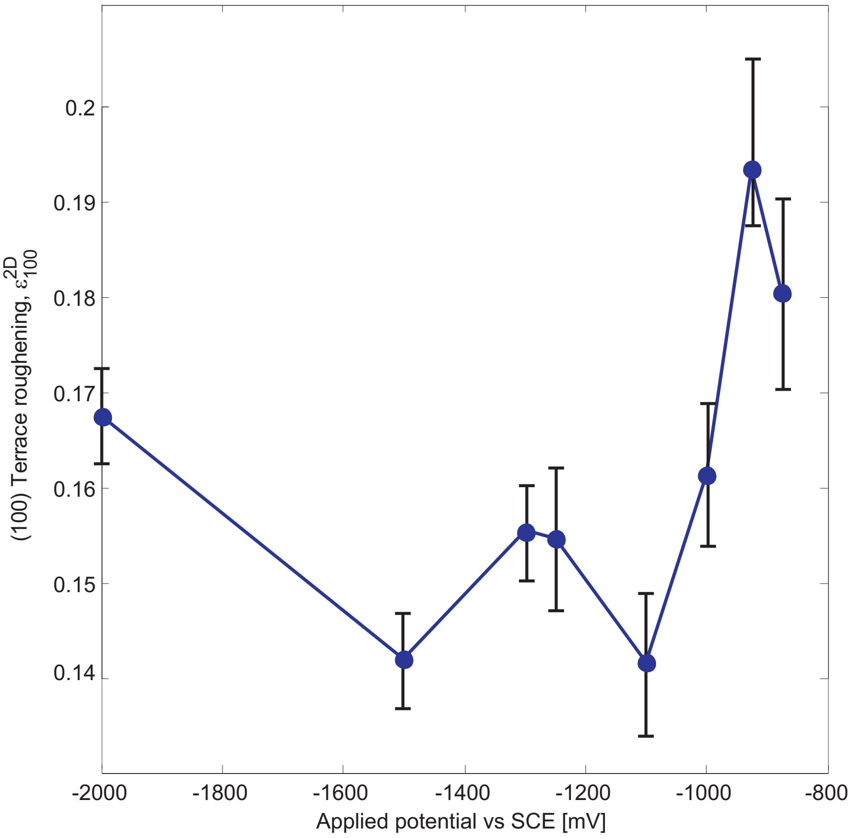

Figure 3.15: *Terrace roughening parameter of (100) surfaces (ε_{100}^{2D}) has a function of the applied potential.*

3.5.2 Vicinity of (100)

Both the wagon-wheel patterns on (100) and (110) substrates contain sidewalls with (100) and near-(100) crystal planes but are oriented in a different way. The data fits have shown that both data sets are required, for reliable model fits in the vicinity of (100).

Terrace roughening, step velocity and passivation

Figure 3.15 shows the (100) terrace roughening parameter (ε_{100}^{2D}) as a function of the applied potential. A visual evaluation of the parameter deviation was performed similar to that of the (111) terrace roughening parameter. The measurements indicate an overall increase in the ε_{100}^{2D} at a more positive potential, analogous to the (111) terrace roughening. However, due to the larger scatter of the measurement points, this trend is not as clear as on the (111) surface. There is also a slight increase in terrace roughening at approximately -1300 mV vs SCE. Due to the larger possible deviation in measurement points, not much can be concluded from this increase, except that it coincides with the (111) terrace roughening minima at the same applied potentials. Figure 3.16 shows the (100) step velocity (v_{k100}) as a function of the applied potential. The results show a decrease of v_{k100} as a result of the electrochemistry. As with the results of (111) step velocity, these results are consistent with cyclic voltammograms measured by Xia et al.

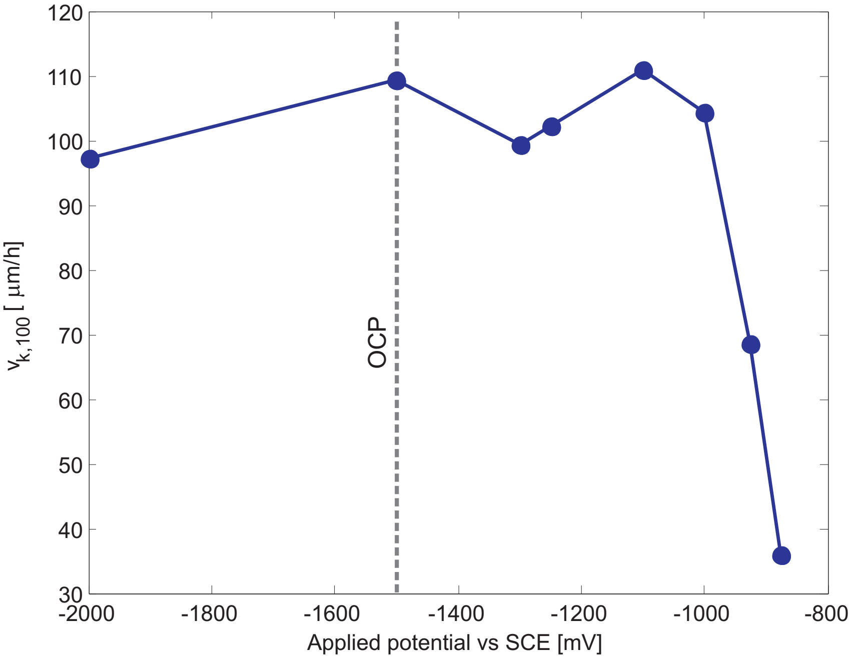

Figure 3.16: *The step velocity parameter of (100) steps (v_{k100}) as a function of the applied potential.*

Step anisotropy and step anisotropy reversal

As can be seen in figure 3.17, the (100) step roughening parameter (ε^{1D}_{100}) shows a similar increasing trend as the (111). Although examination of the etch results and resulting etch shapes did not indicate step anisotropy reversal, the parameter values above -1000 mV show that this phenomenon also occurs on (100) surfaces. The explanation of step anisotropy and reversal in terms of step termination differences, analogous to (111) surfaces, does not directly apply to (100) steps. Although the molecular configurations of the most and least stable steps are different, there is no clear difference in step termination. Crystallographically, the other step anisotropy directions ([1 0 0] family) do not conform to either PBC directions (as defined in normal (100) step anisotropy). There is no straightforward way to experimentally observe (100) step anisotropy decrease and reversal directly. These surfaces do not contain etch pits similar to (111) surfaces. One possible method is to use spherical silicon samples as reported by Shikida et al., the effect should be visible in the resulting convex etch shape of the spherical sample.

3.5.3 Anisotropy ratio

The anisotropic ratio which is defined as the etch rate of (100) divided by the etch rate of (111), gives a measure of the general etch anisotropy of the system. For MEMS fabrication a high anisotropic ratio is generally desired in order to make well-defined structures with a high aspect ratio. From figure 3.18, which shows the anisotropic ratio as a function of the applied potential, it can be seen that the highest anisotropic ratio is at -1250 mV vs. SCE. As the (100) etch rate remains relatively constant at this potential, the anisotropic ratio

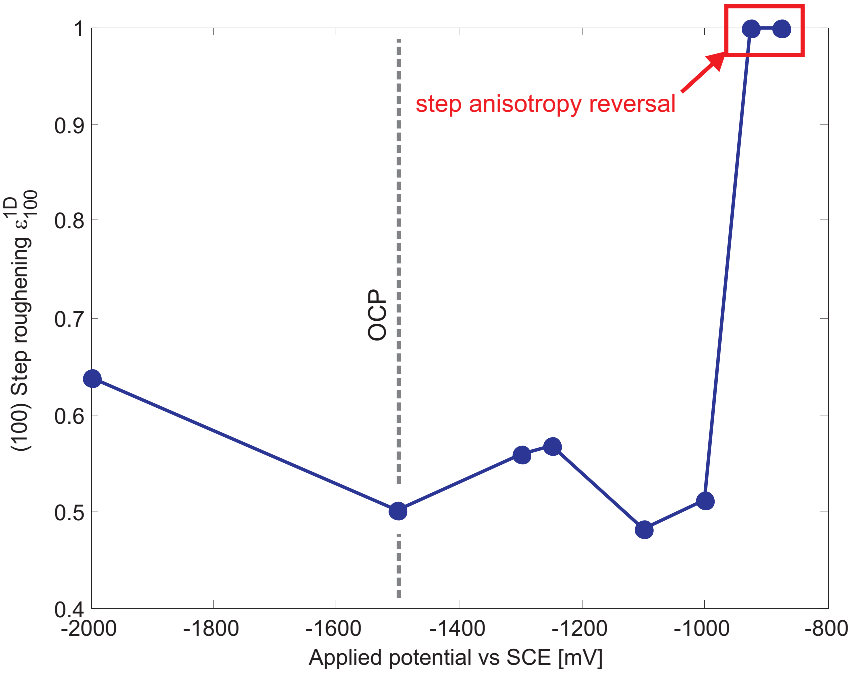

Figure 3.17: *Step roughening parameter (100) type steps(ε^{1D}_{100}) as a function of the applied potential. The applied potentials at which step anisotropy reversal occurs are indicated.*

maximum corresponds to the minimum in (111) etch rate and (111) terrace roughening. Note that the errors in both (100) and (111) terrace roughening have repercussion on the accuracy of the calculated anisotropic ratio, in particular at the maximum. The asymmetry in the ε^{2D}_{111} error leads to an asymmetric in the error of the anisotropy ratio. It is important to note that the applied potential at the maximum does not correspond to the OCP in typical etch situations. As (100) oriented wafers are typically used in MEMS, the OCP lies closer to -1500 mV vs. SCE corresponding to the OCP of the substrate. The optimum, however, is closer to the OCP of (111) surfaces.

3.5.4 (110) morphology

The morphology of the samples, in particular the (110) surface, were observed using scanning electron microscopy (SEM). Figure 3.19 shows the (110) morphology at the bottom surface outside of the wagon-wheel pattern at three different applied potentials. At a potential close to OCP, the typical (110) morphology is observed consisting of roof-tile structures. A more positive potential results in a finer roof-tile structure. At a very positive applied potential, the surface is covered with trapezoidal hillocks. The (110) morphology is discussed in detail in chapter 7 where the influence of the electrochemical oxidation on the (110) morphology formation and evolution is examined using in-situ microscopy.

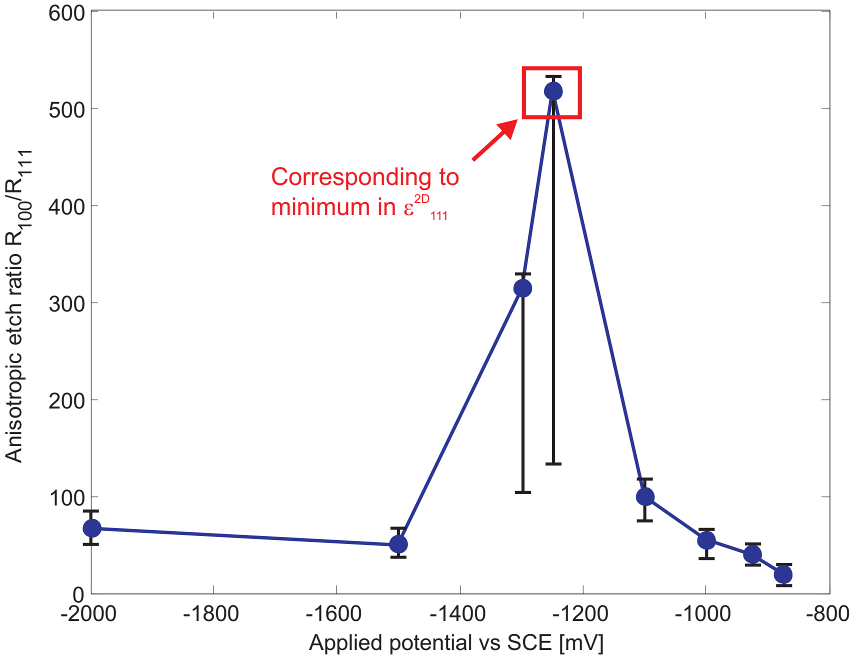

Figure 3.18: Calculated anisotropic ratio as a function of the applied potential

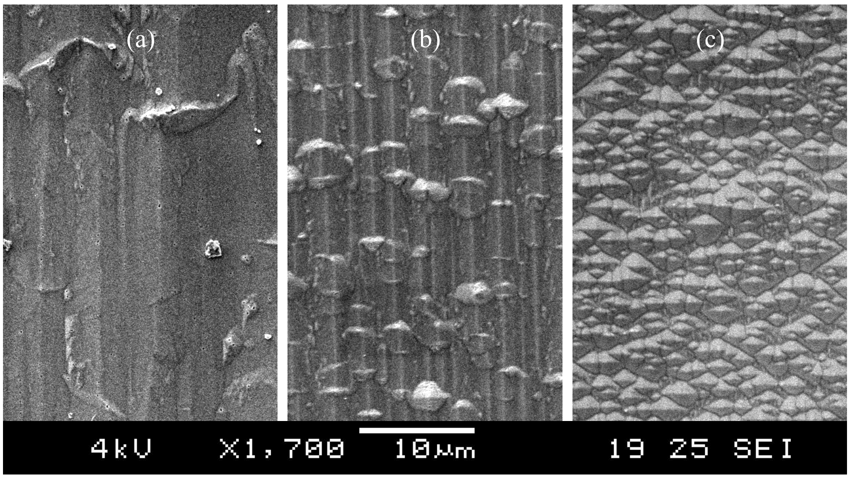

Figure 3.19: *SEM pictures of the (110) morphology at various applied potential. The typical roof-tile morphology is visible at -1500 mV vs SCE(a). At -1000 mV vs SCE (b) the roof-tile features become smaller. At -925 mV vs SCE (c) the surface is covered with trapezoidal hillocks.*

3.6 Conclusions

In this chapter, the effect of a fixed applied potential on the anisotropic etch rate of silicon in a KOH solution has been investigated. The influence of the electrochemistry was described in terms of microscopic properties by using the kinematic wave theory. With the combination of stepflow and birth-and-spread mechanism as its basis, the 7-parameter model can be used to distinguish step velocity, terrace roughening and step anisotropy. Measurements were done using two dry-etched wagon-wheel patterns on (100) and (110) substrates and a masked trench pattern on (110) substrates.

Etch experiments were performed under electrochemical controlled conditions, with an applied potential from -2000 mV to -875 mV vs. SCE. The results show a decrease in step velocity of both steps on (100) and (111) surfaces which can be attributed to electrochemical oxidation of Si to Si-OH and SiO_2. The oxidation and passivation of surface steps as a function of the applied potential mirrors the electrochemical behaviour of bulk Si surfaces as measured using cyclic voltammetry. Step source nucleation on terrace surfaces as described by the terrace roughening parameter (ε_{100}^{2D} and ε_{111}^{2D}) shows an increase at positive applied potential above -950 mV vs. SCE, although the effect is larger on (111) surfaces. This increase can be attributed to an increase in isotropic oxidation of the Si terrace atoms to Si-OH. These sites can either directly etch chemically or contribute to OH-clustering, both of which will result in an increased random step source nucleation. Terrace roughening of (111) (ε_{111}^{2D}) also shows a minimum at -1250 mV vs. SCE (which is closer to OCP of (111) surfaces). The mechanism behind this minimum is unclear. The results however indicate that under these conditions the (111) surface becomes smoother. Coupled to that, the surface etch rate would be at its lowest, as ε_{111}^{2D} terrace roughening is the controlling mechanism for terrace etching. With a relatively stable (100) surface etch rate under these conditions, the anisotropic etch ratio will also show a maximum at -1250 mV vs. SCE.

Step anisotropy, the relative difference between the most stable and least stable step orientation on a crystal surface, shows a decrease at more positive applied potential for steps on (111) to the extent that it becomes isotropic. The data also indicates that at higher potentials step anisotropy reversal occurs, a situation in which the step etch velocity of the dihydride terminated steps on (111) is lower than the (generally more stable) monohydride terminated steps. The step anisotropy under normal conditions and the decrease as function of higher applied potential points to the fact that both chemical etching and electrochemical oxidation of steps is not isotropic. As with chemical etching, the electrochemical oxidation reaction favours dihydride terminated steps showing a higher oxidation rate on these steps. The results additionally show that step anisotropy reversal also occurs on (100) steps at very positive applied potentials (above -875 mV vs. SCE). Unlike (111) steps however, the step orientations of the stable steps in step anisotropy reversal conditions do not correspond to either PBC orientations. The mechanism behind the step anisotropy reversal at (100) is therefore unclear.

Chapter 4

Recognising (111) step site specific interaction

The anisotropy in step velocity of (111) surface steps has previously been regarded as the result of reactivity differences between the mono- and dihydride terminated steps or between kink and step sites. Hexagonal etch shapes observed on (111) etch pits and etched hemispherical samples indicate an additional etch rate difference between different types of step dihydrides. The basic kinematic wave theory does not contain this distinction. The model was therefore extended to incorporate the observed (111) step anisotropy. Using this model, the orientation dependent (111) step velocity can be obtained from detailed etch rate data measured on hemispherical Si samples. Closer examination of the (111) step velocity, coupled to the molecular structure of the surface steps, gives information concerning the reactivity of the different (111) step sites. The effects of TMA^+ *on the different mono- and dihydrides were investigated by examining the changes to the (111) step velocity and anisotropy.*

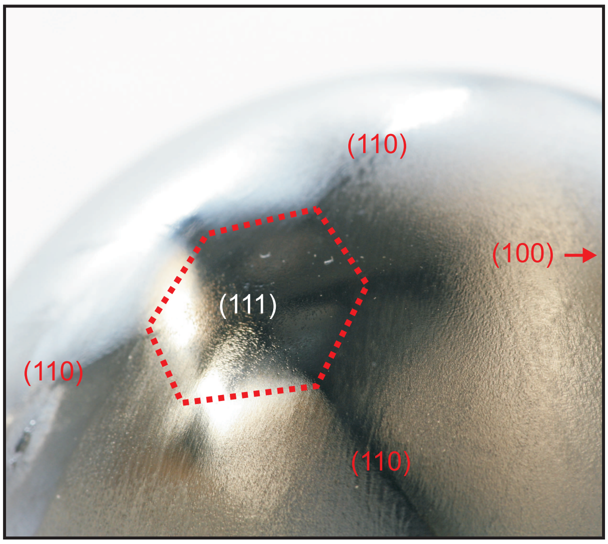

Figure 4.1: *Photograph of the surface of an etched hemispherical Si sample. The hexagonal etch pattern in the vicinity of the (111) orientation is indicated.*

4.1 Introduction

Anisotropic etching of Si in alkaline solution, used in MEMS technology, relies on exploiting the difference in etch rate of different surface orientations. It is well known that this anisotropy is not restricted to Si surfaces alone but also occurs on the steps present on these surfaces (see chapter 1.4). The steps on (111) stable surfaces are of particular interest as the planar step orientation and the observed step anisotropy are clearly coupled to the actual molecular structure of the step edge. A change in this step anisotropy can then be linked to chemical reactions and surface kinetics[21, 36]. In both chapter 1.4 and 3, step anisotropy on (111) surface steps has been regarded as the relative reactivity difference between the mono- and dihydride terminated steps[22, 30, 67, 66]. Hexagonal shapes observed on etched hemispherical samples (figure 4.1) however have shown that, in addition to the mono- and dihydrides, step velocity differences are also observed on different types of dihydrides[41, 50], such as isolated dihydrides. The basic kinematic wave theory (chapter 2), which was previously used to obtain step velocity values from experimental data in chapter 3, does not make any distinction between different dihydrides. The model is therefore extended to incorporate the observed step anisotropy. Together with detailed etch rate data obtained from an etched hemispherical sample, etch velocities can be obtained which can be linked to different step/surface site kinetics. The effect of TMAH can then be investigated in terms of the impact of the TMA^+ ion on different (111) step sites, instead of mono- and dihydride terminated steps alone.

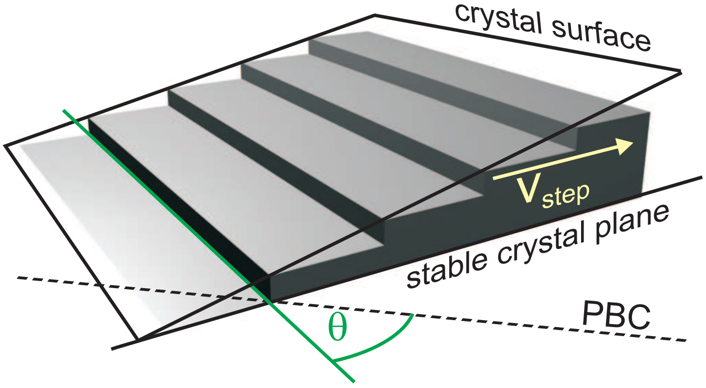

Figure 4.2: *Step velocity (v_{step}) is dependent on the planar step orientation (θ) with regards to PBC directions.*

4.2 Theory

4.2.1 (111) step anisotropy

As was outlined in chapter 1.4, the step velocity of surface steps on stable crystal planes is dependent on the planar orientation (θ) [30, 50, 65, 100] (figure 4.2). This step anisotropy is responsible for phenomena such as a triangular/hexagonal shape of etch pits on (111) surfaces[70] in concentrated KOH solutions. When examining step anisotropy from a crystallographic point of view, the (111) step velocity is solely determined by the kink density at the step edge. Step orientations which do not contain kinks are considered stable steps[40, 51] with a minimum in step velocity. Rotating the step orientation away from the stable steps will increase the kink density and corresponding step velocity. Steps which contain only kink sites are considered the fastest etching steps. This is the basis of the step anisotropy used in the kinematic wave theory as described in chapter 2.

As described in chapter 1.4, both the most stable steps and fastest etching steps are aligned with the PBC directions. The difference in step velocity is caused by the asymmetry in the molecular structure of the PBC. This results in the most stable steps containing only monohydrides, and the fastest etching step containing only dihydrides (see figure 1.4 in chapter 1.4). Step orientations in between contain a combination of mono- and dihydrides. Within this chapter the steps which contain only monohydrides (and are consequently aligned with a PBC) are called *monohydride-terminated steps*. Steps orientations aligned with a PBC and containing only dihydrides are then called *dihydride-terminated steps*. As outlined in chapter 1.4 and chapter 3, the step anisotropy can be viewed from a surface kinetics point of view, where it is reduced to the reactivity difference between the mono- and dihydride terminated steps.

Kinetic Monte Carlo simulations[30, 33, 40, 50] have shown that a distinction must be made between different dihydrides. These include the vertical and horizontal dihydrides. The difference between these two lies in the orientation of the attached hydrogen atoms (see figure 4.3). The hydrogen atoms of horizontal dihydrides lie in the (111) plane, while for the vertical dihydrides the hydrogen atoms lie in a plane perpendicular to the (111) . This difference has consequences for steric hindrance and interactions with neighbouring Si atoms. Si surface atoms that are relatively unhindered and free to distort are generally more reactive. The higher distortion freedom of the vertical dihydride would therefore suggest that it etches faster than the horizontal dihydride. However, using infrared spectroscopy, Jacob et al.[54] have only observed vertical dihydrides at the dihydride terminated steps. This indicates that, at these step orientations, the horizontal dihydrides etch faster than vertical dihydrides in contrast to what is expected from steric effects alone. Flidr et al. have linked the reactivity of these specific sites to the ease of which the pentavalent transition state can be formed (see the reaction mechanism in chapter 1.5) regardless of the distortion freedom. Although this applies to dihydrides which are present at the dihydride terminated steps, it does not necessarily apply to 'isolated' dihydrides at other step orientations (outlined in figure 4.3). The higher distortion freedom at these isolated dihydrides can also result in a higher etch rates. It is therefor also important to distinguish between *dihydrides at the dihydride terminated steps* and *isolated dihydrides*. Gosalvez et al. have shown similar results within the kMC simulation by only dealing with the number of backbonds and the interaction with indirect next-nearest neighbours. Here the number of next-nearest neighbours determines if a dihydride is isolated. By distinguishing a total of seven different (111) step and surface sites, Gosalvez et al. were able to accurately simulate underetch patterns[40]. This distinction between isolated and non-isolated dihydrides is the main distinction made within this chapter.

4.2.2 Hexagonal etch shapes

While etch pits observed on (111) surfaces in KOH solutions are generally regarded as being (rounded) triangular shaped, closer examination shows that the pits are often more hexagonal in shape[70]. When etching silicon in TMAH-based solutions the hexagonal shapes of these pits are much more pronounced[21]. These phenomena are also visible on etched Si hemispheres (see figure 4.1) where the convex etch shape in the vicinity of (111) show similar hexagonal shapes in TMAH based etching solutions[79] and to a lesser extent in high concentration KOH[80]. Regarding the (111) anisotropy as a function of the kink density (as outlined in the previous section) can only predict triangular shapes. From a crystallographic point of view (see chapter 1.4) three local minima are present in the θ-dependent step velocity corresponding to the monohydride terminated steps. A hexagonal shape indicates the presence of additional three local minima corresponding to the dihydride terminated steps. The step orientations inbetween the minima etch faster while the kink density is actually lower than the dihydride terminated steps.

By making the distinction between the different dihydrides, this paradox can be explained. Figure 4.4 shows the molecular structure of the mono- and dihydride terminated step together with the step orientation exactly in between these steps. Close examination of the molecular structure of the dihydride terminated steps show that it is composed of

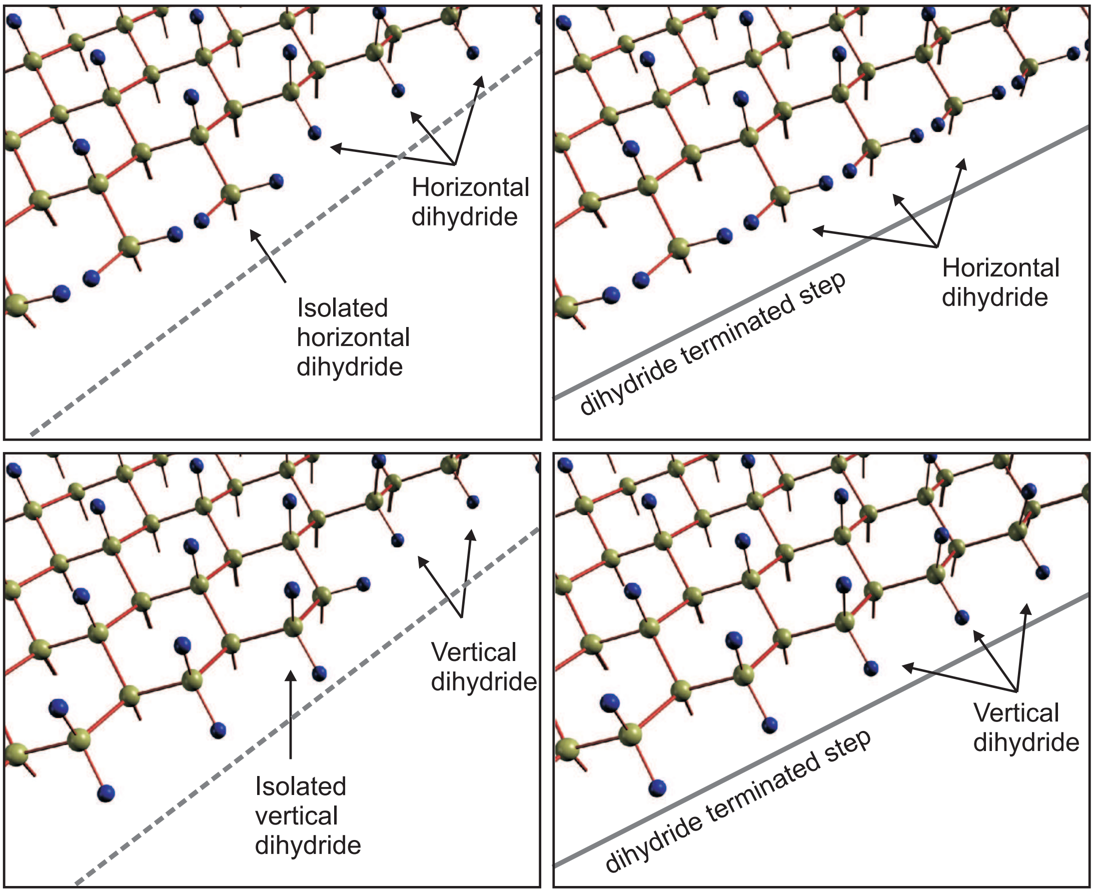

Figure 4.3: *Diagram illustrating the difference between vertical and horizontal dihydrides and isolated dihydrides. The right two figures shows the* dihydride terminated step *orientation where the step is composed entirely of horizontal dihydrides (top right) and vertical dihydrides (bottom right). The left two figures shows a step orientations which is rotated from the dihydride terminated step (in between the di- and the monohydride terminated step orientations). These steps additionally contain isolated horizontal dihydrides (top left) and isolated vertical dihydrides (bottom left). These isolated dihydrides have more distortional freedom due to the presence of fewer neigbouring Si atoms. This results in a higher etch rates of these sites compared to dihydrides on the dihydride terminated step.*

rows of horizontal dihydrides alternated with rows of vertical dihydrides (also visible in figure 4.3). As previously outlined, the observed presence of only vertical dihydrides at these step orientations indicate that the vertical dihydrides etches slower the horizontal dihydrides.

The step edge corresponding to the orientation exactly in between the mono- and dihydride terminated steps is composed of alternating isolated vertical dihydrides and monohydrides. The step velocity would be determined by the slowest etching site, which in this case, would be the monohydrides. However, when the faster etching vertical dihydride is etched away, the monohydride becomes an isolated horizontal dihydride (as shown in figure 4.4). The step velocity is therefore determined by either the isolated vertical or horizontal dihydrides, depending on which one has the slowest etch rate. It is also clear that both these dihydrides have higher distortion freedom and can therefore etch faster than similar sites on the dihydride terminated steps. This explains the observed higher step velocity at step orientations in between the mono- and dihydride terminated steps.

4.2.3 The kinematic wave theory: Step anisotropy

As the previous sections have outlined, the reactivity of the different (111) step sites is responsible for the observed anisotropy in the (111) step velocity . Experimentally determining this step velocity directly is very difficult. Allongue et al.[4] have been able to measure step velocity in-situ using STM. However, as miscut (111) wafers are used, the measurements are restricted to one particular step orientation. As outlined in chapter 2 and 3 the kinematic wave theory can be used to obtain the full orientation dependent step velocity from experimental surface etch data (using for example wagon-wheel patterns). The basic model which is outlined in chapter 2 is based on the crystallographic view of step anisotropy and can therefore only consider step velocity minima at the monohydride terminated steps. It can only predict triangular etch shapes and not the observed hexagonal shapes. The following sections briefly outline the basic mechanisms within the model and the model expansion necessary to describe this hexagonal shape. For a more detail description of both the model and the implementation, refer to chapter 2.

4.2.4 Stepflow / birth-and-spread

Within the kinematic wave theory, the θ-dependent step velocity is described by two processes. The stepflow process (applied to surface steps) determines the step velocity at orientations near the stable step orientation. The step velocity (v_{step})is then a function of the kink velocity (v_k) and the angle from the stable step orientation (θ) (see equation 4.1).

$$v_{step} = v_k \left|\sin\theta\right| \tag{4.1}$$

The birth-and-spread mechanism determines the step velocity at the stable step orientations. It describes the step velocity in terms of step roughening (ε_{111}^{1D}) which is related to random kink nucleation on the step edge (see equation 4.2).

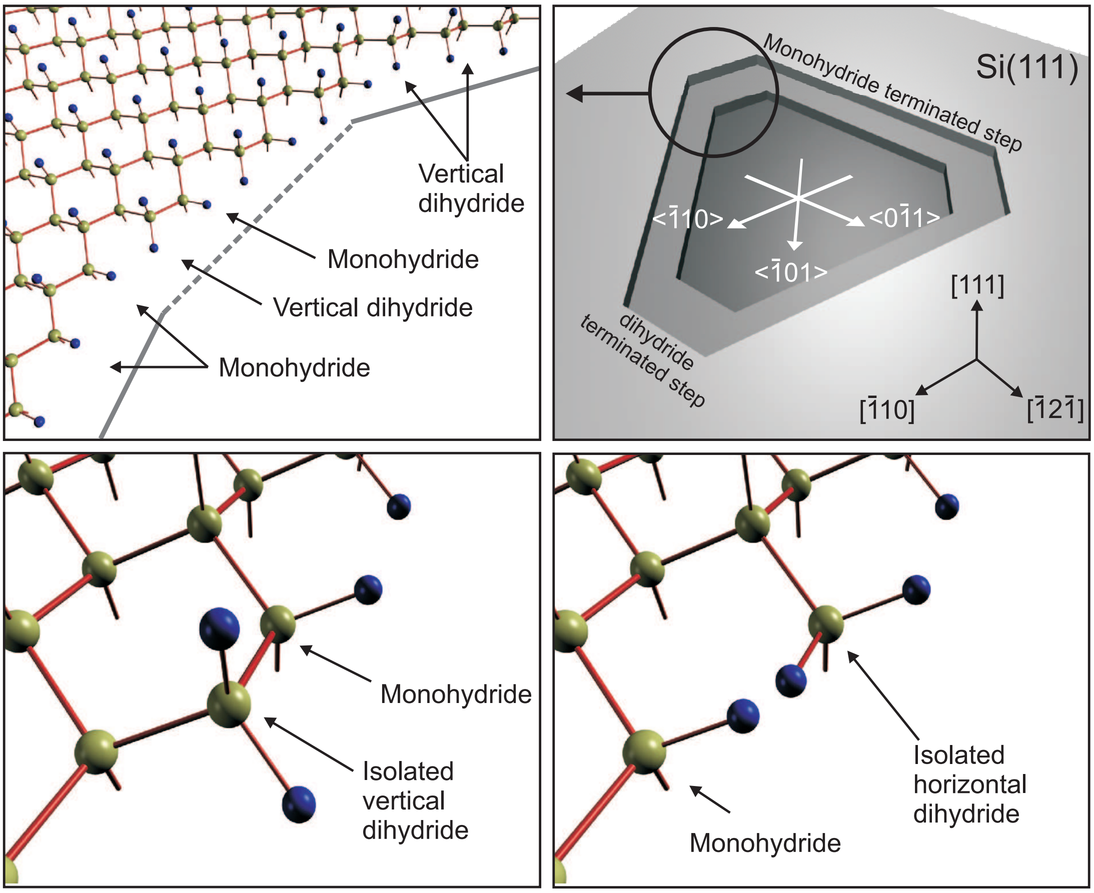

Figure 4.4: *Figure outlining the different dihydride types. Upper left figure shows the molecular structure of the steps indicated in the upper right figure. Both the mono- and dihydride terminated steps are indicated by the solid lines. The step orientation exactly in between these steps is indicated by the dashed line. As the figure shows, these steps are composed of alternating vertical dihydrides and monohydrides. The lower left figure shows a detail of these steps. When the isolated vertical dihydrides etch away, the monohydride becomes a isolated horizontal dihydride which is shown in the lower right figure.*

$$v_{step} = v_k \frac{\varepsilon_{111}^{1D}}{\sqrt{1 - \left(\varepsilon_{111}^{1D}\right)^2}} \tag{4.2}$$

In the basic model, the most stable step orientations of (111) correspond to the three monohydride terminated step orientations (see figure 1.4 in chapter 1.4). A stepflow and birth-and-spread element is present for each of these step orientations. The elements are combined using the elementary network assembly, as outlined in chapter 2, resulting in a continuous θ-dependent step velocity function. With a step roughening value $\varepsilon_{111}^{1D} < 1$ the function contains three local minima corresponding to the monohydride terminated steps. This step velocity function is subsequently used to determine the actual surface etch rate. It is therefore possible to obtaining the step velocity by fitting the model with experimentally obtained surface etch rates.

4.3 Model expansion

4.3.1 (111) step velocity

The hexagonal etch shape suggest local minima in step velocity at both the mono- and dihydride terminated steps. To include this in the model, additional stepflow elements (equation 4.1) are introduced corresponding to the dihydride terminated step orientations. As both the mono- and dihydride terminated steps etch differently (outlined in previous section), a separate birth-and-spread element is introduced (equation 4.2) for the dihydride terminated steps. These additional elements are all similar to the existing elements (including the modifications outlined in chapter 2) except for the orientation of the minima and the step roughening parameter ($\varepsilon_{111}^{1D,SD}$). From an atomistic point of view, the dihydride terminated steps are then considered ‘stable’ and do not contain kink sites. The isolated dihydrides are now considered kink sites instead of the (generic) dihydrides in the original model. Figure 4.6 illustrates the model expansion in terms of the changes in the θ-dependent step velocity.

The new elements are integrated into the model using the elementary network assembly and a parallel interaction type (see chapter 2). Equation 4.3 shows the resulting step velocity as a function of the step orientation (θ), step roughening parameter corresponding to the monohydride terminated steps ($\varepsilon_{111}^{1D,SM}$) and dihydride terminated steps ($\varepsilon_{111}^{1D,SD}$).

$$v_{step,111}(\theta) = \sqrt[-4]{\left(v_{k111}^{n}\right)^{-4} + \left(v_{k111}^{r}\right)^{-4} + \left(v_{k111}\right)^{-4} - \left(2^{-\frac{1}{4}}\left(v_{k111}\right)\right)^{-4}} \tag{4.3}$$

The last two terms in the assembled function are included to both limit and normalise the assembled function, the effects of which is also visualised in figure 4.6. The assembly of all the elements is illustrated in (figure A.4 in appendix A). Equation 4.3 then replaces the existing (111) step velocity equation used in the calculation of the surface etch rate (see chapter 2). It is clear from the new step velocity function that a total of six step velocity minima are present if $\varepsilon_{111}^{1D,SM} < 1$ and $\varepsilon_{111}^{1D,SM} < 1$.

Similar modifications were made for (100) steps (see appendix A figure A.4). Results in chapter 3 indicates the presence of possible step anisotropy reversal on (100) steps

parameter	Range	Description
$v_{k,hkl}$	> 0	Kink velocity
$\varepsilon^{1D}{}_{(hkl)}$	0 – 1	2D Terrace roughening (single atom pit nucleation on terraces)
$\varepsilon^{2D,n}{}_{(hkl)}$	0 – 1	1D Step roughening at original step orientations (monohydride terminated step for (111))
$\varepsilon^{2D,r}{}_{(hkl)}$	0 – 1	1D step roughening at new step orientations (dihydride terminated step for (111))
$C_{(hkl)}$		Step bunching

Figure 4.5: *Table outlining the parameters used in the 10-parameter model. (hkl) can both (100) and (111). The $\varepsilon_{111}^{1D,n}$ correspond to the monohydride terminated steps and are indicated as $\varepsilon_{111}^{1D,SM}$ in this chapter. The $\varepsilon_{111}^{1D,r}$ correspond to the dihydride terminated steps and is called $\varepsilon_{111}^{1D,SD}$. Note that this strong coupling with the molecular structure of the steps is not present for (100) steps ($\varepsilon_{100}^{1D,n}$ and $\varepsilon_{100}^{1D,n}$).*

at very positive potential. As the extended model can also describe this phenomenon, the same modifications are applied to the (100) steps (see appendix A figure A.5). As with (111), the additional step velocity minima is defined at step orientations exactly in between the existing minima. It is important to emphasize that possible step anisotropy reversal at (100) does not have the same molecular basis as at (111). As such it is unclear what can cause (100) step anisotropy reversal. In addition, step bunching on both (111) and (100) was also included which has proven to result in a more accurate model fit. The extended model now contains a total of 10 parameters (see figure 4.5).

4.3.2 Model fit to experimental data

As stated in the previous section, etch rate differences between different (111) surface sites are responsible for the formation of the hexagonal shape on hemispherical samples. Using the detailed etch rate data from these samples, the (111) step velocity can be obtained using the 10-parameter model. The use of these samples is discussed in more detail in chapter 6. Figure 4.7 and 4.8 show the etch rate measurements obtained from a single Si hemisphere etched in a KOH/TMAH mixture with a OH^- concentration of 5.0 mol/l and a TMA^+ concentration of 0.5 mol/l. Additionally, an external electrical bias was applied of -1000 mV vs SCE. The sample was etched at 50°C in the dark. It is important to note that these etching conditions are not commonly used. As outlined in chapter 6, this sample is part of a measurement series specifically designed to investigate the TMA^+ interaction with (111) step sites. It was observed however that, under these process conditions, the hexagonal shape in the vicinity of (111) is clearly visible (figure 4.1). The presence of these features on the hemispheres effectively led to the model modification and more detailed look at the (111) step velocity outlined in this chapter.

Figure 4.9 shows the data fit using the basic model as is outlined by van Veenendaal et al. (see chapter 2). Not only does it fail to describe the hexagonal shape, the data fit shows a circular pattern at (111) which indicates step isotropy. As the model is based on

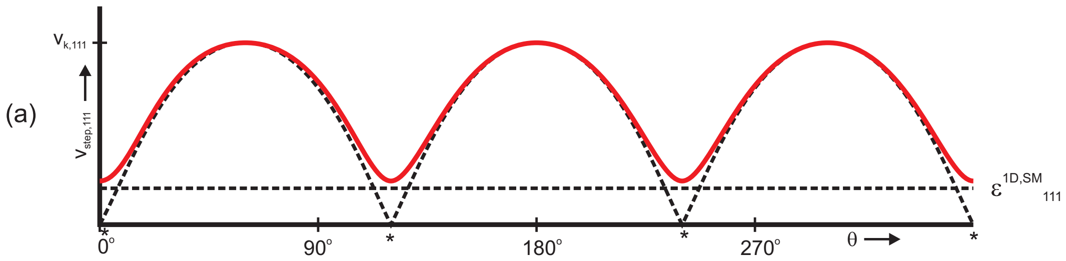

θ-dependent step velocity, monohydride terminated step, stepflow/birth-and-spread elements

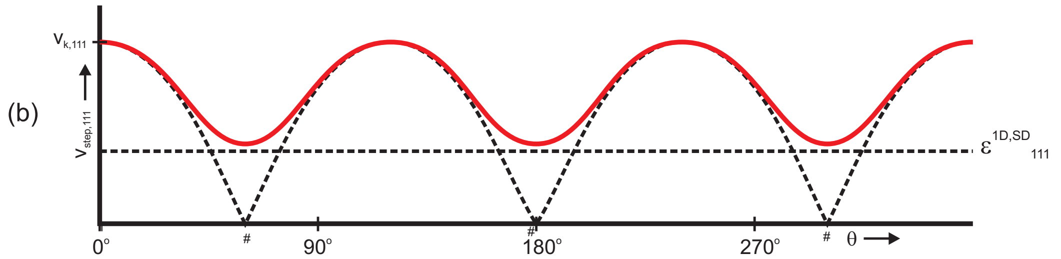

θ-dependent step velocity, dihydride terminated step, stepflow/birth-and-spread elements

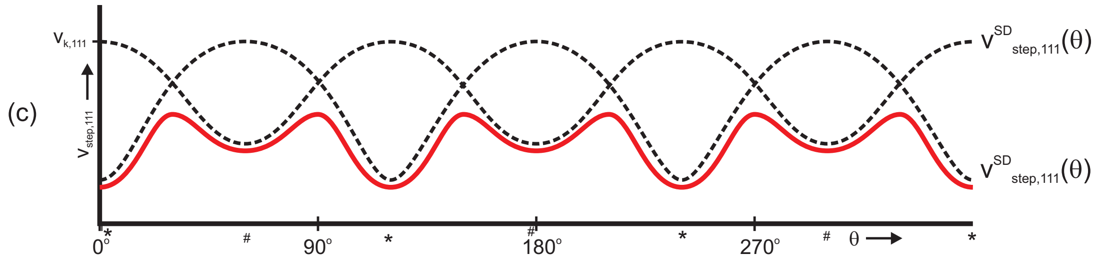

θ-dependent assembled step velocity function

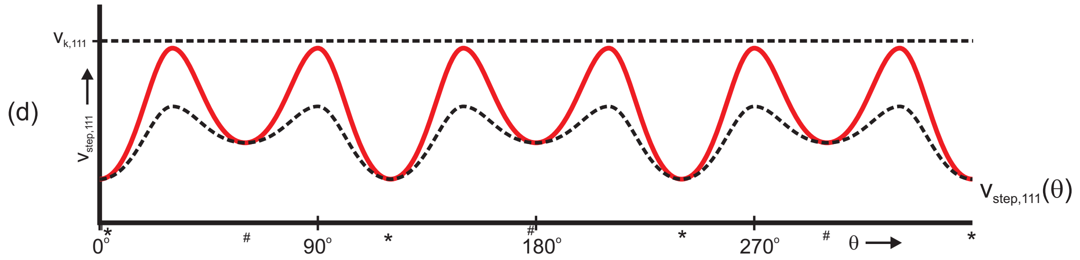

final θ-dependent step velocity function

Figure 4.6: *Graphical plots illustrating the model expansion. The dashed lines represent the original functions. The solid lines represent the assembled functions. The monohydride terminated step orientations are denoted by (∗) while the dihydride terminated step orientations are denoted by (#). The existing assembled step velocity function is shown using an arbitrary* $\varepsilon_{111}^{1D,SM}$ *(a). The new step velocity corresponding to the dihydride terminated steps and an arbitrary* $\varepsilon_{111}^{1D,SD}$ *is shown in (b). Assembling both step velocities using cusp combining assembly results in (c). The final normalised function is shown in (d).*

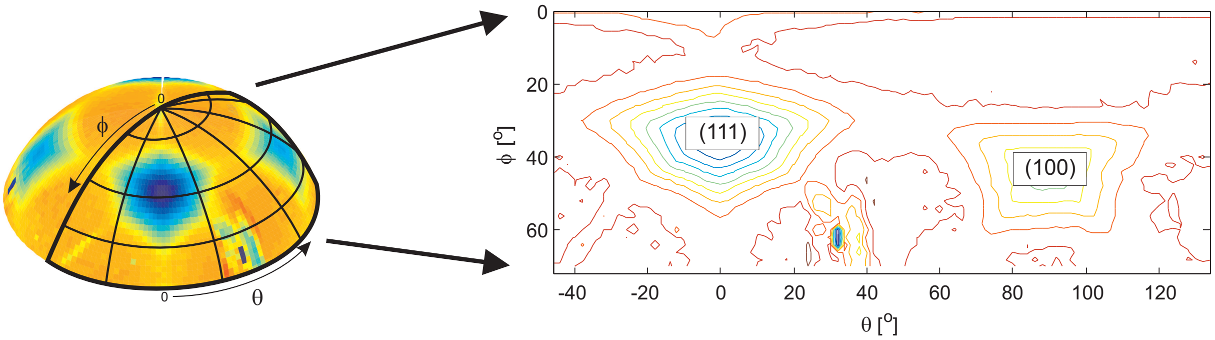

Figure 4.7: *Etch rate data obtained from a Si hemispherical sample. The left figure shows the etch rate as is measured on the sample. The hexagonal shape is clearly visible in the etch data in the vicinity of (111), the right figure shows a unfolded contour plot of a segment of the etch rate data. The (100) and (111) crystal planes are indicated. For all the data,* $\phi = 0^\circ$ *corresponds to the top of the hemispherical shaped Si sample. Note that the increasing distortion of the data in this particular projection of the sphere when* θ *decreases.*

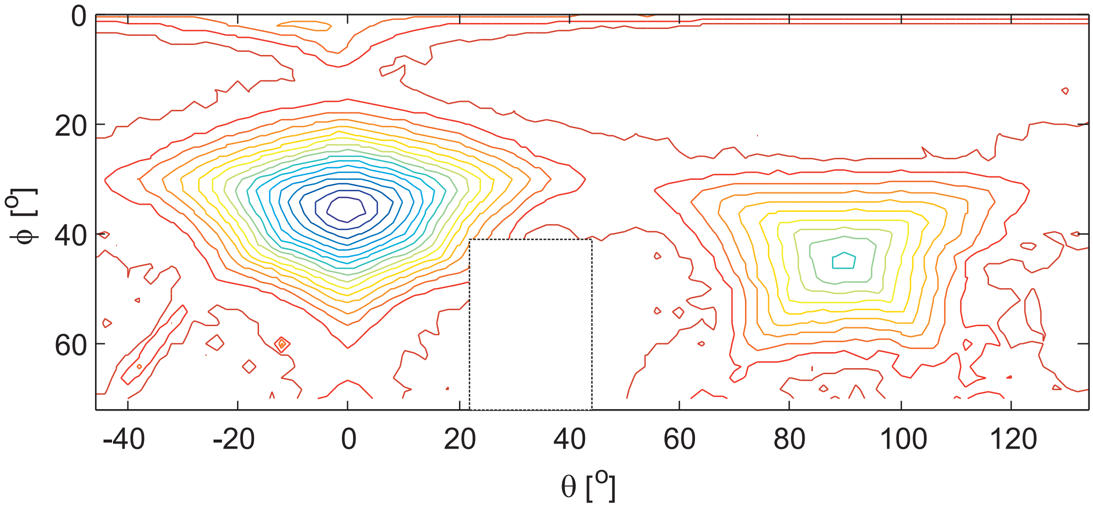

Figure 4.8: *Measured anisotropic etch rates in a KOH/TMAH mixture containing 5 mol/l* OH^- *and 0.5 mol/l* TMA^+ *at 50° and an constant applied potential of -1000 mV vs SCE. Etch rates are obtained from etch experiments using hemispherical shaped Si samples. Data is plotted in spherical coordinates. The blank area corresponds to the mounting bracket position and are therefore excluded from the data analysis.*

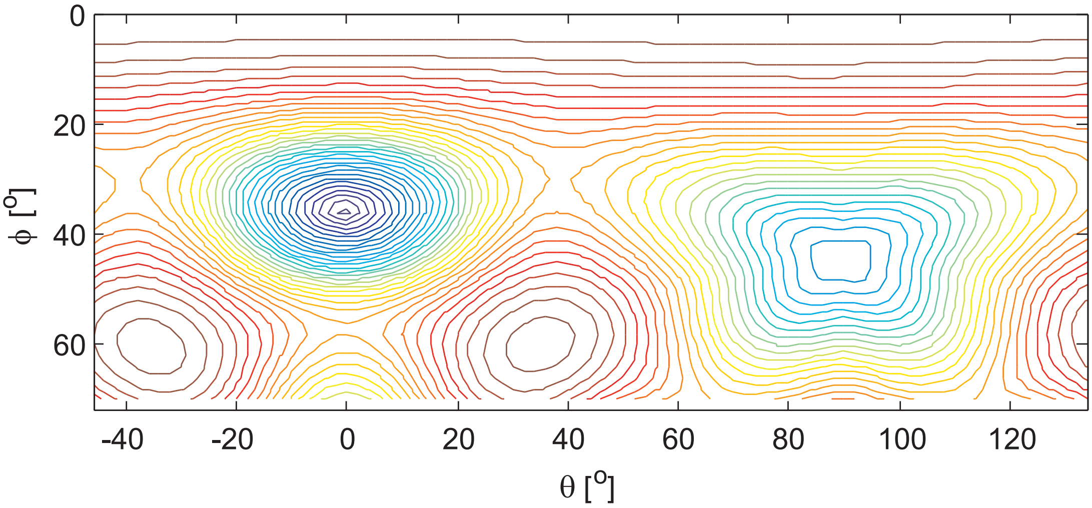

Figure 4.9: *6-Parameters, (100), (111) stepflow/birth-and-spread, base model. Model fit shows a reasonable good fit at the (100) orientations. The (111) shows a circular shape due to the step isotropy fit (note that the shape looks more triangular which is due to the way graph is plotted).*

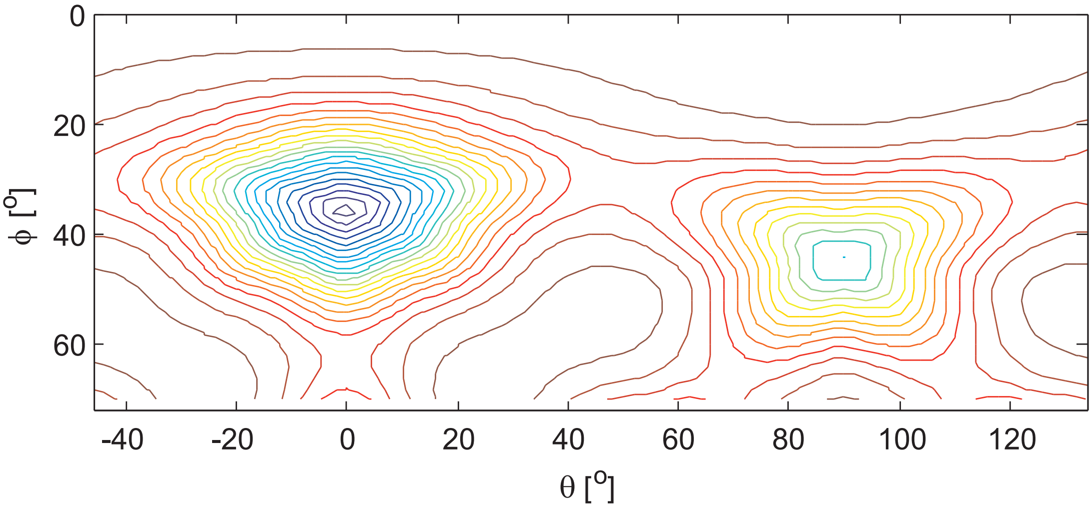

Figure 4.10: *10-Parameters. Step anisotropy is accurately described (orientation of the feature of (111). Additionally a clear hexagonal shape is observed which indicates a step velocity minima at both mono- and dihydride terminated steps.*

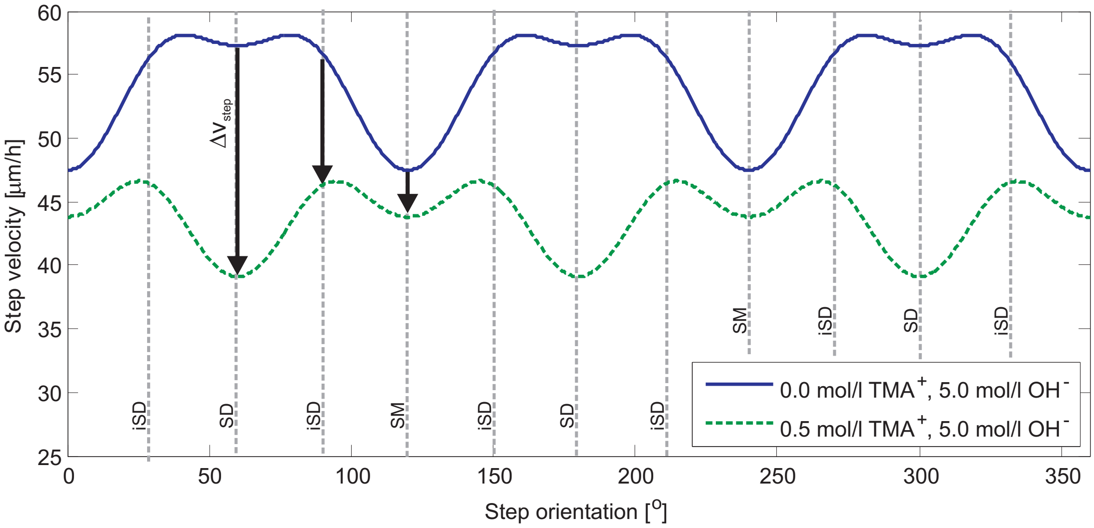

Figure 4.11: *Step velocity as a function of the step orientation (θ) obtained from hemispherical Si samples etched at different TMA$^+$ concentrations. The OH$^-$ concentration is 5.0 mol/l. A potential of -1000 mV vs SCE was applied to the sample. Etching temperature was 50°C. Specific step orientations are indicated in the figure including the dihydride terminated steps (SD), monohydride terminated steps (SM). The orientation exactly in between these steps, where the step edge is composed of alternating isolated vertical dihydrides and monohydrides is indicated by (iSD). The decrease in step velocities (Δv_{step}) due to the addition of TMA$^+$ is indicated by the arrows. This decrease is largest at the dihydride terminated steps (Δv^{SD}_{step}) and smallest at the monohydride terminated steps Δv^{SM}_{step}. It is clear that $\Delta v^{iSD}_{step} < \Delta v^{SD}_{step}$.*

the crystallographic description of the step velocity, it only considers step velocity minima at the dihydride terminated steps. As is also the case in chapter 3, it cannot describe step anisotropy reversal. This phenomena can be described using the 10-parameter extended model which results in an accurate fit in the vicinity of (111) (see figure 4.10). Both the anisotropy reversal and more importantly the hexagonal shape is accurately described. The difference in model fit between the basic 6-parameter and extended 10-parameter function demonstrates the fact that regarding step anisotropy as a result of kink density alone is not sufficient to explain the observed etch features.

4.4 Discussion

The model fit has shown that the extended 10-parameter kinematic wave model can be used to accurately obtain (111) step velocities.

4.4.1 Site specific TMA$^+$ interaction

The most interesting aspect of figure 4.11 is the decrease in step velocity (Δv_{step}) at the indicated step orientations due to addition of TMA$^+$. The change in step velocity (and step anisotropy reversal) due to organic or ionic additives is generally linked to the interaction between these components and the (111) step sites[21, 118]. It is important to note that the exact interaction mechanism is not entirely clear, although processes such as adsorption[118, 116] or electrostatic attraction[21, 22] have been proposed. Both these mechanisms are based on a change in steric effects.

Regardless of the exact mechanism, the influence of an additive is expected to impact all *dihydrides* in a similar fashion. In figure 4.11 the step velocity decrease Δv_{step} is indicated. It is clear that $\Delta v_{step}^{SD} > \Delta v_{step}^{SM}$. This difference, which results in step anisotropy reversal, can be linked to the difference in molecular structure between the mono- and dihydrides[21, 118]

As outlined in the previous sections, the step orientations between the mono- and dihydride terminated steps contain isolated dihydrides (see figure 4.3 and 4.4). As the isolated dihydrides do not differ from the dihydride terminated step in molecular structure, they are expected to show a similar change as a result of TMA$^+$ ($\Delta v_{step}^{SD} \approx \Delta v_{step}^{iSD}$). It is then also expected that the isolated dihydrides will etch more slowly than the monohydrides. The step velocity graph would then only contain maxima at the monohydride terminated steps.

The measurements however show that the step velocity decrease is smaller than expected ($\Delta v_{step}^{SD} > \Delta v_{step}^{iSD}$). Maxima are still present at the step orientation in between the mono- and dihydride terminated steps. This means that TMA$^+$ has a smaller influence on isolated dihydrides compared to the dihydride terminated steps. This indicates that, aside from the molecular structure of the steps, the interaction mechanism between TMA$^+$ and the surface steps is also sensitive to properties such distortion freedom of the surface site and the presence of nearest and next-nearest neighbours.

4.4.2 Electrochemistry

The samples used in this chapter have been etched under electrochemically controlled conditions. In chapter 3, very anodic applied potentials have been used to change the (111) step anisotropy to the point that step anisotropy reversal occurs. This was attributed to the anisotropy in electrochemical oxidation of (111) steps, more specifically between the mono- and dihydride terminated steps. It is unclear if electrochemical oxidation show the same preferences as described above. In contrast to additive interaction, the anisotropy in electrochemical oxidation is based on inherent step reactivity differences and not directly on steric effects. On this basis, the most reactive surface steps, i.e. the isolated dihydrides would show the fastest electrochemical oxidation rate. This would result in a large decrease in step velocity where $v_{step}^{iSD} \leq v_{step}^{SM}$. This would mean that at very positive applied potential (at step anisotropy reversal conditions), monohydride terminated steps would show a maxima in step velocity. This would be visible as a triangular shape in the vicinity of the (111) on the hemispherical samples. Due to step anisotropy reversal under these conditions, the shape would be rotated by 180°.

4.5 Conclusions

As in chapter 3, (111) step anisotropy is commonly regarded as a result of kink site density or the difference in reactivity between mono- and dihydride terminated steps. When etching in both KOH and TMAH based etchants, hexagonal shapes are commonly observed in both (111) etch pits and the convex shape hemispherical Si samples in the vicinity of (111). This specific shape indicates that, for a more detailed evaluation of the (111) step anisotropy, it is necessary to make the distinction between different dihydrides sites depending on the orientation and the neighbouring Si atoms.

The basic kinematic wave model was extended to accurately describe the observed hexagonal shape by introducing additional stepflow/birth-and-spread elements corresponding to the dihydride terminated steps. These elements are independent of the existing step velocity elements. Using the extended 10-parameter model, the (111) step velocity can be determined from surface etch rate data obtained from experiments using hemispherical samples. The addition of an ionic additive (TMA^+) shows a large change in the orientation dependent step velocity. These changes indicate that the interaction between the TMA^+ and (111) steps is site specific. The addition of the TMA^+ show a smaller impact on isolated dihydrides compared to the dihydrides at the dihydride terminated step orientations. The interaction mechanism is therefore sensitive not only tp the molecular structure of the steps (such as mono- or dihydrides) but also to effects such as distortion freedom of the step site or the presence of nearest and next-nearest neighbours.

Chapter 5

Pseudo (110) stepflow/birth and spread mechanism

The etch model for silicon in alkaline solution based on the kinematic wave theory was extended in order to describe the etch features observed in the vicinity (110) orientations. The etch mechanism is assumed to be the result of velocity sources present on the ridges of the (110) roof-tile morphology. Both surface and step etch anisotropy are then a function of the change in velocity source (step nucleation) density. The etch process can be translated into a pseudo stepflow/birth-and-spread mechanism with a single periodic bond chain orientation and a 2-fold symmetry in step anisotropy. Integrating these elements in the existing model will result in a 14-parameter model. Comparison with experimental data obtained from hemispherical Si samples shows that this model can describe the anisotropic etch rate more accurately then the original model. Specific etch features such as the saddle point in etch rate observed in the vicinity of (110) are correctly described.

5.1 Introduction

Wet chemical anisotropic etching of single crystal silicon in concentrated alkaline solutions has been successfully used in MEMS technology[28] for several decades. Exploiting the etch rate differences between crystal plane orientations, complex structures can be fabricated with relative ease. An accurate description and prediction of the anisotropic etch rate at particular process conditions are therefore of importance. The anisotropic etch rate of crystal orientation in the vicinity of (100) and (111) can be accurately described using various physical and engineering models[2, 29, 40, 37, 57, 67, 98, 114] including models based on the kinematic wave theory. The anisotropic etch rate in the vicinity of the (110) surface however still poses problems. Anisotropic etch rate measurements show a peculiar saddle point[97, 98, 104] in the vicinity of (110). This together with the roof-tile morphology generally observed on the surface indicates that the etch mechanism of (110) differs from both (100) and (111) surfaces. Describing the (110) etch rate using the basic kinematic wave theory[66, 67, 104] and the improved 10-parameter model (chapter 4) has proven unsuccessful. This has led to the conclusion that the etch mechanism in the vicinity of (110) cannot be described using simple stepflow/birth-and-spread mechanisms on (100) and (111) alone. Detailed measurements using hemispherical shaped samples, and kinetic Monte Carlo predictions[42], have however led to the introduction of a pseudo (110) stepflow/birth-and-spread mechanism. This addition to the basic model replaces the phenomenological corrections introduced by van Veenendaal et al.[98] for (110) etch rate (see chapter 2). Additional inclusion of (110) step bunching process together with the extension outlined in chapter 4 results in 14-parameter model. Comparing to the etch rate measurements using hemispherical shaped samples, the model has proven capable of accurately describing the (110) anisotropic etch rate.

5.2 Anisotropic etch rate and morphology on (110)

Of all the three major orientations, (110) shows the most atypical etching behaviour. This is observed in both roof-tile morphology commonly present on (110) surfaces and the absolute etch rates in the vicinity of (110). Etch rate measurement using wagon-wheel patterns[67] (see chapter 3) show the presence of an isotropic maximum in the surface etch rate when inclining the surface towards (111). Inclining the surface in the perpendicular direction towards (100), the etch rate show a cusp minimum. Similar patterns are observed on etched hemispherical samples. Detailed measurements using hemispherical samples[104] (see chapter 6) show that both the cusp minimum and isotropic maximum form a saddle point in the vicinity of (110). Figure 5.1 illustrates this saddle point together with the isotropic maximum and cusp minimum. Here, in contrast to the wagon-wheel measurement, the isotropic maximum actually shows a slight minimum. Within this chapter, this feature is however still denoted as an isotropic maximum. It is important to note that the presence and definition of these features greatly depends on the etching conditions.

The morphology commonly observed on (110) surfaces show a roof-tile structure. The size and density of these roof tiles are dependent on etching conditions (as can be seen in

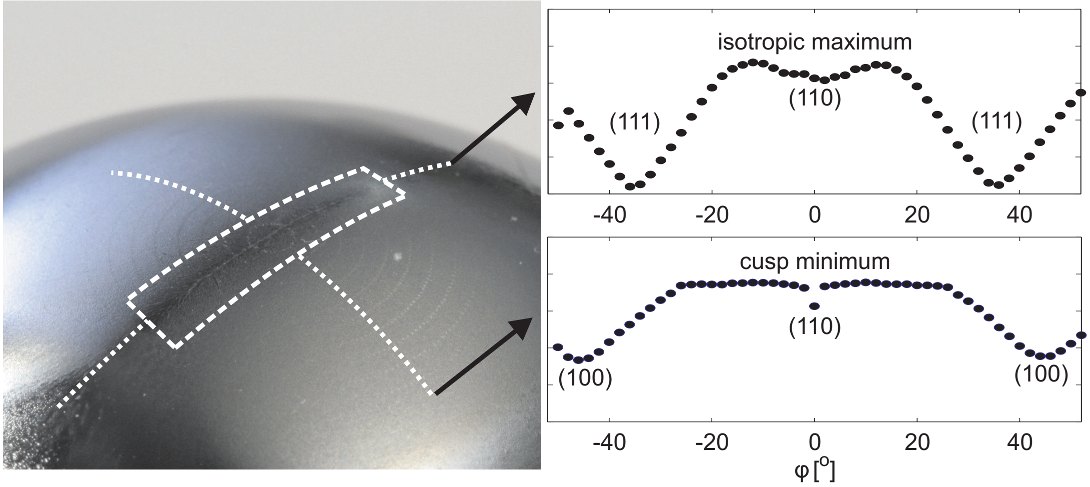

Figure 5.1: *10-Parameters, (100), (111) stepflow/birth-and-spread, step bunching and independent normal and reversed PBC sets. Step bunching for both (100) and (111) steps results in a more accurate model fit at orientations further away from the main (100) and (111) crystal planes.*

microscopic observations in chapter 7). The side walls of the roof tiles are generally considered to be a higher index plane ((xx1) with x > 1). The roof-tile structures themselves have a finite length, terminating in protruding edges (noses). Although it still not clear what the exact mechanism is behind this roof-tile formation, it is clear from kMC[42, 100] simulations that they are composed of (bunched) steps on (111) surfaces. For a more detailed description of the (110) morphology refer to chapter 7.

5.3 Model modifications

For the characterisation of an anisotropic etch system, the kinematic wave etch model as outlined in chapter 2 is used. Based on the stepflow/birth-and-spread mechanism, it is capable of describing the anisotropic etch rate accurately in the vicinity of (111) and (100). However, the basic model as was used in chapter 3 and the extended model as is outlined in chapter 4 cannot describe the etch rate in the vicinity of (110).

5.3.1 General observations

Describing the anisotropic etch behaviour at orientations near the (110) is particularly challenging. The shape of the etch rate graph near (110) coupled with the roof-tile morphology are strong indications that the etch mechanism at these orientations is not straight forward. Using the stepflow/birth-and-spread mechanisms on (100) and (111) as described in the kinematic wave theory will generally predict a higher etch rate than is observed. Examining the etch rate data, it is apparent that no combination of model parameters can result in the isotropic maximum and the sharp cusp minimum observed at orientations near (110). In an effort to overcome this, van Veenendaal et al. have proposed to integrate two additional elements into the basic model[104] (chapter 2). These

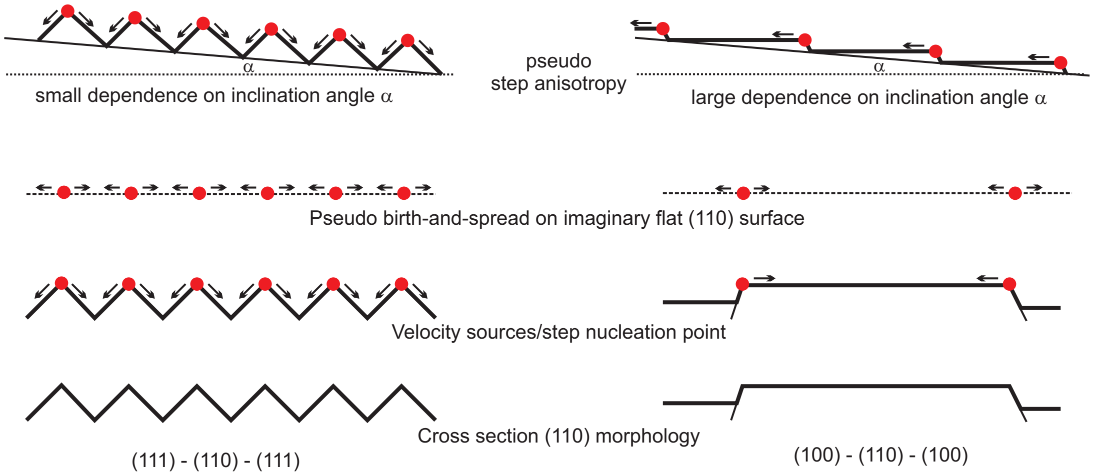

Figure 5.2: *Schematic of the pseudo stepflow/birth-and-spread mechanism on an imaginary flat (110) surface. Two cross-sections (perpendicular to each other) of the (110) zigzag morphology are shown. Velocity sources, denoted by the dots, on the (110) morphology can be translated into velocity sources on imaginary flat plane. Top figure shows the change in velocity source density due to surface inclination which translates into pseudo step anisotropy.*

modification are specifically designed to describe the etching in the vicinity of (110) using two parameters which represent the perpendicular contributions to the (110) etch rate. These additional parameters are phenomenological in nature, lacking a clear physical basis. This is in contrast to the other parameters which are clearly linked to physical processes such as stepflow/birth-and-spread or step bunching. The interaction of these two added elements with the basic model also need to be restricted to orientations near the (110). This makes the implementation of these elements less universal as it is sometimes necessary to 'tailor' the interaction of these additional elements so to be usable with a particular dataset. Closer inspection off the (110) etched surfaces and the etching process using both ex-situ and in-situ microscopy[42, 100, 99] (outlined in chapter 7) and predictions from kMC simulations[42, 100] has shown that on a typical (110) morphology etching mainly occurs along the sides of the roof tiles (figure 5.2). Macro-step movement observed during in-situ observations show stepflow patterns originating from the roof-tile ridges moving towards the base. The ridges can then be regarded as velocity sources and the mayor contribution to step nucleation. The etch process then resembles a birth-and-spread mechanism where the steps are created at the top (birth), subsequent moves along both sides of the roof tile down to the base (spread). Defining an imaginary smooth (110) surface, the etching process of (110) surface can then be regarded as a pseudo birth-and-spread process across this imaginary surface with the 2-dimensional terrace roughening occurring on the roof-tile ridges (figure 5.2). The amount of the terrace roughening is expected to be relatively low compared to other terraces such as (100) as the step nucleation is primarily restricted to the ridges of the roof-tile morphology

5.3.2 (110) inclined towards (111)

Examining the cross-section of the (110) morphology along the (110) direction, surfaces show the typical roof-tile (zigzag) structure. Increasing the inclination angle towards (111) the morphology structure does not change significantly in shape and roof-tile density (figure 5.2). This would mean that the velocity source density will remain relatively constant within small inclination angles (α) range. In this situation, the inclination angle dependent step flow (see equation 2.1) has only a small contribution to the overall etching. The etch process is then largely determined by the birth-and-spread mechanism (see equation 2.2). This is consistent with the observed isotropic etch maximum in the vicinity of (110) on both wagon-wheel patterns on (110) substrates[65] (see chapter 3) and hemispherical samples. It is then also expected that the range of this isotropic maximum is related to the shape of the roof tiles. SEM observations have shown this to be the case, as the angle of the roof tile approximately corresponds to orientations inbetween which the etch rate is isotropic.

5.3.3 (110) inclined towards (100)

Examining the cross-section of the (110) morphology along the (100) direction, the morphology looks distinctly different, resembling stretched trapezoids. Kinetic Monte Carlo has shown that the major velocity sources are present on the ends of the features[42, 100, 99] (noses). Microscopic observations by van Veenendaal et al. have shown an increase in nose density (and decrease in roof-tile length) at increasing inclination angles towards (100). This would result in a step velocity source density which is α-dependent. This indicates that there is a significant stepflow contribution to the overall etch rate on surfaces inclined towards (100). The macro-step patterns observable during in situ etching, in particular the ‘peeling’ etch patterns of the roof tiles (see chapter 7), support the presence of a (significant) stepflow along the length of the roof tiles. Etch rate measurements using wagon-wheel patterns on (100) substrate[65] and hemispherical samples show the presence of a cusp minimum in the etch rate. This is consistent with the fact that the stepflow mechanism determines the overall etch rate at these orientations.

5.3.4 (110) Step anisotropy

In the previous two sections the dominant etch processes (stepflow or birth-and-spread) are outlined depending on the inclination angle and orientation of the (110) morphology. The 2-dimensional birth-and-spread mechanism is a surface process and is independent of the planar orientation (θ). The stepflow mechanism, more specifically the step velocity (equation 2.3), is θ-dependent as outlined in chapter 2. A large difference in step velocity between the step orientations along the [110] direction (minimum step velocity) and along the [100] direction (maximum in step velocity) can account for the observed stepflow. The step orientation at the step velocity minimum coincides with a single PBC which is consistent with it being the most stable step orientation.

5.3.5 (110) pseudo stepflow/birth-and-spread mechanism

Although the morphology of the (110) surface exclude the occurrence of a formal stepflow mechanism (which applies to monolayer steps on a stable surface), the above section has outlined a distinct analogy to the perceived (110) etch mechanism with a pseudo stepflow/birth-and-spread mechanism on an imaginary smooth-(110) surface (figure 5.2). Step flow/birth-and-spread is then the net result of the step movement across this imaginary (110) surface. Terrace roughening is analogous to step nucleation on the top of the ridges, with a velocity source density determined by the roof-tile density. The difference in the overall etch rate due to inclination angle (α) and planar orientation (θ) is explained by the change in velocity source density due to the morphology. This is analogous to a high step anisotropy with a 2-fold symmetry and a single PBC orientation along the [110] direction. Overall, the (110) etch mechanism can be described using the similar stepflow/birth-and-spread mechanisms as (100) and (111) with equation 2.1 to 2.4 as basis. As (110) surfaces have a single (symmetrical) PBC, two minima in the step velocity can be identified corresponding to $\theta = 0°$ and $\theta = 180°$. The step velocity equation 2.3 can then be used directly. Figure A.6 in appendix A shows the assembly of the step velocity element. The stepflow/birth-and-spread mechanisms are considered for the entire (110) family which consists of six crystal planes. The (110) pseudo stepflow/birth-and-spread model elements are integrated into the basic model[104] using the elementary assembly method using the cusp combining method with an interaction parameter $a = -4$ (figure A.7). With the addition of (110) stepflow/birth-and-spread, three additional parameters are added to the model (v_{k110}, ε_{110}^{2D} and ε_{110}^{1D}). Additionally, step bunching[67, 104] is also defined for (110) orientation similar to step bunching on both (100) and (111). With the inclusion of the model expansion outlined in chapter 4, this raising the total number of parameters in the kinematic wave etch model to 14.

5.4 Data fit to experimental data

In the following section, the effect of the model modifications are outlined by fitting the model to actual measurement results. Figure 5.4 shows the etch results obtained from a hemispherical sample etch at 50°C in a mixture of KOH/TMAH which have an OH^- concentration of 5.0 mol/l and a TMA^+ concentration of 0.5 mol/l under electrochemically controlled conditions with an applied potential of -1000 mV vs SCE. For this chapter, it is important for the effects of the pseudo stepflow at (110) to be both clearly observable and measurable. This include a well defined saddle point in the (110) etch rate (cusp minimum and isotropic maximum). Although this saddle point is always present, factors such as high surface roughness or large (110) roof-tile morphology can prevent these features from being visible and/or measurable. The process conditions used here, although uncommon, produce well defined (110) etch features.

Figure 5.3 shows a simplified plot of the data together with the positions of the mayor crystal orientations. Graphs 5.5 and 5.6 show the datafit using various parameter combinations while figures 5.7 and 5.8 show the model fit specifically at the isotropic maximum and cusp minimum. The corresponding parameter value and data fit correlation coefficient are shown in table 5.9.

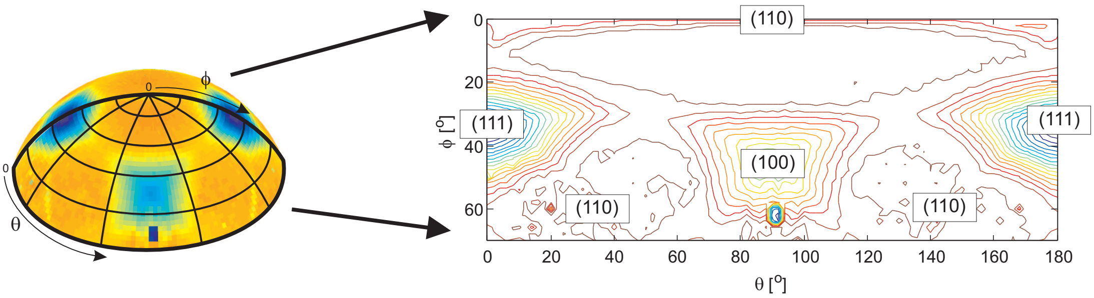

Figure 5.3: *Etch rate data obtained from a Si hemispherical sample. Left figure shows the etch rate measured on the sample. The (110) features are clearly visible as lines on the surface. The right figure shows the unfolded contour plot of part of the etch rate data. The (100) and (111) planes are indicated. A total of three (110) planes are visible in the data.*

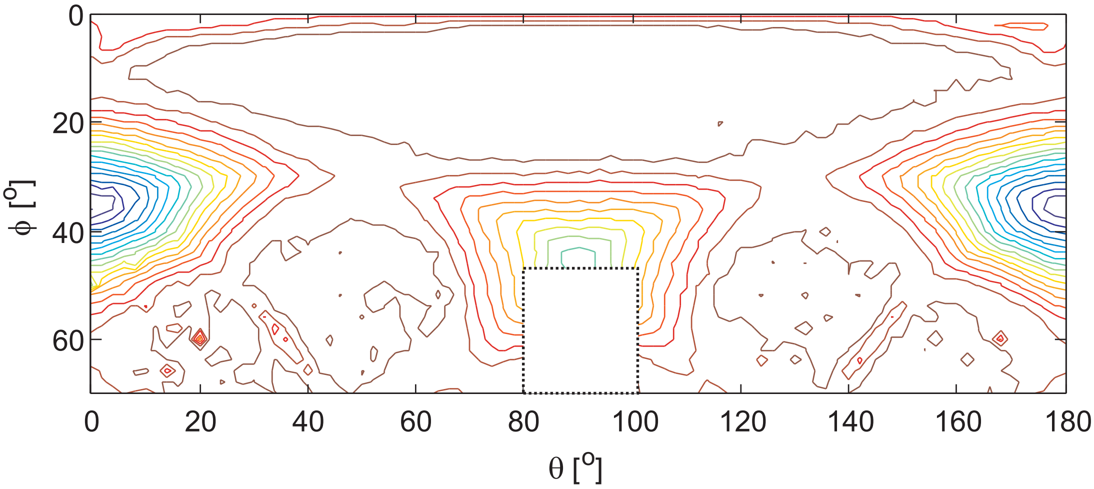

Figure 5.4: *Measured anisotropic etch rates in a KOH/TMAH mixture containing 5 mol/l* OH^- *and 0.5 mol/l* TMA^+ *at 50°C and an applied a constant applied potential of -1000 mV vs SCE. Etch rates obtained from hemispherical shaped Si sample etch experiments. Data is plotted in spherical coordinates. The blank area corresponds to the mounting bracket positions and are therefore excluded from the data analysis.*

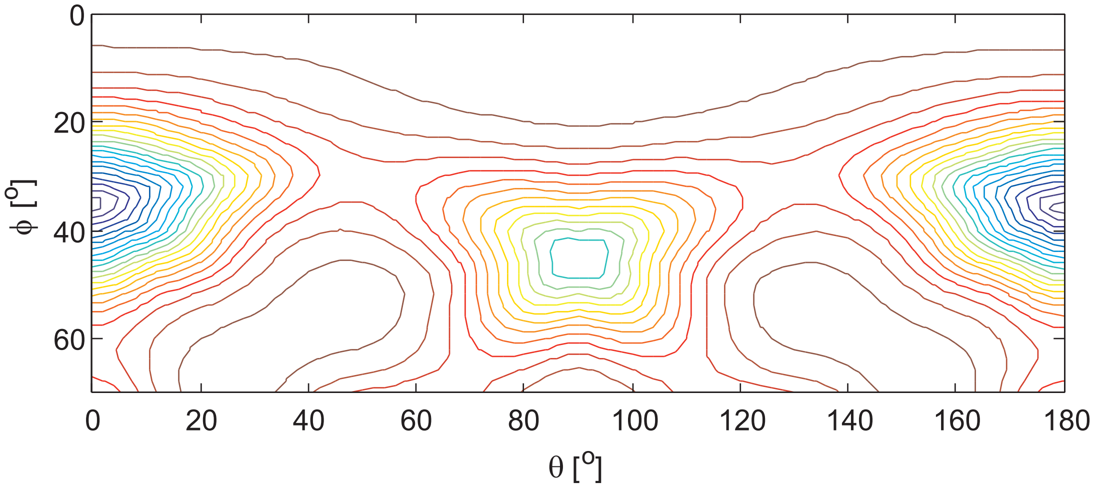

Figure 5.5: *Model fit using the 10-parameter kinematic wave model which includes (100) and (111) stepflow/birth-and-spread, step anisotropy reversal and step bunching. It shows a good fit in the vicinity of both (100) and (111) but it does not describe the (110) saddle point.*

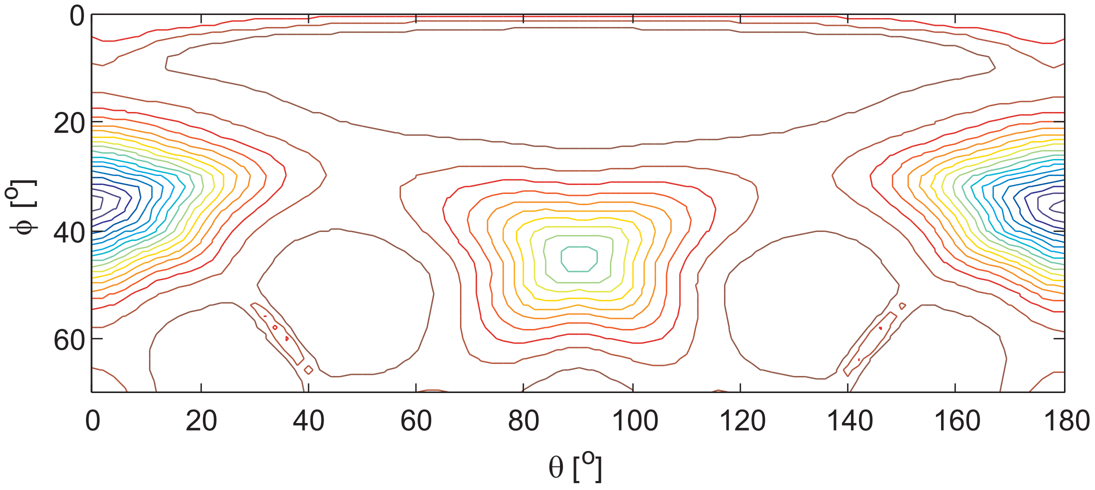

Figure 5.6: *Model fit using the 14-parameter kinematic wave etch model which include stepflow/birth-and-spread, step anisotropy reversal and step bunching for (100), (111) and (110). The (110) etch features are accurately described.*

10-Parameters (100), (111) stepflow/birth-and-spread and step bunching

Figure 5.5 shows the data fit using the extended 10-parameter model, as described in chapter 4. The basis of this model is the stepflow/birth-and-spread mechanism on both (100) and (110). It does not contain the (110) elements as is outlined in this chapter or the phenomenological correction as van Veenendaal et al. have introduced. Close to the (111) and (100) the model fit is good. The model fit in the vicinity of (110) is poor as both figure 5.7 and 5.8 also shows. This model fit illustrate the fact that the basic etch model cannot describe the cusp minimum and isotropic maximum features observed at a (110).

14-Parameters (100),(111),(110) (pseudo)stepflow/birth-and-spread and step bunching

Including the pseudo-stepflow/birth-and-spread for (110), as described in the previous sections, results in a good data fit at the (110) orientations (figure 5.6). Both the isotropic maximum and the cusp minimum are described very well (figure 5.7 and 5.8). Examining the actual model parameters (see table 5.9), it is clear that the absolute value for the 1-dimensional step roughening (ε_{110}^{1D}) is relatively low. This indicates high step anisotropy on the pseudo (110) plane. This is consistent with the expectation outlined in the previous section. The 110 step velocity (v_{k110}) is however very high compared to both the v_{k111} and v_{k100}. Preliminary observation of the macro-step peeling on (110) shows that step velocity of a bunched step can be higher than expected. However, the absolute value obtained from the data fit remains unreasonably high. Examining the (100) and (111) parameter values in table 5.9, it is clear that the introduction of the pseudo (110) stepflow/birth-and-spread also have an influence on both (100) and (111) orientations as the values of the parameters controlling these orientations are different from the 10-parameter model.

From the experimental data shown above, it is clear that the 14-parameter model can describe the anisotropic etch rate accurately. It is important to emphasize that the model fit in vicinity of (110) is very dependent on the experimental data. For an reliable fit, (110) etch features, such as the cusp minimum and isotropic maximum, have to be clearly visible in the experimental data. Depending on the actual measurement technique or etching conditions, these features are not always observable (i.e. due to a low lateral accuracy/resolution) and/or present (i.e. due to surface roughness). Using the 14-parameter model in these circumstances will not result in an reliable model fit.

5.5 Conclusion

In this chapter we have introduced an expansion to the kinematic wave etch model designed to describe the anisotropic etch rate of orientations in the vicinity of (110). From limited ex-and in-situ observations of the (110) roof-tile morphology together with predictions from kMC simulation, the (110) etch process is translated to a pseudo stepflow/birth-and-spread process on an imaginary smooth (110) surface. Velocity sources and step nucleation on the ridges of the roof-tile structures are analogous to terrace roughening on an imaginary smooth surface. Velocity density increase due to surface inclination is

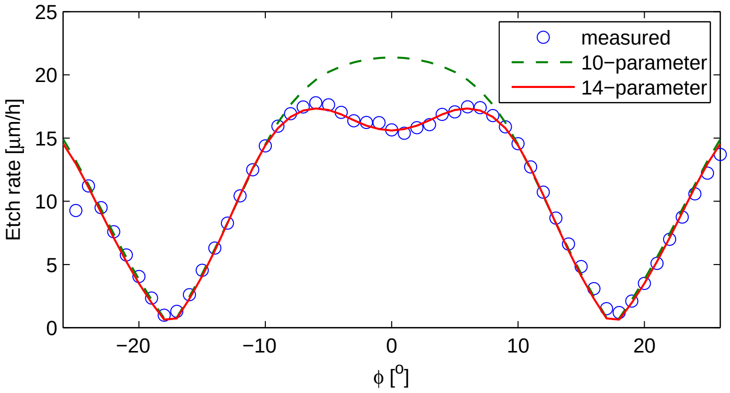

Figure 5.7: *This figure shows the isotropic maximum in the anisotropic etch rate when inclining the surfaces towards (111). Both the graphs calculated from the 10 and 14 parameter models are included. It is clear that unlike the 10-parameter model, the 14-parameter model can describe the isotropic maximum.*

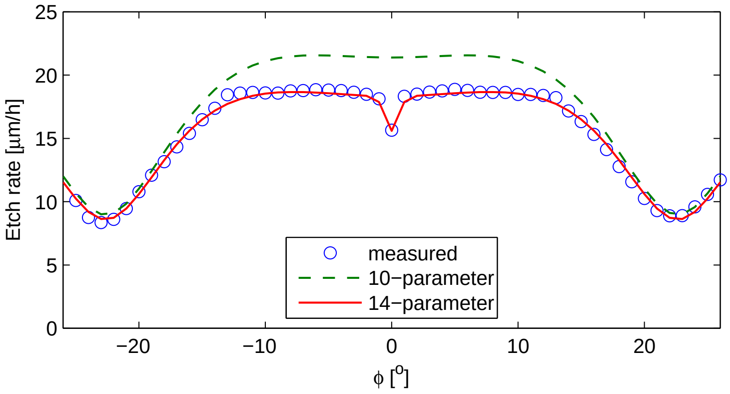

Figure 5.8: *This figure shows the cusp minimum in the anisotropic etch rate when inclining the surfaces towards (100). Both the graphs calculated from the 10 and 14 parameter models are included. The cusp minimum is accurately described using the 14-parameter model.*

	$v_{k(hkl)}$			$\varepsilon^{2D}_{(hkl)}$		
# parameter	(100)	(111)	(110)	(100)	(111)	(110)
10	92.03	72.80		0.10	0	
14	105.16	68.00	776.90	0.08	0	0.24

	$\varepsilon^{1D}_{(hkl)}$					$C_{(hkl)}$			R^2
# parameter	(100)		(111)		(110)	(100)	(111)	(110)	
10	0.55	1	0.54	0.49		-0.67	1.37		0.913
14	0.48	0.66	0.52	0.45	0.08	-0.69	2.35	2.35	0.956

Figure 5.9: *Table showing the model parameters obtained from the data fits of both the 10 and 14-parameter models, together with the regression coefficient (R^2). For the ε^{1D} parameter for (100) and (111),both the $\varepsilon^{1D,n}$ (left) and $\varepsilon^{1D,r}$ (right) is given (see chapter 2 and 4 for more detail on these parameters). Examining the values it can be seen that the (100) and (111) parameter values changes with the introduction of the four (110) parameters. This indicates that the (110) pseudo stepflow/birth-and-spread has a influence on both the (111) and (100) orientations.*

analogous to step anisotropy. Using these simplifications, the (110) surface was simulated as a smooth surface with a single PBC orientation (2-fold symmetry) on which regular stepflow/birth-and-spread occurs. These model elements are integrated into the existing kinematic wave etch model using the elementary assembly method. Comparison with experimental etch data shows a more accurate data fit than the basic model. Characteristic (110) etch features including the characteristic isotropic maximum and cusp minimum (saddle point) in the vicinity of the (110) can be accurately described. The introduction of the (110) elements also have an influence on both (100) and (111) as changes are observed in the parameter values associated with these orientations.

Chapter 6

Examining TMAH-Si interaction mechanism

A proposed coulombic interaction mechanism, responsible for the effect of TMAH etchant on the etch anisotropy is investigated using electrochemical controlled etch experiments with hemispherical Si samples. The interaction mechanism ascribes the observed changes in etching characteristic to differences in electrostatic attraction between the TMA^+ *cation and different (111) surface steps. With the introduction of electrochemical oxidation via an applied potential, a combined effect can be defined. It is proposed that a (partially) oxidised (111) surface step will result in a stronger electrostatic interaction. By controlling both the cation concentration and exploiting the anisotropy in oxidation of (111) surface steps, the combined effect would be visible as a disproportionate change in the step anisotropy. Electrochemical controlled etch experiments have been performed using hemispherical shaped samples in a TMAH/KOH mixture. The orientation dependent step velocity was obtained from the measurement data using the kinematic wave theory. The measurements show the influence of both the electrochemistry and the* TMA^+ *concentration on the anisotropic etch rate and (111) step velocity. The results however did not confirm the electrostatic interaction mechanism as the expected disproportionate change in step anisotropy is not observed under these process conditions.*

6.1 Introduction

The use of organic or ionic additives is a common way to change the characteristics of anisotropic etching of silicon in concentrated alkaline solutions. Additives such as isopropyl alcohol (IPA) have large effects on both the etch anisotropy and the resulting surface morphology[2, 5, 8, 20, 23, 117]. Changing the actual etchant also results in large differences. A common alternative to KOH is tetramethyl ammonium hydroxide (TMAH) which is widely used in the MEMS industry due to its higher selectivity towards siliconoxide. These etchants generally produces smoother surfaces than KOH, which makes them very suitable for applications within MEMS technology[21, 117]. Although TMAH etchant is widely used, the exact mechanism behind the difference in etch characteristics compared to KOH is unclear. Understanding this mechanism can lead to a better understanding of the influence of organic or ionic additives in general. As such, Cheng et al.[22] have regarded the TMA^+ as a large, organic, positively charged additive and introduced a possible interaction between the cation and the silicon surface. This interaction is based on an electrostatic attraction between the cation and the electronegatively charged hydrogen terminated Si surface step sites. Within this work we aim to investigate this interaction mechanism by using electrochemistry.

The anisotropic step oxidation can be used to investigate the step/TMA^+ interaction mechanism. In chapter 3 it was shown that hydrogen terminated surface sites can be (electrochemically) oxidised by applying an external electrical potential. The results have also shown that the electrochemical oxidation of (111) steps is anisotropic, and favors the dihydride terminated steps over the monohydride terminated steps. By controlling the oxidation states of the Si steps, the site specific interaction of the Si surface with the TMA^+ cation can be investigated.

6.2 TMAH / Si interaction

6.2.1 Cation interaction

The influence of different alkaline etchants such as KOH, NaOH, EDP or TMAH have been well documented in the literature[8, 85, 60]. The choice of etchant has an impact on the absolute overall etch rate, etch anisotropy and resulting surface morphology. Organic additives such as isopropyl alcohol (IPA)[20, 114] or Triton X-100[5, 23] show similar effects on the etch system. The mechanism behind these changes is not clear however. Cheng et al.[21, 22] have performed etch experiments using different TMAH concentrations and examined its impact on the (111) step anisotropy. These observations have led Cheng et al. to propose an electrostatic-based interaction between the cation (TMA^+) and the electronegative Si molecules on the (111) step edges (step termination sites). As outlined in chapter 1.4 and chapter 4, step sites of (111) steps can be distinguished between two main types depending on their molecular structure, the monohydrides and dihydrides (figure 6.1). The difference in molecular structure (number of backbonds and number of attached hydrogen atoms) will result in a difference in charge distribution over the total step site, in turn resulting in a difference in electrostatic interaction. Dihydrides, containing two dangling hydrogen atoms, will contain a stronger overall negative charge

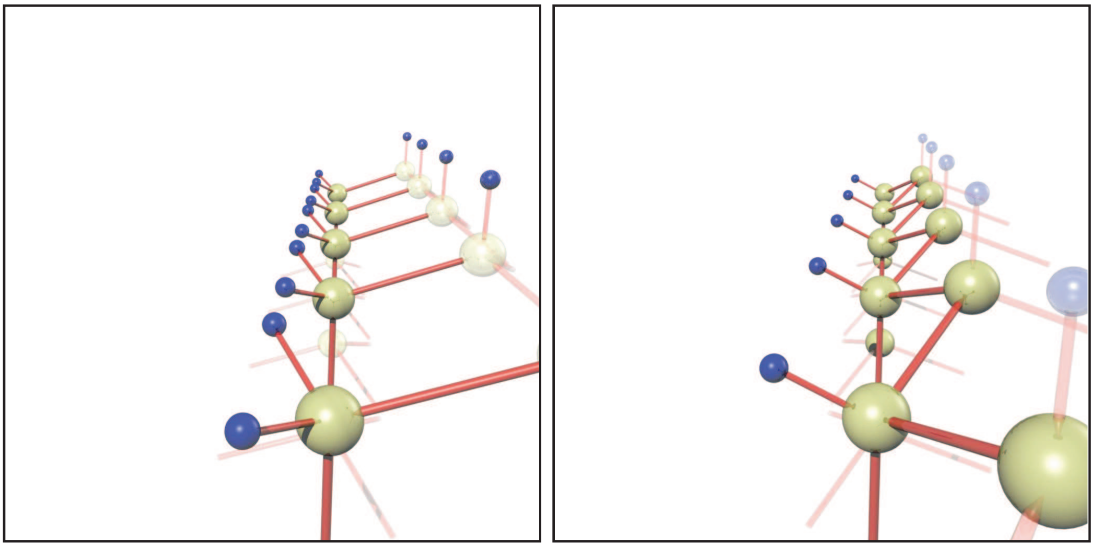

Figure 6.1: *Figure showing the structure of a dihydride terminated step (left) and a monohydride terminated step (right)*

resulting in a stronger attraction to the TMA$^+$ cation compared to monohydrides (figure 6.2). This in turn will result in larger steric hindrance and ‘shielding’ of the step site by the large TMA$^+$ cations. This shielding will therefore effectively reduce the step etch rate. Monohydrides, which contain a single dangling hydrogen atom, will also show a similar but smaller interaction due to its smaller electronegativity. Increasing the TMA$^+$ concentration will therefore ultimately result in a situation where the dihydrides, generally the faster etching step, will effectively become more stable than the monohydrides. This situation is called step anisotropy reversal[66] or pit rotation[41] as the orientation of the triangular shaped etch pits visible on (111) is rotated. It is possible that electrostatic interaction is not limited to TMAH. In theory, it can be extended to any additive of significant size with a positive charge or substantial dipole.

6.2.2 Cation interaction and electrochemistry, the combined effect

Electrochemical oxidation of both Si terrace sites[75] and step sites[65, 67] have been shown to be anisotropic. In chapter 3 it is shown that step anisotropy reversal or pit rotation can be induced by applying a very positive bias. Careful control of the electrochemical conditions makes it possible to control the step anisotropy by influencing the oxidation of both the (111) mono- and dihydride terminated steps. Although it is not possible to selectively oxidise a particular (111) step type, a difference in oxidation rate between the two surface sites can be achieved. This can be used as a tool to investigate the step interaction mechanism by externally changing the oxidation state of the steps and examining the effect of this change on the overall step interaction.

A step site which is (partially) oxidised to a hydroxide-terminated step (OH-termination) is expected to result in a higher interaction with TMA$^+$ cation as the hydroxide is more

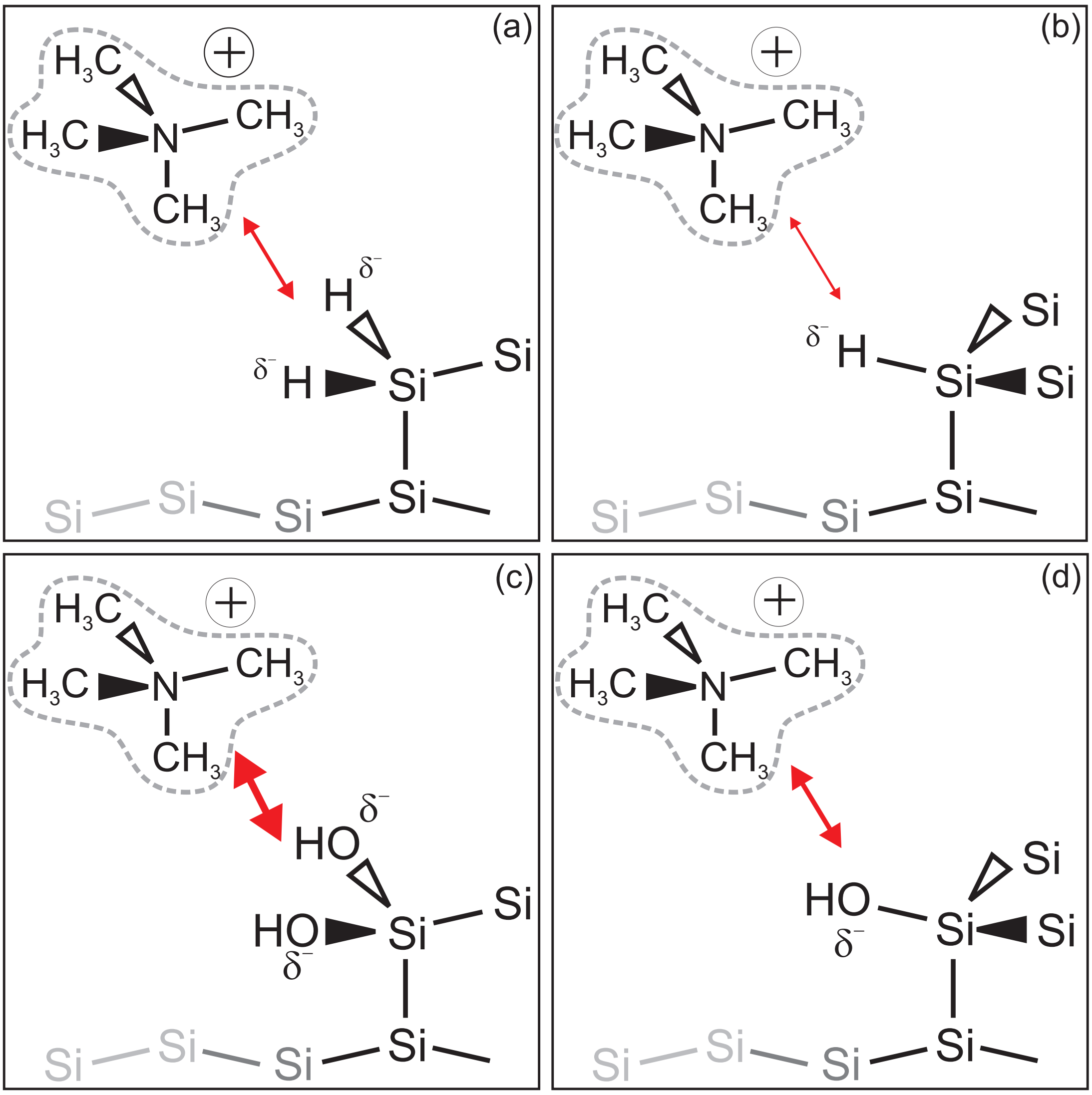

Figure 6.2: *Outline of the electrostatic interaction between the TMA$^+$ cation and the Si (111) step sites. The dihydride terminated step (a) contains a larger electronegative charge than the monohydride terminated steps (b) resulting in a stronger electrostatic attraction. Additionally, the combined cation interaction and electrochemical oxidation effect is shown. Oxidation of the dangling hydrogen atom of both the dihydride terminated step (c) and monohydride terminated step (d) will result in a much larger electronegativity of the step. The interaction with the TMA$^+$ cation will increase.*

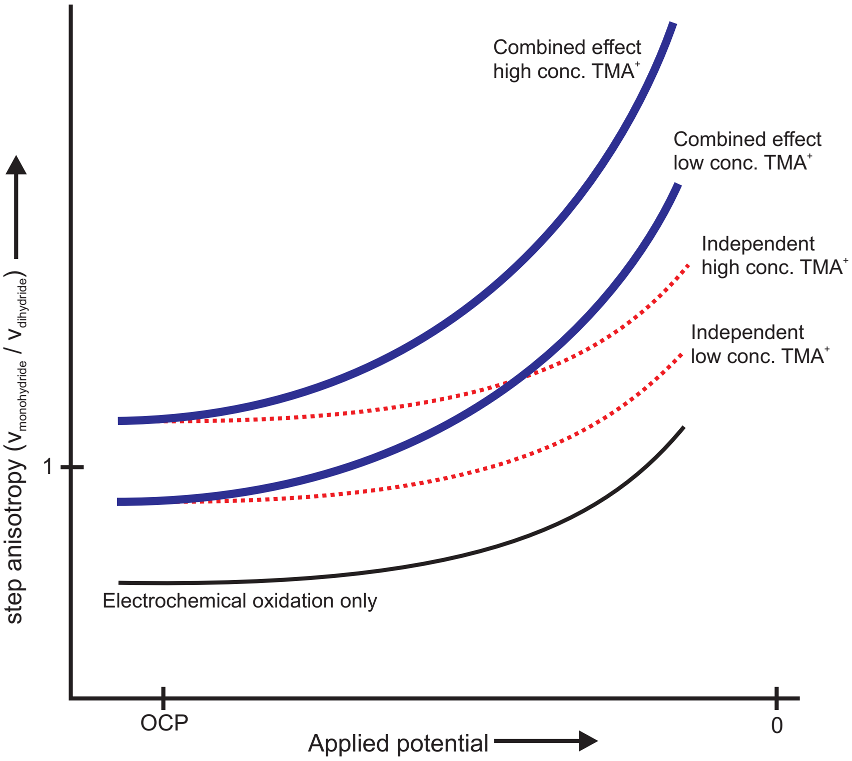

Figure 6.3: *This figure schematically outlines the cation/electrochemistry combined effect on the (111) step anisotropy ($v_{monohydride}/v_{dihydride}$). The thin solid line shows the step anisotropy as a function of electrochemical oxidation (which is only dependent on the applied potential). The dashed lines shows the step anisotropy with the addition of TMA$^+$ in the absence of a combined effect. This will only result in a vertical shift in the graph. The thick solid lines show the expected step velocity, in the case that electrochemical oxidation enhances the cation interaction (combined effect). The graph would show a disproportionate change in step anisotropy larger than the sum of both individual effects.*

electronegative than hydrogen. An (partially) oxidised step site in a TMA$^+$ containing etchant will therefore be additionally stabilized (figure 6.2b and c). Electrochemical oxidation therefore enhances the TMA$^+$ interaction due to hydroxide termination on the surface steps. The presence of both factors should then results in a *combined effect* which is expected to be larger than the sum of both individual effects. Etch experiments with different TMA$^+$ concentrations and controlled electrochemical oxidation, using applied electrical bias, are therefore expected to produce an disproportionate change in the (111) step anisotropy (see figure 6.3). To calculate the step anisotropy, the step velocity of both the mono- and dihydride terminated steps are needed. In chapter 4 it is shown that the orientation dependent (111) step velocity can determined using the 10-parameter model in combination with etch rate data obtained from hemispherical Si samples.

6.3 Experimental

6.3.1 Hemispherical Samples

In chapter 3, dry etched maskless wagon-wheel patterns have been used to characterize a particular etch system. The wide range of available surface orientations when using three sample types (wagon-wheel patterns on (110) and (100) substrates together with the trench offset pattern on (110)) has proven to be sufficient to obtain reliable model fits using the basic kinematic wave theory[67, 104].

An arguably superior experimental method is the use of hemispherical Si samples[78, 87, 100]. Unlike wagon-wheel patterns, these samples theoretically contain an infinite number of surface orientations. Hemispherical Si samples have been used successfully to characterize etch systems with a single etch experiment. This creates a fast and accurate experimental method. However, aside from the manufacturing costs and availability, they have several additional important disadvantages for the experiments outlined in this chapter. As the sample is convex, the faster etching orientations will eventually overlap the slower etching planes during etching. This effectively reducing the number of available crystal orientations. This includes the slowest etching planes in the vicinity of (111), which makes these samples unsuitable for direct (111) etch rate measurements. A second issue is related to electrical properties of standard doped Si. Unlike samples manufactured from 500 μm thick wafers (as used in chapter 3), the large size of the available hemispherical samples (40 mm in diameter) means that the resistivity of the bulk silicon material cannot be neglected in electrochemical experiments. With the experimental setup used, the resistance of the standard doped silicon (10-15 Ω.cm) can cause a significant potential drop in the radial direction of the sphere, which is dependent on the current passing through the electrical circuit.

6.3.2 Experimental Setup

To evaluate the cation/electrochemistry combined effect on (111) step anisotropy, etch experiments using hemispherical shaped samples have been performed under electrochemical controlled conditions. The oxidation state of both the types of surface steps was controlled by externally applying a constant electrical potential. The specific potentials were chosen using the results obtained from wagon-wheel pattern experiments[67] (chapter 3). To isolate the effect of TMA^+ cation, a mixture of TMAH (Chameleon Reagents for electronics 25%) and KOH (Chameleon Reagents for electronics 85%) in deionised water (Millipore, 18MΩ.cm) was used. The concentration of TMA^+ cation can then be controlled without influencing the pH of the system. The kinematic wave theory was used to express the measured etch rate data in terms of microscopic properties such as step/kink velocity, terrace and step roughening. The OH^- concentration used for all experiments was 5.0 mol/l. Three TMA^+ concentrations were used for the experiment, which were 0.0, 0.5 and 1.0 mol/l.

All experiments were performed at the Micromachining and MEMS lab at Nagoya University in Japan, where both the polished hemispherical samples and analysis equipment were available. The samples were p-type normal-doped (110) oriented samples with a diameter of 40 mm. A 1 μm thick SiO_2 mask was created on the bottom and the orientation flats of the samples using wet oxidation at 800°C. The silicon oxide was removed from the spherical surface using a 1% HF solution while the wafer flats and bottom were protected by photoresist and resist foil respectively. Prior to etching, the samples were cleaned in concentrated H_2SO_4 (Hagashi pure chemical 99.8%) at 80°C for 30 min, followed by deionised water for an additional 30 min. An ohmic contact between the Si and a gold connection pen was achieved by locally removing the SiO_2 using a diamond tip pen and applying GaIn eutectic (Sigma Aldrich 99.99%+ GaIn eutectic). The sample was mounted in a KelF sample holder and the electrical contact was protected from the solution using Teflon coated Viton and silicone O-rings. The sample was held in place by three KelF rods positioned in a radial pattern around the sphere. The etch setup consisted of a standard electrochemical cell with a platinum plate electrode (Radiometer M24Pt) acting as a counter electrode. As a reference electrode, a standard calomel electrode (SCE, Radiometer REF401) was used. The etch vessel itself was made from Teflon and was partly submerged in a water bath at a constant temperature. The etchant solution was constantly bubbled with Argon gas prior and during the etching experiment to remove dissolved oxygen. External electrical potentials were applied using a potentiostat (PalmSens). Current and potential were monitored using the same potentiostat. The etch time for all experiments was 4 hours. This etch time will result in a etch depths smaller than of 150 μm. The experiments were performed at a constant temperature of 50°C in the dark. After etching, the samples were quenched in diluted H_2SO_4 to stop the etch process and remove KOH residue. The four (set point) potentials chosen were (vs SCE):

- -1500 mV: Close to the OCP of the actual sample and of bulk (100) and (110) surfaces.
- -1250 mV: Close to the OCP of bulk (111) surfaces.
- -1000 mV: Close to the oxidation peak potential of both (100).
- -750 mV: slightly past the passivation potential[110].

Due to the potential drop over the radius of the sphere, the actual potential of the Si surface does not necessarily correspond to the set point. The surface potential is then dependent on the exposed surface and the anodic current through the sample. The anodic current is in turn dependent on the applied potential and the electrochemical oxidation rate. As the rate of electrochemical oxidation can change during the etch experiments due to the evolving silicon surface, the actual surface potential can drift. If the surface potential drifts to a very positive value (close to the passivation potential), passivation occurs, creating an oxide layer on the exposed Si surface. Due to the etchant composition (KOH + TMAH) this oxide is etched away very slowly, disrupting the etch experiment. These issues make it difficult to both determine and predict the actual surface potential. The final surface potential was calculated after completion of the etch experiments from the measured currents.

Anisotropic etch rates were determined by measuring the local etch depth using a tactile coordinate measuring machine (Zeiss UMPC 850 Carat) which contains a 1 mm diameter spherical sapphire tip and uses a contact force of 0.1 N. The total measured range

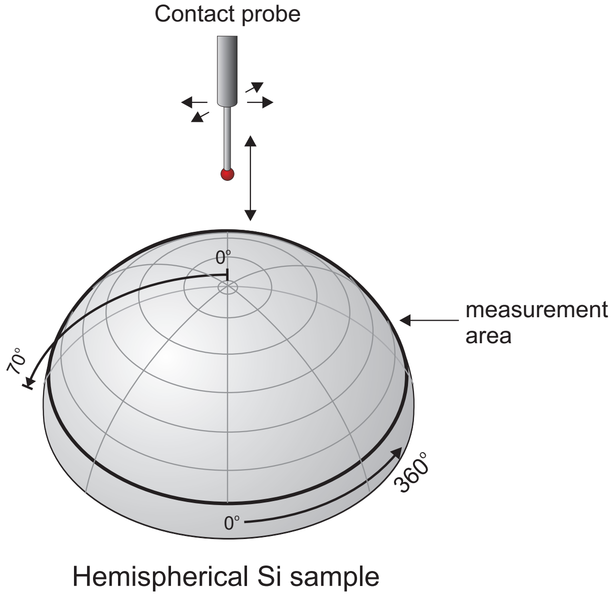

Figure 6.4: *Outline of the measurement of a hemispherical Si sample. The measurement range spans from the top of the sphere to 70° towards the bottom and 360° around the sphere. The four alignment flats are located outside of the measurement area at the bottom of the hemisphere.*

spans 70° from the top of the sphere (figure 6.4) with a spacing of 2°. The center point of the hemisphere was determined by measuring the protected bottom and alignment flats.

6.4 Observations and Analysis

6.4.1 General observations

Figure 6.5 shows several graphical plots of the measured hemispheres at three different conditions. From the resulting etch shapes, it can be clearly seen that the addition of TMA^+ to the etching solution results in a decrease in the overall etch rate. A second phenomenon which is visible in the vicinity of (111), is the presence of a hexagonal shape which is a result of (111) step anisotropy. A change in the orientation of the hexagonal shape at both 0.5 and 1.0 mol/l TMA^+ indicates step anisotropy reversal(figure 6.5b and c).

Figure 6.6 shows several measurements at different applied potential. From the figure it is clear, that changing the potential results in smaller changes to the anisotropic etch rates compared to the changes at different TMA^+ concentrations. The hexagonal shape remains relatively unchanged, indicating only small changes in the step anisotropy.

The saddle point in the vicinity of (110) previously observed in wagon-wheel samples[67, 98] (chapter 3) and outlined in detail in chapter 5 are visible as a straight line running from the (111) to the (100) orientations on the surface (figure 6.5c) . Although this feature is clearly visible on the majority of the samples, it is not always visible in the actual measurement data using the measurement device (figure 6.5b) . This indicates that, for these samples, the lateral resolution of the measurement is not high enough to reliably measure this feature. This fact has consequences for the model fit outlined in the following sections.

6.4.2 Potential drop within the hemisphere

As stated in previous sections, the size of the hemispheres causes a significant potential drop in the radial direction which leads to difficulties in both predicting the applied surface potential before the experiment and controlling the potential during the experiment. The potential drop is determined by the current passing through the sample. The current is in turn dependent on the surface kinetics of electrochemical oxidation. The driving force for these reactions is the potential of the silicon surface. A change in the exposed surfaces due to etching changes the electrochemical oxidation and in turn results in a drift in the actual surface potential. What is clear is that any potential drop caused by the resistivity of the Si bulk material will result in a *more negative surface potential* than the set point potential. In order to compensate for this, the potential drop was estimated using the measured (stable) current at the end of the experiment. Together with the resistance of the Si, the potential drop can be calculated in the radial direction of the hemisphere. These corrected applied potentials are shown in figure 6.7. For the remainder of this chapter, the corrected applied potential will be used instead of the set point potential.

6.4.3 Kinematic wave theory

To investigate the step anisotropy in more detail, the kinematic wave theory (chapter 2) was used. Within this chapter, the model is mainly used to obtain the (111) θ-dependent step velocity. Using the 10-parameter model which is described in chapter 4 it is possible to fit the data in the vicinity of both the (100) and (111) orientations. In order to reliably fit the whole data set however, the 14-parameter model, which includes the (110) pseudo stepflow mechanism, can be used. As described in chapter 5, the use of the 14-parameter model is problematic if the specific (110) features (cusp minimum and isotropic maximum) are not visible in the data set, even if the features are present on the samples themselves. This is the case for several of the samples. For a fair comparison, the 10-parameter model is therefore used to characterise the data. The possible cation/electrochemistry combined effect will be investigated by examining the change in the (111) step velocity and step anisotropy as a function of both the cation concentration and the applied potential. It should be noted that successful use of the 14-parameter model can result in different (100) and (111) parameter values compared to the 10-parameter model, as outlined in chapter 5. For (111) step velocity parameter, it is expected to result in a change in the absolute values, and not in the parameter trends.

6.4.4 (111) step velocity from kinematic wave theory

Figure 6.7 shows the (111) step velocities obtained from the experimental data. It is clear that all the graphs show step velocity minima at both the dihydride terminated steps, and monohydride terminated steps (as outlined in chapter 4). Step anisotropy

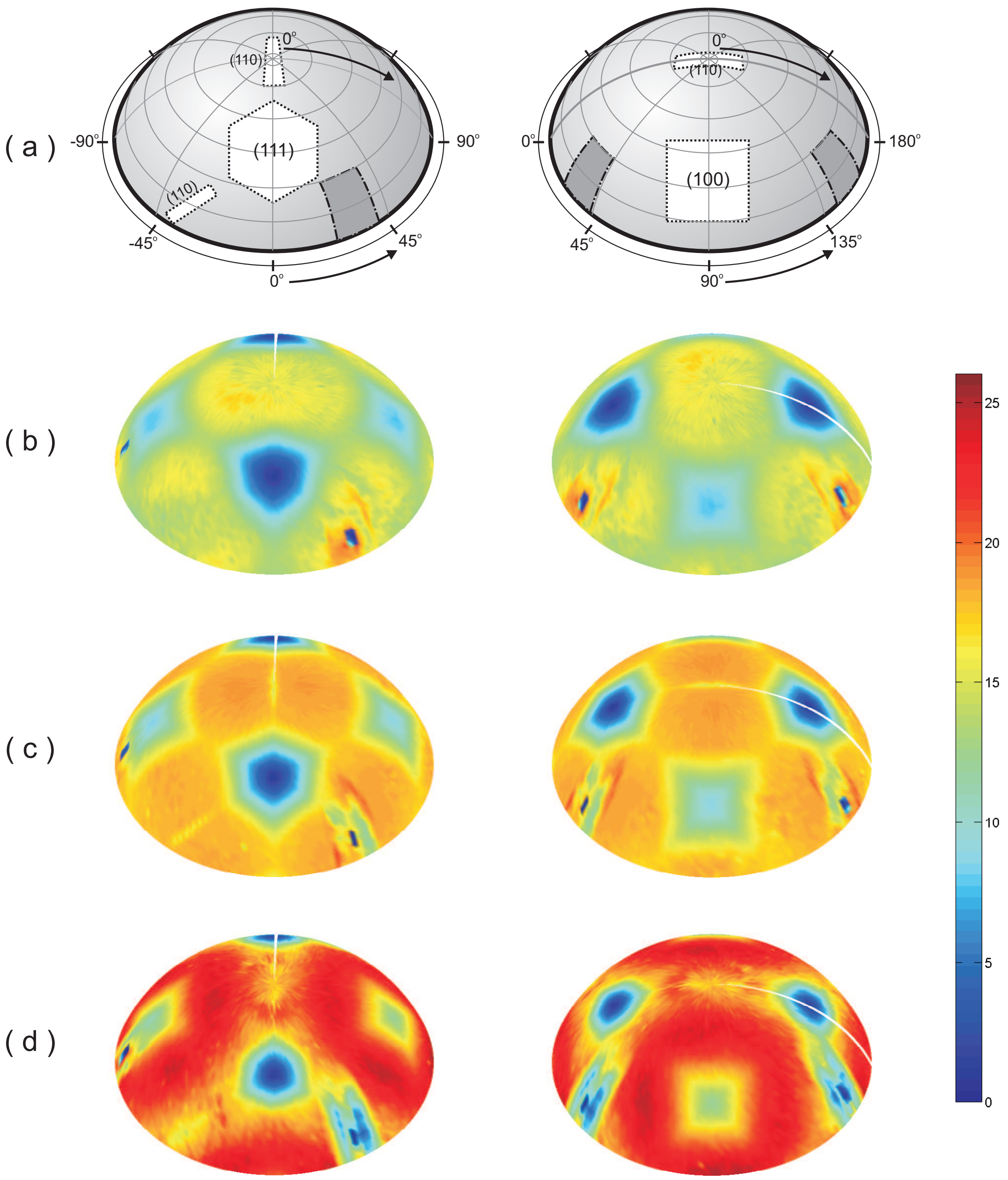

Figure 6.5: *Three dimensional plots of hemispheres etched at three different etchant conditions. (a) outlines the major crystal orientations (100), (111) and (110) and the areas of interest in the vicinity of these orientations. The right plot is a 90° rotation of the left plot. The hemispheres were etched with an applied potential of -1030 mV vs SCE and a TMA$^+$ concentration of (b) 1.0 mol/l, (c) 0.5 mol/l and (d) 0.0 mol/l. Note that the overall etch rate decreases with the addition of TMAH. Additionally, the change in the etch shape in the vicinity of (111) confirms step anisotropy reversal.*

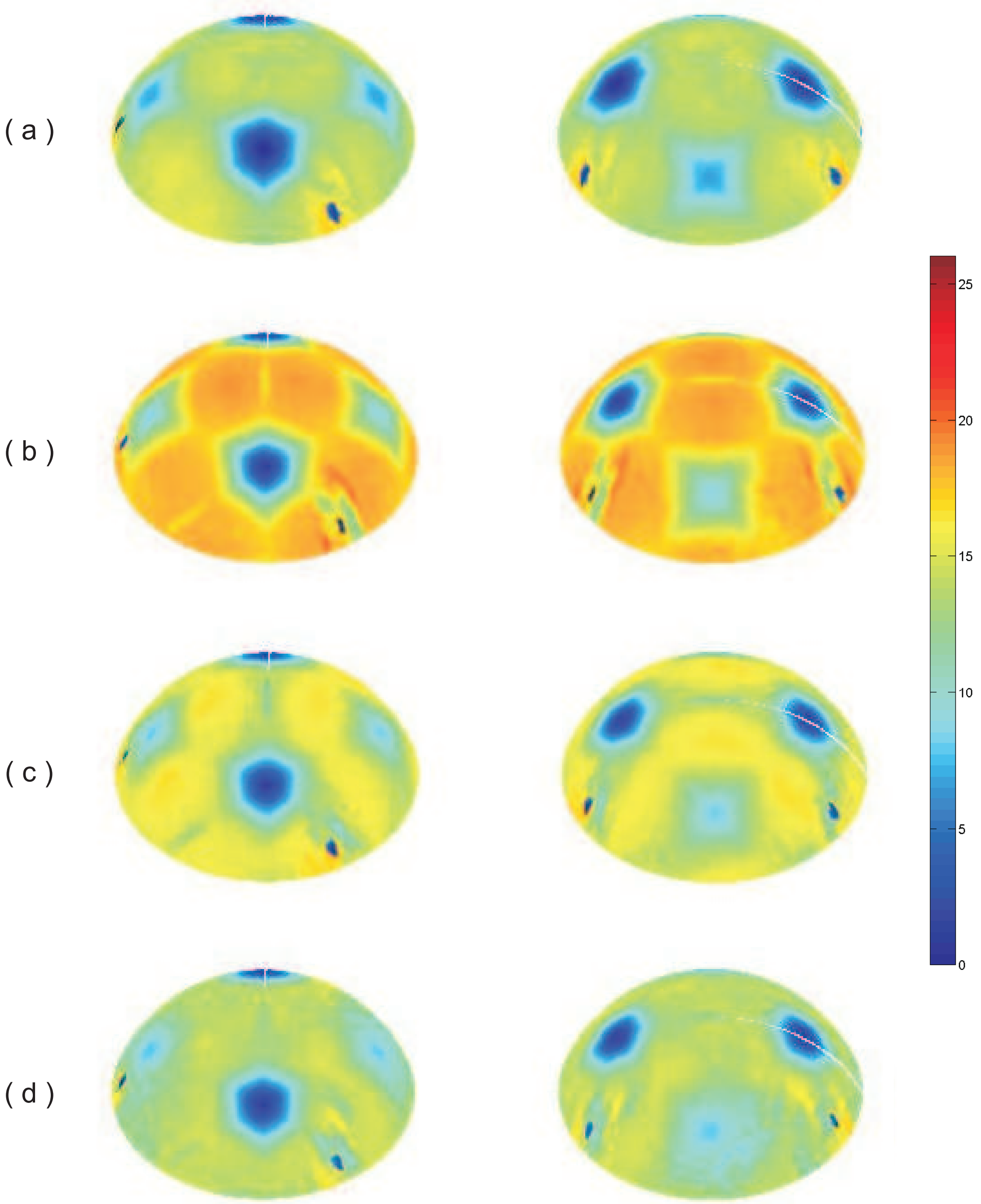

Figure 6.6: *Three dimensional plots of hemispheres etched at four different electrochemical conditions conditions. Orientations of the plots are identical to the ones on figure 6.5. The hemispheres were etched with a concentration of 5.0 mol/l* OH^- *and 0.5 mol/l* TMA^+. *The corrected applied potentials are (a)-850 mV, (b) -1030 mV, (c) -1280 mV and (d) 1500 mV vs SCE. Note that, although the overall etch rate changes, the shape and orientation of the (111) etch shape remains relatively constant.*

reversal is clearly visible at both 0.5 and 1.0 mol/l TMA^+ as the step velocity at the monohydride terminated steps is higher than dihydride terminated steps. Examining the results without TMA^+, it can be seen that only the overall step velocity changes as a function of the applied potential (figure 6.8). The step anisotropy (shape of the step velocity graph) remains largely unchanged. Similar trends are observed at both the 0.5 and 1.0 TMA^+ concentration as the step anisotropy shows only small changes while the overall step velocity changes significantly.

6.4.5 The combined effect

Figure 6.9 shows the ratio in step velocity between the dihydride terminated steps (at $\theta = 60°$, $\theta = 180°$ and $\theta = 300°$) and monohydride terminated steps (at $\theta = 0°$, $\theta = 120°$ and $\theta = 240°$). Included in the figure is the same ratio obtained from the electrochemical controlled wagon-wheel experiments (chapter 3). It is important to note that the surface potential of the hemispheres do not necessarily correspond to the applied (set point) potential. This is a result of the potential drop across the sample, as outlined in a previous section. For a fair comparison with the wagon-wheel samples, the actual surface potential is estimated from the average measured current and the sample geometry. It is clear that the addition of even the lowest concentration of TMA^+ results in step anisotropy reversal as the $v_{monohydride}/v_{dihydride} > 1$. The step anisotropy is higher at the higher TMA^+ concentration which is consistent with measurement by Cheng et al. All the measurements, however, show a near constant step velocity ratio as a function of the applied potential. This is in contrast to the wagon-wheel pattern which show an steady increase above -1250 mV vs SCE. As described in previous sections, a cation/electrochemistry combined effect is expected to change the $v_{monohydride}/v_{dihydride}$ in a disproportionate manner. This change is expected to be significantly larger than sum of the individual changes as a result of both the electrochemistry and TMA^+ alone (see figure 6.3). The absence of this disproportionate change indicates that the electrostatic interaction, as described in this work, does not occur. The results suggests that the TMA^+ and the electrochemistry are both independent processes.

There are however two reservations. It is possible that the experimental window chosen is inappropriate for these experiments, due to the limited number of experimental samples. As step anisotropy reversal already occurs at the lowest TMA^+ concentration, a possibility exists that the TMA^+ concentration is too high to determine an additional change in the step velocity ratio due to an applied potential. The effect of TMA^+ alone would then determine the measured step anisotropy. The measurement window is then too wide in terms of TMA^+ concentrations.

A second reservation deals with electrochemical issues (as outlined in the previous section). The step anisotropy which is obtained from the experiments with only KOH in the etching solution remain nearly constant as a function of the applied potential. These measurements should however be similar to the wagon-wheel measurement. This might indicate that the actual surface potentials are more negative than estimated, due to a larger potential drop. As effects of electrochemical oxidation are only clearly observable at more positive applied potential the chosen applied potential range might be too narrow.

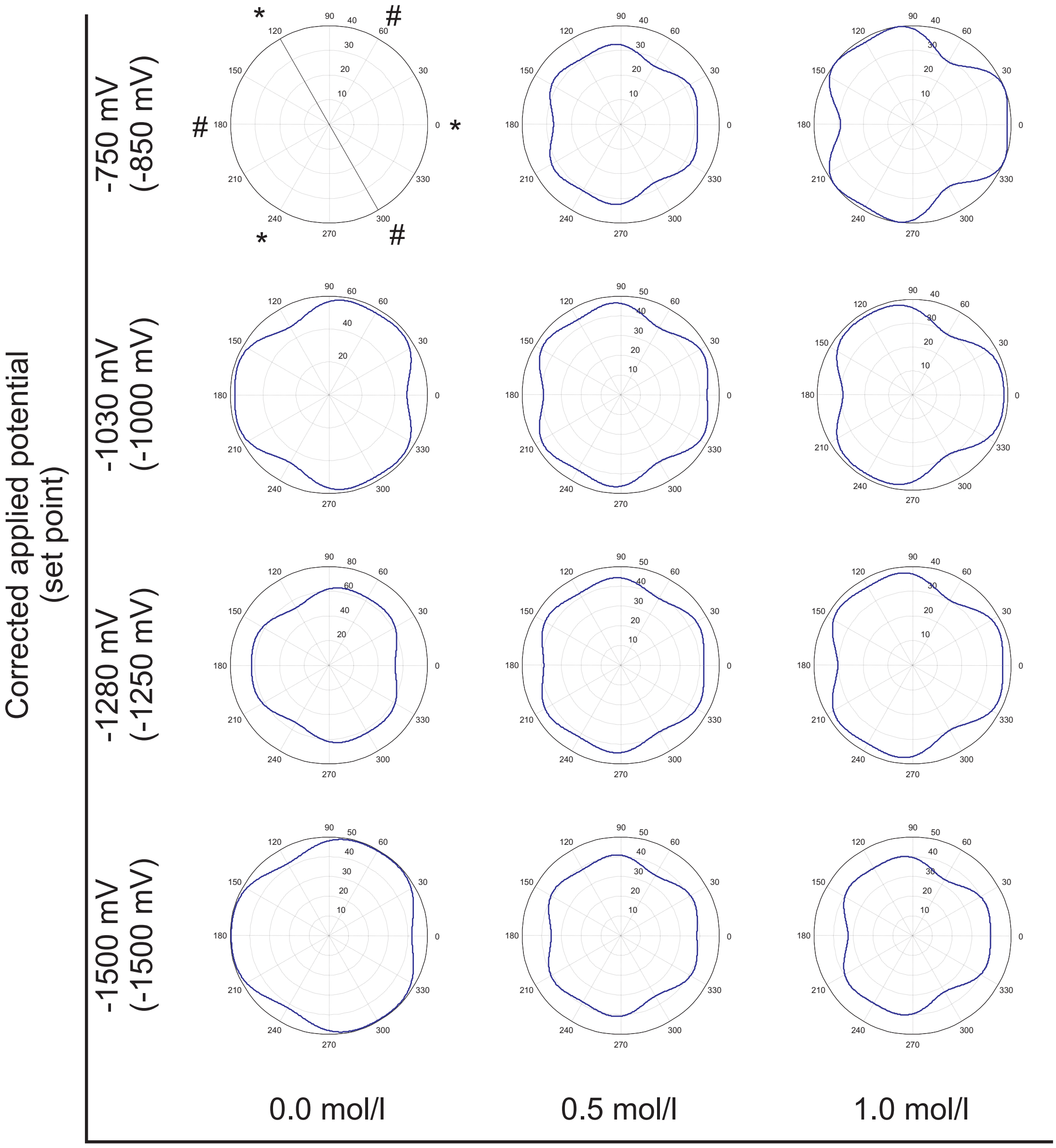

Figure 6.7: *Figure showing the (111) step velocity of all measured hemispheres displayed in polar plots. The top left plot, indicates the positions of the relevant step orientations. The monohydride terminated steps (*) and dihydride terminated steps (#) are indicated. The orientations exactly in between are composed of alternating monohydrides and isolated vertical dihydrides. Note that applied potentials are given as a set point (displayed in between brackets) and the corrected (surface) potential.*

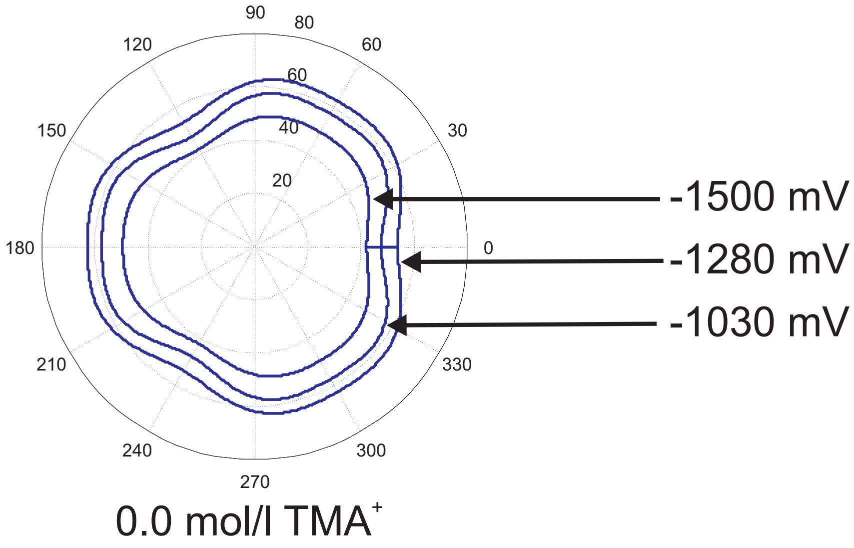

Figure 6.8: *Figure showing the step velocity of the measurements at different applied potential with 0.0 mol/l TMA$^+$ plotted within one polar plot. It can be clearly seen that the step anisotropy changes very little as the shape of the step velocity plot is similar at all conditions. Measurement at different TMA$^+$ concentrations show similar results.*

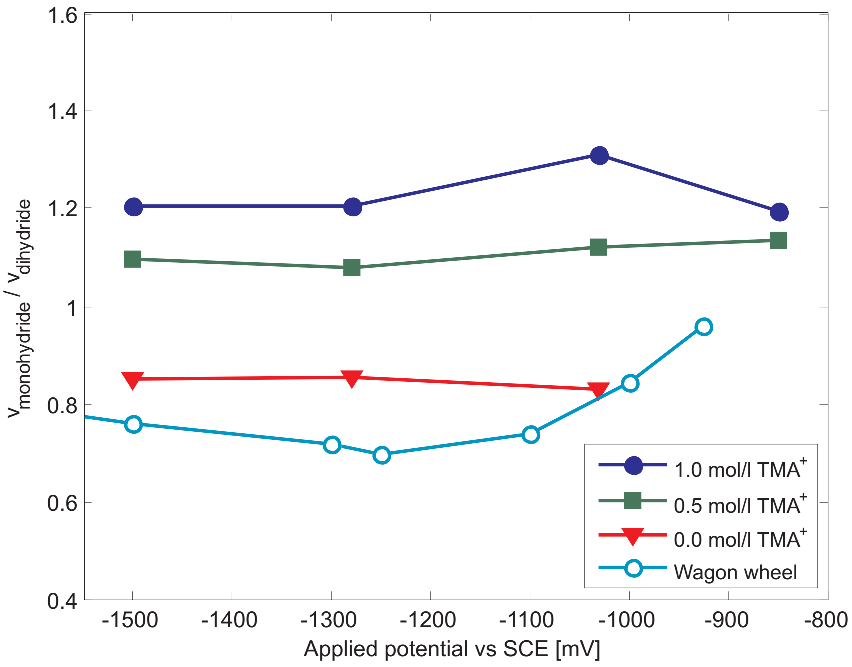

Figure 6.9: *Figure showing the ratio of the mono- and dihydride terminated step velocities (step anisotropy). The results obtained from the wagon-wheel patterns are also plotted. The electrochemical/electrostatic combined effect should result in a disproportionate change in the graph with the addition of both TMA$^+$ and increase electrochemical oxidation. The plot however shows that the addition of TMA$^+$ results in step anisotropy reversal $v_{monohydride}/v_{dihydride} > 1$, additional electrochemical oxidation does not increase the step anisotropy. This indicates that the combined effect does not occur.*

6.4.6 Step site specific interaction

Chapter 4 has outlined the importance of differentiating between isolated dihydrides and dihydrides at the dihydride terminated steps. It is shown that TMA^+ interaction is larger at the dihydride terminated step.

Figure 6.10 shows the change in step velocity due to the addition of TMA^+ at a constant applied potential (-1280 mV vs SCE). It is clear that the dihydride terminated step orientations (such as at $\theta = 60°$) become local minima. These minima are lower than the step velocity at the monohydride terminated steps (at $\theta = 0°$ for example) showing step anisotropy reversal. Maxima in the step velocity are present at orientations in between the mono- and dihydride terminated steps. As outlined in chapter 4, step orientations exactly in between (such as at $\theta = 30°$) are composed of alternating isolated vertical dihydride and monohydride sites. The actual step velocity is determined by either the isolated vertical dihydride or horizontal dihydride (which due to steric effects etch differently than the dihydrides at the dihydride terminated steps, see chapter 4).

Figure 6.11 shows the change in step velocity (Δv_{step})which is defined with the following equation:

$$\Delta v_{step} = \frac{v_{step,0.0TMA^+}}{v_{step,0.5TMA^+}} \tag{6.1}$$

As in chapter 4, the dihydride terminated steps ($\theta = 60°$) show the highest decrease, with the monohydride terminated ($\theta = 0°$) the lowest. Due to the similarities in molecular structures, it is expected that isolated dihydrides at ($\theta = 30°$) behave similar to the dihydrides at ($\theta = 60°$). The results however show smaller Δv_{step} then expected. This is consistent to chapter 4 where it is stated that the TMA^+ interaction is smaller on isolated dihydrides compared to dihydride terminated steps.

Figure 6.11 also shows the Δv_{step} at all three step orientations as a function of the applied potential. It is clear that the ratio $\frac{\Delta v_{step,dihydride}}{\Delta v_{step,verticaldihydride}}$ remains relatively constant. This indicates that, although electrochemical etching is different on mono- and dihydrides, it does not show a preference in the dihydrides sites. This was suggested in chapter 4 on the basis of the chemical mechanism behind the anisotropy in step oxidation.

6.5 Conclusions

In this chapter we have investigated the proposed electrostatic interaction between TMA^+ cation and electronegatively charged Si surface step sites. By exploiting the anisotropy in electrochemical step oxidation when an electrical potential is applied, the difference in oxidation state of (111) between the monohydride and dihydride terminated steps can be controlled. Similar to the electrostatic interaction mechanism, it is expected that the TMA^+ interaction will show a stronger attraction toward oxidised surface steps. The combination of both TMA^+ and controlled electrochemical oxidation is than expected to result in a combined effect which is stronger than both effects individually. Etch experiments have been performed on hemispherical samples at different electrochemical potentials and TMA^+ concentrations. The anisotropic etch rate data obtained from the experiments are analysed using the kinematic wave theory. Using the 10-parameter model, the (111)

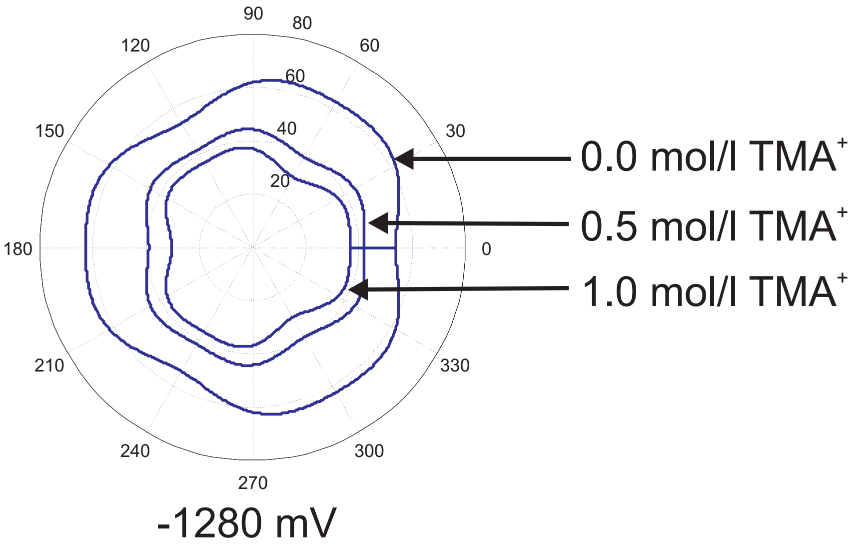

Figure 6.10: *Figure showing the step velocity of the measurements at TMA$^+$ concentration with an applied potential of -1280 mV vs SCE plotted within one polar plot. It can be clearly seen that the addition of TMA$^+$ results in a change in the shape of the step velocity. The shape indicate step anisotropy reversal.*

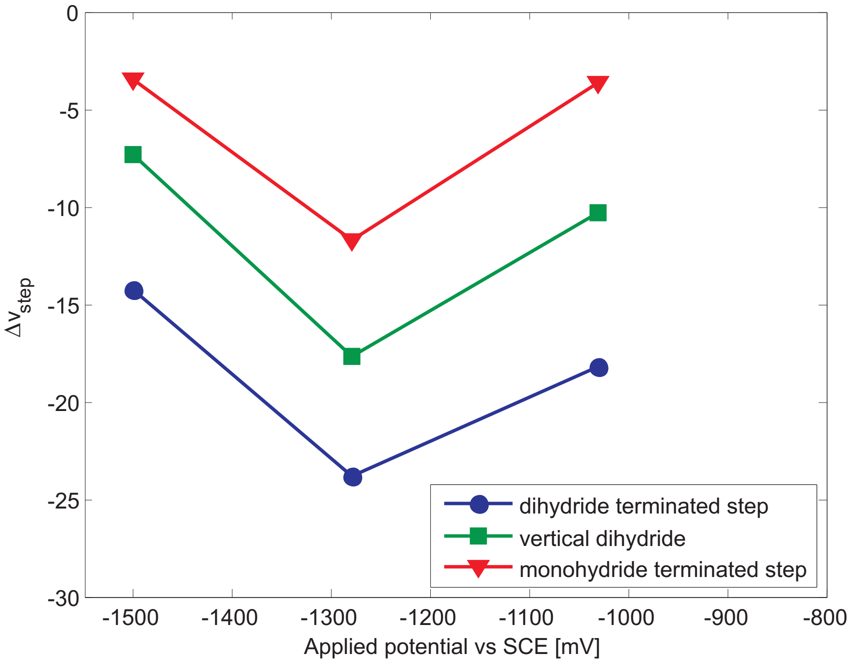

Figure 6.11: *Figure showing the change in step velocity of specific step orientations due to the addition of 0.5 mol/l TMA$^+$.*

orientation dependent step velocity was obtained from the anisotropic etch data. Examining (111) step velocity as a function of TMA^+ concentration has shown that TMA^+ interaction is (111) step site specific. The interaction with dihydrides at the dihydride terminated step orientation is larger compared to isolated dihydrides. Additionally, examining the step velocity change as a function of the applied potential indicates that electrochemical oxidation shows no distinction between these different dihydride sites. The proposed cation interaction/electrochemistry combined effect is expected to cause a disproportionate change in the ratio of the mono- and dihydride terminated step velocity . This disproportionate change was however not observed in the measurements. The results suggests that the both TMA^+ interaction and electrochemistry are two independent effects both capable of changing the step anisotropy. The proposed cation interaction based on electrostatic attraction therefore does not occur.

There are some reservations however, as there is a possibility the choice of experimental window for these experiments is not entirely suitable to observe the combined effect.

Chapter 7

Morphology of Si(110) surfaces etched in KOH solution: In-situ study of an evolving surface.

By using in-situ optical microscopy, we were able to study changes in the morphology that are induced by electrochemical oxidation of the surface. During the experiment, pictures were taken at regular time intervals under etching conditions and were converted into a series, which enabled us to monitor the morphology evolution. An image analysis procedure was used to characterize the changes. In addition to the observations during electrochemical oxidation of the surface, the effects of KOH etchant concentration and the presence of low concentrations of hydrogen peroxide are considered.

7.1 Introduction

The etching of silicon in KOH solution is strongly anisotropic, i.e. the dissolution rate depends on the crystallographic orientation of the exposed surface [27, 26, 66, 107, 41, 84]. In addition, there is a strong anisotropy in anodic oxidation. For applications in microelectromechanical systems (MEMS), (100) and (111)-oriented substrates are generally used, while (110) wafers are used far less frequently. Unlike both (100) and (111), anisotropic etching of Si(110) does not produce smooth surfaces which makes it less suitable for MEMS manufacturing, as the surface roughness can adversely affect device performance. Due to this fact, the reaction and surface kinetics of this crystal orientation have not been investigated extensively. It is known, however, that the morphology is very sensitive to process conditions and it can change drastically as a function of an etchant composition[80, 86, 87, 90] or applied potential[65]. The use of TMAH-based (tetramethyl ammonium hydroxide) etchants for example can result in far smoother surfaces than those obtained in KOH solutions [44, 100, 79]. In chapter 3, etch rates were determined as a function of an applied potential using a deep-etched wagon-wheel geometry. It was observed, that the morphology of the (110) surface was different at the various potentials[65]. This chapter describes a more elaborate study of the (110) morphology in which the effect of an applied potential, the presence of an oxidizing agent (hydrogen peroxide, H_2O_2) and the concentration of the KOH solution were investigated using ex-situ and in-situ optical microscopy. This work aims to provide primarily a visual description of the (110) morphology during the etching in real time. The evolution of the surface morphology and the morphological transitions induced by different electrochemical conditions were investigated *in-situ* by observing the etching surface with an optical microscope in a flow cell. By performing potential-step experiments, the slow transitions in the surface morphology could be investigated in real time. Such observations were done during the formation of the characteristic (110) roof-tile morphology under open-circuit conditions, starting from a polished surface. The changes after applying different anodic potentials were also studied. By taking pictures at regular time intervals it was possible to study the time-dependent changes. Due to the fact that the typical size of the morphological features on Si(110) is relatively large, i.e. on the scale of microns, the surface could be studied at relatively small optical magnification. The advantage of such an *in-situ* approach is that the complex morphology is visualised and the 'active' regions can be identified. It is important to note that this method is different from one in which performing a large series of experiments are performed at different etch times. In contrast to this ex-situ method, where an overall morphology of different samples is evaluated, the in-situ method allows the monitoring of the morphology of one particular region in a single experiment. The surface kinetics can then be examined on a local scale with a relatively high sampling rate. Using the visual observations and an image processing procedure, we have analysed the morphology in terms of three geometric parameters from which the relative change in feature size and shape could be determined. Morphology features observed here are compared to ex-situ observations and predictions from kinetic Monte Carlo (kMC) simulations[42].

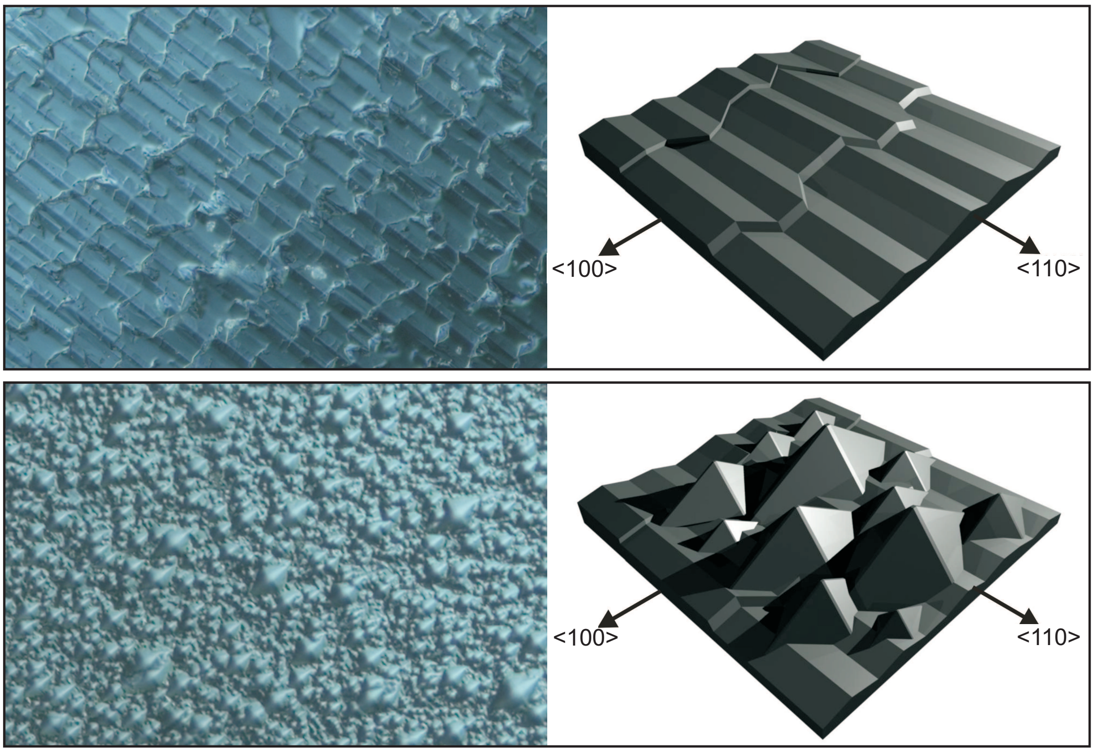

Figure 7.1: *Microscopic observations (left) and schematic representations (right) of the two major (110) surface features. The roof-tile morphology (top) was formed in 5.0 mol/l KOH at open-circuit potential. The trapezoidal hillock morphology (bottom) was formed in 10.0 mol/l KOH at open-circuit potential. Conditions: 60 minutes etching at 50.0°C. The crystallographic directions are indicated.*

7.2 Outline of the (110) Morphology

7.2.1 Steady-state (110) morphology

Although the morphology of (110) surfaces etched in KOH solutions has been widely reported in the literature [42, 80, 84, 107, 100, 104], little information is available concerning the exact geometry and molecular structure of the observed features. The molecular etching mechanism and surface kinetics are also not completely clear. *Ex-situ* microscope observations of etched surfaces have shown that the morphology primarily consists of roof tile shaped structures which are aligned along the [110] direction (see Figure 7.7). Observations of the morphology cross section using SEM have shown that, under these etching conditions, the angles of the roof-tile faces are approximately 18° from the 'true' (110) crystallographic surface. Under certain conditions, such as high concentrations of KOH, a different morphology can be observed that mainly consists of trapezoidal hillocks. These features can be seen as 'superimposed' on the roof-tile morphology (see Figure 7.1). Previous experiments (in chapter 3 have shown that etching with a very positive applied potential, i.e. very close to the point of anodic passivation, also results in the formation of trapezoidal hillocks[65].

7.2.2 Atomistic view of (110) morphology

Gosalvez et al.[42] have performed extensive kinetic Monte Carlo (kMC) simulations in an attempt to obtain a more detailed description of the morphology in terms of the molecular and microscopic structure. They have determined that the typical roof-tile structure is composed of steps on (111) surfaces. These steps are monohydride terminated which, under typical etching conditions in KOH, are considered the most stable steps. As the roof-tile ridges are similarly composed of monohydride terminated steps, these are also stable. The fact that the roof-tile faces do not correspond to the (111) can be attributed to step bunching, which effectively forms high index planes (generally (xx1) with $x > 1$). By including step bunching in their kMC model, simulations have shown that the roof-tile morphology is inherently stable. The main requirement is that the monohydride terminated steps are more stable than other (111) step types.

For the trapezoidal hillock morphology, Gosalvez et al. have shown that these features can be formed under the following conditions. As the faces of such a hillock are composed of (111) dihydride terminated steps, the stability of these steps should be higher than that the other (111) step types in order for these features to be formed. Additionally, both the apex and the ridges of the structures are inherently unstable and need to be stabilised for the formation of these features. To form the trapezoidal hillock, the requirements are therefore a stable dihydride terminated (111) step (compared to other (111) steps) and the presence of apex and ridge stabilisation. The exact mechanism responsible for this stabilisation is not clear although several suggestions have been given in the literature, such as the adsorption of dissolved metals[90] or silicate particles[72, 99].

Wagon-wheel pattern experiments performed in chapter 3 have shown that, due to the anisotropy in electrochemical oxidation, step anisotropy reversal occurs under high oxidation conditions[67]. This is consistent with the presence of trapezoidal hillocks on the Si surfaces, as the dihydride terminated steps are effectively the most stables step under these conditions. The kMC simulations provide good insights into the chemical/physical requirements for both the roof-tile and hillock morphology. It should be stated, however, that typical kMC systems are several orders of magnitude smaller than the typical size of the actual (110) morphology. It is unclear how the kMC simulations and predictions translate to micrometer size features.

7.3 Experimental

7.3.1 Sample preparation and cleaning

All experiments were performed on p-type Si (110) samples diced from 4 inch Czochralski grown Si wafers (5-10 Ω·cm). Before use, the samples were cleaned in concentrated nitric acid (Merck 65% p.a. quality, 30-min immersion) to remove organic deposits. Subsequently the samples were immersed for 15 min. in deionized water ($\rho \sim 16$ MΩ·cm). The etchant was prepared from 'VLSI grade' KOH (Merck, Selectipur, used as received) and deionized water . The etchant solution was purged with argon prior to and during all experiments, to remove dissolved gases. The sample was mounted in a Kel-F holder where the electrical contact was isolated from the solution by means of a Viton O-ring (see figure 7.2) Ohmic contact between the silicon and the copper connection was achieved by scratching and applying GaIn eutectic on the back of the sample. The silicon was the working electrode in the electrochemical cell with a platinum counter electrode and a saturated calomel electrode (SCE) as reference. All potentials are given with respect to SCE. A potentiostat (EG&G Princeton Applied Research, PAR-273-A) was computer-controlled by LabVIEW (National Instruments). A temperature sensor (Pt-100) and a thermostatic bath (Haake Fisons F3 and S) were used to control the temperature in the cell (accuracy of 0.1°C). For the ex-situ experiments, etching was performed in the dark. Native oxide on the silicon was dissolved in the KOH solution, which could be monitored by measuring the open-circuit potential (OCP) over time[17]. After etching for a given time, the sample was 'quenched' in a 10% sulfuric acid solution (prepared from Merck, p.a. quality, 15 min immersion). After this step the samples were rinsed again with deionized water and blown dry in a stream of argon. Sebsequently, the samples were studied with an optical microscope (Zeiss, Axioplan-2).

7.3.2 In-situ optical microscopy

The in-situ measurements were performed with a flow cell, which allowed us to monitor the surface morphology with optical microscopy under etching conditions. Sample preparation was performed as described in the previous section. A schematic representation of the setup is depicted in Figure 7.2. Using a long working distance objective lens (Nikon, CFI-L-Plan-Epi-SLWD, 20 ×, working distance 24.0 mm) on the microscope equipped with a CCD camera, it was possible to view the etching sample via a quartz window at the top of the cell. For these experiments illumination by the microscopy was therefore unavoidable. Two different adapters could be placed in front of the CCD (1.0 × and 0.63 ×). The CCD had an effective resolution of 1388×1040 px. The 20× objective together with the 1× adapter translates to a field of view of 360×270 μm on the Si surface.

The flow cell was made from Teflon and Kel-F and the thickness of the liquid layer above the sample surface was 6.0 mm. To allow for electrochemical measurements, the flow cell contained a reservoir in which the counter and reference electrode were positioned together with a thermocouple (Fluke, # 80-PK-1, K-type). The etchant was circulated with a peristaltic pump (Watson-Marlow, SciQ-323) via Viton tubing (Watson-Marlow, # 970.0080.016, internal diameter 8.0 mm). The liquid flow was kept as low as possible, and was set to a value at which gas bubbles evolved during etching were transported away from the surface, outside the optical pathway of the microscope, thus minimizing any 'blocking' effects. However, a certain flow is needed to maintain a constant temperature of the etchant in the flow cell (volume flow was typically 700 mL/min resulting in an approximate linear velocity of 6.5 cm/s within the cell) and to prevent local etchant depletion. The temperature was monitored continuously using a thermocouple that was positioned in the vicinity of the sample and connected to a signal converter (Fluke, # 80-TK) and a voltmeter. To minimize liquid pulsation effects, the flow was split before being led over a double pump head with three rollers each, which were placed under an offset of half a turn. Both flows were combined, before being returned to the etchant reservoir (etchant volume $\sim$ 500 mL) in the thermostatic water bath. All connections to the reservoir were made using Teflon and PEEK adapters (Omnifit, # 1074, # 3222, and

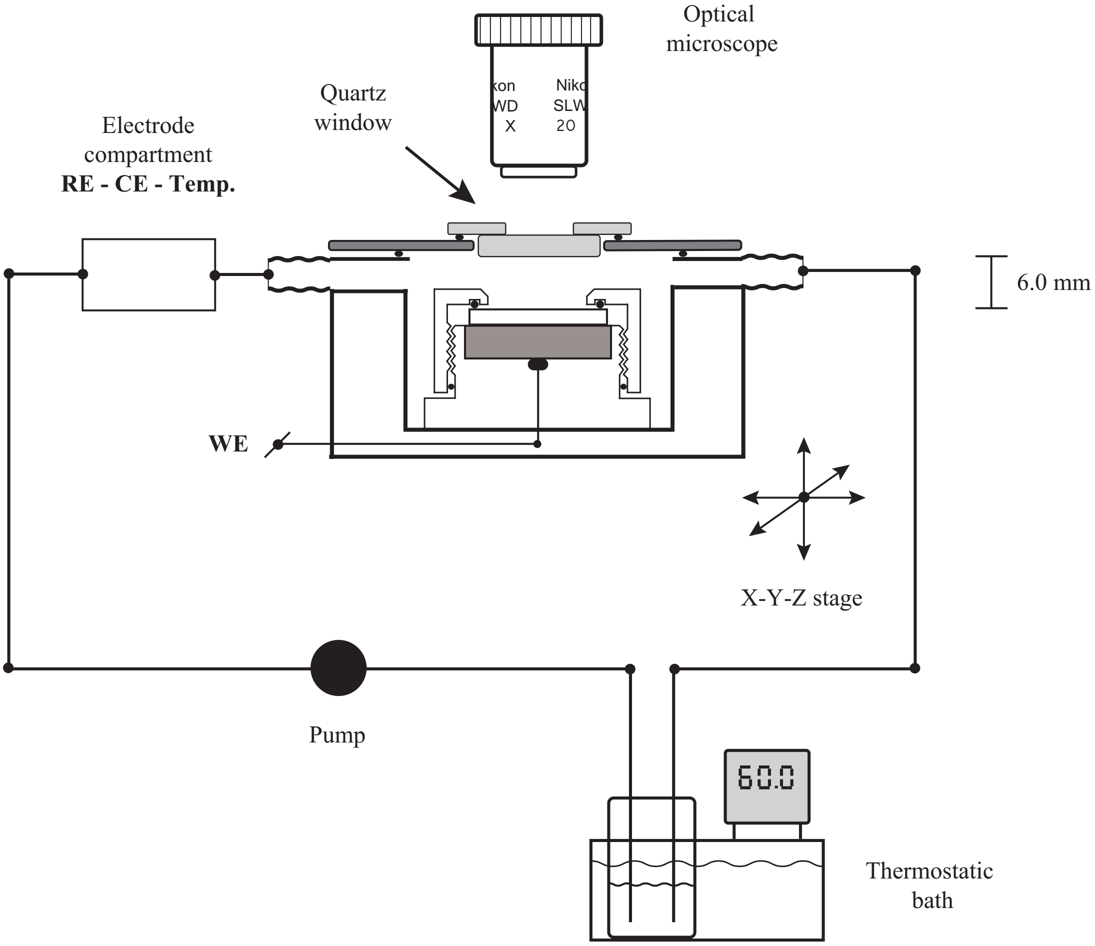

Figure 7.2: *Schematic representation of the electrochemical flow cell for in situ microscopy. The cell was mounted on the stage of the microscope, which was equipped with a long working distance objective lens. The interior of the cell consisted of Kel-F and Teflon parts. The etchant was continuously circulated via the tubing, using a peristaltic pump. The liquid layer above the sample surface was 6.0 mm. The temperature of the etchant was controlled by a thermostatic bath.*

3240).

7.3.3 Post-measurement analysis

The *in-situ* microscopy observations were combined into a movie for clear visualisation of the morphology evolution. However, without a method of quantifying the morphology and the observed changes, the microscopic observations remains primarily qualitative

In this work, an image processing procedure was used to quantify the morphology. It is important to state that image processing is, in a sense, a blind analysis method. It analyses the graphical features on the image regardless of the actual surface morphology that those features represent. The measured values are then determined by threshold values of the image analysis procedure and the characteristics of the image itself and do not necessarily correspond to the actual morphology. A total of three morphology parameters are obtained from the image analysis procedure:

- Average feature surface area. This is determined by measuring the area (expressed in pixels^2) of each uninterrupted region in the image with a greyscale value above a certain threshold level.
- Total feature perimeter length. This is the sum of the perimeter length (expressed in pixels) of each of the areas determined during the average feature size procedure. By correlating the average feature surface area with the total feature perimeter length, an indication of the morphology is obtained. At a constant average feature size, a higher total perimeter length indicates longer roof tiles while for a low perimeter length more square-shaped roof tiles are expected. With the same total perimeter length, an increase in average feature surface area indicates a larger size of the roof-tile structures.
- Feature uniformity. The standard deviation in the series of separately determined feature surface areas gives a measure for the uniformity in the shape distribution that is present at the surface.

As stated above, the measured values do not necessarily correspond to the *actual* size and shape of the features. This would require a much more sophisticated analysis involving complex methods such as object recognition. However, with a large enough sample size both in terms of the number of successive microscope images, and the number of visible features per individual image this procedure has proven successful in quantifying the morphology changes.

7.4 Results and discussion

In the following sections, results of both *ex-situ* and *in-situ* experiments are outlined. The influence of an applied potential on the (110) surface morphology will be discussed first. In addition to the observations during electrochemical oxidation of the surface, the effects of the presence of low concentrations of hydrogen peroxide and the concentration of the KOH solution are also considered. In-situ experiments with an electrochemical flow cell will then be discussed and analyzed with the image processing procedure. The observations are interpreted on the basis of results from kMC simulations.

7.4.1 The influence of an applied potential

To study the effect of an applied potential on the (110) surface morphology, samples were etched for 60 min at various anodic potentials. Subsequently, etching was 'quenched' and the surface was studied ex-situ using optical microscopy. The potentials applied are indicated in the voltammogram in Figure 7.3. When the potential is scanned towards more positive values, the current gradually increases and reaches a peak value after which it drops considerably. In the potential range from open-circuit up to the current peak, the surface is anodically oxidized. For values more positive than the peak potential, such as -800 mV, the surface becomes covered with an oxide layer and etching is prevented: no morphology will be developed at potentials more positive than that value. Five potentials were applied in the anodic potential range; the corresponding microscopic images are shown in Figure 7.4. It is important to emphasize that in general micromachining, silicon is etched at open-circuit potential (OCP). After native oxide removal in the KOH solution, the morphology starts to evolve; the current increased with time and reached an almost constant value after approximately 15 min. When the silicon is etched, macroscopic features develop as the surface (partially) oxidizes. The current reached after etching for 60 min shows the same trend as a function of potential as for a voltammogram measured after development of the steady-state morphology and is only slightly larger. The morphology observed for potential 'A', i.e. -1250 mV, is already different from that observed under open-circuit conditions: the general 'shape' of the features is similar but their size is larger (see Figure 7.4(a)). The surface features become smaller and the typical roof-tile morphology disappears on going to more positive potentials (from (b) to (e)).

From in-situ IR spectroscopy work on Si(100) surfaces performed by Schiffrin and co-workers, it is known that the Si-H termination gradually disappears on going to more anodic potentials. The silicon hydride present at OCP is removed when the anodic potential is applied; the surface gets more oxidized and SiH bonds are replaced by SiOH and Si-O-Si. At sufficiently positive potential, the electrode reaches a passivated state in which the surface is covered with an oxide layer, which prevents silicon dissolution. Using in-situ STM, Allongue and co-workers have investigated step-flow etching and anodic oxidation of Si(111) surfaces. With the latter technique, local changes in the interface chemistry are measured as variations in the tunneling probability. However, the interpretation is less straightforward, due to the absence of a *direct* coupling between the actual surface termination and measurements. Recently, these observations were extended with in-situ FTIR measurements by Philipsen et al.[74], who studied the transient changes in the surface chemistry during anodic oxidation and passivation of Si(111). For the case of (110) surfaces, however, no such spectroscopic work has been performed under etching conditions in KOH solution. Although the (110) surface morphology is fairly complex and its origin is only understood to a limited extent (see previous section), we conclude that the observed differences in the surface morphology are induced by primarily surface oxidation.

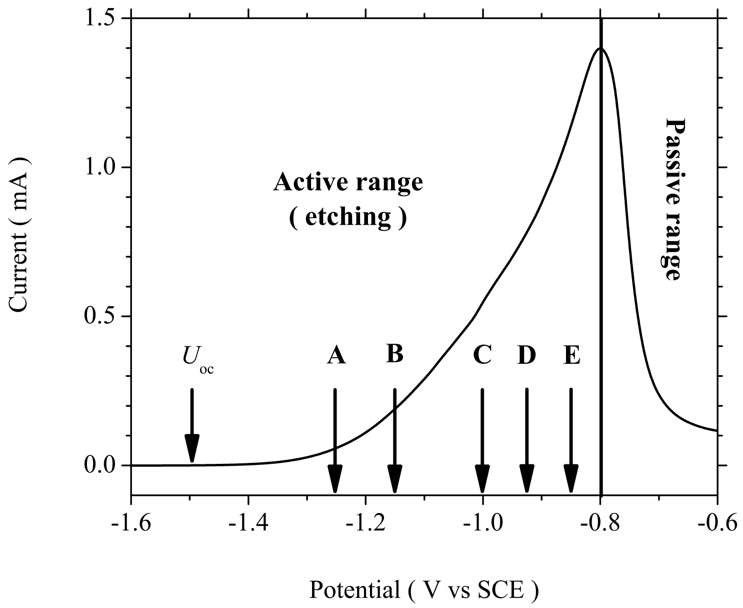

Figure 7.3: *Voltammogram of p-Si(110). The surface morphology was developed first under open-circuit conditions. Subsequently, the applied potential was scanned at a fixed rate towards more positive values and the current was recorded. The open-circuit potential (OCP) is located at about -1500 mV and the peak potential at -800 mV. Anodic potentials at which samples were etched for 60 min, are indicated. After etching, the dissolution reaction was 'quenched' and the surface was studied using optical microscopy (the corresponding microscopic images are shown in Figure 7.4).*

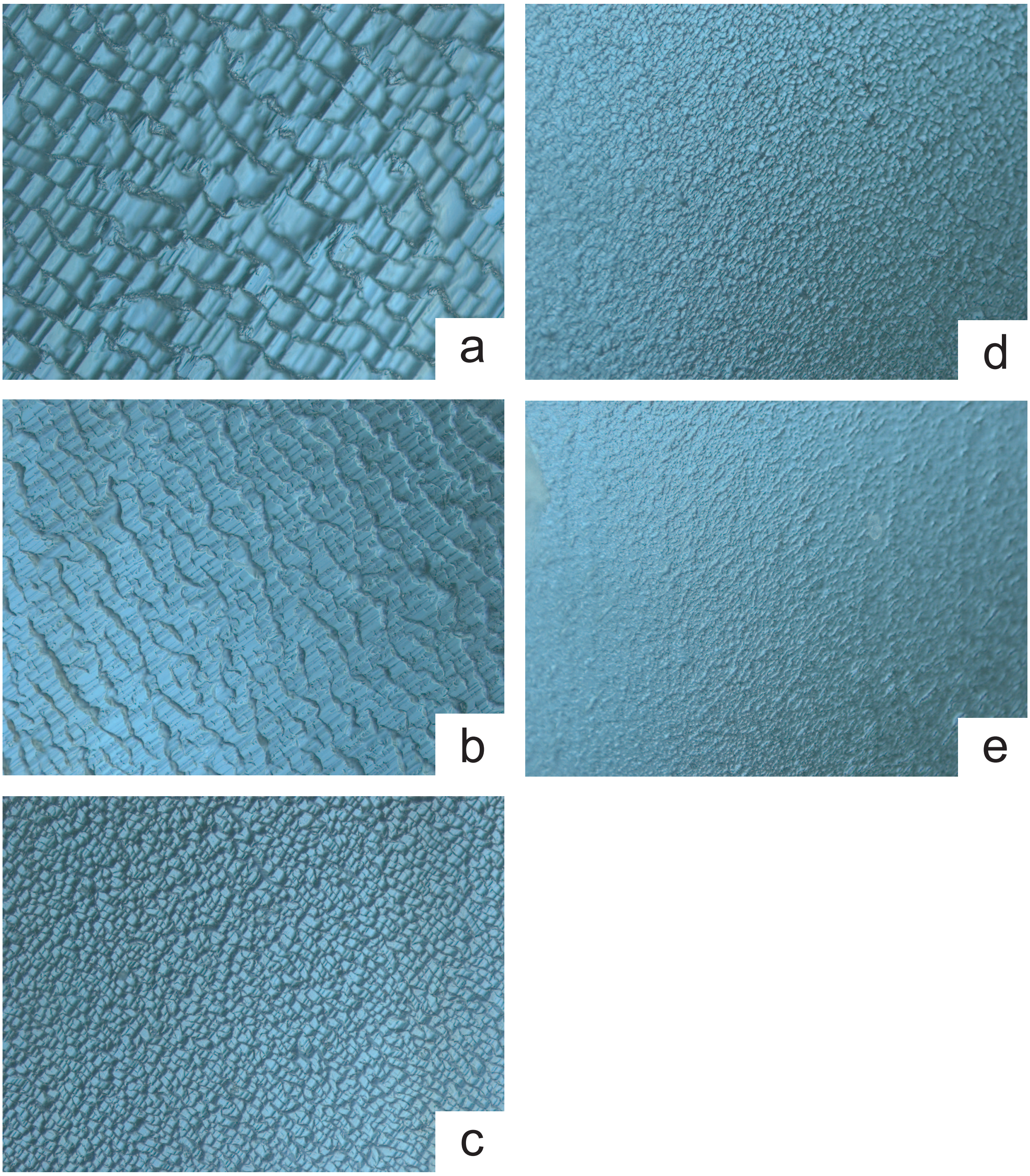

Figure 7.4: Ex-situ *microscope observations of the morphology of p-type Si(110) after 60 min etching at various applied potentials. (a) -1250 mV vs. SCE, (b) -1150 mV, (c) -1000 mV, (d) -925 mV, and (e)-850 mV. These potentials correspond to the ones indicated in Figure 7.3. Conditions: 5.0 mol/l KOH at 50.0°C. Optical magnification: 50 ×.*

The optical microscopy pictures shown in figure 7.4 were obtained ex-situ. Measurement of current transients and experiments with different etching times already give an indication of the very slow evolution of the (110) morphology and the large differences for the various potentials. These experiments also allowed us to use a larger optical magnification than was be possible under etching conditions.

7.4.2 The influence of the concentration KOH

From the literature it is known that the concentration of KOH in solution strongly influences the (110) surface morphology[100, 41, 80]. In the current work, we also studied the effect of concentration, under conditions similar to those used for the experiments with applied potential. Samples were etched for 60 min at the open-circuit. After etching was quenched, the morphology was studied *ex-situ* with an optical microscope (see Figure 7.5 for the results). For concentrations below 10.0 mol/l, the morphology consists of roof-tile features. Changes in roof-tile length and size can be observed as a function of the concentration. For the samples etched in 10.0 mol/l KOH solution (see Figure 7.5(e)), the surface is fully covered with trapezoidal hillocks (see figure 7.1). Both characteristic morphologies were previously discussed.

7.4.3 Hydrogen peroxide

As part of this work, we studied ex-situ the morphology with addition of small amounts of hydrogen peroxide (H_2O_2). Figure 7.6 shows the effect of the addition of H_2O_2 to the etchant solution on the surface morphology. To create well-defined initial Si surfaces, native oxide was first removed using a KOH solution. Subsequently the H_2O_2 added, and the sample was etched for 60 min at OCP. At increasing H_2O_2 concentrations, both the ridges and noses of the roof-tile pattern remain visible. However, the regions in between the individual roof tiles seem to show a smoother surface. The base of the roof tiles become less pronounced. The surface etched with 250 μL H_2O_2 added is most likely close to passivation. At even higher concentration, i.e. with the addition of 500 μL H_2O_2, the surface was covered with an oxide layer that prevented etching[93, 94]. STM investigations by Neuwald et al.[64] have shown that a strong oxidiser, i.e. H_2O_2, chemically oxidises the (111) surface isotropically. No preference was observed for different surface sites. In addition to this work, FTIR spectroscopy provided more direct information on surface species[15]. Sugita et al. have performed a FTIR analysis on both (100) and (111) surfaces, confirming the results of Neuwald et al. Previous work on (100) Si surfaces etched in KOH solution [17, 110] have additionally shown that the formation of pyramidal features is suppressed in the presence of oxidising agents. It was also observed that anodic polarisation has comparable effects. This was explained on the basis of an increased oxidation of the pyramid faces. This then results in roughening of these near-(111) surfaces, leading to the effective removal of the feature. It is striking that, although both H_2O_2 and an applied anodic potential (partially) oxidize the Si surface, large differences are observed in the resulting (110) morphology. The absence of trapezoidal hillocks under near-passivation conditions, i.e. at the highest concentrations of H_2O_2, is the most obvious difference. This indicates that, although monohydride stability is decreased (roof-tile features disappear

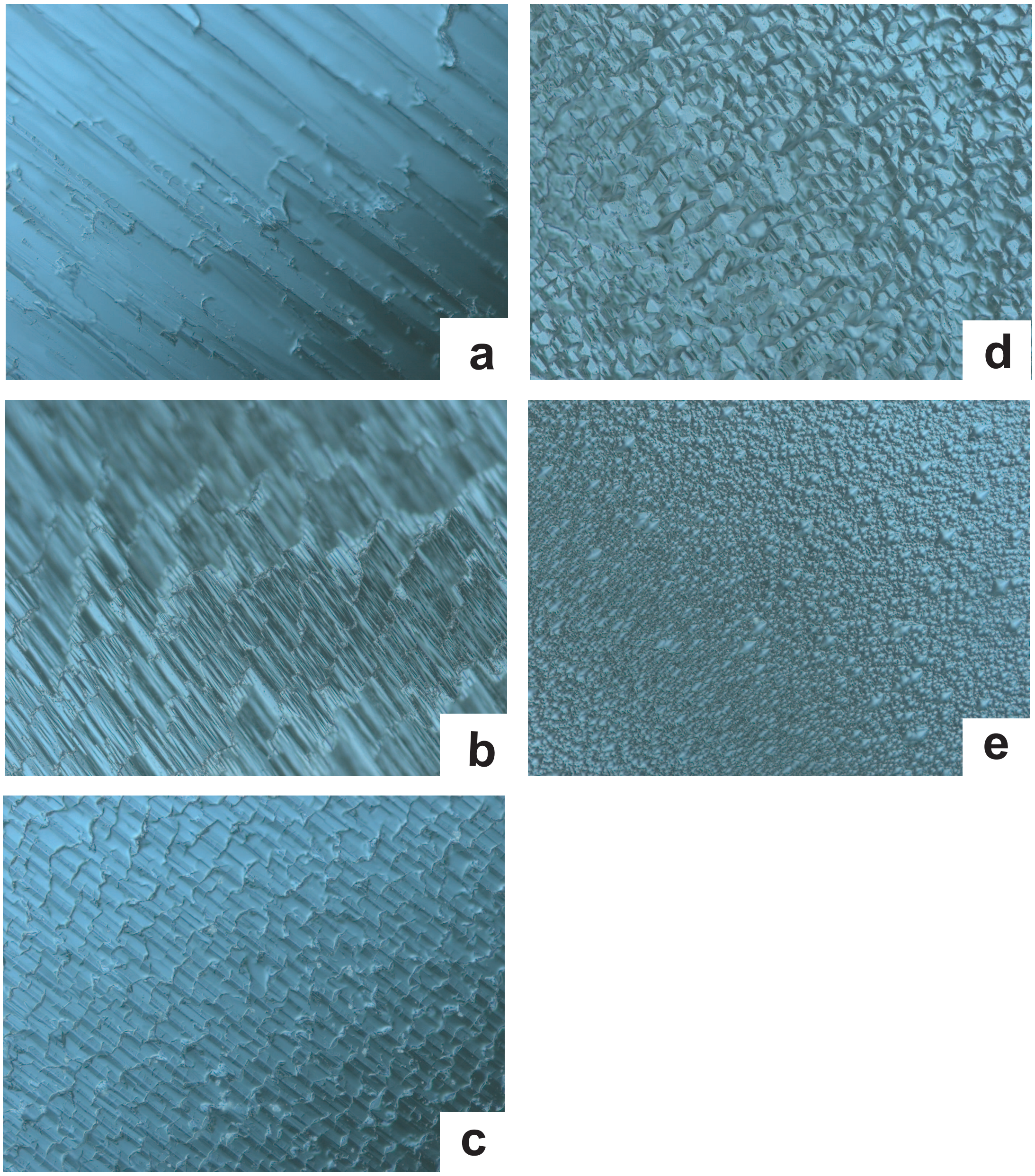

Figure 7.5: Ex situ *microscope observations of the morphology of p-type Si(110) after 60 min etching under open-circuit conditions in KOH solution of various concentrations. (a) 1.0 M KOH, (b) 2.5 M, (c) 5.0 M, (d) 7.5 M, and (e) 10.0 M. Conditions: 50.0° C. Optical magnification: 50 ×.*

with increasing H_2O_2 concentration), step anisotropy reversal does not occur. Under these conditions, the stability of dihydride steps is lower than that of monohydride-terminated steps. As high dihydride stability is one of the main requirements for stable trapezoidal hillocks, such features are therefore not observed. With an externally applied potential, step anisotropy reversal, which originates from the anisotropy in electrochemical oxidation of monohydrides and dihydrides can occur[65, 67] (see chapter 3). The absence of step anisotropy reversal in the presence of H_2O_2 indicates that the additive oxidizes the step orientations isotropically. This is consistent with the observations by Neuwald et al.

7.4.4 In-situ monitoring of (110) evolution and transistion

To obtain more insight into the formation of surface features and their evolution with time, the morphology was studied using the in-situ setup. After native oxide removal, the surface was monitored during a total experimental time of 210 min. Microscopic images were taken every 30 sec. For these measurements, it was necessary to adjust the microscope focus regularly to compensate for the change in surface position due to the etching of the Si sample. Figure 7.7 show microscope images of the (110) surface at specific points during etching at OCP and with an applied potential (points I to X). Figure 7.8 shows the three morphology parameters obtained from the image analysis procedure as a function of time. In addition the relative change in morphology shape and size during the experiment is shown figure 7.9.

Morphology formation from polished surface at OCP

Images I to V of figure 7.7 show the morphology formation from a polished wafer surface at OCP. The microscope images show a gradual formation of small elongated roof tiles which merge to form larger features. After approximately 50 min (III), this morphology remains relatively stable in size and position. A more detailed description of the morphology evolution can be obtained from the image analysis. Figures 7.8 and 7.9 show that from point I to II small and elongated roof tiles are initially formed with a low uniformity (high standard deviation for the feature size, see the lower frame of figure 7.8) as expected for the formation from a polished wafer surface. As the etching continues, the roof tiles merge to form more square-like features (point II to III) with increasing uniformity. From point III onwards, the morphology is relatively uniform, the feature size and shape still continues to evolve slowly. From III to IV the features merge length-wise as they become both larger and more elongated. Finally, the morphology stabilises at V as can be seen from both graphs 7.8 and 7.9.

Morphology transition from OCP to -850 mV

Between image V and VI the morphology undergoes a transition which is induced by switching the applied potential from OCP to a positive potential close to Si passivation (-850 mV vs SCE). It is clear from both the microscopic pictures and the analysis that the change in applied potential results in an abrupt change in morphology. The -850 mV morphology is observed after point VI and remains relatively stable afterwards. The analysis indicates the presence of small features with a high uniformity. However, due to

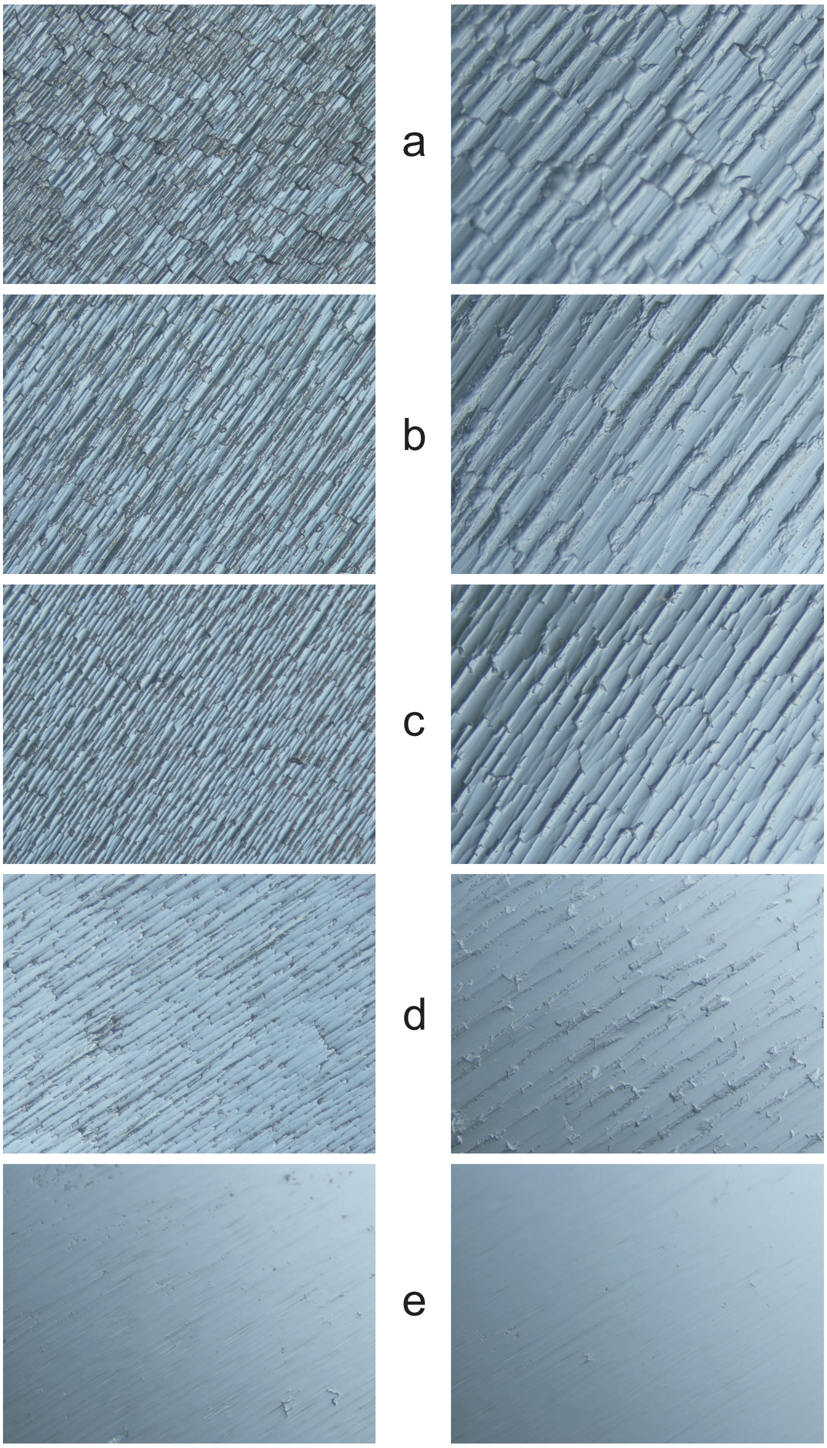

Figure 7.6: Ex situ *microscope observations of the morphology after 60 min etching under open-circuit conditions in 5.0 mol/l KOH at 50.0 °C, with hydrogen peroxide present. The added amounts of hydrogen peroxide were (a) 10 μL, (b) 25 μL, (c) 75 μL, (d) 100 μL, and (e) 250 μL of a 30% solution to 150 mL etchant (initial concentration peroxide after adding* 10 *μL amounts to 0.5 mM). Left column: magnification 20× and right column: 50×.*

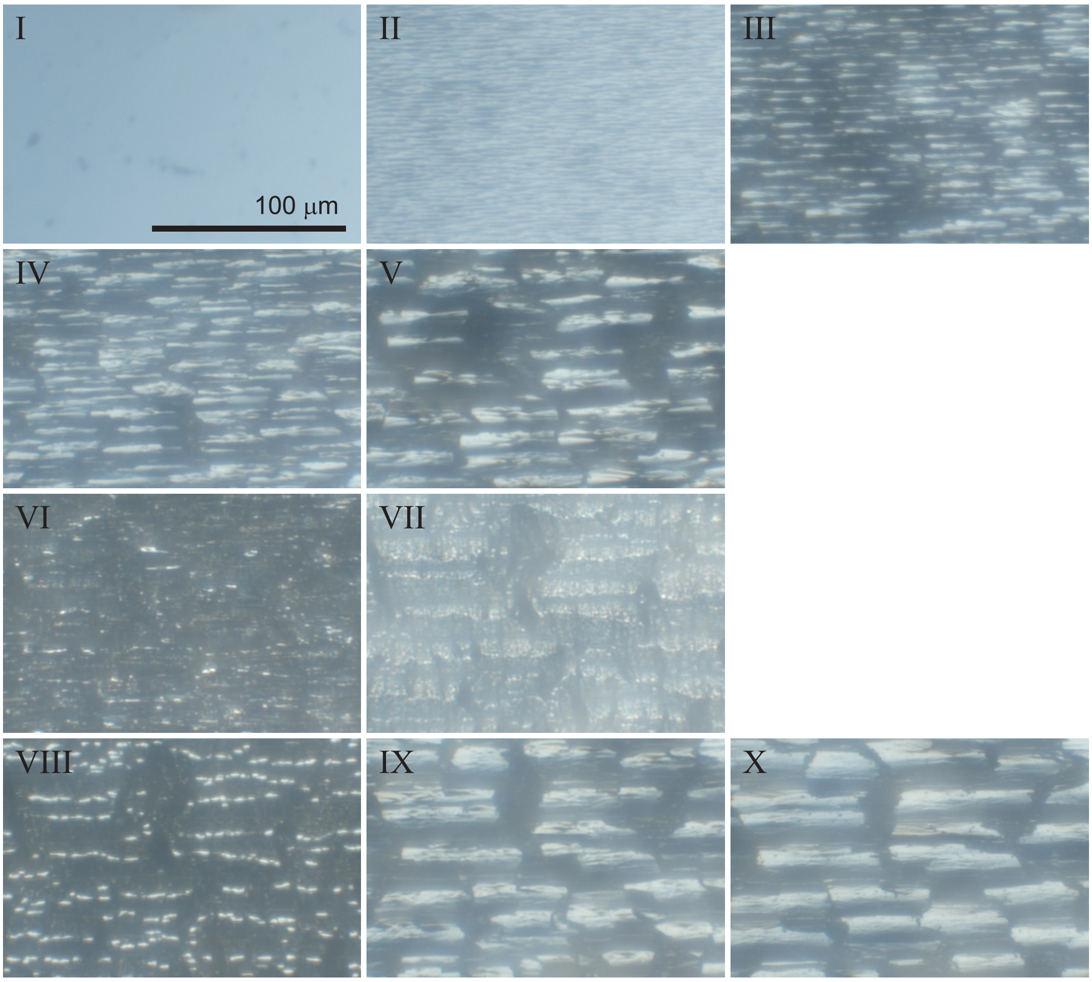

Figure 7.7: *Details of microscope observations of the morphology during the in situ etch experiments. Images I to V show the (110) morphology at OCP from a polished surface. Images VI and VII shows the morphology transition when a potential of -850 mV vs SCE was applied. Images VIII to X show the transition and evolution of the morphology after the potential was switched to -1250 mV vs SCE*

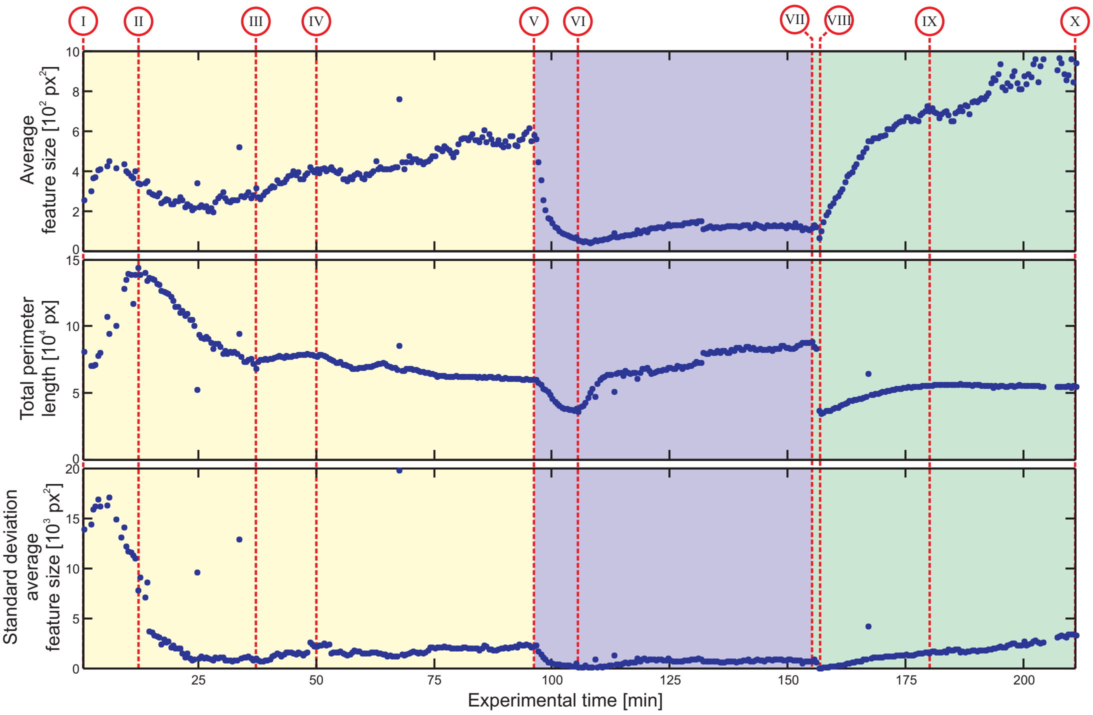

Figure 7.8: *Morphology parameters as a function of time obtained from image analysis. The three frames show the average feature surface area (top frame), total feature perimeter length (middle frame) and standard deviation in the feature size data (lower frame). Points I to X correspond to the microscopic images in figure 7.7. The background shadings indicate the applied potential (from left to right: OCP, -850, and -1250 mV vs SCE). The data points for which the image analysis was unreliable, i.e. due to the presence of gas bubbles in the image have been removed for clarity. The graphs clearly show the morphology evolution and the abrupt transitions due to a change in applied potential (at points V and VII).*

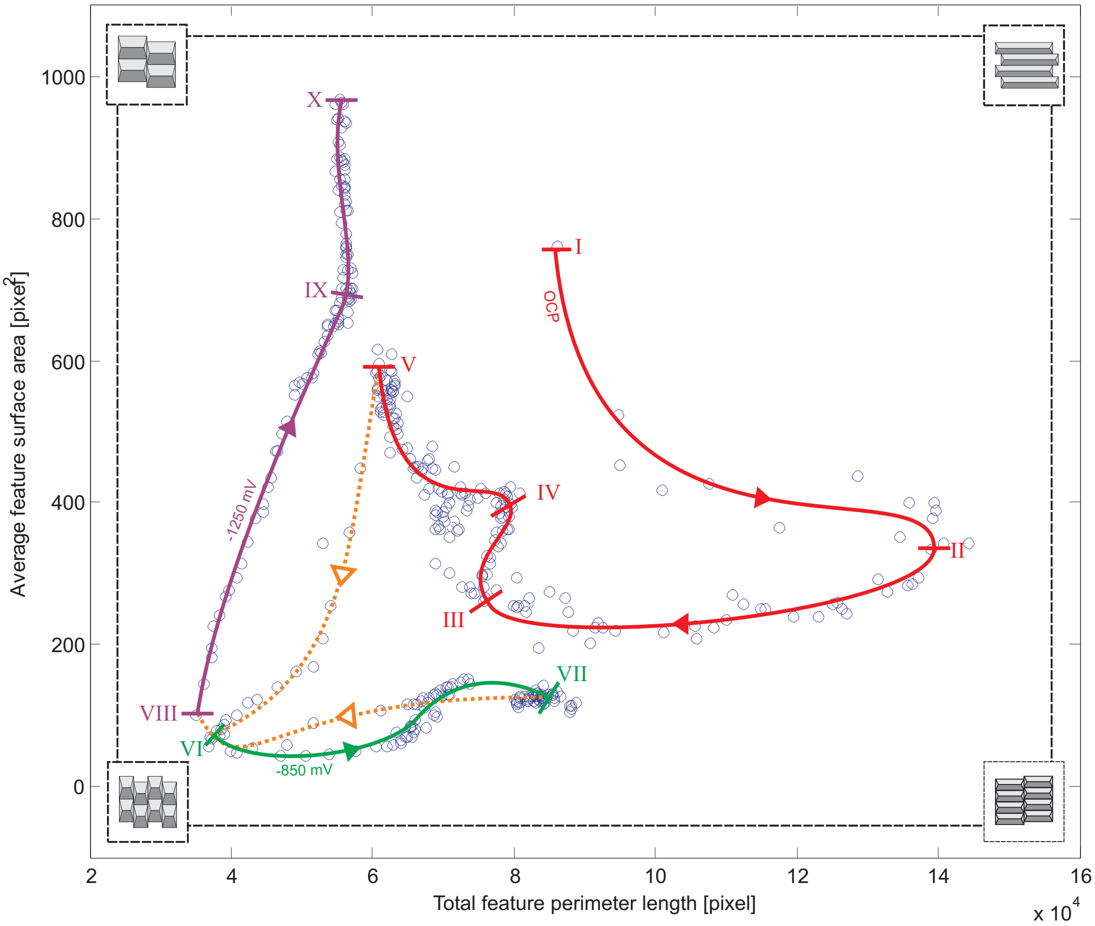

Figure 7.9: *Diagram showing the shape evolution during the in-situ experiment. Results from images I to X of figure 7.7 are indicated. The expected shapes corresponding to the different regions are shown at the corners. A large surface area together with a low perimeter length indicates large, square-like features, whereas larger lengths indicate elongated features. Smaller surface areas indicate smaller features. Solid lines represent morphology formation and evolution, while abrupt morphology transitions induced by changing the potential are represented with dashed lines.*

the relatively small size of the features compared to the resolution of the CCD camera, subtle variations in size and and shape cannot be resolved. Ex-situ SEM observations have shown that the surface becomes rougher and looses its roof-tile structure to a certain extent. This is consistent with both the kMC prediction by Gosalvez et al.[42] and the previous results described in chapter 3. In that chapter it was shown that at such positive applied potentials, step anisotropy reversal occurs. Under these conditions the dihydride terminated steps become more stable than the monohydride terminated steps on (111). Gosalvez et al. have shown that one of the requirements for the formation of a stable roof-tile structure is that monohydride terminated steps are the most stable step type. Step anisotropy reversal will therefore result in a decrease in roof-tile stability. The roughening of the surface is also consistent with the increase in isotropic electrochemical oxidation of terrace sites which will result in a higher terrace roughening [67]. From the ex-situ observations, a trapezoidal hillock morphology is expected under these conditions, which is not observed. Gosalvez et al. have stated that that one of the main requirements for stable hillocks is step anisotropy reversal which is present under these condition. A second requirement, however, is the stabilisation of the apex and ridges of the hillocks. The absence of hillocks might indicate that the specific characteristics of the experiments such as a constant liquid flow through the in-situ cell might prevent the second requirement from being met.

Morphology transition from -850 mV to -1250 mV vs SCE

Images VII to X mark the transition from -850 mV to an applied potential of -1250 mV. Both the analysis and the microscopic pictures show the abrupt transition after the potential step (images VII to VIII). After VIII, smaller roof tiles merge to become both larger and more elongated, ultimately forming the final morphology (IX onwards). While from IX to X the feature size continues to increase slowly, the shape remains relatively stable. It is interesting to note that the positions of the newly formed roof tiles are very similar to the ones observed on the morphology at V (see figure 7.7). This indicates that, while at -850 mV vs SCE (image VI to VII) the roof-tile stability decreases, the original roof-tile morphology does not disappear entirely. The residual roof-tile features serve as starting points for the morphology formation from VIII onwards. Additionally, it is interesting to note that the morphology evolution from IX to X seems similar that from IV to V. This indicates that the general shape of the roof tiles at OCP and at -1250 mV is similar. The main difference is the larger size of the features at -1250 mV (see figure 7.9).

macro-step peeling

The observations show that the (110) morphology is relatively stable. Both the feature size and position remain constant during etching. The optical observations also show the formation of macro steps at the ridges of many of the roof-tile structures. Continued etching of these steps results in a movement along the roof-tile faces towards the base and ends of the feature. These step patterns resemble ‘peeling’ of the roof tiles (outlined in figure 7.10). As described in previous sections, kMC simulations predict an etching mechanism which consists of step flow coupled with step bunching. The presence and direction of these macro steps is consistent with these mechanisms. What the peeling

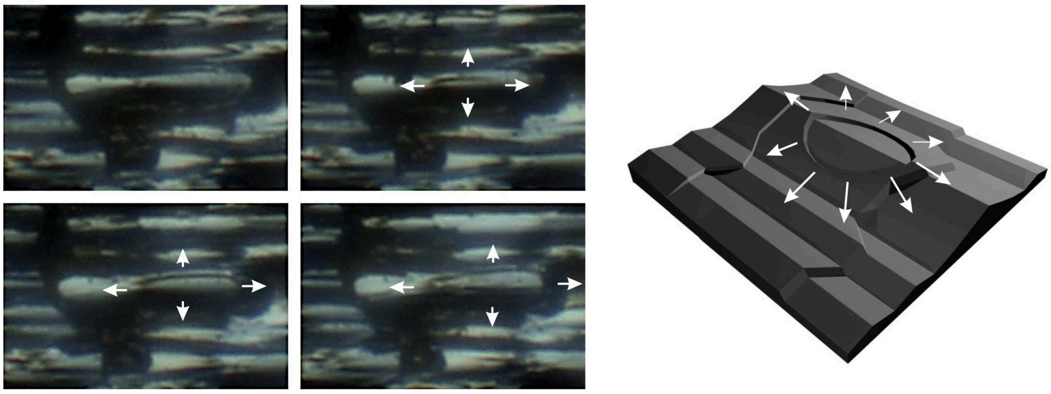

Figure 7.10: *Microscopic observation together with a graphical representation of the macro-step peeling phenomenon. The pictures on the left show the morphology evolution of the same surface within the span of several minutes. A macro-step pattern is observed originating from the ridges and moving along the (110) side planes in a peeling fashion. This is illustrated in the figure on the right.*

effect also indicates is the presence of a stepflow along the roof-tile structures parallel to the [110] direction, perpendicular to the stepflow direction predicted by Gosalvez et al. The results indicate that the morphology features at -1250 mV remains relatively stable after IX, only increasing in size. The analysis also shows that the morphology is very similar (although with larger features) to that observed at OCP. Examining the microscopic observations however shows that the macro-step peeling phenomenon which is observed at OCP is not visible during etching at -1250 mV. It is not clear if this is due to a decrease in the formation of these macro-steps or a decrease in step bunching. The latter can prevent steps from becoming large enough to become visible with this experimental method.

7.5 Conclusions

In this chapter, the etching of Si(110) surfaces in KOH solution was studied *in-situ* with an optical microscope and an electrochemical flow cell. The morphology could be analysed by using an image processing procedure which characterized the surface features in terms of the average size, the total perimeter length and the standard deviation of the size distribution.

The evolution of the characteristic (110) roof-tile morphology from a polished surface was initially examined under open-circuit conditions. Both the optical observations and image analysis showed the formation of small, elongated features which merge into the larger, characteristic roof-tile structures. After the initial nucleation and growth of the tiles, they remain relatively stable over time, in not only size and shape, but also in position on the surface. The optical observations also clearly show the formation and movement of macro steps at the ridges. The etching of these reactive steps resulted in a net displacement by ‘peeling’ along the roof-tile sides towards the base of the feature. This phenomenon is consistent with the macroscopic etch mechanism predicted by kMC simulations, which describes a step flow process in the same direction that is coupled with step bunching. The morphology changes observed on going to more positive applied potentials could be explained by step anisotropy reversal; the roof-tile morphology is destabilized by the change in the *relative* step stability of monohydride with respect to dihydride terminated steps.

The addition of low concentrations of hydrogen peroxide to the etchant solution, influences the steady-state morphology considerably. It was concluded that the additive oxidizes the (111) surface steps isotropically.

From the observations presented in this chapter, it is clear that the (110) surface morphology is complex and various parameters, such as the concentration of the KOH solution, the presence of an oxidizing agent (H_2O_2) and the application of a potential, all influence the morphology to a large extent. Although a detailed understanding of the effects of all these parameters was not obtained in the present work, considerable insight has been gained by analyzing the *in-situ* observations and comparing these results with kMC simulations from the literature. Nevertheless, additional work is clearly needed to fully understand the etching of (110) surfaces in alkaline solutions.

Chapter 8

Overall Conclusions and outlook

The main conclusions of the previous chapters are recapitulated in this chapter. In addition, several future challenges and possibilities for new or supplementary research, based on the observations and conclusions within this thesis, are outlined.

8.1 Overall conclusions

Within this thesis we have aimed to use the kinematic wave theory to both characterise and analyse anisotropic etching of silicon in alkaline solutions. With the stepflow/birth-and-spread mechanism as a basis, microscopic properties including step/kink velocity, terrace and step roughening can be directly obtained from experimental data using the basic model.

By measuring the surface etch rate, using a combination of micromachined wagon-wheel patterns and masked trench offset patterns, the influence of an applied potential on the etching of Si in concentrated KOH solutions was investigated. The analysis of the experimental data using the kinematic wave theory has shown an anisotropy in electrochemical surface oxidation between (100) and (111) which is consistent with the literature. More interestingly, an anisotropy in oxidation was additionally observed on (111) steps as a function of the applied potential. The results show that electrochemical oxidation favours the (111) dihydride terminated steps over (the more stable) monohydride terminated steps. This results in a change in step anisotropy at more positive potentials. At very anodic potentials the higher oxidation of dihydride terminated steps can eventually lead to a lower step velocity compared to the monohydride terminated steps. This is called step anisotropy reversal.

To investigate anisotropic etching in more detail, etch experiments on hemispherical Si samples have been performed which provides a wider range in surface orientations than wagon-wheel patterns. Detailed etch rate measurements show the presence of etch patterns which are not directly predicted by the basic model. By extending the basic model to a 10-parameter model which includes stepflow/birth-and-spread elements at the dihydride terminated steps, the hexagonal etch shape observed in the vicinity of (111) can be accurately described. Using the extended model, the (111) step velocity as a function of the step orientation was obtained from the measured data. The step velocity shows that (111) step anisotropy is not solely the result of the difference in the reactivity between mono- and dihydride terminated steps. It is necessary to distinguish between different dihydride types such as vertical or horizontal dihydrides and isolated dihydrides.

Examining the change in (111) step velocity as a result of to the addition TMA^+ has shown that, TMA^+ has a smaller impact on isolated dihydrides compared to (non-isolated) dihydrides at the dihydride terminated steps. TMA^+ interaction is therefore not only sensitive to the molecular structure of the steps (difference between mono- or dihydride) but also to the orientation (vertical or horizontal dihydrides) and the surrounding crystal structure (presence of nearest and next-nearest neighbours). The results also show that, unlike TMA^+, electrochemical oxidation due to an applied potential is the same on all dihydrides types.

The anisotropy in electrochemical oxidation of (111) steps surface sites can be used to investigate step site interaction. A proposed electrostatic interaction between TMA^+ with the (111) steps can then be investigated. Partially (electrochemical) oxidised steps are expected to show an enhanced electrostatic attraction due to the higher electronegativity. This should result in a disproportionate change in the (111) step anisotropy. Investigating the step velocity as a function of both the TMA^+ cation concentration and an applied potential have shown that both the TMA^+ and electrochemistry must be considered as independent processes. The absence of the expected change in step anisotropy indicates that the electrostatic interaction between TMA^+ and (111) step sites does not occur.

An etch pattern commonly observed on both the wagon-wheel patterns and hemispherical Si samples is a saddle point in anisotropic etch rate at the (110) orientation. Ex- and in-situ observations, together with kinetic Monte Carlo simulations in the literature indicate that the (110) etch process can be translated to a pseudo stepflow/birth-and-spread process on an imaginary smooth (110) surface. Integrating these processes using the single PBC direction (2-fold symmetry) within the kinematic wave theory results in a 14-parameter model which can successfully describe the observed saddle point at the (110). Successful use of this model have shown that the additional (110) mechanism also influences both (100) and (111) orientation. Changes are observed in the absolute parameter values associated with these orientations compared to the basic and the extended 10-parameter model.

The formation and evolution of (110) morphology during etching are investigated using in-situ optical microscopy under electrochemical controlled conditions. An image analysis procedure was used to characterise the (110) surface features. The observations shows the presence of a ‘peeling effect’ which is consistent with etch mechanism predicted by kMC and is also similar to the pseudo stepflow/birth-and-spread mechanism. The observed morphology changes as a result of an applied potentials are consistent with changes in (111) step anisotropy as the roof-tile morphology destabilises. This is a result of the change in relative step stability between mono- and dihydride terminated steps. Ex-situ observations of (110) morphology with increasing concentration of hydrogen peroxide (H_2O_2) have shown similar destabilisation of roof-tile features. The formation of a smoother surface and the absence of trapezoidal hillock features points to the fact that H_2O_2 oxidises (111) surface steps isotropically, in contrast to electrochemical oxidation via an applied potential.

8.2 Outlook

The ability to determine the (111) step velocity from anisotropic etch rates using the kinematic wave theory in combination with sample geometries such as hemispheres or wagon-wheel patterns allows for the investigation of (specific) step site reactions and interactions on a microscopic scale. Due to the complexity of the model used, the 14-parameter model in particular, it is important to compare the obtained (111) step velocities with actual measurements. Unfortunately, there are no straight-forward methods currently available to *directly* measure the step velocity at any arbitrary step orientation.

By using electrochemistry (by applying a external electrical potential), (111) step site interaction can be investigated. Many phenomena observed in this work can be studied in more detail using this method. Both the effects of TMA^+ and OH^- in a TMAH/KOH etchant mixture are worth further study in order to determine the (111) step site specific effects and interactions in more detail. These measurements can be expanded to include different organic or ionic additives such as isopropanol. Ideally the measured step velocity would be directly coupled to specific surface site reaction rates (such as isolated hydrides or vertical/horizontal dihydrides). This however requires a closer comparison between the orientation dependent step velocity, the molecular structure of the steps and the reaction kinetics (using kMC for example).

Electrochemical factors including hydrogen peroxide and applied potentials outlined in this thesis should also be studied in more detail. Additional measurements using hemispherical Si samples can show the expected isotropy in electrochemical oxidation using H_2O_2. These studies can also confirm the fact that an applied potential shows no preference toward different dihydrides. For these measurements however, the issues related to the potential drop created by an anodic current will have to be solved in order to obtain reliable measurements at very positive applied potentials. Other electrochemical factors of interest include dissolved oxygen and metals commonly used in MEMS technology.

The in-situ measurements have provided both an abundance of information and additional questions. The method, which has proven successful in observing (110), is worth expanding to different surface orientations such as (100) and (111). Additional physical parameters such as the etchant composition and flowrate can be examined in-situ. Closer investigation of observed phenomena such as prologued hydrogen bubble adhesion, can provide additional insight into the etching process.

Although, currently very dependent on the experimental data, successful use of the 14-parameter model can provide insight into the (110) morphology. Additional measurements are necessary to insure that the (110) parameters correctly reflect the observed anisotropic etch rate and morphology. With a link between the model parameters and phenomena such as morphology roof-tile shape and density, the model can then be used for reliable characterisation of (110).

Appendix A

Construction of etch model based on kinematic wave theory

This appendix shows diagrams which outlines the construction and modification of the etch model based on the kinematic wave theory. These diagrams are a convenient way to visualise the different model elements and the assembly of these elements[104] to form the final model. Each element is outlined in a single block. The way the blocks are connected describes the particular interaction type used in the assembly of the individual blocks (i.e. parallel or serial interaction). The interaction parameter a is given in the top left corner of each assembly.

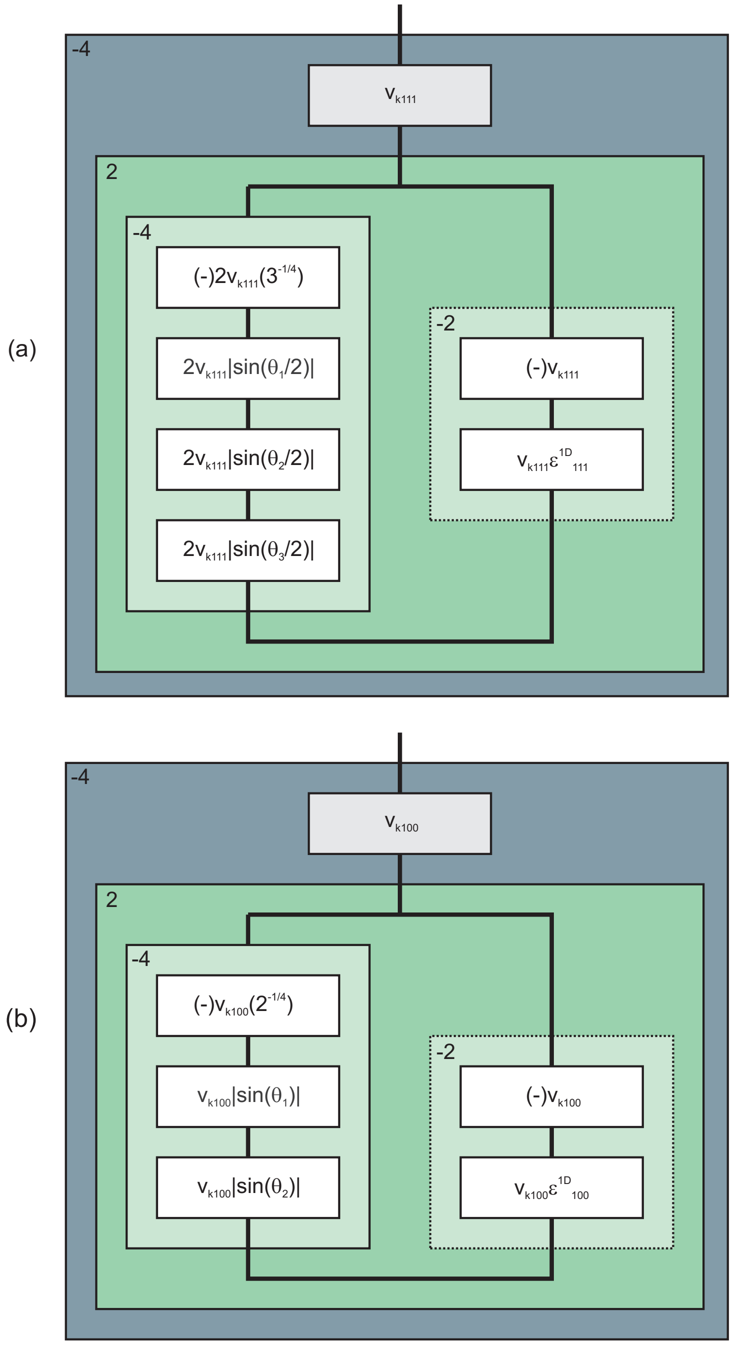

Figure A.1: *Graphical illustration outlining the construction of the step anisotropy element for both (111) (a) and (100) (b) from individual stepflow (left tree) and birth-and-spread element (right tree). Note that the birth-and-spread element is the same as equation 2.2 but written as a network assembly. An inverted element is denoted with (-).*

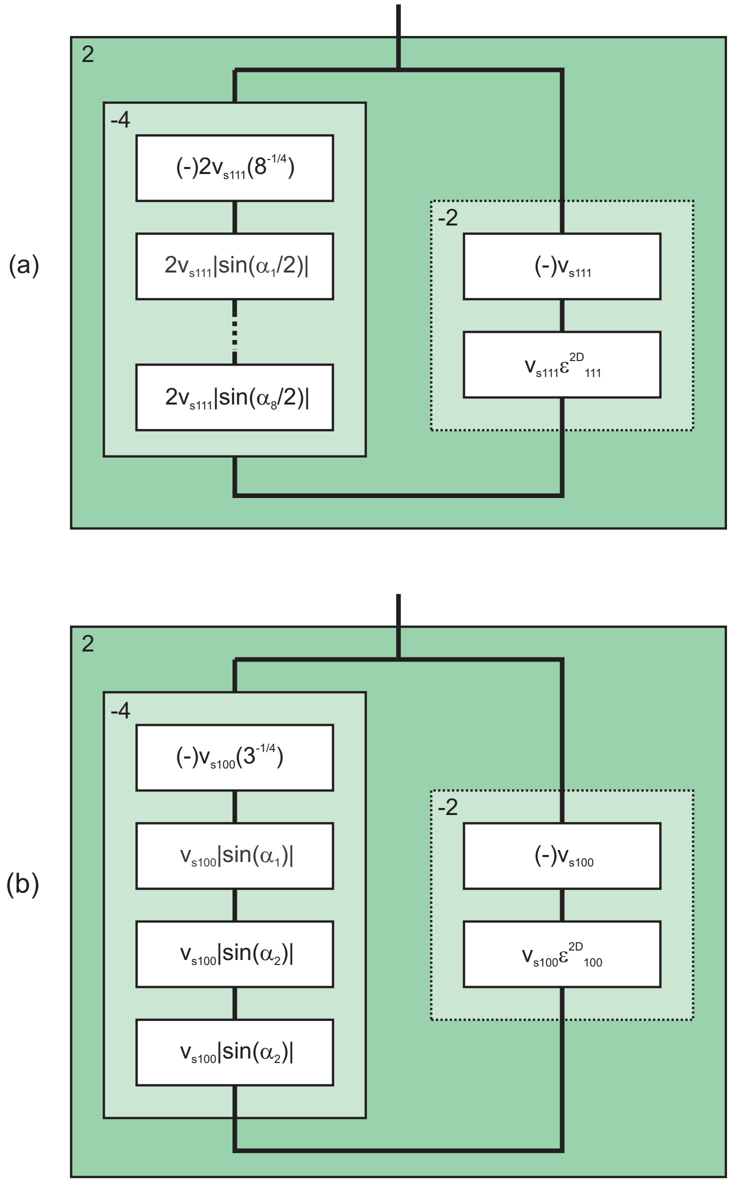

Figure A.2: *Graphical illustration outlining the construction of the surface anisotropy element for both (111) (a) and (100) (b) from individual stepflow (left tree) and birth-and-spread element (right tree). Note that the birth-and-spread elements is the same as equation 2.2 but written as an network assembly. An inverted element is denoted with (-). For the (111) surface anisotropy a total of 8 step anisotropy elements are assembled while for (100) surface anisotropy only 3 elements are used*

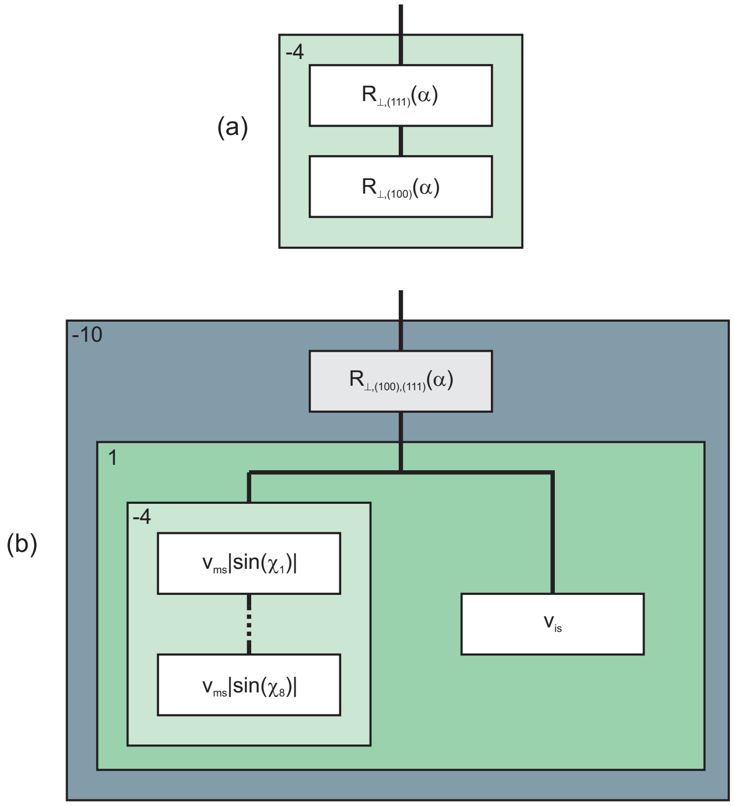

Figure A.3: *Graphical illustration outlining the construction the total anisotropic etch rate function. (a) Assembly of the (111) surface anisotropy element and the (100) surface anisotropy element results in the basic 6-parameter model. (b) outlines the integration of the (110) phenomenological elements including the eight (110) macro-step elements (left tree) and the single (110) isotropic element (right tree).*

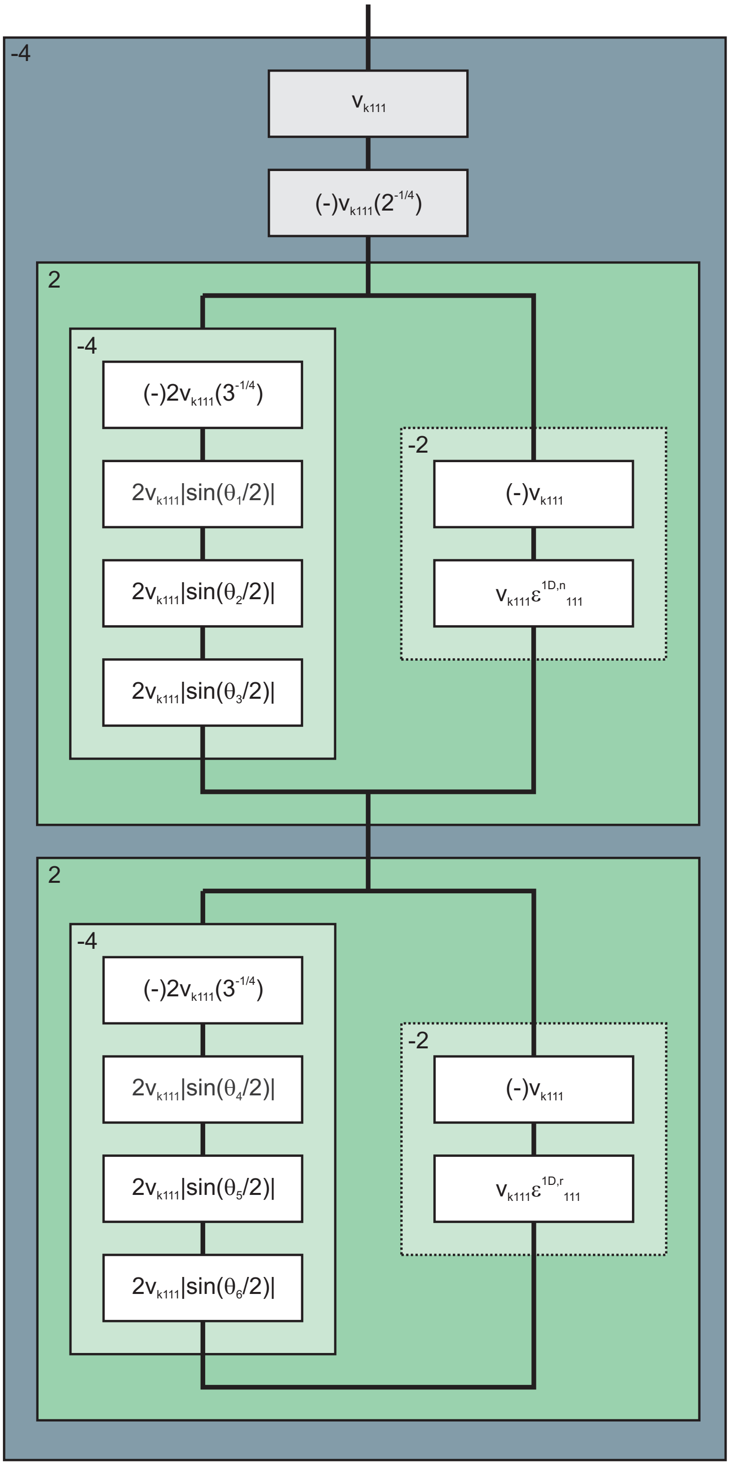

Figure A.4: *Figure illustrating the extended model for (111) steps. The top elements are the existing (111) step velocity elements, while the bottom elements are the new step velocity elements corresponding to the dihydride terminated step.*

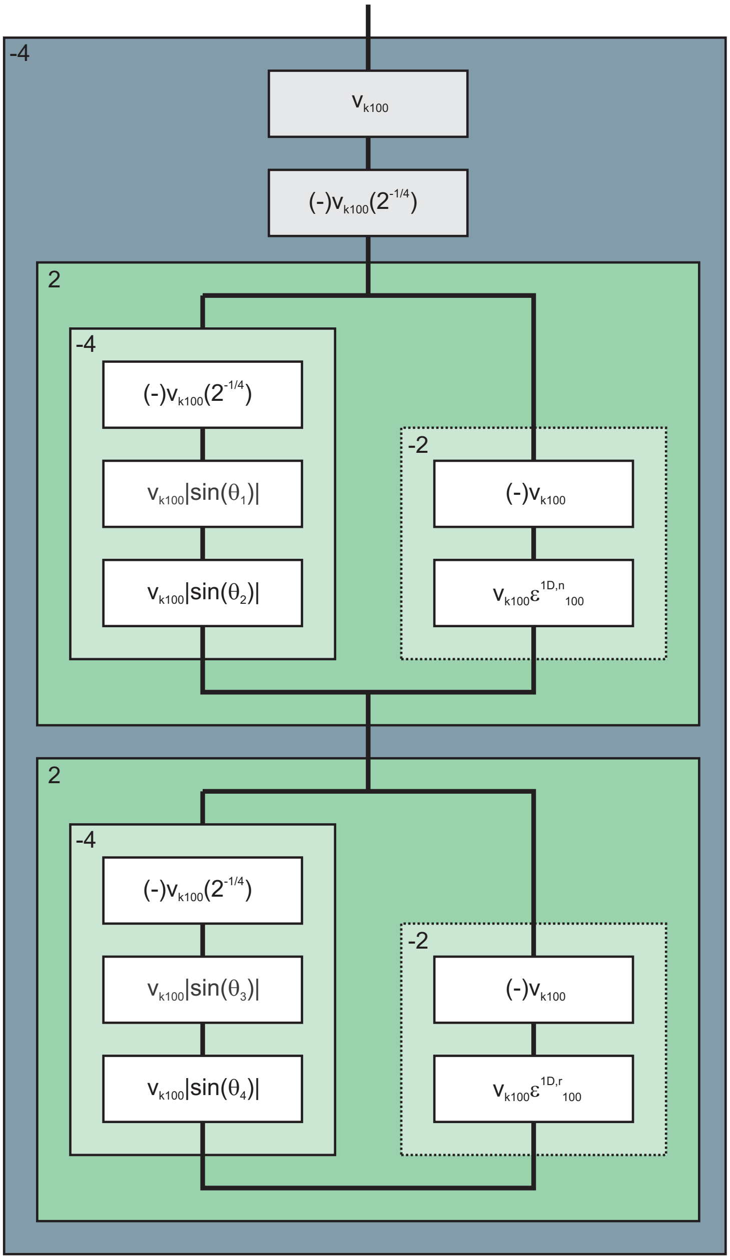

Figure A.5: *Figure illustrating the extended model for (100) steps. The top elements are the existing (100) step velocity elements.*

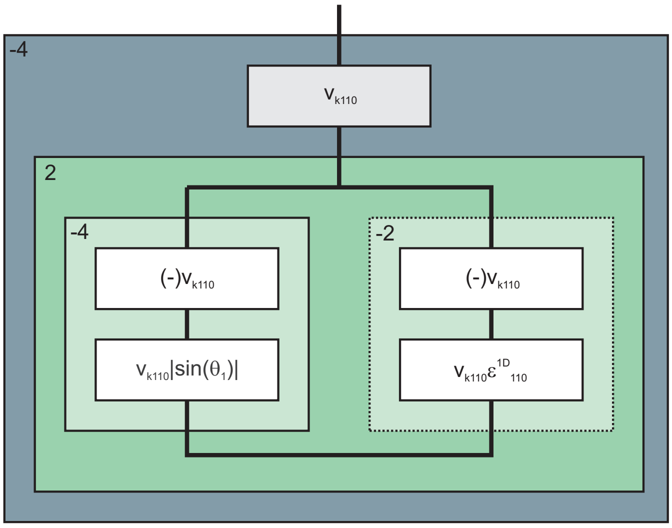

(b)

Figure A.6: *Graphical illustration outlining the construction of the step anisotropy element for (110) steps. Note that with a single (symmetrical) PBC, only a single step flow element (left tree) is defined.*

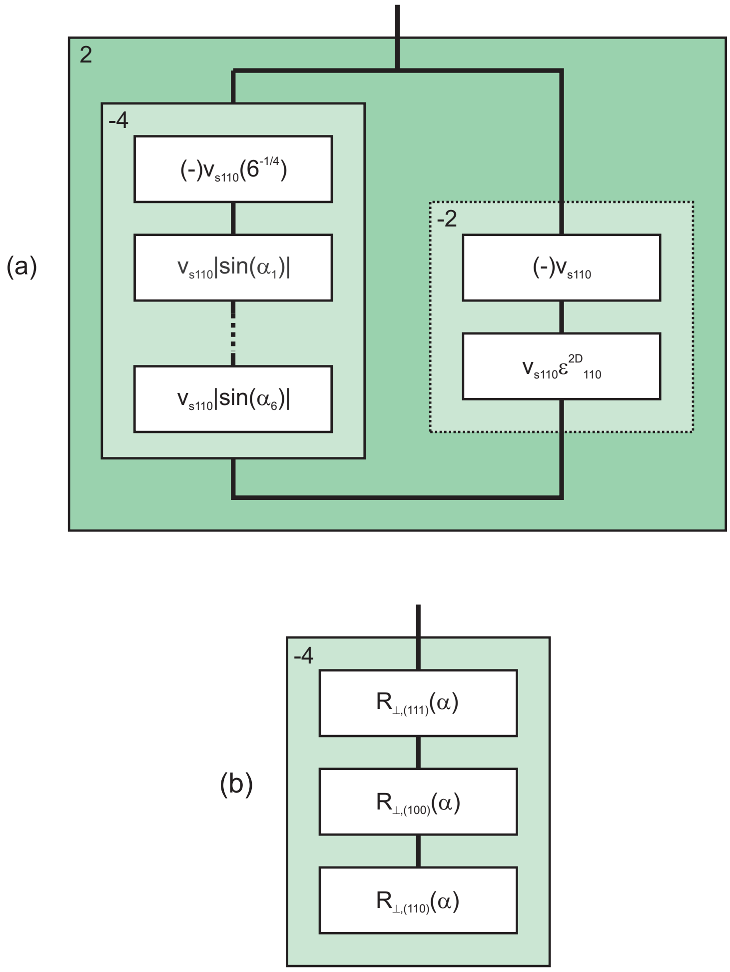

Figure A.7: *Graphical illustration outlining the construction of the surface anisotropy element for (110) steps (a). Note that a total of six step flow elements are assembled in the left tree. The final (110) surface anisotropy element is assembled into the etch function using a parallel interaction mechanism (b)*

Appendix B

Prolonged hydrogen bubble adhesion

One of the practical problems when using the in-situ setup, as described in chapter 7, is the constant hydrogen formation during etching. The flow speed of the cell is generally set to such a velocity so that the average residence time of a growing hydrogen bubble in the microscope optical path is less than 30 sec. This is to ensure that the images taken every 30 sec. are as free of bubbles as possible. Additional in-situ observations however have shown some profound effects of *prolonged* hydrogen bubble adhesion on the Si surface.

From figure B.1 it is clear that a hydrogen bubble on the surface influences the etch characteristic of the surface underneath. After the bubble is detached, a circular pattern is observed at at the former position of the bubble. These patterns are similar to the bubble imprints outlined by Hais et al.[43]. A decrease in etch rate and increase in surface roughness under these conditions has been attributed to local 'shielding' of the surface by the attached hydrogen bubbles[12, 11, 20, 43]. This shielding depends on both the bubble size and contact angle. The observed increase in etch rate is, however, counterintuitive. Haiss et al. have attributed this increase to a higher KOH concentration in the diffusion layer which surrounds the hydrogen bubble. They have observed both a decrease underneath the bubble (due to shielding) and an increase in the vicinity of the solid|liquid|gas junction (contact area between the diffusion layer and the Si surface).

Closer examination of the hemispherical samples used in chapter 6 have shown similar effects underneath the mounting rods (see figure B.2). Note that this is an extreme case where bubbles are physically trapped during a long etch time (up to 4 hours). Examining the samples indicates that the hydrogen bubble adhesion results in an decrease in etch rate when etching in KOH. An increase is, however, observed on samples etched in KOH/TMAH mixture. As with IPA[11], TMA^+ is a surfactant which decreases the surface tension. This results in a decrease in contact angle between the Si and hydrogen bubble. This should, in turn, result in a larger contact area between the Si surface and the diffusion layer where the etch rate increases[43]. The fact that the bubbles are physically trapped in the same situation for a long etching time will then result in the (measurable) etch rate differences.

It is important to emphasize the fact that these are side observations in experiments which are designed for different purposes. The in-situ observations, however, clearly shows a direct correlation between the formation, growth and adhesion of a hydrogen bubble and the resulting bubble-imprint patterns. The effects observed here are worth

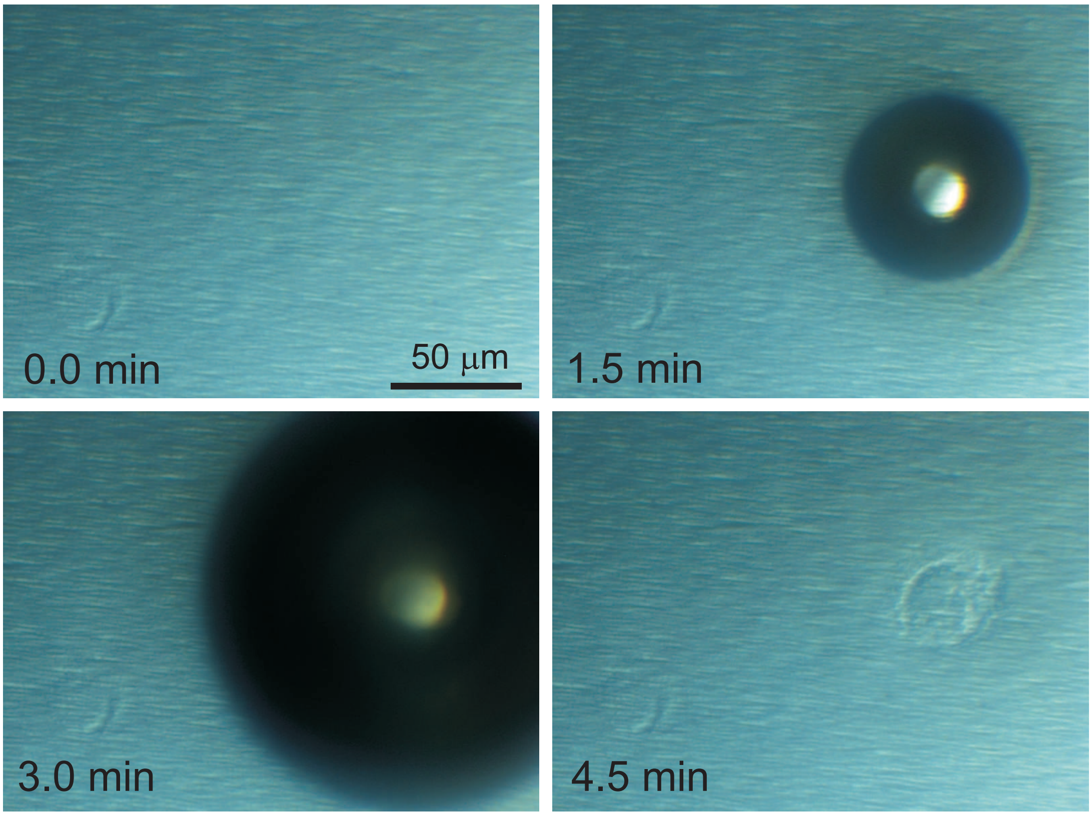

Figure B.1: *Microscope images illustrating the effect of prolonged bubble adhesion. These in-situ images show the formation and growth of a hydrogen bubble on the surface. After the bubble has detached from the surface, a 'bubble imprint' is clearly observed.*

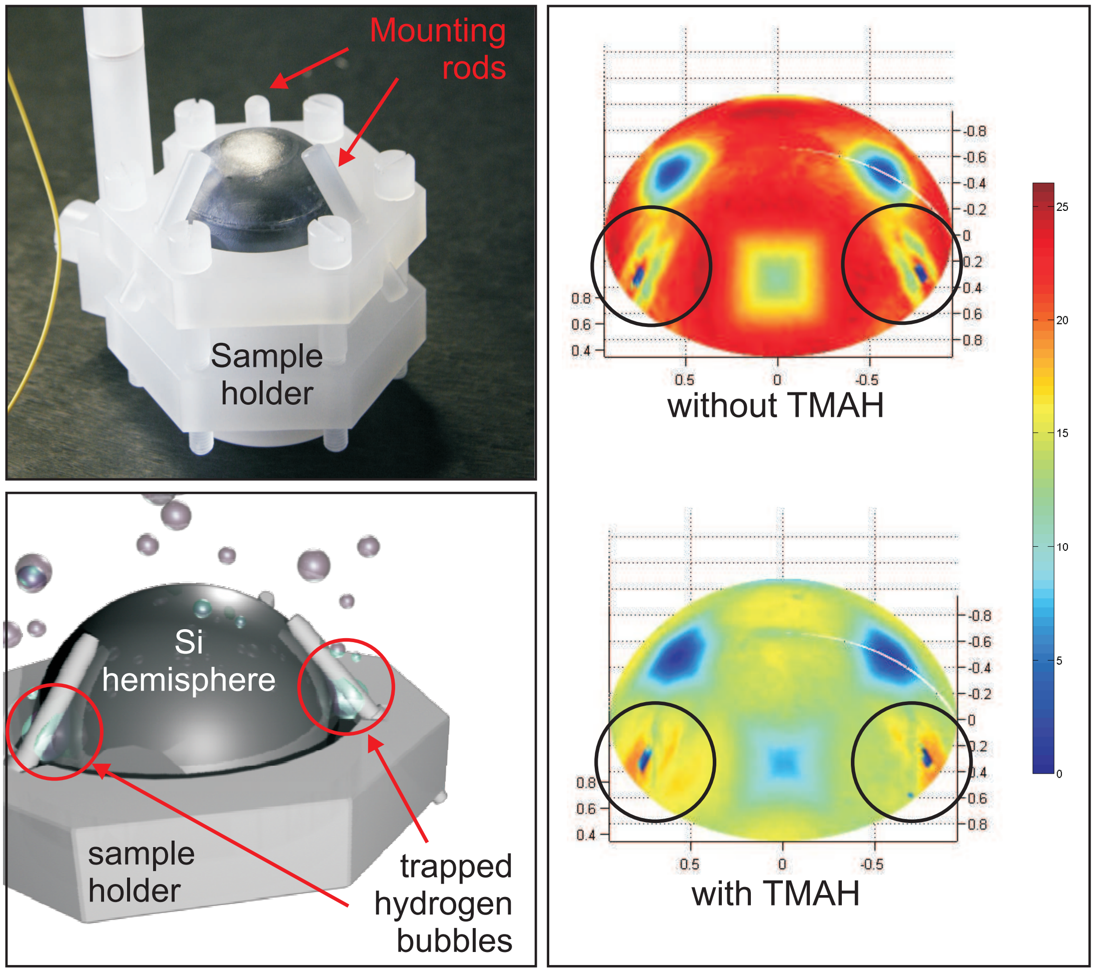

Figure B.2: *The effect of a trapped hydrogen bubble on the local etch rate is shown in this figure. The upper left picture shows an etched hemispherical sample mounted inside the Kel-F sample holder as was used for experiments in chapter 6. The bottom left figure illustrates the trapped hydrogen bubbles underneath the mounting rods. The figures on the right show the etch rate measurement of two samples. Both these were etched at 50° C and an applied potential of -1250 mV vs SCE for a duration of 4 hours. The top figure shows the result of the sample etched in a 5.0 mol/l* OH^-. *The bottom sample was etched in a 5.0 mol/l* OH^- *and 1.0 mol/l* TMA^+ *mixture. The position of the mounting rods are highlighted in the figures. Note that no etching occurs where the mounting rods make actual contact with the silicon. It is clear that without TMAH, the etch rate in the direct vicinity of the mounting rods is lower then the surrounding area. In the presence of* TMA^+, *the opposite is observed as the etch rate here is higher.*

examining in closer detail with sample geometries and experiments specifically designed for this purpose.

Appendix C

In-situ observations of a masked wagon-wheel pattern

In the past, various methods have been used to measure etch rates for the wet chemical etching of silicon in alkaline solutions. In chapter 3 this has been briefly discussed, including the masked wagon-wheel pattern[27, 84, 89] and the convex pre-etched wagon-wheel pattern. Seidel et al.[84] have used wagon-wheel mask patterns to study the etch rate of a wide range[106, 107] (see figure 3.3 in chapter 3). Various groups have shown that the chemical etch rate of silicon in alkaline solution can be influenced by applying an electrochemical potential to the substrate[112]. Maskless wagon-wheel patterns have also been used go investigate the anisotropy in anodic oxidation in more detail (see chapter 3). For macroscopic silicon surfaces, such an anisotropy has been observed (see section 1.4). The measurements have shown that this anisotropy is also present in the electrochemical oxidation of surface steps.

Preliminary in-situ measurements using samples with a design identical to the ones used in chapter 3 have shown that the complex etch shape is difficult to observe. Therefore, the sample design was adapted. A silicon nitride mask layer, which prevents the etching of the top surface, was deposited (see figure C.2). During the experiments, the focal plane of the microscope remained at the mask layer, which made the visualisation unambiguous. In essence, this sample geometry is a combination of both Seidel's and Wind's designs. In this appendix we show that one can monitor the mask under etch for such a sample design.

Figure C.1 shows several microscope images under etching conditions, i.e. in-situ. In the images, the nitride layer on top of the Si appears purple. When the Si underneath is removed, the nitride layer takes on a green colour (compare figures C.1a and C.1b). During etching, hydrogen gas is produced, the amount of which is related to the Si dissolution rate, i.e. it depends strongly on the crystallographic orientation of the sidewalls. For the fast-etching orientations, a considerable gas production is visible (see figure C.1a).

Although the underetch is clearly visible (see figure C.1c), these observations cannot be used for etch-rate measurements. Figure C.2 shows a schematic representation of the etch shape for both a masked and maskless wagon wheel. As Wind et al. have shown, the actual sidewall etch rate of a maskless wagon wheel is related to the wedge-point retraction length. A masked wagon-wheel pattern forms a different etch shape. Due to

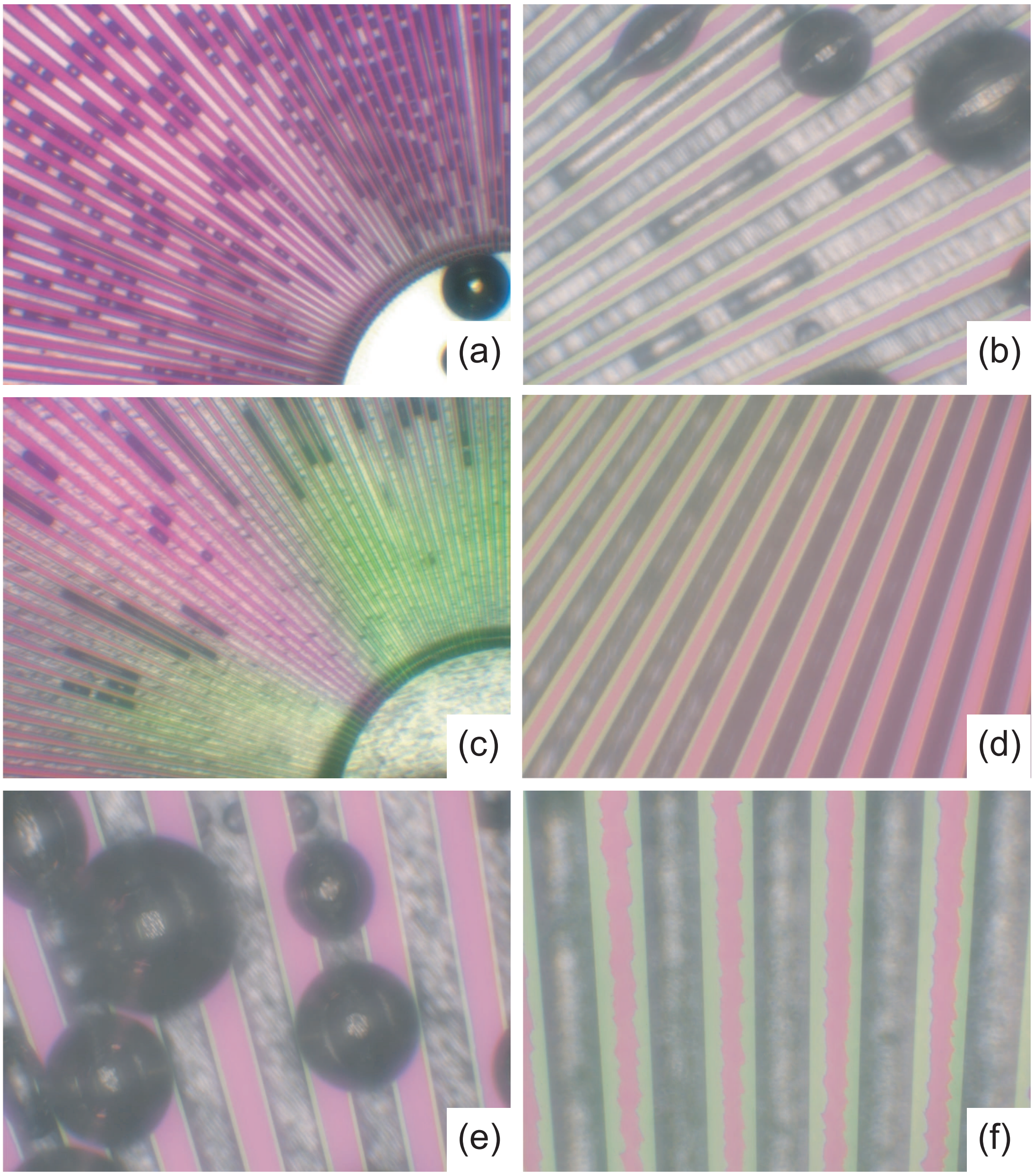

Figure C.1: *In-situ monitoring of the etching of a wagon-wheel structure. Additional comments on the various observations can be found in the text.*

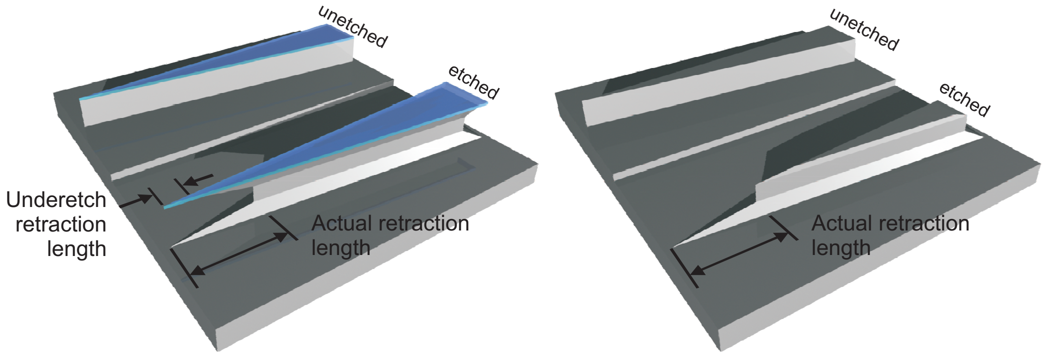

Figure C.2: *Graphical illustration outlining different etch shapes of a conventional wagon-wheel pattern(right) and a mask wagon-wheel pattern(left). An unetched and etched wedge is shown for both patterns. It is clear that the etching a masked wedge will result in a different etch shape. The actual retraction length (which is related to the etch rate of the sidewalls) does not correspond with the underetch retraction length underneath the mask. When examining these wedges from the top, the etch rate cannot be determined as the the actual retraction length is obscured by the top of the wedge.*

the presence of a mask layer on top of the wedge, the geometry of an etched wedge is different (compare figures C.2a and b). As these patterns are observed from the top, only the under-etch retraction is visible, which does not necessarily correspond to the actual retraction length.

For near-(111) orientations, the observed underetch corresponds to the actual surface etch rate of the side walls. Additionally, gas bubble production is far less. Therefore in-situ experiments should be possible with less bubble 'interference'. Therefore, it should be possible to use a design containing only near-(111) wedges to investigate in-situ the under etch under various process conditions, such as externally applied potential, the presence of additives or the dependence of the etch rate on the etching time. These samples will then be very similar to the trench offset samples as used in chapter 3.

References

[1] P. Abgrall and A. Gue. Lab-on-chip technologies: making a microfluidic network and coupling it into a complete microsystem - a review. *J. Micromech. Microeng.*, 17:R15–R49, 2007.

[2] P. Allongue, V. Bertagna, V. Kieling, and H. Gerischer. Probing by in-situ scanning-tunneling-microscopy the influence of an organic additive on si etching in NaOH. *Journal of Vacuum Science & Technology B*, 12(3):1539–1542, May 1994.

[3] P. Allongue, V. CostaKieling, and H. Gerischer. Etching of silicon in NaOH solutions .1. insitu scanning tunneling microscopic investigation of n-Si(111). *J. Electrochem. Soc.*, 140(4):1009–1018, Apr. 1993.

[4] P. Allongue, V. CostaKieling, and H. Gerischer. Etching of silicon in NaOH solutions .2. electrochemical studies of n-Si(111) and n-Si(100) and mechanism of the dissolution. *J. Electrochem. Soc.*, 140(4):1018–1026, Apr. 1993.

[5] P. Allongue, V. Kieling, and H. Gerischer. Atomic-structure of Si surfaces etched in Triton/NaOH solutions. *J. Phys. Chem.*, 99(23):9472–9478, June 1995.

[6] J. Appelbaum, G. Baraff, and D. Hamann. The Si (100) surface. III. surface reconstruction. *Phys. Rev. B: Condens. Matter Mater. Phys.*, 14:588–601, 1976.

[7] N. Austin and J. Prendergast. Use of kinematic wave theory to model irrigation on cracking soil. *Irrigation Sci.*, 18:1–10, 1997.

[8] Y. Backlund and L. Rosengren. New shapes in (100) Si using KOH and EDP etches. *J. Micromech. Microeng.*, 2:75–79, Sept. 1992.

[9] E. Bassous and E. Baran. Fabrication of high precision nozzles by anisotropic etching of (100) silicon. *J. Electrochem. Soc.*, 125:1321–1327, 1978.

[10] E. Bassous, H. Taub, and L. Kuhn. Ink jet printing nozzle arrays etched in silicon. *Appl. Phys. Lett.*, 31:135–137, 1977.

[11] T. Baum, J. Satherley, and D. Schiffrin. Contact angle, gas bubble detachment, and surface roughness in the anisotropic dissolution of Si(100) in aqueous KOH. *Langmuir*, 14(10):2925–2928, May 1998.

[12] T. Baum and D. Schiffrin. AFM study of surface finish improvement by ultrasound in the anisotropic etching of Si<100> in KOH for micromachining applications. *J. Micromech. Microeng.*, 7(4):338–342, Dec. 1997.

[13] T. Baum and D. Schiffrin. Kinetic isotopic effects in the anisotropic etching of p-Si(100) in alkaline solutions. *J. Electroanal. Chem.*, 436(1-2):239–244, Oct. 1997.

[14] P. Bennema, H. Meekes, S. Boerrigter, H. Cuppen, M. Deij, J. van Eupen, P. Verwer, and E. Vlieg. Crystal growth and morphology: New developments in an integrated Hartman-Perdok-connected net-roughening transition theory, supported by computer simulations. *Cryst. Growth Des.*, 4:905–913, 2004.

[15] F. Bensliman, Y. Sawada, K. Tsujino, and M. Matsumura. Oxidation of atomically flat and hydrogen-terminated Si(111) surface by hydrogen peroxide. *J. Electrochem. Soc.*, 154:F102–F105, 2007.

[16] J. Bonar, R. Childs, and R. Laming. Advancements in passive planar lightwave circuits and hybrid integration devices. *C. R. Phys.*, 4:51–64, 2003.

[17] P. Bressers, J. Kelly, J. Gardeniers, and M. Elwenspoek. Surface morphology of p-type (100) silicon etched in aqueous alkaline solution. *J. Electrochem. Soc.*, 143(5):1744–1750, May 1996.

[18] P. Bressers, S. Pagano, and J. Kelly. Ferricyanide reduction as a probe for the surface-chemistry of silicon in aqueous alkaline-solutions. *J. Electroanal. Chem.*, 391(1-2):159–168, July 1995.

[19] W. Burton, N. Cabrera, and F. Frank. The growth of crystals and the equilibrium structure of their surfaces. *Philos. Trans. R. Soc. London, Ser. A*, 243(866):299–358, 1951.

[20] S. Campbell, K. Cooper, L. Dixon, R. Earwaker, S. Port, and D. Schiffrin. Inhibition of pyramid formation in the etching of Si p[100] in aqueous potassium hydroxide-isopropanol. *J. Micromech. Microeng.*, 5(3):209–218, Sept. 1995.

[21] D. Cheng, M. Gosalvez, T. Hori, K. Sato, and M. Shikida. Improvement in smoothness of anisotropically etched silicon surfaces: Effects of surfactant and TMAH concentrations. *Sens. Actuators, A*, 125(2):415–421, Jan. 2006.

[22] D. Cheng, M. Gosalvez, M. Shikida, and K. Sato. A universal parameter for silicon anisotropic etching inalkaline solutions. In *19th IEEE International Conference on Micro Electro Mechanical Systems, 2006. MEMS 2006 Istanbul.*, 2006.

[23] E. Conway and V. Cunnane. Electrochemical characterization of si in tetra-methyl ammonium hydroxide (TMAH) and tmah:Triton-X-100 solutions under white light effects. *J. Micromech. Microeng.*, 12(2):136–148, Mar. 2002.

[24] H. de Bree, P. Leussink, T. Korthorst, H. Jansen, T. Lammerink, and M. Elwenspoek. The μ-flown: a novel device for measuring acoustic flows. *Sens. Actuators, A*, 54:552–557, 1996.

[25] P. Dumas, Y. Chabal, and P. Jakob. Morphology of hydrogen-terminated Si(111) and Si(100) surfaces upon etching in HF and buffered-HF solutions. *Surf. Sci.*, 270:867–878, May 1992.

[26] Z. Elalamy, L. Landsberger, M. Kahrizi, A. Pandy, I. Stateikina, and S. Michel. Modelling of anisotropic etching of silicon: Anomalies due to facet boundary effects. *Sensor. Mater.*, 15(2):67–81, 2003.

[27] Z. Elalamy, L. Landsberger, A. Pandy, M. Kahrizi, I. Stateikina, and S. Michel. Anomalies in modeling of anisotropic etching of silicon: Facet boundary effects. *Journal of Vacuum Science & Technology A-Vacuum Surfaces and Films*, 20(6):1927–1933, Nov. 2002.

[28] M. Elwenspoek and H. Jansen. *Silicon Micromachining, Cambridge Studies in Semiconductor Physics and Microelectronic Engineering.* Number 7. Cambridge University Press, Cambridge, Cambridge, 1998.

[29] J. Flidr, Y. Huang, and M. Hines. An atomistic mechanism for the production of two- and three-dimensional etch hillocks on Si(111) surfaces. *J. Chem. Phys.*, 111(15):6970–6981, Oct. 1999.

[30] J. Flidr, Y. Huang, T. Newton, and M. Hines. The formation of etch hillocks during step-flow etching of Si(111). *Chem. Phys. Lett.*, 302(1-2):85–90, Mar. 1999.

[31] F. Frank. *Growth and Perfection of Crystals.* Wiley, New York, New York, 1958.

[32] S. Garcia, H. Bao, and M. Hines. Effects of diffusional processes on crystal etching: Kinematic theory extended to two dimensions. *J. Phys. Chem. B*, 108(19):6062–6071, May 2004.

[33] S. Garcia, H. Bao, M. Manimaran, and M. Hines. Measuring the site-specific reactivity of impurities: The pronounced effect of dissolved oxygen on silicon etching. *J. Phys. Chem. B*, 106(33):8258–8264, Aug. 2002.

[34] H. Gardeniers, R. Luttge, E. Berenschot, M. de Boer, S. Yeshurun, M. Hefetz, R. van't Oever, and A. van den Berg. Silicon micromachined hollow microneedles for transdermal liquid transport. *J. Microelectromech. S.*, 12:855–862, 2003.

[35] H. Gatos. Semiconductor electronics and the birth of the modern science of surfaces. *Surf. Sci.*, 300:1–23, 1994.

[36] M. Gosalvez, D. Cheng, R. Nieminen, and K. Sato. Apparent activation energy during surface evolution by step formation and flow. *New J. Phys.*, 8:–, Nov. 2006.

[37] M. Gosalvez, A. Foster, and R. Nieminen. Atomistic simulations of surface coverage effects in anisotropic wet chemical etching of crystalline silicon. *Appl. Surf. Sci.*, 202(3-4):160–182, Dec. 2002.

[38] M. Gosalvez, A. Foster, and R. Nieminen. Dependence of the anisotropy of wet chemical etching of silicon on the amount of surface coverage by OH radicals. *Sensor. Mater.*, 15(2):53–65, 2003.

[39] M. Gosalvez and R. Nieminen. Surface morphology during anisotropic wet chemical etching of crystalline silicon. *New J. Phys.*, 5:–, July 2003.

[40] M. Gosalvez, R. Nieminen, P. Kilpinen, E. Haimi, and V. Lindroos. Anisotropic wet chemical etching of crystalline silicon: atomistic monte-carlo simulations and experiments. *Appl. Surf. Sci.*, 178(1-4):7–26, July 2001.

[41] M. Gosalvez, K. Sato, A. Foster, R. Nieminen, and H. Tanaka. An atomistic introduction to anisotropic etching. *J. Micromech. Microeng.*, 17:S1–S26, 2007.

[42] M. Gosalvez, Y. Xing, T. Hynninen, H. Uwaha, A. Foster, R. Nieminen, and K. Sato. Faster simulations of step bunching during anisotropic etching: formation of zigzag structures on Si(110). *J. Micromech. Microeng.*, 17:S27–S37, Mar. 2007.

[43] W. Haiss, P. Raisch, L. Bitsch, R. Nichols, X. Xia, J. Kelly, and D. Schiffrin. Surface termination and hydrogen bubble surfaces during anisotropic dissolution adhesion on Si(100) in aqueous KOH. *J. Electroanal. Chem.*, 597(1):1–12, Nov. 2006.

[44] J. Haneveld, H. Jansen, E. Berenschot, N. Tas, and M. Elwenspoek. Wet anisotropic etching for fluidic 1D nanochannels. *J. Micromech. Microeng.*, 13:S62–S66, 2003.

[45] P. Hartman and W. Perdok. On the relations between structure and morphology of crystals .2. *Acta.Cryst.*, 8(9):521–524, 1955.

[46] P. Hartman and W. Perdok. On the relations between structure and morphology of crystals .3. *Acta.Cryst.*, 8(9):525–529, 1955.

[47] A. Hein, S. Finkbeiner, J. Marek, and E. Obermeier. The effects of thermal treatment on the anisotropic etching behavior of Cz- and Fz-silicon. *Sens. Actuators, A*, 86(1-2):86–90, Oct. 2000.

[48] W. Hillig. A derivation of classical 2-dimensional nucleation kinetics and associated crystal growth laws. *Acta Metall.*, 14(12):1868–&, 1966.

[49] M. Hines. The picture tells the story: using surface morphology to probe chemical etching reactions. *Int. Rev. Phys. Chem.*, 20(4):645–672, Oct. 2001.

[50] M. Hines. In search of perfection: Understanding the highly defect-selective chemistry of anisotropic etching. *Annu. Rev. Phys. Chem.*, 54:29–56, 2003.

[51] M. Hines, Y. Chabal, T. Harris, and A. Harris. Measuring the structure of etched silicon surfaces with Raman-spectroscopy. *J. Chem. Phys.*, 101(9):8055–8072, Nov. 1994.

[52] Y. Huang, J. Flidr, T. Newton, and M. Hines. Effects of dynamic step-step repulsion and autocatalysis on the morphology of etched Si(111) surfaces. *Phys. Rev. Lett.*, 80(20):4462–4465, May 1998.

[53] R. Huber, J. Conrad, L. Schmitt, K. Hecker, J. Scheurer, and M. Weber. Fabrication of multilevel silicon structures by anisotropic deep silicon etching. *Microelectron. Eng.*, 67-8:410–416, June 2003.

[54] P. Jakob, Y. Chabal, K. Raghavachari, R. Becker, and A. Becker. Kinetic-model of the chemical etching of Si(111) surfaces by buffered HF solutions. *Surf. Sci.*, 275(3):407–413, Sept. 1992.

[55] R. Jolly and R. Muller. Miniature cantilever beams fabricated by anisotropic etching of silicon. *J. Electrochem. Soc.*, 127:2750–2754, 1980.

[56] D. Kandel and J. Weeks. Theory of impurity-induced step bunching. *Phys. Rev. B: Condens. Matter Mater. Phys.*, 49(8):5554–5564, Feb. 1994.

[57] J. Kasparian, M. Elwenspoek, and P. Allongue. Digital computation and in situ STM approach of silicon anisotropic etching. *Surf. Sci.*, 388(1-3):50–62, Oct. 1997.

[58] M. Koper. Combining experiment and theory for understanding electrocatalysis. *J. Electroanal. Chem.*, 574:375–386, 2005.

[59] H. Kretschmer, X. Xia, J. Kelly, and A. Steckenborn. Anisotropic etching of three-dimensional shapes in silicon - the important role of galvanic interaction. *J. Electrochem. Soc.*, 151(10):C633–C636, 2004.

[60] L. Landsberger, S. Naseh, M. Kahrizi, and M. Paranjape. On hillocks generated during anisotropic etching of Si in TMAH. *J. Microelectromech. S.*, 5(2):106–116, June 1996.

[61] L. Landsberger, A. Pandy, and M. Kahrizi. Silicon etch anisotropy in tetra-methyl ammonium hydroxide: Experimental and modeling observations. *Sensor. Mater.*, 13(5):293–301, 2001.

[62] V. Lehmann. *Electrochemistry of Silicon.* Wiley-VCH, 2002.

[63] D. Moore, M. Lutwyche, N. Fujimaki, and K. Gotoh. Fabrication of suspended microstructures for devices. *Semicond. Sci. Technol.*, 4:401–105, 1991.

[64] U. Neuwald, A. Feltz, E. Memmert, and R. Behm. Chemical oxidation of hydrogen passivated Si(111) surfaces in H_2O_2. *J. Appl. Phys.*, 78:4131, 1995.

[65] Q. Nguyen and M. Elwenspoek. Influence of an applied potential on the anistropic etch rates of silicon in KOH. In *16th Micromechanics Europe (MME) Workshop*, pages 45–, 2005.

[66] Q. Nguyen and M. Elwenspoek. Characterisation of anisotropic etching in KOH using network etch rate function model: influence of an applied potential in terms of microscopic properties. In *International MEMS Conference 2006 (iMEMS 2006)*, pages –, 2006.

[67] Q. Nguyen and M. Elwenspoek. Influence of applied potentials on anisotropic etching of silicon described using kinematic wave etch model. *J. Electrochem. Soc.*, Submitted:–, 2007.

[68] A. Nijdam, J. Berenschot, J. van Suchtelen, J. Gardeniers, and M. Elwenspoek. Velocity sources as an explanation for experimentally observed variations in Si{111} etch rates. *J. Micromech. Microeng.*, 9(2):135–138, June 1999.

[69] A. Nijdam, J. Gardeniers, J. Berenschot, E. van Veenendaal, J. van Suchtelen, and M. Elwenspoek. Influence of the angle between etched (near) Si{111} surfaces and the substrate orientation on the underetch rate during anisotropic wet-chemical etching of silicon. *J. Micromech. Microeng.*, 11(5):499–503, Sept. 2001.

[70] A. Nijdam, J. Gardeniers, C. Gui, and M. Elwenspoek. Etching pits and dislocations in si{111}. *Sens. Actuators, A*, 86(3):238–247, Nov. 2000.

[71] A. Nijdam, J. van Suchtelen, J. Berenschot, J. Gardeniers, and M. Elwenspoek. Etching of silicon in alkaline solutions: a critical look at the {1 1 1} minimum. *J. Cryst. Growth*, 199:430–434, Mar. 1999.

[72] A. Nijdam, E. van Veenendaal, H. Cuppen, J. van Suchtelen, M. Reed, J. Gardeniers, W. van Enckevort, E. Vlieg, and M. Elwenspoek. Formation and stabilization of pyramidal etch hillocks on silicon {100} in anisotropic etchants: Experiments and Monte Carlo simulation. *J. Appl. Phys.*, 89(7):4113–4123, Apr. 2001.

[73] R. Oosterbroek, J. Berenschot, S. Schlautmann, G. Krijnen, T. Lammerink, M. Elwenspoek, and A. van den Berg. Designing, simulation and realization of in-plane operating micro valves, using new etching techniques. *J. Micromech. Microeng.*, 9:194–198, 1999.

[74] H. Philipsen, J.-N. Chazalviel, P. Allongue, F. Ozanam, and K. J.J. In situ ir spectroscopy to study anodic oxidation of Si(111) in koh solution. *ECS Trans.*, 6:481–488, 2007.

[75] H. Philipsen and J. Kelly. Anisotropy in the anodic oxidation of silicon in KOH solution. *J. Phys. Chem. B*, 109(36):17245–17253, Sept. 2005.

[76] H. Philipsen, N. Smeenk, H. Ligthart, and J. Kelly. Exploiting anisotropy for in situ measurement of silicon etch rates in KOH solution. *Electrochem. Solid-State Lett.*, 9(7):C118–C121, 2006.

[77] G. Pietsch, Y. Chabal, and G. Higashi. The atomic-scale removal mechanism during chemomechanical polishing of Si(100) and Si(111). *Surf. Sci.*, 333:395–401, July 1995.

[78] K. Sato, M. Shikida, Y. Matsushima, T. Yamashiro, K. Asaumi, Y. Iriye, and M. Yamamoto. Characterization of orientation-dependent etching properties of single-crystal silicon: effects of KOH concentration. *Sens. Actuators, A*, 64(1):87–93, Jan. 1998.

[79] K. Sato, M. Shikida, T. Yamashiro, K. Asaumi, Y. Iriye, and M. Yamamoto. Anisotropic etching rates of single-crystal silicon for TMAH water solution as a function of crystallographic orientation. *Sens. Actuators, A*, 73(1-2):131–137, Mar. 1999.

[80] K. Sato, M. Shikida, T. Yamashiro, M. Tsunekawa, and S. Ito. Roughening of single-crystal silicon surface etched by KOH water solution. *Sens. Actuators, A*, 73(1-2):122–130, Mar. 1999.

[81] H. Scheel. Historical spects of crystal growth technology. *J. Cryst. Growth*, 211:1–12, 2000.

[82] W. Schneider. Kinematic-wave theory of sedimentation beneath inclined walls. *J. Fluid Mech.*, 120:323–346, 1982.

[83] H. Schroder, E. Obermeier, and A. Steckenborn. Micropyramidal hillocks on KOH etched {100} silicon surfaces: formation, prevention and removal. *J. Micromech. Microeng.*, 9(2):139–145, June 1999.

[84] H. Seidel, L. Csepregi, A. Heuberger, and H. Baumgartel. Anisotropic etching of crystalline silicon in alkaline solutions. I. orientation dependence and behavior of passivation layers. *J. Electrochem. Soc.*, 137(11):3612–3626, 1990.

[85] H. Seidel, L. Csepregi, A. Heuberger, and H. Baumgartel. Anisotropic etching of crystalline silicon in alkaline solutions. II. influence of dopants. *J. Electrochem. Soc.*, 137(11):3626–3632, 1990.

[86] M. Shikida, K. Sato, K. Tokoro, and D. Uchikawa. Differences in anisotropic etching properties of KOH and TMAH solutions. *Sens. Actuators, A*, 80(2):179–188, Mar. 2000.

[87] M. Shikida, K. Tokoro, D. Uchikawa, and K. Sato. Surface morphology of anisotropically etched single-crystal silicon. *J. Micromech. Microeng.*, 10(4):522–527, Dec. 2000.

[88] S. Tan, R. Boudreau, and M. Reed. Anisotropic etching of silicon on {111} and near {111} planes. *Sensor. Mater.*, 13(5):303–313, 2001.

[89] S. Tan, M. Reed, H. Han, and R. Boudreau. Morphology of etch hillock defects created during anisotropic etching of silicon. *J. Micromech. Microeng.*, 4(3):147–155, Sept. 1994.

[90] H. Tanaka, Y. Abe, K. Inoue, M. Shikida, and K. Sato. Effects of ppb-level metal impurities in aqueous potassium hydroxide solution on the etching of si{110} and {100}. *Sensor. Mater.*, 15(1):43–51, 2003.

[91] H. Tanaka, Y. Abe, T. Yoneyama, J. Ishikawa, O. Takenaka, and K. Inoue. Effects of small amount of impurities on etching of silicon in aqueous potassium hydroxide solutions. *Sens. Actuators, A*, 82(1-3):270–273, May 2000.

[92] H. Tanaka, S. Yamashita, Y. Abe, M. Shikida, and K. Sato. Fast etching of silicon with a smooth surface in high temperature ranges near the boiling point of KOH solution. *Sens. Actuators, A*, 114(2-3):516–520, Sept. 2004.

[93] J. van den Meerakker. The reduction of hydrogen peroxide at silicon in weak alkaline solutions. *Electrochim. Acta*, 35:1267–1272, 1990.

[94] J. van den Meerakker and M. van der Straaten. A mechanistic study of silicon etching in NH_3/ H_2O_2 cleaning solutions. *J. Electrochem. Soc.*, 137:1239–1243, 1990.

[95] J. van Suchtelen, A. Nijdam, and E. van Veenendaal. The velocity source concept. *J. Cryst. Growth*, 199:17–21, 1999.

[96] J. van Suchtelen and E. van Veenendaal. The construction of orientation-dependent crystal growth and etch rate functions I. mathematical and physical aspects. *J. Appl. Phys.*, 87(12):8721–8731, June 2000.

[97] J. van Suchtelen and E. van Veenendaal. The structure of an underetched convex mask corner explained as the evolution of a saddlepoint vertex. *Sensor. Mater.*, 13(6):325–342, 2001.

[98] E. van Veenendaal, A. Nijdam, J. van Suchtelen, K. Sato, J. Gardeniers, W. van Enckevort, and M. Elwenspoek. Simulation of anisotropic wet chemical etching using a physical model. *Sens. Actuators, A*, 84(3):324–329, Sept. 2000.

[99] E. van Veenendaal, K. Sato, M. Shikida, A. Nijdam, and J. van Suchtelen. Micromorphology of single crystalline silicon surfaces during anisotropic wet chemical etching in KOH: velocity source forests. *Sens. Actuators, A*, 93(3):232–242, Oct. 2001.

[100] E. van Veenendaal, K. Sato, M. Shikida, and J. van Suchtelen. Micromorphology of single crystalline silicon surfaces during anisotropic wet chemical etching in KOH and TMAH. *Sens. Actuators, A*, 93(3):219–231, Oct. 2001.

[101] E. van Veenendaal, P. van Beurden, W. van Enckevort, E. Vlieg, J. van Suchtelen, and M. Elwenspoek. Monte Carlo study of kinetic smoothing during dissolution and etching of the Kossel (100) and silicon (111) surfaces. *J. Appl. Phys.*, 88(8):4595–4604, Oct. 2000.

[102] E. van Veenendaal, P. van Hoof, J. van Suchtelen, W. van Enckevort, and P. Bennema. Kinetic roughening of the Kossel (100) surface: comparison of classical criteria with Monte Carlo results. *Surf. Sci.*, 417(1):121–138, Nov. 1998.

[103] E. van Veenendaal, P. van Hoof, J. van Suchtelen, W. van Enckevort, and P. Bennema. Kinetic roughening of the Kossel (1 0 0) surface. *J. Cryst. Growth*, 199:22–26, Mar. 1999.

[104] E. van Veenendaal, J. van Suchtelen, W. van Enckevort, K. Sato, A. Nijdam, J. Gardeniers, and M. Elwenspoek. The construction of orientation-dependent crystal growth and etch rate functions II: Application to wet chemical etching of silicon in potassium hydroxide. *J. Appl. Phys.*, 87(12):8732–8740, June 2000.

[105] M. Weldon, B. Stefanov, K. Raghavachari, and Y. Chabal. Initial H_2O-induced oxidation of Si(100)-(2x1). *Phys. Rev. Lett.*, 79(15):2851–2854, Oct. 1997.

[106] R. Wind and M. Hines. Macroscopic etch anisotropies and microscopic reaction mechanisms: a micromachined structure for the rapid assay of etchant anisotropy. *Surf. Sci.*, 460(1-3):21–38, July 2000.

[107] R. Wind, H. Jones, M. Little, and M. Hines. Orientation-resolved chemical kinetics: Using microfabrication to unravel the complicated chemistry of KOH/Si etching. *J. Phys. Chem. B*, 106(7):1557–1569, Feb. 2002.

[108] O. Wolter, T. Bayer, and J. Greschner. Micromachined silicon sensors for scanning force microscopy. *J. Vac. Sci. Technol., B*, 9:1353–1357, 1991.

[109] X. Xia, C. Ashruf, P. French, and J. Kelly. Galvanic cell formation in silicon/metal contacts: The effect on silicon surface morphology. *Chem. Mater.*, 12(6):1671–1678, June 2000.

[110] X. Xia, C. Ashruf, P. French, J. Rappich, and J. Kelly. Etching and passivation of silicon in alkaline solution: A coupled chemical/electrochemical system. *J. Phys. Chem. B*, 105(24):5722–5729, June 2001.

[111] X. Xia and J. Kelly. The influence of oxidizing agents on etching and passivation of silicon in KOH solution. *Electrochim. Acta*, 45(28):4645–4653, 2000.

[112] X. Xia and J. Kelly. Chemical etching and anodic oxidation of (100) silicon in alkaline solution: the role of applied potential. *Phys. Chem. Chem. Phys.*, 3(23):5304–5310, 2001.

[113] L. Zimmermann, J. Ebersohl, F. Lehung, J. Berry, F. Baillieu, P. Rey, B. Diem, S. Renard, and P. Caillat. Airbag application - a microsystem including a silicon capacitive accelerometer, CMOS switched-capacitor electronics and true self-test capability. *Sens. Actuators, A*, 46:190–195, 1995.

[114] I. Zubel. The model of etching of (hkl) planes in monocrystalline silicon. *J. Electrochem. Soc.*, 150(6):C391–C400, June 2003.

[115] I. Zubel and I. Barycka. Silicon anisotropic etching in alkaline solutions I. the geometric description of figures developed under etching Si(100) in various solutions. *Sens. Actuators, A*, 70(3):250–259, Oct. 1998.

[116] I. Zubel, I. Barycka, K. Kotowska, and M. Kramkowska. Silicon anisotropic etching in alkaline solutions IV - the effect of organic and inorganic agents on silicon anisotropic etching process. *Sens. Actuators, A*, 87(3):163–171, Jan. 2001.

[117] I. Zubel and M. Kramkowska. The effect of isopropyl alcohol on etching rate and roughness of (100) Si surface etched in KOH and TMAH solutions. *Sens. Actuators, A*, 93(2):138–147, Sept. 2001.

[118] I. Zubel and M. Kramkowska. Etch rates and morphology of silicon (h k l) surfaces etched in KOH and KOH saturated with isopropanol solutions. *Sens. Actuators, A*, 115(2-3):549–556, Sept. 2004.

Summary

Anisotropic etching of silicon (Si) in alkaline solutions have remained a reliable bulk micromachining process for micro electrical mechanical systems (MEMS) for several decades. The anisotropy, or (surface) orientation dependence, in the silicon etch rate allows for the fabrication of complex, micrometer-sized structures with well-defined geometries. Using smart mask designs in combination with other bulk and surface micromachining processes, complex MEMS devices can be fabricated for various applications such as sensor, actuator or micro-fluidics systems. Although wet chemical etching is widely used within the industry, the fundamental basis behind the actual etch process is not entirely clear. Anisotropic etching of Si has proven to be a very complex system, where in-depth knowledge is required ranging from a chemical scale (i.e. surface reactions) to a macroscopic scale (e.i. surface morphology and etch features). While the surface etch reactions are purely chemical in nature, more recent investigations have shown the additional importance of the electrochemistry within the system, which further increases the complexity of the system.

Within this thesis we aim to investigate the influence of the electrochemistry on anisotropic etching. We focus on the impact of a constant applied potential on a more microscopic scale. The electrochemistry of Si in an alkaline solution (such as concentrated potassium hydroxide (KOH)) on a chemical scale is well established. It is, however, not entirely clear how the electrochemistry affects microscopic phenomena such as the step or surface anisotropy, roughening and step velocity. Understanding this not only gives more insight into the electrochemistry and electrochemical oxidation mechanism, but also the etch mechanism as a whole. For MEMS application and processing, this can lead to increased control and predictability of the etch process. This in turn can help in the design and fabrication of better structures and surface quality, which increases device performance. Investigating the etch mechanism on a microscopic scale is however not straight forward. The processes, phenomena and properties of interest on this scale, are very difficult to measure directly. To overcome this, we have used the kinematic wave theory to determine these properties indirectly. The kinematic wave theory can be used to construct a continuous etch model where the etch rate is a function of the Si surface orientation and several physical parameters. These parameters are linked to the microscopic properties of interest. Using measured etch rate data obtained from primarily wagon-wheel patterns, these parameters can then be determined.

Changes in these parameters and related physical processes can be investigated as a function of the electrochemical oxidation (applied potential). The results show that an anisotropy in electrochemical oxidation is not only present on surfaces, but also on surface steps. At very positive potentials, step anisotropy reversal is observed, where

the anisotropic oxidation leads to the fastest etching steps effectively becoming the most stable steps and visa versa.

Focusing on the (111) surface steps shows that step anisotropy is commonly regarded as the reactivity difference between step and kink sites (mono- and dihydride terminated steps). However, etch experiments using hemispherical shaped Si samples, which provides a much wider and more detailed measurement range, show a different picture. The results indicate that a distinction between different kinds of dihydride sites is necessary to account for the observed etch patterns. The (111) step velocity as a function of the step orientation can then be accurately determined from the experimental data using an extended etch model based on the kinematic wave theory. Changes in the step velocity due to the addition of tetramethylammonium hydroxide (TMAH), indicates that the interaction between TMAH and the (111) sites is step-type specific, with 'isolated' dihydrides showing the largest interaction. Information on how the step velocity is dependent on the electrochemistry can be used to investigate step interaction mechanisms with additives. By changing the electrochemical oxidation state of the (111) steps and observing the change in the interaction between the additive and the (111) steps, the interaction mechanism can be investigated. In this work we investigated a proposed electrostatic interaction between (111) steps and the TMA^+ cation. The results, however, show that this mechanism is not consistent with the observed changes in step velocity as a function of both the applied potential and TMA^+ concentration. This indicates the presence of different interaction mechanisms.

Of all the three major orientations, (110) shows the most peculiar etch rate and surface morphology. In order to describe the saddle point in the etch rate in the vicinity of (110), a pseudo stepflow/birth-and-spread mechanism is added to the etch model. Although accurate, the use of this model is currently very dependent on the available data. To investigate the characteristic roof-tile/trapezoidal hillock morphology, in-situ experiments have been performed. The obtained microscope images, together with an image analysis procedure and the kinetic Monte Carlo simulations in the literature, provide information concerning the formation and evolution of the (110) morphology. Changes to the morphology due to an applied potential, are investigated in-situ, while changes due to the addition of hydrogen peroxide or an increase in KOH concentrations are investigated ex-situ. The observed destabilisation of the typical roof-tile morphology and the formation of the trapezoidal hillocks are consistent with the expected changes the (111) step anisotropy.

The work outlined in this thesis, provides more insight into the effect of the electrochemistry on the anisotropic etching of silicon. It demonstrates the use of the kinematic wave theory for the determination of 'difficult' microscopic properties such as terrace roughening and step velocity. In combination with either wagon-wheel patterns or hemispherical samples, future experiments can focus on the influence of different process parameters including other organic/ionic additives and electrochemical oxidisers. In addition, it was shown that in-situ monitoring of surface morphology is possible. These measurements can also be expanded, incorporate different process conditions and Si surfaces. All this information can lead to a better understanding of, not only the etch mechanism, but also the formation mechanism of different morphologies and surface features. This allows for better predictability and control of wet chemical etching within MEMS.

Samenvatting

Nat chemisch etsen van silicium (Si) in alkalische oplossingen heeft zich in de afgelopen decennia bewezen als een betrouwbare fabricage methode binnen MEMS (micro electrical mechanical system) technology. De anisotropie (oppervlakte orientatie afhankelijkheid) in de ets snelheid maakt de fabricage van complexe structuren op micrometer schaal met goed gedefinieerde geometriën het mogelijk. Door gebruik te maken van slimme masker ontwerpen en te combineren met andere bulk en oppervlakte fabricage methodes kunnen MEMS apparaten worden gemaakt maken voor toepassingen zoals sensor, actuator of micro fluidische systemen. Ondanks het feit dat anisotroop etsen algemeen toegepast wordt, is de fundamentele achtergrond van het ets process nog niet geheel duidelijk. Anisotroop etsen is een heel complex systeem gebleken, waar gedetailleerde kennis op chemische schaal (zoals oppervlakte reacties) tot aan een microscopische schaal (zoals morphology en ets patronen) noodzakelijk is. De ets reactie zelf kan beschouwd worden als een chemisch process. Recenter onderzoek heeft echter het belang van de elektrochemie in het ets systeem aangetoond, wat de complexiteit van het systeem verder verhoogd.

Het werk binnen dit proefschrift richt zich primair op het onderzoeken van de invloed van de elektrochemie op anisotroop etsen. De focus ligt op het bekijken van de invloed van een constant aangelegde spanning op het ets gedrag. De elektrochemie van silicium in een alkalische oplossing (zoals geconcentreerde kaliumhydroxide (KOH)) op een chemische schaal is algemeen bekend. Wat de invloed van de elektrochemie is op microscopische eigenschappen, zoals stap en oppervlakte anisotropie, verruwing en stap snelheid is echter nog niet duidelijk. Informatie over deze invloed kan niet alleen leiden tot een beter begrip van de elektrochemie en elektrochemische oxidatie maar ook van het ets mechanisme in zijn geheel. Voor MEMS applicaties betekent dit een betere controle en voorspelbaarheid van de ets methode. Dit op zijn beurt kan leiden tot de fabricage van betere strukturen en oppervlakte kwaliteit wat de apparaat prestaties bevorderd. Het ets mechanism onderzoeken op een microscopische schaal is echter niet triviaal. Het direkt bepalen van de, op deze schaal, interessante processen en eigenschappen is uitermate moeilijk. Binnen dit werk hebben we de kinematic wave theorie gebruikt voor het (indirekt) bepalen van deze eigenschappen. The kinematic wave theorie kan worden gebruikt om een ets model op te bouwen, waar de oppervlakte ets snelheid een functie is van de Si oppervlakte orientatie en verscheidene, fysisch relevante parameters. Deze parameters zijn gekoppeld aan interessante microscopische eigenschappen. Door vervolgens gebruik te maken van ets snelheid metingen, hoofdzakelijk verkregen met wagenwiel patronen, kunnen deze parameters worden bepaald.

Veranderingen in deze parameters en de gerelateerde processen als een functie van de electrochemische oxidatie (de aangelegde spanning) kunnen dan worden onderzocht. De resultaten laten zien dat een anisotropie in electrochemische oxidatie van oppervlakte stappen aanwezig is. Bij zeer positieve aangelegde potentialen is stap anisotropie reversie te zien, waar de snelst etsende oppervlakte stappen door de anisotropie in oxidatie de meest stabiele stappen worden en omgekeerd. Op (111) oppervlakken wordt de stap anisotropy algemeen beschouwd als het verschil in reactiviteit tussen stap en kink locaties (mono- en dihydride getermineerde stappen). Ets experimenten met hemispherische Si monsters, waarmee de anisotropische ets snelheid gedetailleerde kan worden gemeten, laten een ander beeld zien. Om de geobserveerde ets patronen te verklaren moet een distinctie gemaakt worden tussen verschillende soorten dihydride locaties. Met een uitgebreide ets model, kan dan de (111) stap snelheid als een functie van de stap orientatie worden bepaald uit experimentele data. Veranderingen in de stap snelheid door toevoeging van tetramethylammonium hydroxide (TMAH) wijzen op een stap locatie specifieke interactie tussen (111) oppervlakte stappen en TMAH. De grootste interactie wordt waargenomen bij geïsoleerde dihydrides. Deze informatie kan worden gebruikt om interactie mechanismen tussen Si stappen en additieven te bestuderen. Door de oxidatie toestand van de (111) stappen te veranderen en de verandering in interactie tussen de additieven and (111) stappen te observeren kunnen deze mechanismen worden bestudeerd. In dit werk hebben we een mogelijke electrostatische interactie mechanisme tussen (111) stappen en TMA$^+$ kation onderzocht. Dit mechanisme bleek echter niet consistent met de geobserveerde veranderingen in de stap snelheid als functie van de aangelegde spanning en TMA$^+$ concentratie. Dit duidt op de aanwezigheid van een andere interactie mechanisme.

Van de drie belangrijkste kristal orientaties, vertoont de (110) familie de meest uitzonderlijke ets snelheid en oppervlakte morphology. Om het zadelpunt in de ets snelheid bij de (110) orientatie te beschrijven, is een pseudo stepflow/birth-and-spread mechanisme aan het basis etsmodel toegevoegd. Ondanks het feit dat het model de (110) ets snelheid nauwkeurig kan beschrijven, is het gebruik ervan erg afhankelijk van de beschikbare meetdata. Om de karakteristieke dakpan/piramide morphologie nader te onderzoeken, zijn in-situ experimenten gedaan. De verkregen microscoop beelden, samen met een beeld analyse procedure en de kinetic Monte Carlo simulaties in de literatuur, verschaffen veel informatie over de vorming en evolutie van de (110) morphologie. Veranderingen in de morphologie door een aangelegde spanning zijn in-situ onderzocht, terwijl de veranderingen als een gevolg van de toevoeging van waterstofperoxide of een verhoging van de KOH concentratie zijn ex-situ onderzocht. De geobserveerde destabilisatie van de dakpan morphology en de vorming van piramides zijn consistent met de verwachte veranderingen in de (111) stap anisotropie.

Dit proefschift geeft meer inzicht in het effect van de elektrochemie op het anisotroop etsen van Si. Verder wordt de kinematic wave theorie gebruikt voor het bepalen van de microscopische eigenschappen zoals stap snelheid. In combinatie met wagen-wiel patronen of hemispherische Si monsters zijn er veel mogelijkheden tot vervolg experimenten met de focus op factoren zoals de invloed van organisch/ionische additieven en oxidatoren. Verder is de mogelijkheid om oppervlakte morphology in-situ te volgen gedemonstreerd. Deze metingen kunnen worden uitgebreid met experimenten met andere proces condities and oppervlakken. Deze informatie kan leiden to een beter begrip van niet alleen het ets mechanism, maar ook de formatie van verschillen morphologien en oppervlakte structuren.

Publications

Journal papers

Q.D. Nguyen and M.C. Elwenspoek. Influence of applied potentials on anisotropic etching of silicon described using kinematic wave etch model. *Submitted*, 2007.

Conference contribution

Q.D. Nguyen and M.C. Elwenspoek. Characterisation of anisotropic etching in KOH using network etch rate function model: influence of an applied potential in terms of microscopic properties. *International MEMS Conference 2006 (iMEMS 2006)*, Singapore, May 9-12, 2006.

Q.D. Nguyen and M.C. Elwenspoek. Recognising step anisotropy reversal behaviour using an extended network etch rate function model. *Fifth international workshop on Physical Chemistry of Wet Etching of Semiconductors (PCWES)*, Saarbrücken, Germany, June 19-21, 2006.

Q.D. Nguyen and M.C. Elwenspoek. Influence of electrochemistry on step anisotropy. *Progress in anisotropic wet chemical etching (PiAWCE)*, Levi, Finland, 2007.

Posters

Q.D. Nguyen and M.C. Elwenspoek. Influence of an applied potential on the anisotropic etch rates of silicon in KOH. *16th Micromechanics Europe (MME) Workshop*, Göthenburg, Sweden, 2005.

Acknowledgements

The end of a four year journey approaches, filled with a lot of work, stress, frustration and a huge amount of plain old good fun. But of course, one does not embark on this journey alone. I would like to acknowledge the people who have helped and accompanied me along the way. First and foremost, I would like to thank my supervisor Miko Elwenspoek for his guidance and support. I am grateful for the amount of freedom and trust you have given me to shape my own research and for your critical eye for the times my own ideas wander off too far.

As this research is part of a larger project involving two other universities, I would like to thank Prof. dr. John Kelly and Prof. dr. Elias Vlieg, for their support, discussions and insights, expanding the project beyond micromachining alone. I would also like to thank my two counterparts in Utrecht and Nijmegen with whom I spend (too) many hours discussing the project. These discussions inevitably end with more questions. All-in-all the cooperations was very enjoyable. Harold, you still are way too easy to bribe with a good steak (à point, s'il vous plaît). Ismail, I do think we went off the deep end a bit during the noodle-filled ID32 night shift ("Walk like an egyptian").

During my project I had the opportunity to spend some time at the Micromachining and MEMS lab at the Nagoya university. Although my stay was short I have very fond memories of my time there. I am especially grateful to Sato-sensei for your guidance and hospitality. A special thanks to Rembri for your insights, discussions, enthusiasm and for helping me getting my bearings in Japan. I would also like to thank Kato-san for all her help even after I left Japan. Thanks to Xing, Prem and the rest of the group members for making it such an enjoyable time. I should also not forget Chi. Thank you for welcoming me and for all your help.

I am very lucky to have worked in a group like TST, or more lovingly called MicMec. A creative, casual, fun and at times slightly dysfunctional group of people containing many characters, cultures and disciplines. The many barbecues, sailing trips and smikkelparties is a sign of the enjoyable atmosphere in the group. To be honest, you need a certain amount of eccentricity, sense of humor and a thick skin, especially when you want to join the infamous lunchtime discussions.

A special thanks to my paranimfs. Laura, my four year companion in exile. I did not expect to be put somewhere in a forgotten room, far removed from the other PhDs. With you as a roommate, the fun and laughs more then make up for it, even when I ‘convince’ you to help clean the chemical lab or ruin your plating bath (”you should cover it with aluminium foil...”). And Doekle, you are one of the few people who understands and shares my passion for photography. Although I think Marije (thank you for the bike) does not really appreciates having two cameras pointing at her simultaneously.

Thanks to Pino for his help in designing and building my experimental setups. Even if some of the setups end up being impractical (the surface profiler) and slightly dangerous (the infamous microwave). I would also like to thank Henk who helped to me to build a microscope setup for the wagon-wheel measurements procedure which improved from head-ache inducing to acceptably tedious. Thanks to Henri for your wild but useful ideas (thanks a lot for the microwave suggestion..) and Erwin for being one of the very few people in the group who is actually enthusiastic about KOH etching.

A big thanks to all the Micmeccers, past and present, staff, PhD’s, students and all the people who have made this such an enjoyable group to work in; Antonella, Arjan, Berker, Deladi, Dannis, Dennis, Dick, Doekle, Edin, Gijs, Hanh, Hien, Imran, Ingrid, Jeroen, John, Joost, Judith, Kees, Liesbeth, Luis, Marcel, Maryana, Marcus, Meint, Mink, Nataliya, Nema, Niels, Remco, Ram, Roald, Sandeep, Saravanan, Shahina, Susan, Srinivas, Theo, Toon, Vitaly, Yiping and to everybody I have forgotten to mention.

Although I have not spend as much time as others in the cleanroom, I would like to thank all the cleanroom staff for their help and support.

One also never forgets old friends, especially best of friends. Tom, although distances have become greater, my close friendship with you and Verena has not diminished. Where ever I will end up from now on I know it will not fade. Of course, an internet connection really helps.

A special thanks to Bao Han for walking beside me and keeping me company from the other side of the world. As everyday life has intruded, keeping in touch has become more difficult. Although they have become increasingly rare, I always cherish our little talks, telephones calls, emails or text messages.

Lovely Quyen, I did not expect to meet somebody like you during my stay in Japan. With a smile I think back at all the fun and laughs we had on the road, from a deserted Tokyo to the almost blossoming sakura at the foot of a windy castle. You have become very important to me and you made it so very hard for me to leave Japan again.

My sister Loan has undertaken a similar journey before me. Your strength, intelligence and determination does not match your physical size. You have always been an inspiration to me, although as a kid one cannot really appreciate a sister who is older, smarter, taller and stronger. Your life with Richard and little Luka and Jenny shows me how much catching up I still have to do.

Finally I want to thank my parents. Bo va Me, thank you for always allowing me to chose my path, for giving me the tools to shape my own life and for being with me every step of the way. Thank you for your trust and support, for your wisdom and love.

Curriculum Vitae

Quoc Duy Nguyen was born on the 30th of September in Saigon, Vietnam but came to the Netherlands before his first birthday. He attending the elementary schools in both Oss and Weert. In 1996, Duy successfully passed the pre-university education (VWO) at the Philips van Horne Scholen Gemeenschap in Weert.

After wards he started studying Chemical Engineering and Chemistry at the Eindhoven University of Technology. During his study he spend an eight month period at Akzo Nobel Chemical Research in Arnhem, The Netherlands. Here he worked on the modeling and optimalisation of the absorber-stripper section of existing CS_2 production plants. His final graduation project was done at the Chemical Engineering and Chemistry group led by Prof. dr. J. Schouten. In 2002 he obtained his Master of Science degree investigating the influence of suspended catalyst particles on gas-liquid mass transfer in a stirred slurry column.

Desiring to make small side step away from chemistry, he joined Prof. dr. Elwenspoek's Transducers Science and Technology group at the University of Twente, as a PhD student. Here he investigated the influence of electrochemistry on the anisotropic etching of silicon using the kinematic wave theory. The results of this study are presented in this thesis.